Tuning guidelines for model-free control

Dissertation

zur Erlangung des Grades
des Doktors der Ingenieurwissenschaften
der Naturwissenschaftlich-Technischen Fakultät
der Universität des Saarlandes

von

Peter Michael Scherer

Saarbrücken

2025

Tag des Kolloquiums:	9. Dezember 2024
Dekan:	Prof. Dr.-Ing. D. Bähre
Berichterstatter:	Prof. Dr.-Ing. habil. J. Rudolph Prof. Dr. H. Mounier
Vorsitz:	Prof. Dr. K. Flaßkamp
Akad. Mitarbeiter:	Dr.-Ing. C. Bur

Eidesstattliche Versicherung

Hiermit versichere ich an Eides statt, dass ich die vorliegende Arbeit selbstständig und ohne Benutzung anderer als der angegebenen Hilfsmittel angefertigt habe. Die aus anderen Quellen oder indirekt übernommenen Daten und Konzepte sind unter Angabe der Quelle gekennzeichnet. Die Arbeit wurde bisher weder im In- noch im Ausland in gleicher oder ähnlicher Form in einem Verfahren zur Erlangung eines akademischen Grades vorgelegt.

Saarbrücken, 14. Januar 2025
Ort, Datum

Peter Michael Scherer

Zusammenfassung

Die Regelung komplexer Systeme ohne Kenntnis eines detaillierten physikalisch-mathematischen Modells, wie es die meisten gängigen Ansätze erfordern, ist ein erstrebenswertes Ziel. In Anbetracht der Tatsache, dass die Komplexität moderner Systeme ständig zunimmt, wächst der Bedarf an einer universellen Regelungsstrategie. Fliess und Join (2009, 2013) haben einen signalbasierten Ansatz vorgeschlagen, der weder ein physikalisch motiviertes Modell des Systems benötigt noch auf zeitaufwändiges und datenintensives Training angewiesen ist. Die systematische Auslegung dieser so genannten modellfreien Regler stellt jedoch weiterhin eine anspruchsvolle Aufgabe dar. In dieser Arbeit wird mit dem Abtasten des Parameterraums für ein Proportionalventil und eine magnetisch gelagerte Platte die Grundlage für eine systematische Auslegung des betrachteten Reglers gelegt. Es wird gezeigt, dass die Stabilität des geschlossenen Regelkreises mit Hilfe des verallgemeinerten Hermite-Biehler-Theorems analysiert werden kann. Theoretische Grenzen für die Reglerparameter werden am Beispiel eines Gleichstrommotors berechnet und durch diverse Experimente validiert. Zusätzlich wird die Parametrierung der algebraischen Ableitungsschätzer untersucht, die zur Schätzung der unbekannten Größen sowie für die Implementierung des Regelgesetzes verwendet werden. Mit diesen neuen Erkenntnissen werden Leitlinien abgeleitet, die zu einer systematischen Parametrierung des modellfreien Reglers führen.

Abstract

The control of complex systems without the need of deriving a detailed physics-based mathematical model of the system, which is a necessity for most of the common control approaches, is a desirable goal. Considering the fact that the complexity of modern systems is ever increasing, the need for a universal control solution is also growing. Fliess and Join (2009, 2013) have proposed a signal-based control approach that neither requires a physically-motivated model of the system considered nor relies on time-consuming and data-intensive training. However, the systematic tuning of these so-called model-free controllers is still a challenging task. In this thesis, the sampling of the control parameter set for a proportional valve and a magnetically supported plate lay the foundation for a systematic tuning approach of the proposed control method. It is shown that the stability of the closed loop can be analysed using the generalised Hermite-Biehler theorem. Theoretical bounds for the controller parameters are calculated for a DC motor as a basic example and validated by various experiments. Additionally, the parametrisation of the algebraic differentiators used to estimate the unknown quantities required for the implementation of the control law is investigated. With these new findings, guidelines can be formulated leading to a systematic tuning of the model-free control law.

Contents

Chapter 1

Introduction

Established model-based control approaches such as flatness-based control (see, e.g. Fliess et al. (1992, 1995) and for an introduction see Rudolph (2021)), model preditive control (cf. Qin and Badgwell (2003) for a survey on this topic) or passivity-based control (see, e.g. Willems (1972) for an introduction), just to name a few, rely on physically motivated mathematical models of the systems considered. These models are often derived using conservation laws, e.g. conservation of mass, momentum or energy. As the complexity of modern systems increases, so does the effort required to describe them with corresponding mathematical models. Especially effects such as friction, magnetic hysteresis or ageing are often cumbersome to derive up to a point at which the benefit of the additional accuracy is overshadowed by the modelling effort required. Another aspect of the model-based control approaches, beside the acquisition of the model, is the parameter identification, i.e. the search for numerical values of the parameters such that the model of the system approximates the experimental data well enough. Not only that an additional step for the implementation of the control law is required, the parameter identification brings its own difficulties and the number of parameters to be identified also increases with the complexity of the model and so does the effort for identifying them.

So-called model-free control (MFC) approaches, i.e. approaches that do not rely on physically motivated mathematical models, e.g. proportional integral derivative (PID) control, fuzzy control (see, e.g. Zadeh (1965) for an introduction to fuzzy sets and Mamdani (1974) for an early application of fuzzy control) or neuronal networks (cf. Yeşildirek and Lewis (1995)) represent an alternative to model-based control. In contrast to the latter methods, Fliess and Join (2009, 2013)[1] have proposed a signal-based approach that neither relies on physically motivated models of the systems nor requires time consuming and data intensive training. For the proposed algorithm, the system under consideration is locally approximated for a short period of time by a so-called ultra-

[1] In the following, the acronym MFC will refer only to the method proposed by Fliess and Join (2009, 2013).

local model, i.e. a low-order differential equation with unknown parts. The unknown part of the system combines unmodelled dynamics as well as disturbances, whereas no distinction between the latter is considered. To realise a controller based on an ultra-local model, the unknown parts have to be estimated for a subsequent compensation. Algebraic differentiators as first introduced in Mboup et al. (2007, 2009) are closely linked to the MFC method considered, as they can be used for the estimation task. In recent years, the algebraic differentiators have proven to be a powerful tool (see, e.g. Othmane et al. (2022, Sec. 6) for an overview of possible applications) and with that different viewpoints emerged on how to parametrise them. Kiltz and Rudolph (2013) and Mboup and Riachy (2014, 2018), for example, consider a frequency-domain interpretation of the algebraic differentiators that is, to the best of the author's knowledge, not explicitly considered for the design of the MFC laws. With the works Kiltz (2017) and Othmane (2022b) a systematic parametrisation of the algebraic differentiators with specific frequency-domain characteristics such as cutoff frequency and filter order is possible. The additional insight gained for the algebraic differentiators should also lead to a better understanding of the MFC approach considered, e.g. regarding the parametrisation and the stability of the closed loop, but has up until now not been considered in the literature.

In Section 1.1, the state of the art regarding MFC is briefly presented, followed by the motivation and the aim of the thesis in Section 1.2. After that, the contribution of this work is stated and two peer-reviewed and published journal papers are summarised in Section 1.3. The chapter concludes with a short presentation of the thesis structure in Section 1.4.

1.1 State of the art

The MFC approach proposed by Fliess and Join (2009, 2013) has already been applied in numerous applications ranging from different technical domains. In the field of electronics, recent examples of a successful implementation of the MFC method considered are discussed in Zhang et al. (2022) for AC/DC converters, in Li et al. (2022) for buck converters, and in Wachter et al. (2023) for grid-tied inverters. Besides the use in the control of electronic systems, automotive applications are also of interest, e.g. active suspensions in Haddar et al. (2019) or direct fuel injection systems in Carvalho et al. (2024). Nonetheless, a more important field is autonomous driving which is considered in Villagra and Herrero-Pérez (2012), Menhour et al. (2017), Polack et al. (2017, 2019), and Hegedűs et al. (2022). The works of Al Younes et al. (2014), Bekcheva et al. (2018), and Barth et al. (2020), show that the control of unmanned aerial vehicles is also possible with the methods introduced by Fliess and Join (2009, 2013). Successful simulation studies in the field of renewable energy can be found in Bara et al. (2017) for photovoltaic energy generation and in Lafont et al. (2020) for the control of wind turbines. More exotic applications of the MFC approach are found in Gédouin et al.

(2011) for shape memory alloys, in De Miras et al. (2013) and Moraes and da Silva (2015) for magnetic levitation, in Ziane et al. (2023) for alkaline water electrolysis, in Lafont et al. (2015) for green houses, and in Fliess and Join (2023) for video streaming. This vast list of examples shows the capabilities of this powerful method that can be incorporated in various domains.

Besides the application of the approach, various authors have published insightful contributions to the topic of MFC. In d'Andréa-Novel et al. (2010) the connection of the MFC approach to a classical PID controller is presented. Therein, the integral part is approximated by a Riemann sum and the derivative part using the difference quotient. With these approximations, a parameter combination can be found, leading to an identical parametrisation of both approaches.

A so-called adaptive model-free approach is proposed in Doublet et al. (2016) and Polack et al. (2017). In these contributions, the input gain is adapted online by an estimation using the ultra-local model under the assumption of a piece-wise constant input gain. This approach ultimately leads to better simulation results for systems with unknown delay and varying velocities of the considered 7 degree of freedom vehicle model, in Doublet et al. (2016) and Polack et al. (2017), respectively.

The importance of the input gain is also discussed in Gédouin et al. (2011). Therein, the input gain function $y \mapsto \alpha g(y)$ of the ultra-local model

$$\dot{y}(t) = F(t) + \alpha g\left(y(t)\right) u(t) \tag{1.1}$$

is a polynomial of degree three. This choice leads to an increased performance of the MFC law based on (1.1). The parameters of the polynomial are identified using steady-state displacements $y(t)$ and constant inputs $u(t)$ of the considered shape memory alloy.

Another combination of MFC with model information is presented in Bekcheva et al. (2018). This contribution presents a cascaded-model-free control approach for a quadcopter. The slower outer-loop, comprising MFC of the positions, is providing reference trajectories for the desired orientation of the copter in combination with model information in the form of a simplified model of the horizontal-plane dynamics considering the orientation of the copter. The obtained orientation trajectories are then the reference for the underlying attitude control which is also based on MFC laws.

In Polack et al. (2019) the brake and velocity control of an autonomous driving car is considered. The effects of the discretisation of the algebraic differentiators used is analysed and in addition to that a tuning procedure for the input gain is presented.

Another systematic tuning approach in the context of vehicle control is suggested in Hegedűs et al. (2022). Therein, a so-called error-based ultra-local model approach is presented which uses a priori model information in the form of a nominal model, in this case the single-track bicycle model. To find a nominal input gain, several simulations are made and the value resulting in the lowest lateral error is chosen. Furthermore, an optimal input gain depending on the lateral velocity is acquired in the same way using

the nominal value as a baseline. Consequently, the used input gain in the MFC law is a function of the lateral velocity. Additionally, a decision tree for choosing the input gain is added to ensure the stability of the closed loop.

The contributions Li et al. (2022) as well as Zhang et al. (2022) are analysing the MFC approach with classical control theoretical tools in the frequency domain. In both cases, the analysis is backed with experiments on a buck converter in Li et al. (2022) and a single-phase AC/DC converter in Zhang et al. (2022), showing the robustness of the approach against parameter variations.

In Delaleau (2014) and Belhadjoudja et al. (2023) the stability of the MFC approach is analysed. Methods from linear systems and the influence of time delays are considered in Belhadjoudja et al. (2023) and tested on an electronic throttle valve, whereas Delaleau (2014) considers a nonlinear single-input single-output (SISO) system with linear input dependence and without occurring input derivatives for the analysis.

The contribution Othmane et al. (2021b) considers a pendulum on cart where the force of the pendulum is regarded as an unknown disturbance to the cart dynamics. The tuning of algebraic differentiators used for the approximation of the unknown part of the ultra-local model is investigated by comparison to an approach based on a disturbance observer. Using the algebraic differentiators results in a better disturbance rejection for the simulated system.

Hereafter, the motivation and aim of the present work can be stated in light of the current literature.

1.2 Motivation and aim of the work

Fliess and Join (2009, 2013) are giving a new point of view on the topic of MFC resulting in very powerful tools that are capable of handling control problems from various domains as discussed in Section 1.1. The works of, e.g. Polack et al. (2019) and Hegedűs et al. (2022) are illustrating that there is a need for a systematic parametrisation of the MFC approach. In the opinion of the author, this demand should be pursued and in addition to that more details concerning the implementation should be added to the current literature to fully unleash the potential of this powerful control method, leading to an increased accessibility for a broader audience. Kiltz and Rudolph (2013) and Mboup and Riachy (2014, 2018) opened an insightful perspective, by interpreting the algebraic differentiators used as filters in the frequency domain. Based on the latter contributions, the works Kiltz (2017) and Othmane (2022b) proposed the parametrisation of the filters with specific frequency-domain characteristics such as cutoff frequency and a filter order, concepts that are on a basic level from an engineering perspective. With this interpretation, the parametrisation of the MFC in the sense of Fliess and Join (2009, 2013) can be further simplified. The contributions Polack

et al. (2019) and Scherer et al. (2023, 2024) already shed some light on a systematic parametrisation approach. Nevertheless, the latter contributions are still missing a formal stability analysis depending on the input gain as well as the controller parameters, i.e. proportional and differential gains, for systems approximated with first-order and second-order ultra-local models.

1.3 Contributions of this work

The main contribution of this work is the insight that the stability analysis of systems controlled by MFC laws based on ultra-local models of first or second order can be done by using methods from the domain of time-delay systems (TDSs). In addition to that, systematic tuning guidelines of the MFC law can be derived, further simplifying the use of the powerful control approach as first introduced by Fliess and Join (2009, 2013). The stability analysis of the TDS, depending on the parameters of the controller, is done using the generalised Hermite-Biehler theorem (see, e.g. Silva et al. (2005, Ch. 5)) and a mathematical model of the system under investigation. By doing so, theoretical bounds of the controller parameters can be derived. The theoretical findings are validated by experimental results obtained from a DC motor. This work differs from existing research in explicitly considering new tuning methods for the algebraic differentiators used for the estimation of unknown quantities necessary for the implementation of the MFC law. The results of these new findings have implications for a broader use of the MFC approach which is important, as the complexity of modern systems continues to increase and at a certain point the cost of modelling exceeds its benefits. The application of the stability analysis is constrained by the necessity of a mathematical model of the system under consideration, which is contradictory to the implementation of a MFC approach. Additionally, the influence of neglected dynamics and nonlinearities is not explicitly considered in this thesis and has to be analysed in future work as this would contribute to a more comprehensive understanding. However, the basic example of a DC motor can be viewed as a first step to get a deeper insight of the MFC approach used. The theory employed provides a framework for understanding the observed phenomena in the parameter set already investigated in the two peer-reviewed and published journal papers Scherer et al. (2023) and Scherer et al. (2024) which are an essential part of this thesis and included in Chapter 5. A short summary of each paper is given in the following as well as an overview on recently gained insights concerning the stability of the closed loop of a system controlled by a MFC law based on first-order and second-order ultra-local models.

1.3.1 Combining model-based and model-free approaches for the control of an electro-hydraulic system

In the contribution Scherer et al. (2023) (see Section 5.1), a combination of model-based and model-free approaches is proposed for the control of an electro-hydraulic system consisting of a piston and four proportional valves (see Fig. 1.1). Details are given on the systematic tuning and the implementation of algebraic differentiators as well as the MFC law using a first-order ultra-local model.

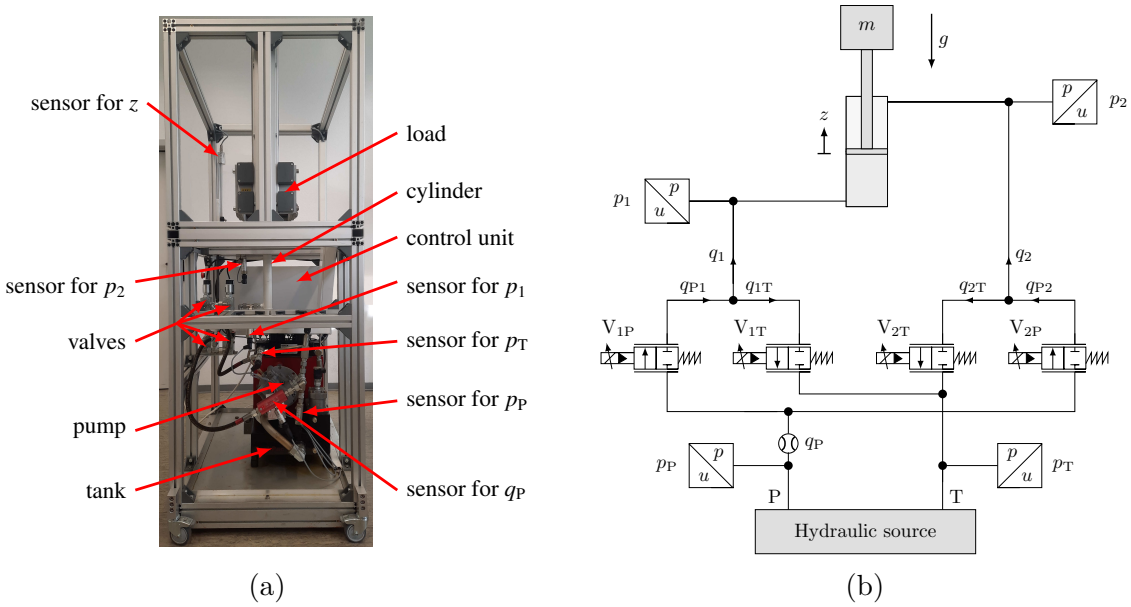

(a) (b)

Fig. 1.1: Photo (a) and hydraulic circuit diagram (b) of the system considered, ©2023 Elsevier. These figures were published in Scherer, P. M., Othmane, A., and Rudolph, J. (2023). Combining model-based and model-free approaches for the control of an electro-hydraulic system. *Control Engineering Practice*, 133:105453. DOI: 10.1016/j.conengprac.2023.105453

A model of the double-acting hydraulic piston actuator is presented and it is shown that this model is flat with the flat output $y = (z, p_\Sigma)$. The quantity z denotes the position of the piston with respect to the middle of the cylinder and the quantity p_Σ denotes the sum of the pressures in each chamber. The inputs of the cylinder subsystem are the flow rates $q_c, c \in \{1, 2\}$ into each chamber. The mathematical formulation of the subsystem is utilised for a model-based nonlinear control law for the flat output y, which results in desired flow rates $q_{\mathrm{d},c}, c \in \{1, 2\}$. A nonlinear disturbance observer, with linear error dynamics, is used to estimate the state of the cylinder subsystem required for the model-based feedback law.

Four pilot-operated proportional valves provide the flow rates that are needed for the cylinder subsystem as an input. These valves are cumbersome to model due to their design with main and pilot spool as well as due to effects such as hysteresis of the

magnets and friction. Nevertheless, exploiting an approximate model relating flow rate $q(t)$, pressure difference and electrical current $i(t)$, a feed-forward control is designed. Alternatively, circumventing the modelling of the valves, they can be approximated with the first-order ultra-local model

$$\dot{q}(t) = f(t) + \gamma i(t),$$

with $\gamma > 0$ and the unknown part $f(t)$, to design the MFC law

$$i(t) = \frac{1}{\gamma}(\dot{\hat{q}}_{\mathrm{d}}(t) - k_{\mathrm{p}}\hat{e}(t) - \hat{f}(t)),$$

with the estimates

$$\dot{\hat{q}}_{\mathrm{d}}(t) = \int_{t-T-\varepsilon}^{t-\varepsilon} \dot{g}(t-\tau) q_{\mathrm{d}}(\tau) \mathrm{d}\tau, \quad T, \varepsilon > 0$$
$$\hat{e}(t) = \int_{t-T}^{t} g(t-\tau) e(\tau) \mathrm{d}\tau, \quad e(t) = q(t) - q_{\mathrm{d}}(t),$$

and

$$\hat{f}(t) = \int_{t-T-\varepsilon}^{t-\varepsilon} \dot{g}(t-\tau) q(\tau) - \gamma g(t-\tau) i(\tau) \mathrm{d}\tau,$$

where g is an algebraic differentiator in the sense of Mboup et al. (2007, 2009) as introduced in Section 2.1.

At first, the MFC law is tested only on the valves using a flow rate sensor. To do so, a parametrisation of the algebraic differentiators, used to realise the MFC law, is chosen and the parameters k_{p} and γ are varied, to determine a parameter combination that leads to a stable closed-loop behaviour. The parameters of the algebraic differentiators, namely $\alpha = \beta$ and the cutoff frequency ω_{c}, are also varied to show that not only one specific parametrisation leads to a stable closed loop. Inspecting some experiments made, which are on specific lines in the k_{p}-γ parameter set, it is revealed that only the ratio of k_{p} and γ is important for the parametrisation of the MFC law. Intensive testing and comparison of the proposed algorithms, i.e. the MFC law and the feed-forward control, shows that the MFC law clearly outperforms the feed-forward control.

To be able to use the MFC law in the overall system, the individual flow rates for each chamber are required but not measured. Therefore, the mathematical model of the cylinder subsystem is utilised together with an observer to provide an estimate of the needed values without the use of a flow rate sensor. For the valve subsystem two control strategies are presented. On one hand, each individual valve is controlled and on the other hand, each pair of valves is controlled leading to comparable results. Experiments on the overall system are showing that especially for low piston velocities, the MFC law can achieve a high position accuracy. For increasing piston velocity, the results degrade. Nevertheless, the MFC law still outperforms the feed-forward control. The reason for the degrading performance is the estimation of the flow rates that is

mainly dependent on the piston velocity. Due to the limited distance that the cylinder rod can travel, the starting and ending phases of the respective velocity trajectories are resulting in a dominant error. Nevertheless, the latter mentioned observation is not a drawback of the proposed combination of model-based and model-free control.

Furthermore, the robustness of the proposed algorithms is tested by simulating the leakage of a valve in the overall system. In comparison to the feed-forward controller, the MFC law shows a much better performance when the leakage applies, proving the capabilities of the chosen approach.

The contributions of this work are listed in the following:

- Control of a pilot-operated proportional valve with a MFC law based on a first-order ultra-local model and comparison to a model-based feed-forward control.
- Variation of the parametrisation of the algebraic differentiators used to estimate the unknown quantities.
- Investigating the influence of the parameters γ and k_p of the MFC law on the stability of the closed loop by sampling of the parameter set.
- Observing that only the ratio of γ and k_p has an influence on the tracking behaviour.
- Controlling either the individual valve or the pair of valves with a MFC law that feeds back the reconstructed flow rate.
- Division of the system into parts that can be analysed by model-based and model-free approaches.

1.3.2 Model-free control of a magnetically supported plate

In the contribution Scherer et al. (2024) (see Section 5.2), the MFC of a magnetically supported plate is presented (see Fig. 1.2). Therein, the systematic design and tuning of algebraic differentiators and MFC algorithms based on a second-order ultra-local model is investigated for a multiple-input multiple-output (MIMO) system. The test bed considered consists of a rigid outer frame with four electromagnets and a rectangular aluminium plate with four laminated iron packs at each corner, located under the magnets.

At first, a mathematical representation of the system is presented. This model is utilised to design a model-based feedback control law in combination with a simple linear disturbance observer as a benchmark for the proposed MFC approach. After that, four MFC algorithms with varying inputs are designed using different degrees of model information. In each step, the used second-order ultra-local model is compared

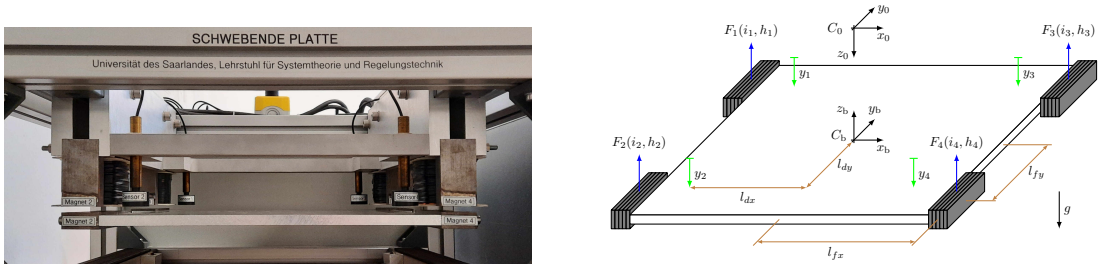

(a) (b)

Fig. 1.2: Photo (a) and schematic drawing (b) of the magnetically supported plate borrowed from Scherer et al. (2024).

with the already determined and more detailed mathematical model, to get a better understanding of estimated disturbances and to choose the input gain of the controllers. Consequently, designing the MFC laws can be simplified.

After the control design, it is shown that the proposed estimation of the unknown part is a generalisation of the approach commonly used in the literature (see, e.g. Bekcheva et al. (2018)). It can be seen that this generalisation is sometimes needed to reduce discretisation errors of the algebraic differentiators used. Once more, the main focus of parametrising the algebraic differentiators is set at the cutoff frequency ω_c and the filter order $\mu = \min(\alpha, \beta) + 1$ with $\alpha = \beta$, which are concepts that are easy to understand from an engineering perspective and can be set in a systematic way. Varying these parameters shows an interesting behaviour. For some parameter combinations, i.e. for low values of $\alpha = \beta$ and for high values of ω_c, the closed-loop system is unstable. The reason for this still needs further investigation. To parametrise the MFC law, the input gain of the algorithm using the highest amount of model information is chosen according to the model of the system and the parameters k_p and k_d are varied.

To get a fair comparison of the model-based control and the MFC approach, the cutoff frequencies of both estimation approaches are chosen equal and additional low-pass filters are added to the disturbance observer used to realise the model-based algorithm. With this, the transfer functions of both approaches have the same filter order.

The capabilities of each presented algorithm with respect to trajectory tracking and robustness against sensor and actuator faults are extensively tested in several experiments. Overall, the results show that the performance of the MFC approach degrades using less model information. Nevertheless, the latter algorithm can outperform the model-based approach in almost all experiments, especially if an actuator fault occurs. Only for abrupt sensor fault, the model-based control shows a better performance which is due to the additional low-pass filters, smoothening the reaction of the controller. The latter becomes clear by comparing the reaction of the filters to a unit step.

The contributions of this work are listed in what follows:

- Control of a magnetically supported plate by a MFC law based on a second-order ultra-local model using different amounts of model information.
- It is shown that using the algebraic differentiators with $\alpha = \beta \neq 2$ is a generalisation of the approach commonly used in the literature to estimate the unknown part.
- Investigating the effects of discretisation errors on the tracking error and how to eliminate these errors.
- Investigating the influence of the parametrisation of the algebraic differentiators on the closed-loop behaviour of the proposed MFC laws.
- Fair comparison of the model-based control with a MFC law, by designing filters with the same frequency-domain characteristics.
- Investigating the influence of the parameters k_p and k_d of the MFC law on the stability of the closed loop by sampling of the parameter set.

1.3.3 Additional results

In the Chapters 2 and 3, the system under consideration is a DC motor. The latter system is controlled by a MFC law based on a first-order and second-order ultra-local model. It is shown that the resulting closed loop is a TDS, the stability of which is analysed using the generalised Hermite-Biehler theorem (see, e.g. Silva et al. (2005, Ch. 5)). Using the mathematical model of the DC motor, theoretical bounds on the parameters of the MFC laws considered can be calculated with the latter theorem. These boundaries are validated by extensive experiments on a real test bed. Additionally, the influence of the algebraic differentiators used to estimate the unknown quantities needed for the feedback is analysed. Furthermore, guidelines for the design of the MFC laws are given.

1.4 Structure of the thesis

This work is organised as follows. Chapter 2 starts with a short overview on the algebraic differentiators, as first introduced by Mboup et al. (2007, 2009), used to estimate the unknown quantities needed for the feedback. Moreover, the control based on first-order and second-order ultra-local models is briefly recalled and the estimation of the unknown part is derived using different points of view leading to a generalisation of the approach commonly used in the literature. After that, the system under consideration,

a DC motor with a three stage gearbox and a load, is presented and a mathematical model of the system is derived. The theoretical considerations are followed by the application of MFC to the DC motor. It can be shown that the differential equation of the tracking error is a TDS, the stability of which is analysed using the generalised Hermite-Biehler theorem (see, e.g. Silva et al. (2005, Ch. 5) as well as Appendix A). With this approach, theoretical bounds on the controller parameters are calculated.

Chapter 3 contains a presentation of the experimental setup as well as the parameter identification used. Besides that details concerning the implementation are shared. Furthermore, the influence of the algebraic differentiators on the stability of the closed-loop system is analysed by varying their cutoff frequency as well as the filter order. The theoretical findings obtained through the application of the generalised Hermite-Biehler theorem are validated by a sampling of the parameter set. Moreover, guidelines for the parametrisation of the algebraic differentiators as well as the controller design based on first-order and second-order ultra-local models are formulated to enable a systematic design of the MFC. Additionally, the formulated guideline for first-order ultra-local models is compared to the approach proposed by Polack et al. (2019).

A conclusion of the thesis can be found in Chapter 4. Therein, a brief summary of the findings is presented and open research problems are discussed.

The two peer-reviewed and published journal papers, Scherer et al. (2023) and Scherer et al. (2024), are included in Chapter 5 and the contribution of each author is listed in detail.

Chapter 2

Model-free control

In this chapter, the model-free control (MFC) approach as introduced in Fliess and Join (2009, 2013) is presented and applied to a DC motor. At first, a very brief introduction to algebraic differentiators, which are used to estimate the unknown quantities employed for a successful application of the MFC, is given. This introduction is followed by the discussion of the control based on ultra-local models of the first and second order, including the estimation of the unknown part. After that, a short introduction of the system under consideration, a DC motor, is given and the mathematical model used to describe the motor is presented. Finally, it is shown how the MFC approach considered can be applied to the DC motor, where the stability depending on the parameters plays a key role.

2.1 On algebraic differentiators

Estimating the n-th derivative of a signal $t \mapsto x(t)$, denoted by $x^{(n)}$, is a common problem in control engineering, met, e.g. in state feedback control or parameter identification (see, e.g. Othmane et al. (2022, Sec. 6)). Simple methods such as the difference quotient can be used to get an estimate. However, if the signal of interest is corrupted by additive disturbances $\eta(t)$, i.e. $y(t) = x(t) + \eta(t)$, the ill-posed character of the problem comes to light, since small disturbances can lead to significant distortions in the estimates, especially when using simple methods such as the difference quotient (see, e.g. Fig. 2.1 (a) and (b) for the estimation of the first derivative of a disturbed signal). Thus, filtering the signal, e.g. with low-pass filters of order μ and with cutoff frequency ω_c, becomes inevitable, which imposes its own challenges such as phase distortion. More elaborate methods such as algebraic differentiators, initially developed in Mboup et al. (2007, 2009) and discussed, e.g. in Kiltz (2017) or Othmane (2022b) are available, combining estimation and filtering (see, e.g. Fig. 2.1 (c) for the application of the algebraic differentiators, parametrised in a similar fashion as the filter used in

(b)). The interested reader is referred to Othmane et al. (2022) for an excellent survey of this topic. Nevertheless, the deployment of such techniques necessitates a profound knowledge of mathematical concepts, which typically constrains their implementation in practical contexts. To circumvent this, the easy to use open-source toolbox AlgDiff (see Othmane (2022a)) is used for the implementation of the differentiators. Therein, all calculations regarding the design and discretisation is already done, such that only the needed filter coefficients have to be exported for further use. The tutorial like contribution Othmane and Rudolph (2023) gives a good introduction on how to use AlgDiff. In the following, a brief introduction on the algebraic differentiators is given, highlighting the important topics to apply them systematically in the context of MFC.

Consider the square Lebesgue integrable function x and its derivatives up to a finite order $n \in \mathbb{N}$, denoted by $x^{(n)}$. This function and its derivatives up to the order $n < \min(\alpha, \beta) + 1$, with real scalar parameters $\alpha, \beta > -1$, can be approximated by the N-th order truncated generalised Fourier expansion as

$$\hat{x}^{(n)}(t) = \int_{t-T}^{t} g^{(n)}(t-\tau)x(\tau)\mathrm{d}\tau, \tag{2.1}$$

on a sliding time window $[t-T, t]$ with the filter window length T. In (2.1), the kernel

$$g(\tau) = g^{(\alpha,\beta)}_{N,T,\vartheta}(\tau) = \begin{cases} \frac{2w^{(\alpha,\beta)}(\nu(\tau))}{T} \sum_{j=0}^{N} \frac{P_j^{(\alpha,\beta)}(\vartheta)}{\left\|P_j^{(\alpha,\beta)}\right\|^2} P_j^{(\alpha,\beta)}(\nu(\tau)), & \tau \in [0,T], \\ 0, & \text{otherwise}, \end{cases} \tag{2.2}$$

depends on the quantity ϑ (all quantities occurring in (2.2) are discussed in Remark 2.2), which parametrises the small but known estimation delay

$$\delta_t = \begin{cases} \frac{\alpha+1}{\alpha+\beta+2}T, & N = 0, \\ \frac{1-\vartheta}{2}T, & N \neq 0, \end{cases} \tag{2.3}$$

leading to the estimate $\hat{x}^{(n)}(t) \approx x^{(n)}(t-\delta_t)$. An estimation without any delay is possible for a parametrisation of the algebraic differentiators with $N > 0$ and $\vartheta = 1$ but according to Mboup et al. (2009) allowing a small but known delay increases the accuracy of the approximation.

Remark 2.1 *Consider the signal of interest $t \mapsto x(t)$, an additive disturbance $t \mapsto \eta(t)$ and the measurement $t \mapsto y(t) = x(t) + \eta(t)$. Using the algebraic differentiators, the estimates $\hat{x}(t)$ and $\dot{\hat{x}}(t)$ can be obtained by*

$$\begin{aligned} \hat{y}^{(n)}(t) &= \int_{t-T}^{t} g^{(n)}(t-\tau)y(\tau)\mathrm{d}\tau, \\ \hat{y}^{(n)}(t) &= \int_{t-T}^{t} g^{(n)}(t-\tau)x(\tau)\mathrm{d}\tau + \int_{t-T}^{t} g^{(n)}(t-\tau)\eta(\tau)\mathrm{d}\tau, \\ \hat{y}^{(n)}(t) &\approx \int_{t-T}^{t} g^{(n)}(t-\tau)x(\tau)\mathrm{d}\tau, \end{aligned}$$

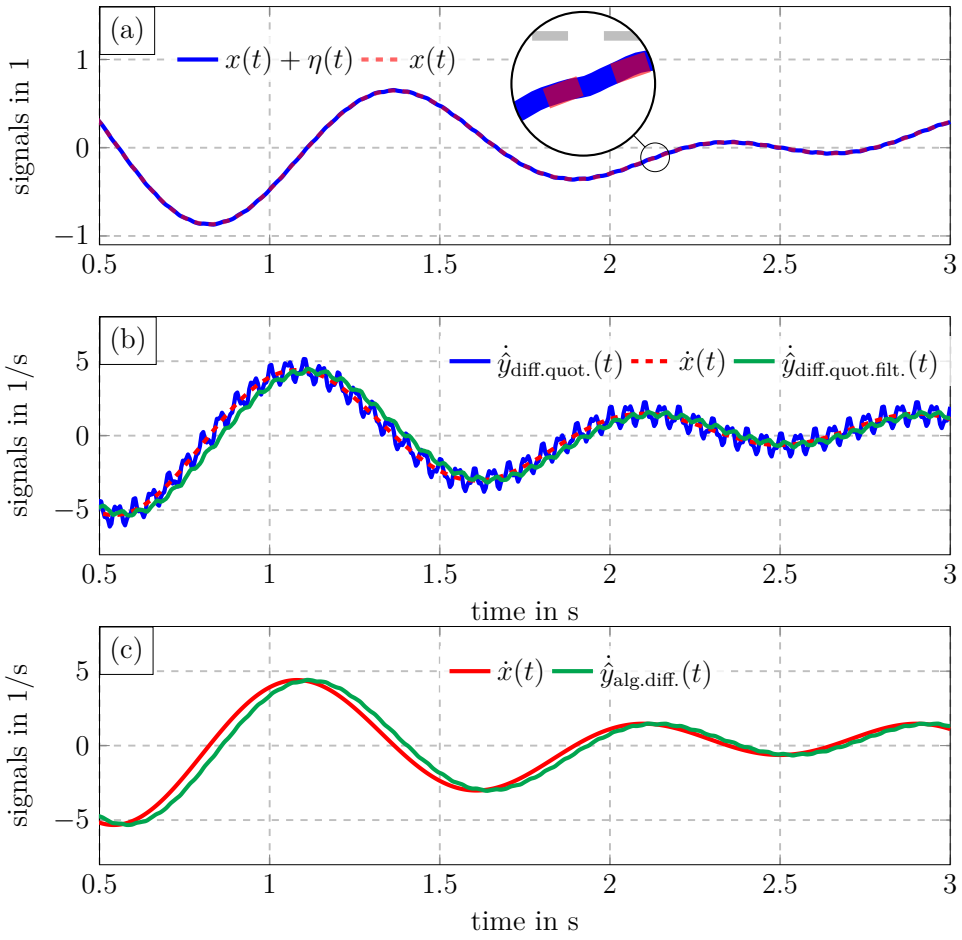

Fig. 2.1: High frequency disturbances $t \mapsto \eta(t) = \sum_{j=1}^{3} A_{\eta,j} \sin(2\pi f_{\eta,j} t)$ with small amplitude corrupting the signal of interest $t \mapsto x(t) = \sum_{j=1}^{2} A_{x,j} \sin(2\pi f_{x,j} t)$, leading to the measurement $y(t) = x(t) + \eta(t)$. The estimation of the first derivative $\hat{\dot{y}}_{\text{diff.quot.}}(t)$, realised by the difference quotient, is heavily affected by the disturbance. By using a low-pass filter, the resulting estimate $\hat{\dot{y}}_{\text{diff.quot.filt.}}(t)$ can be smoothed but the phase distortion of the filter occurs. Applying the algebraic differentiators leads to the more accurate but also delayed estimate $\hat{\dot{y}}_{\text{alg.diff.}}(t) \approx \dot{x}(t - \delta_t)$. The parameters are chosen according to Table 2.1.

resulting in $\hat{y}^{(n)}(t) \approx \hat{x}^{(n)}(t)$*, with* $n \in \{0, 1\}$*. As depicted in Fig. 2.2, the influence of the disturbance* $\eta(t)$ *is suppressed but the estimation is delayed by the known* δ_t *which results in the approximations* $\hat{x}(t + \delta_t) \approx x(t)$ *and* $\hat{\dot{x}}(t + \delta_t) \approx \dot{x}(t)$*, or* $\hat{x}(t) \approx x(t - \delta_t)$ *and* $\hat{\dot{x}}(t) \approx \dot{x}(t - \delta_t)$*, respectively.*

The algebraic differentiators can also be interpreted in two different ways. For example, as shown in Kiltz and Rudolph (2013); Kiltz (2017); Mboup and Riachy (2014, 2018) and Othmane et al. (2022), the kernel $g_{N,T,\vartheta}^{(\alpha,\beta)}(\tau)$ from (2.2) can be interpreted in the frequency domain as a low-pass filter with the Fourier transform $\omega \mapsto \mathcal{G}_{N,T,\vartheta}^{(\alpha,\beta)}(\mathrm{j}\omega)$ of the

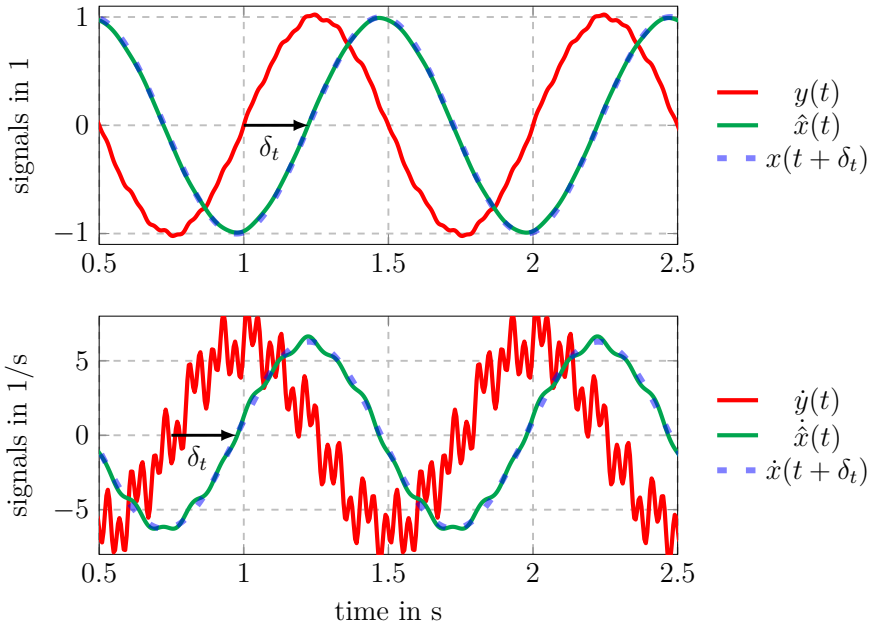

Fig. 2.2: Visualisation of the known delay δ_t on the estimates $\hat{x}(t)$ and $\dot{\hat{x}}(t)$ obtained by the algebraic differentiators. The used measurement $y(t) = x(t) + \eta(t)$ is corrupted by the disturbance $t \mapsto \eta(t) = \sum_{j=1}^{3} A_{\eta,j} \sin(2\pi f_{\eta,j} t)$, the influence of which is suppressed by the estimators. The parameters are chosen according to Table 2.1.

kernel. The filter window length T can be associated with a desired cutoff frequency ω_c (see, e.g. Othmane et al. (2022, Sec. 4.2.2, Eq. (31))) and the parameters α and β yield a desired filter order $\mu = 1 + \min(\alpha, \beta)$ (see, e.g. Fig. 2.3). According to Othmane et al. (2022, Sec. 4.2.2), the algebraic differentiator for the n-th order derivative has a stopband slope of $20(\mu - n)\,\mathrm{dB}$ (see, e.g. Fig. 2.4 for a comparison of an ideal and an algebraic differentiator). From an engineering prospective, this interpretation has the benefit that it makes the filter design much more intuitive. Another possible interpretation is that the estimate of $x^{(n)}$ is the output of a finite impulse response (FIR) filter with window length T driven by the input x.

Up until now, the derivative approximation problem has been considered solely in the continuous-time setting. However, in most real-world applications $x(t)$ is only available at discrete sampling instants. Therefore, the convolution integral in (2.1) has to be approximated with an appropriate quadrature method. In the following, equidistant sampling with time t_s is assumed. In this context, the notation $x[k] = x(kt_s), k \in \mathbb{N}$, for x evaluated at the time kt_s is introduced. Because of the sampling, the filter window length T is chosen as an integral multiple of the sampling time t_s, i.e. $T = n_s t_s$. By

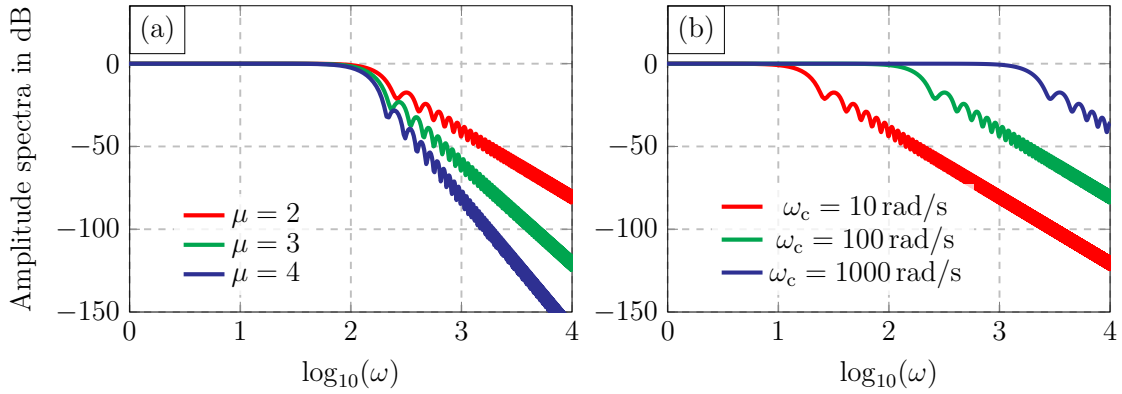

Fig. 2.3: Comparison of the continuous amplitude spectra of algebraic differentiators with different parametrisations and $N = 1$. Parametrisation in (a) $\alpha = \beta$ and in (b) $\alpha = \beta = 2$.

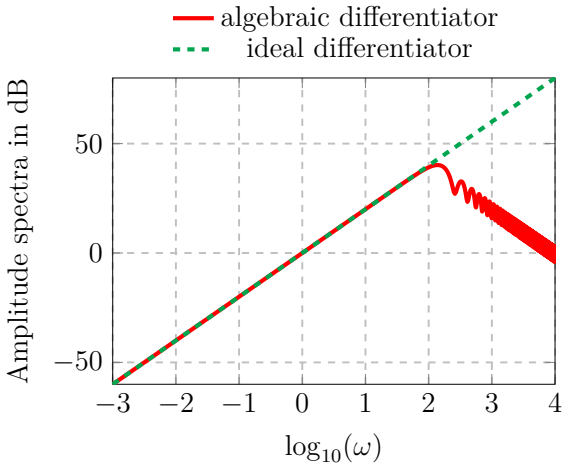

Fig. 2.4: Comparison of the continuous amplitude spectra of an ideal and an algebraic differentiator with the parametrisation $N = 1$, $\alpha = \beta = 1$, and $\omega_c = 100\,\mathrm{rad/s}$ for the first derivative of a signal.

using this notation, the convolution (2.1) can be approximated with

$$\hat{x}^{(n)}[k+\theta] = \frac{1}{\Phi_n} \sum_{j=0}^{L-1} w_n[j]x[k-j], \tag{2.4}$$

$$\Phi_n = \frac{t_s^n}{n!} \sum_{j=0}^{L-1} w_n[j](-j)^n,$$

where the quantities θ, L, and $w_n[j]$ depend on the numerical integration method used, as described in Othmane et al. (2022, Sec. 4.3). For example using the mid-point rule these parameters are $\theta = 1/2$, $L = n_s$ and $w_n[j] = t_s g^{(n)}[j + 1/2]$. Luckily, the most important discretisation methods like mid-point, trapezoidal, and Simpson's rule, to name just a few, as well as analytic integration methods are already implemented in

AlgDiff (see Othmane (2022a), see also Kiltz (2017, Sec. 3.4.2) and Othmane et al. (2022, Sec. 4.3) for more information about the discretisation). To quantify the quality of the discretisation, Kiltz (2017, Sec. 3.4.2) (see also (Othmane et al., 2022, Sec. 4.3)) introduced the cost function $\mathcal{J}_n$, with the order n of the derivate to be estimated. As shown in Polack et al. (2019, Sec. 3.1), Othmane et al. (2022, Sec. 4.3) and Scherer et al. (2024, Sec. 4.1) it is important to check the discretisation especially for low frequencies, as it results in a bad estimation. Increasing the parameters α and β can reduce this discretisation error, but according to (2.3) it will increase the delay of the resulting filter.

Remark 2.2 *Introduce the orthogonal Jacobi polynomial of degree $N \in \mathbb{N}$*

$$P_N^{(\alpha,\beta)}(\tau) = \sum_{k=0}^{N} \binom{N}{k} c_k^{(\alpha,\beta)} (\tau - 1)^k,$$
$$c_k^{(\alpha,\beta)} = \frac{\Gamma(\alpha + N + 1)\Gamma(\alpha + \beta + N + k + 1)}{2^k N! \Gamma(\alpha + \beta + N + 1)\Gamma(\alpha + k + 1)}$$

on the interval $[-1, 1]$, with the associated weight function

$$w^{(\alpha,\beta)}(\tau) = \begin{cases} (1-\tau)^\alpha (1+\tau)^\beta, & \tau \in [-1, 1] \\ 0, & \textit{otherwise}, \end{cases}$$

with real scalar parameters $\alpha, \beta > -1$ and Γ denoting the gamma function. In the following, $\|z\| = \sqrt{\langle z, z \rangle}$ is the norm induced by the inner product

$$\langle z, y \rangle = \int_{-1}^{1} w^{(\alpha,\beta)}(\tau) z(\tau) y(\tau) \mathrm{d}\tau$$

and

$$\nu(\tau) = 1 - 2\tau/T.$$

According to, e.g. Ushirobira (2018) or Othmane (2022b), the Jacobi polynomials are not the only orthogonal polynomials that can be used for the estimation. The Laguerre or the Hermite polynomials can also be a suitable choice.

Remark 2.3 *The algebraic differentiators based on the Jacobi polynomials have an additional property that can be utilised in the filter design. For the parametrisation $\alpha = \beta$ and $N = 0$ the transfer function has zeros which correspond to those of the Bessel function of the first kind and order $\alpha + 1/2$ as mentioned in Kiltz and Rudolph (2013) and Kiltz (2017, Sec. 3.3.3). With this, the characteristics of a notch filter are already included into the differentiator without additional effort. This can for example be utilised for quantised signals as shown in Othmane et al. (2021a).*

With the introduction of algebraic differentiators in this section, an investigation into their use in MFC based on ultra-local models can now be conducted.

Table 2.1: Chosen parameters of the signals $t \mapsto \eta(t)$ and $t \mapsto x(t)$ as well as the algebraic differentiators for Fig. 2.1 and Fig. 2.2.

parameter	value for Fig. 2.1	value for Fig. 2.2
$A_{\eta,1}$	$5 \cdot 10^{-3}$	$1 \cdot 10^{-2}$
$A_{\eta,2}$	$1 \cdot 10^{-3}$	$1 \cdot 10^{-2}$
$A_{\eta,3}$	$1 \cdot 10^{-4}$	$2 \cdot 10^{-2}$
$A_{x,1}$	$5 \cdot 10^{-1}$	1
$A_{x,2}$	$5 \cdot 10^{-1}$	-
$f_{\eta,1}$	20 Hz	25 Hz
$f_{\eta,2}$	50 Hz	5 Hz
$f_{\eta,3}$	65 Hz	10 Hz
$f_{x,1}$	0.8 Hz	1 Hz
$f_{x,2}$	1 Hz	-
f_s	200 Hz	200 Hz
ω_c	30 rad/s	100 rad/s
$\alpha = \beta$	1	30
N	0	0
discretisation method	mid-point	mid-point

2.2 Control based on ultra-local models

In the following, the control based on so-called ultra-local models as introduced by Fliess and Join (2009, 2013) is presented. To this end, consider an arbitrary SISO system, the input-output behaviour of which can be described by the differential equation

$$E(y(t), \dot{y}(t), \ldots, y^{(n)}(t), u(t), \dot{u}(t), \ldots, u^{(m)}(t)) = 0 \tag{2.5}$$

with $n, m \in \mathbb{N}$, the input $u(t)$ and the output $y(t)$, whereas E is assumed to be a sufficiently smooth polynomial function of its arguments with real coefficients. Furthermore, it is assumed that an integer $\nu \in [0, n]$ exists such that

$$\frac{\partial E}{\partial y^{(\nu)}}(y(t), \dot{y}(t), \ldots, y^{(n)}(t), u(t), \dot{u}(t), \ldots, u^{(m)}(t)) \neq 0$$

holds. Applying the implicit function theorem yields the local representation

$$y^{(\nu)}(t) = \mathcal{E}(y(t), \dot{y}(t), \ldots, y^{(\nu-1)}, y^{(\nu+1)}, \ldots, y^{(n)}(t), u(t), \dot{u}(t), \ldots, u^{(m)}(t)) \tag{2.6}$$

of the system described by (2.5). For a short period of time (2.6) can be approximated with a so-called ultra-local model

$$y^{(\nu)}(t) = f(t) + \rho u(t), \tag{2.7}$$

with the input gain ρ and the quantity $f(t)$ that consists of the input and output dynamics from the right hand side of (2.6) as well as unmodelled dynamics and disturbances, without any distinction between the latter. For the sake of simplicity, the quantity $f(t)$ is called unknown part for the rest of this work. Commonly in the literature the cases $\nu = 1$ (see, e.g. Gédouin et al. (2011) or Ziane et al. (2023)) or $\nu = 2$ (see, e.g. Bekcheva et al. (2018) or Neves and Angélico (2021)) are considered and will be discussed in the following.

2.2.1 First-order ultra-local models

Based on the latter considerations, a SISO system of arbitrary order can be approximated at least locally, during a short period of time, with the first-order ultra-local model

$$\dot{y}(t) = f(t) + \rho u(t), \tag{2.8}$$

whereas the input gain ρ is assumed to be positive to simplify the discussion. The representation of a system approximated by the ultra-local model (2.8) is beneficial in comparison to an approach that relies on a physical model of the system because a cumbersome modelling and a parameter identification is obsolete. Nonetheless, a value for the input gain ρ is still necessary.

Remark 2.4 *As shown in several publications like Gédouin et al. (2011); Doublet et al. (2016); Hegedűs et al. (2022) or Scherer et al. (2024), just to name a few, the input gain ρ does not have to be constant and can be time dependent.*

Assuming, that an estimate $\hat{f}(t)$ of $f(t)$ at each time instant t is available, a simple feedback law for (2.8) can be designed as

$$u(t) = \frac{1}{\gamma}\left(\dot{y}_\mathrm{r}(t) - k_\mathrm{p} e(t) - \hat{f}(t)\right), \tag{2.9}$$

with the tracking error $e(t) = y(t) - y_\mathrm{r}(t)$, a sufficiently smooth reference trajectory $t \mapsto y_\mathrm{r}(t)$ and the design parameters $\gamma > 0$ and k_p. The choice of γ and k_p has a significant influence on the performance of the control law (2.9) and has to be discussed in the following. Therefore, the error dynamics of the system (2.8) controlled by (2.9)

$$\dot{y}(t) - \frac{\rho}{\gamma}\dot{y}_\mathrm{r}(t) + \frac{\rho}{\gamma} k_\mathrm{p} e(t) = f(t) - \frac{\rho}{\gamma}\hat{f}(t). \tag{2.10}$$

has to be analysed. For a constant reference trajectory $t \mapsto y_\mathrm{r}(t)$, (2.10) simplifies to

$$\dot{e}(t) + \frac{\rho}{\gamma} k_\mathrm{p} e(t) = f(t) - \frac{\rho}{\gamma}\hat{f}(t).$$

If a priori knowledge of the input gain is available, i.e. $\gamma \approx \rho$ is chosen, the error dynamics further simplifies to

$$\dot{e}(t) + k_\mathrm{p} e(t) \approx f(t) - \hat{f}(t),$$

showing that a good approximation $\hat{f}(t)$ of the unknown part $f(t)$ is necessary to get the first-order differential equation of the error

$$\dot{e}(t) + k_\mathrm{p} e(t) \approx 0.$$

The latter equation suggests that $k_\mathrm{p} > 0$ is a necessary condition for stability, if the assumptions $\gamma \approx \rho$ and $f(t) \approx \hat{f}(t)$ hold.

The approximation using a first-order ultra-local model can be applied to many different systems such as a green house in Lafont et al. (2015), an alkaline electrolysis system in Ziane et al. (2023), or a grid-tied inverter in Wachter et al. (2023). However, in many cases, the proposed approximation with a first-order ultra-local model (2.8) is insufficient. A solution to that problem is discussed in the next section.

2.2.2 Second-order ultra-local models

Especially for mechatronic systems such as a magnetically supported body in Moraes and da Silva (2015), a quadcopter in Bekcheva et al. (2018), an active suspension in Haddar et al. (2019) as well as a reaction wheel inverted pendulum and a 2-DOF Helicopter in Neves and Angélico (2021), the approach presented in Section 2.2.1 is inadequate. Then, the considered system can be approximated using a second-order ultra-local model

$$\ddot{y}(t) = f(t) + \rho u(t) \tag{2.11}$$

with the input gain $\rho > 0$. A feedback law for (2.11) can be designed in the same manner as in Section 2.2.1 under the assumption that an estimate $\hat{f}(t)$ of the unknown part $f(t)$ is available, yielding

$$u(t) = \frac{1}{\gamma}\left(\ddot{y}_\mathrm{r}(t) - k_\mathrm{d}\dot{e}(t) - k_\mathrm{p} e(t) - \hat{f}(t)\right), \tag{2.12}$$

with the tracking error $e(t) = y(t) - y_\mathrm{r}(t)$ and the design parameters $\gamma > 0, k_\mathrm{p}$, and k_d. The influence of the design parameters on the error dynamics can be analysed by substituting the feedback law (2.12) into (2.11) which leads to

$$\ddot{y}(t) - \frac{\rho}{\gamma}\ddot{y}_\mathrm{r}(t) + \frac{\rho}{\gamma}k_\mathrm{d}\dot{e}(t) + \frac{\rho}{\gamma}k_\mathrm{p} e(t) = f(t) - \frac{\rho}{\gamma}\hat{f}(t).$$

For a constant reference trajectory $t \mapsto y_\mathrm{r}(t)$, the error dynamics reads

$$\ddot{e}(t) + \frac{\rho}{\gamma}k_\mathrm{d}\dot{e}(t) + \frac{\rho}{\gamma}k_\mathrm{p} e(t) = f(t) - \frac{\rho}{\gamma}\hat{f}(t),$$

and with a priori model knowledge, i.e. an approximation of the input gain $\rho \approx \gamma$, the influence of the estimated unknown part in

$$\ddot{e}(t) + k_\mathrm{d}\dot{e}(t) + k_\mathrm{p}e(t) \approx f(t) - \hat{f}(t)$$

is clearly visible. Assuming that the available estimate satisfies $\hat{f}(t) \approx f(t)$ yields

$$\ddot{e}(t) + k_\mathrm{d}\dot{e}(t) + k_\mathrm{p}e(t) \approx 0.$$

The latter suggests that $k_\mathrm{d}, k_\mathrm{p} > 0$ is a necessary condition for stability, if the assumptions $\gamma \approx \rho$ and $f(t) \approx \hat{f}(t)$ hold.

2.2.3 Remarks and open questions

With the approaches presented in Section 2.2.1 and Section 2.2.2 many complex control problems can be solved (see, e.g. Section 1.1). To the authors knowledge, the case $\nu = 3$ for the ultra-local model (2.7), has not been considered in the literature but might lead to better results if an approximation based on a second-order ultra-local model is insufficient. Furthermore, the Sections 2.2.1 and 2.2.2 show that the controller design based on ultra-local models is straightforward. However, the tuning of the controller parameters, i.e. γ, k_p and k_d, might be challenging. Based on the considerations from Section 2.2.1 and Section 2.2.2, the following three questions arise:

Open Questions

1. What are the necessary steps to obtain the estimate $\hat{f}(t)$ required for a successful implementation of feedback laws such as (2.9) and (2.12)?
2. How can the parameter γ in the feedback laws (2.9) and (2.12) be chosen?
3. Is the approximation $\hat{f}(t) \approx f(t)$ justified or respectively, is $k_\mathrm{d}, k_\mathrm{p} > 0$ sufficient for a stable closed loop?

The subsequent sections will address the aforementioned questions.

2.3 Estimation of the unknown part

In this section, the estimation of the unknown part $f(t)$ that is used in the MFC laws (2.9) and (2.12) is analysed from different view points.

2.3.1 Estimation for first-order ultra-local models

In the following, the estimate $\hat{f}(t)$ is derived using Laplace transformation. Thereafter, it is shown that the estimate can also be derived using the algebraic differentiators presented in Section 2.1, which generalises the first approach.

An algebraic point of view

Following Fliess and Join (2013), consider the ultra-local model (2.8) and assume that the unknown part $t \mapsto f(t)$ is constant. Applying the Laplace transform (see, e.g. Doetsch (1974)) to (2.8) yields

$$sY(s) - y(0) = \rho U(s) + \frac{1}{s}F, \tag{2.13}$$

with Y, U, and F the Laplace transforms of y, u, and f, respectively, and $y(0)$ the initial condition of (2.8). To eliminate the influence of the initial condition $y(0)$, (2.13) is differentiated with respect to s, resulting in the relation

$$Y(s) + s\frac{\mathrm{d}Y}{\mathrm{d}s}(s) = \rho\frac{\mathrm{d}U}{\mathrm{d}s}(s) - \frac{1}{s^2}F, \tag{2.14}$$

which cannot be implemented because of the occurrence of the variable s in $s\frac{\mathrm{d}Y}{\mathrm{d}s}(s)$. To get rid of this quantity and increase the attenuation of high-frequency disturbances on the measurement, both sides of (2.14) are multiplied by s^{-2} yielding

$$\frac{1}{s^2}Y(s) + \frac{1}{s}\frac{\mathrm{d}Y}{\mathrm{d}s}(s) = \frac{\rho}{s^2}\frac{\mathrm{d}U}{\mathrm{d}s}(s) - \frac{1}{s^4}F. \tag{2.15}$$

The relation (2.15) has to be transformed back into the time domain using the inverse transformations

$$\frac{\mathrm{d}^n}{\mathrm{d}s^n}X(s) \bullet\!\!-\!\!\circ\ (-t)^n x(t) \tag{2.16a}$$

$$\frac{1}{s^n} \bullet\!\!-\!\!\circ\ \frac{t^{n-1}}{(n-1)!} \tag{2.16b}$$

$$\frac{X(s)}{s} \bullet\!\!-\!\!\circ\ \int_0^t x(\sigma)\mathrm{d}\sigma, \tag{2.16c}$$

according to Doetsch (1974, App.) and it follows that

$$\frac{t^3}{3!}f = -\int_0^t \int_0^{\sigma_1} y(\tau)\mathrm{d}\tau\mathrm{d}\sigma_1 + \int_0^t \tau y(\tau)\mathrm{d}\tau - \rho\int_0^t \int_0^{\sigma_1} \tau u(\tau)\mathrm{d}\tau\mathrm{d}\sigma_1.$$

Using the Cauchy-formula for repeated integration (see, e.g. Doetsch (1974, Ch. 11)) simplifies the latter expression, yielding

$$f = -\frac{3!}{t^3}\int_0^t (t-2\sigma)y(\sigma) + \rho(t-\sigma)\sigma u(\sigma)\mathrm{d}\sigma.$$

Hereafter, considering only the arbitrary bounded interval $[0, T]$ instead of $[0, t]$ leads to

$$f = -\frac{3!}{T^3}\int_0^T (T-2\sigma)y(\sigma) + \rho(T-\sigma)\sigma u(\sigma)\mathrm{d}\sigma.$$

Introducing a moving time window $[t-T-\varepsilon, t-\varepsilon]$ with $\varepsilon > 0$ by evaluating the signals y and u at $\sigma + t - T - \varepsilon$ instead of σ yields

$$f(t) = -\frac{3!}{T^3}\int_0^T (T-2\sigma)y(\sigma+t-T-\varepsilon) + \rho(T-\sigma)\sigma u(\sigma+t-T-\varepsilon)\mathrm{d}\sigma,$$

which is now a function of time. After that, the substitution $\tau = \sigma + t - T - \varepsilon$ and further trivial simplifications are leading to

$$f(t) = \frac{3!}{T^3}\int_{t-T-\varepsilon}^{t-\varepsilon} (T-2(t-\tau-\varepsilon))y(\tau) - \rho(t-\tau-\varepsilon)(T-(t-\tau-\varepsilon))u(\tau)\mathrm{d}\tau. \tag{2.17}$$

However, in reality the unknown part is not constant in opposition to the assumption previously stated and the input gain ρ of the ultra-local model (2.8) is not known. Under these aspects, (2.17) leads to the estimate

$$\hat{f}(t) = \frac{3!}{T^3}\int_{t-T-\varepsilon}^{t-\varepsilon} (T-2(t-\tau-\varepsilon))y(\tau) - \gamma(t-\tau-\varepsilon)(T-(t-\tau-\varepsilon))u(\tau)\mathrm{d}\tau \tag{2.18}$$

of the unknown part $f(t)$. This means that the unknown part $f(t)$ is approximated by a constant on the moving time window $[t-T-\varepsilon, t-\varepsilon]$. The expression (2.18) is frequently found in the literature, e.g. in De Miras et al. (2013), except that the current time t appears in the filter kernel, the parameter ε is explicitly considered and the sign of the expression $(T-2(t-\tau-\varepsilon))$ differs.

A system theoretic point of view

To get a more general estimate of the unknown part $f(t)$ as in the previous paragraph, the estimation techniques as introduced in Section 2.1 can be used, leading to

$$\hat{f}(t) = \int_{t-T-\varepsilon}^{t-\varepsilon} g(t-\tau-\varepsilon)f(\tau)\mathrm{d}\tau, \quad \varepsilon > 0, \tag{2.19}$$

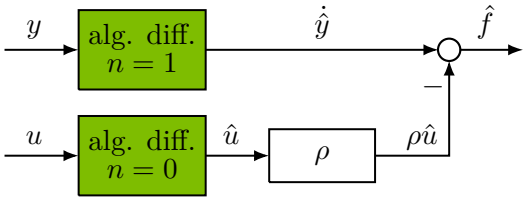

Fig. 2.5: Diagram of the proposed estimation algorithm for the disturbance $f(t)$ based on the first-order ultra-local model (2.8).

with $g = g^{(\alpha,\beta)}_{N,T,\vartheta}$ denoting the kernel of an algebraic differentiator. This means that the unknown part is approximated by the N-th order truncated generalised Fourier expansion using Jacobi polynomials on a sliding time window $[t-T-\varepsilon, t-\varepsilon]$. Nonetheless, the unknown part $f(t)$ is not directly accessible. Instead the ultra-local model (2.8) can be used to get

$$f(t) = \dot{y}(t) - \rho u(t)$$

and with the latter equation, the estimate (2.19) yields

$$\hat{f}(t) = \int_{t-T-\varepsilon}^{t-\varepsilon} \dot{g}(t-\tau-\varepsilon)y(\tau) - \rho g(t-\tau-\varepsilon)u(\tau)\mathrm{d}\tau, \tag{2.20}$$

which is only depending on the known signals u and y as depicted in Fig. 2.5. However, for the use of (2.20) in a MFC law, the unknown input gain ρ has to be replaced by γ.

The special parametrisation of the algebraic differentiators $N = 0$ (see, e.g. Othmane (2024)), leads to

$$g^{(\alpha,\beta)}_{0,T,\vartheta}(\tau) = \begin{cases} \frac{(\alpha+\beta+1)!}{\alpha!\beta!T^{\alpha+\beta+1}}\tau^{\alpha}(T-\tau)^{\beta}, & \tau \in [0,T], \\ 0, & \text{otherwise}, \end{cases}$$

and further choosing $\alpha = \beta = 1$ yields

$$\bar{g}(\tau) := g^{(1,1)}_{0,T,\vartheta}(\tau) = \begin{cases} \frac{3!}{T^3}\tau(T-\tau), & \tau \in [0,T], \\ 0, & \text{otherwise}. \end{cases} \tag{2.21}$$

Calculating the first derivative of $\bar{g}$ with respect to τ reads

$$\frac{\mathrm{d}\bar{g}}{\mathrm{d}\tau}(\tau) = \begin{cases} \frac{3!}{T^3}(T-2\tau), & \tau \in [0,T], \\ 0, & \text{otherwise}. \end{cases} \tag{2.22}$$

Finally, using (2.21) and (2.22) in (2.20) leads to the same estimate as in (2.17). The latter analysis shows that a generalisation of the results that are commonly used in the literature is possible using the estimation techniques introduced in Section 2.1.

With the latter findings, the unknown part $f(t)$ of a first-order ultra-local model can be estimated. In the following section, the estimation using a second-order ultra-local model is considered.

2.3.2 Estimation for second-order ultra-local models

The same reasoning, i.e. using the Laplace transformation, as in Section 2.3.1 can be applied to the second-order ultra-local model (2.11). Consequently, this results in the estimate (see, e.g. Scherer et al. (2024))

$$\hat{f}(t) = \frac{5!}{2T^5} \int_{t-T-\varepsilon}^{t-\varepsilon} \Big(T^2 - 6T\sigma + 6\sigma^2\Big) y(\tau) - \frac{\rho}{2}\sigma^2(T-\sigma)^2 u(\tau)\mathrm{d}\tau, \quad \varepsilon > 0, \tag{2.23}$$

with $\sigma = t - \tau - \varepsilon$, on the moving time window $[t - T - \varepsilon, t - \varepsilon]$.

Using the estimation techniques as presented in Section 2.1, the approximation of $f(t)$ can be generalised yielding

$$\hat{f}(t) = \int_{t-T-\varepsilon}^{t-\varepsilon} g(t - \tau - \varepsilon) f(\tau)\mathrm{d}\tau, \tag{2.24}$$

with the kernel $g = g_{N,T,\vartheta}^{(\alpha,\beta)}$ of the algebraic differentiator. Since the unknown part cannot be measured directly, the ultra-local model (2.11) can be used to express $f(t)$ in (2.24) leading to the estimate

$$\hat{f}(t) = \int_{t-T-\varepsilon}^{t-\varepsilon} \ddot{g}(t - \tau - \varepsilon) y(\tau) - \rho g(t - \tau - \varepsilon) u(\tau)\mathrm{d}\tau, \tag{2.25}$$

which only depends on the known signals u and y. As shown in Scherer et al. (2024, App.), the approximation $\hat{f}(t)$ of $f(t)$ in (2.25) can be realised with the special parametrisation of the algebraic differentiator $g = g_{0,T,\vartheta}^{(2,2)}$, leading to the expression (2.23) and proving that the proposed estimation (2.25) generalises the approach commonly used in the literature (see, e.g. Bekcheva et al. (2018)). For the use in the MFC law (2.12) the parameter ρ has to be replaced by γ.

The findings from the Sections 2.3.1 and 2.3.2 provide an answer to Question 1 raised in Section 2.2.3 on how to get an estimate of the unknown part required for the successful implementation of the MFC laws considered. The remaining questions will be answered in the following.

2.4 Application to the DC motor

In the following, the considerations made in Section 2.2.1 are applied to a DC motor, the mathematical model of which is presented in Section 2.4.1. In Sections 2.4.2 and 2.4.3, the MFC of the angular velocity and the angle, respectively, are presented.

2.4.1 System under consideration

The system under consideration is a DC motor with a three-stage gearbox and load as shown in Fig. 2.6. This system is chosen as an illustrative example because it is

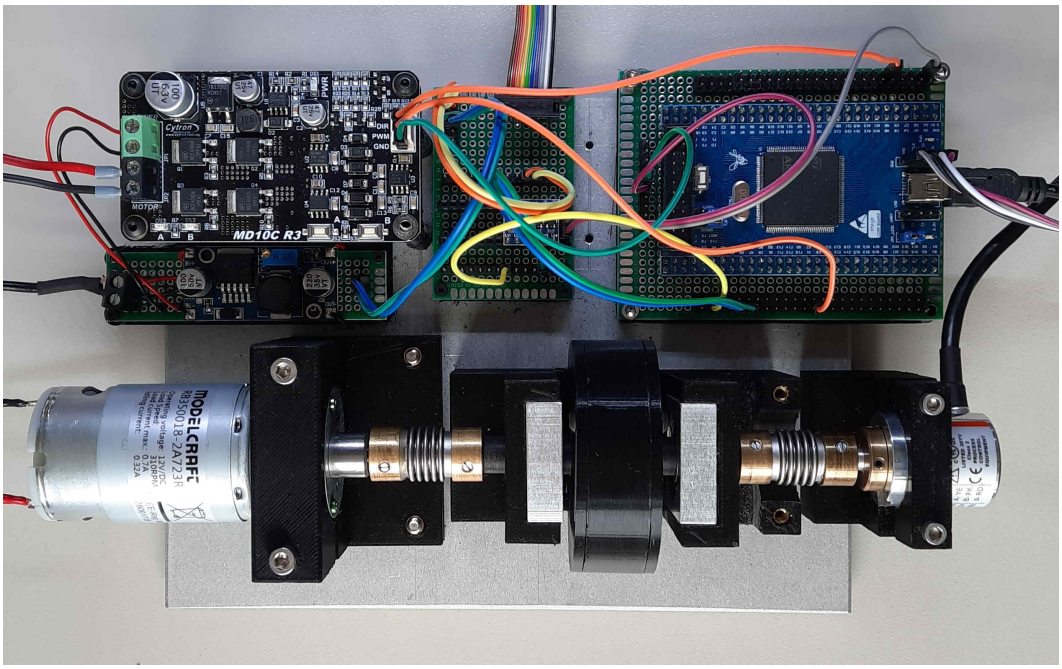

Fig. 2.6: Photo of the considered test bed, consisting of a DC motor with gearbox, load, and couplings as well as the necessary electronics for power supply and control of the system.

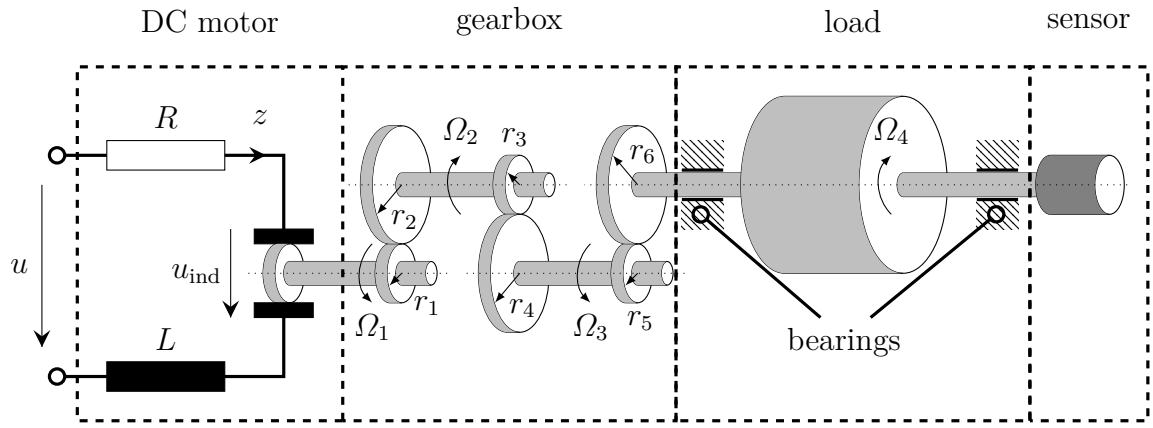

Fig. 2.7: Equivalent circuit diagram of the considered DC motor and sketch of the gearbox with load. The couplings between gearbox and load as well as load and sensor are neglected.

well understood, easy to model and it can be interpreted as a first-order or second-order model, if either considering the angular velocity or the angle of the load as its output, respectively. An advantage of this system is that occurring effects regarding the parametrisation of the MFC approach can be assigned more easily. In the following, a mathematical model of the DC motor is derived which relates the input voltage to the angle of the load.

Applying Kirchhoff's voltage law to the equivalent circuit diagram in Fig. 2.7 results in

$$u(t) = L\dot{z}(t) + Rz(t) + u_{\mathrm{ind}}(t), \tag{2.26}$$

with the input voltage $u(t)$, the current $z(t)$, the electromotive force $u_{\mathrm{ind}}(t)$, and the parameters R and L describing the electrical resistance and the inductance of the coil, respectively. Under the assumptions that each shaft in Fig. 2.7 is a rigid body and the coupling between gearbox and load (see Fig. 2.6) is neglected, the torques applied to each shaft can be calculated, which yields

$$J_1\dot{\Omega}_1(t) = r_1F_1(t) + \tau_{\mathrm{el}}(t), \tag{2.27a}$$
$$J_2\dot{\Omega}_2(t) = r_3F_2(t) - r_2F_1(t), \tag{2.27b}$$
$$J_3\dot{\Omega}_3(t) = r_5F_3(t) - r_4F_2(t), \tag{2.27c}$$
$$J_4\dot{\Omega}_4(t) = -r_6F_3(t), \tag{2.27d}$$

with the radii of the gears $r_j, j \in \{1, 2, \ldots, 6\}$, the motor torque $\tau_{\mathrm{el}}(t)$ as well as $\Omega_j(t), j \in \{1, 2, 3, 4\}$ and $J_j, j \in \{1, 2, 3, 4\}$ the angular velocities and moments of inertia of each shaft with respect to the rotational axis, respectively. Under the assumption of an ideal transmission the radial velocities of each individual gear are related by

$$r_1\Omega_1(t) = r_2\Omega_2(t), \tag{2.28a}$$
$$r_3\Omega_2(t) = r_4\Omega_3(t), \tag{2.28b}$$
$$r_3\Omega_3(t) = r_6\Omega_4(t). \tag{2.28c}$$

The mechanical and electrical parts of the motor are connected, assuming a constant field flux, by the relations (see, e.g. Krishnan (2001, Sec. 2.2 and 2.3))

$$u_{\mathrm{ind}}(t) = k_{\mathrm{m}}\Omega_1(t), \tag{2.29a}$$
$$\tau_{\mathrm{el}}(t) = k_{\mathrm{m}}z(t), \tag{2.29b}$$

with the motor constant k_{m}. Since only a dependence of the input voltage $u(t)$ and the load velocity $\Omega_4(t)$ is of interest, (2.26)–(2.29) can be combined to

$$\dot{\Omega}_4(t) = -a\Omega_4(t) + bu(t) - c\dot{z}(t), \tag{2.30}$$

with the positive parameters

$$d = J_1\frac{r_2r_4r_6}{r_1r_3r_5} + J_2\frac{r_1r_4r_6}{r_2r_3r_5} + J_3\frac{r_1r_3r_6}{r_2r_4r_5} + J_4\frac{r_1r_3r_5}{r_2r_4r_6},$$
$$a = \frac{1}{d}\frac{k_{\mathrm{m}}^2r_2r_4r_6}{Rr_1r_3r_5},$$
$$b = \frac{1}{d}\frac{k_{\mathrm{m}}}{R},$$
$$c = \frac{1}{d}\frac{Lk_{\mathrm{m}}}{R}.$$

In the sequel, the index of the load velocity $\Omega_4(t)$ is dropped and in addition to that, the corresponding load angle $\theta(t)$ is introduced. Thereafter, the quantity $c\dot{z}(t)$ in (2.30) is replaced by $\eta(t)$ to additionally account for modelling errors and disturbances, stemming from the couplings and the friction of the gearbox as well as the backlash in the gearbox, resulting in

$$\dot{\theta}(t) = \Omega(t) \tag{2.31a}$$

$$\dot{\Omega}(t) = -a\Omega(t) + bu(t) + \eta(t). \tag{2.31b}$$

From here on out, (2.31) will be the basis of further considerations and the system comprising of the motor, the gearbox and the load is only referred to as the DC motor. Being able to approximate the system with a mathematical model will be a huge benefit later on, to understand the effects that are occurring during parametrisation of the MFC laws.

2.4.2 Control of the angular velocity

To control the angular velocity $\Omega(t)$, the ultra-local model

$$\dot{\Omega}(t) = f_\Omega(t) + \rho_\Omega u(t) \tag{2.32}$$

is considered, which reveals, by comparing (2.32) with (2.31b), the unknown part $f_\Omega(t) = \eta(t) - a\Omega(t)$ and the input gain $\rho_\Omega = b$. According to (2.9) the corresponding MFC law for the angular velocity $\Omega(t)$ reads

$$u(t) = \frac{1}{\gamma_\Omega}\left(\dot{\Omega}_\mathrm{r}(t) - k_\mathrm{p} e_\Omega(t) - \hat{f}_\Omega(t)\right), \tag{2.33}$$

with the tracking error $e_\Omega(t) = \Omega(t) - \Omega_\mathrm{r}(t)$ and the sufficiently smooth reference trajectory $t \mapsto \Omega_\mathrm{r}(t)$. With the control law (2.33) and the estimation techniques from Section 2.3.1 the control design is completed. Nevertheless, the acquisition of the angular velocity must be discussed.

Obtaining the angular velocity

Typically, incremental encoders are used to measure the angle $\theta(t)$ of the load. This grants access to the angular velocity by different methods. The simplest way to obtain the angular velocity $\Omega(t)$ is to use the difference quotient

$$\Omega(kt_\mathrm{s}) \approx \frac{\theta[k] - \theta[k-1]}{t_\mathrm{s}}. \tag{2.34}$$

Considering the resolution w of the sensor, the smallest angle increment to detect is $\Delta\theta_\mathrm{min} = 2\pi/w$. Thus, the resulting error from the quantisation of the sensor, corrupting the obtained values of $\Omega(kt_\mathrm{s})$, is at least $\Delta\theta_\mathrm{min}/t_\mathrm{s}$ using (2.34). The latter value

is increasing if the sampling time t_s is reduced which is a drawback of the difference quotient (2.34). Exploiting the low-pass filter characteristic of the algebraic differentiator, the influence of the error from the quantisation can be reduced, which leads to the MFC law

$$u(t) = \frac{1}{\gamma_\Omega}\left(\dot{\Omega}_\mathrm{r}(t) - k_\mathrm{p}\hat{e}_\Omega(t) - \hat{f}_\Omega(t)\right) \tag{2.35}$$

with

$$\hat{e}_\Omega(t) = \int_{t-T}^{t} g(t-\tau)e_\Omega(\tau)\mathrm{d}\tau, \tag{2.36}$$

and the kernel $g = g_{N,T,\vartheta}^{(\alpha,\beta)}$ of the algebraic differentiator as discussed in Section 2.1.

Remark 2.5 *Using a simple low-pass filter is also a valid solution to decrease the influence of the error stemming from the quantisation. Nonetheless, a simple low-pass filter introduces a phase distortion which depends on the frequency of the filter input signal. This is in contrast to the signal independent time delay δ_t of the algebraic differentiators which is known in advance and can be calculated according to* (2.3)*.*

Another method to get access to the angular velocity $\Omega(t)$, is to apply the algebraic differentiators directly on the measurement of the angle $\theta(t)$ by

$$\hat{\Omega}(t) = \int_{t-T}^{t} \dot{g}(t-\tau)\theta(\tau)\mathrm{d}\tau.$$

If this is done, two aspects have to be considered. Firstly, it is necessary to delay the reference trajectory $t \mapsto \Omega_\mathrm{r}(t)$ as discussed in Scherer et al. (2024, Sec. 4.3.1) by δ_t. Otherwise, the system is ahead of the reference. Secondly, to get the estimation of the unknown part, the angular acceleration $\ddot{\theta}(t) = \dot{\Omega}(t)$, has to be estimated based on the measurement $\theta(t)$, which has an impact on the parametrisation of the algebraic differentiators. The order n of the derivative to be estimated, i.e. in this case $n = 2$, is restricting parameters α and β according to $n - 1 < \min(\alpha, \beta)$, denying the parametrisation $\alpha = \beta = 1$.

However, the first method using the difference quotient is considered in the following because in general a direct measurement of the output for a first-order ultra-local model is available. The parametrisation of the algebraic differentiators with $\alpha = \beta = 1$ is taken into account in Section 3.4.1 which would not be possible otherwise as $1 < \min(\alpha, \beta)$ must hold.

The subsequent part of this section addresses the tuning of the input gain γ_Ω and its effect on the choice of the parameter k_p. Therefore, two cases are considered:

Case 1: the error dynamics resulting from the ultra-local model (2.32) controlled by the MFC law (2.35),

Case 2: the error dynamics resulting from of the DC motor model (2.31) controlled by the MFC law (2.35).

Case 1: Considerations based on the ultra-local model

If no model information of the system under consideration is available, the ultra-local model (2.32) has to be considered. Using the MFC law (2.35) in (2.32) leads to

$$\dot{\Omega}(t) = f_\Omega(t) + \frac{\rho_\Omega}{\gamma_\Omega}\left(\dot{\Omega}_\mathrm{r}(t) - k_\mathrm{p}\hat{e}_\Omega(t) - \hat{f}_\Omega(t)\right). \tag{2.37}$$

After that, subtracting $\dot{\Omega}_\mathrm{r}(t)$ from both sides of (2.37) and rearranging the expressions yields

$$\dot{e}_\Omega(t) + k_\mathrm{p}\frac{\rho_\Omega}{\gamma_\Omega}\hat{e}_\Omega(t) = \left(\frac{\rho_\Omega}{\gamma_\Omega} - 1\right)\dot{\Omega}_\mathrm{r}(t) + f_\Omega(t) - \frac{\rho_\Omega}{\gamma_\Omega}\hat{f}_\Omega(t). \tag{2.38}$$

For a constant reference trajectory $t \mapsto \Omega_\mathrm{r}(t)$, the error dynamics (2.38) can be simplified to

$$\dot{e}_\Omega(t) + k_\mathrm{p}\frac{\rho_\Omega}{\gamma_\Omega}\hat{e}_\Omega(t) = f_\Omega(t) - \frac{\rho_\Omega}{\gamma_\Omega}\hat{f}_\Omega(t). \tag{2.39}$$

Assuming that the estimate of the unknown part is $\hat{f}_\Omega(t) \approx \frac{\gamma_\Omega}{\rho_\Omega} f_\Omega(t)$ leads to an autonomous error dynamics. In a next step, the time delay δ_t according to (2.3) introduced by the algebraic differentiator is explicitly considered. In addition to that, effects such as approximation errors and disturbances are neglected leading to $\hat{e}_\Omega(t) \approx e_\Omega(t - \delta_t)$ (see Remark 2.6).

Remark 2.6 *Consider the error $e_\Omega(t) = \Omega(t) - \Omega_\mathrm{r}(t)$ used in the MFC law (2.35). As the angular velocity $\Omega(t)$ is not directly measured an estimate is obtained by using the difference quotient (2.34), i.e. $\Omega_{\mathrm{diff.}}(t) = \Omega(t) + \zeta(t)$ is considered for the calculation of the error. In the latter equation, $\zeta(t)$ is used to denote a disturbance introduced by the approximation (2.34). Applying the algebraic differentiator to the error as stated in (2.36) leads to*

$$\begin{aligned}
\hat{e}_\Omega(t) &= \int_{t-T}^{t} g(t-\tau)\Big(\Omega(\tau) + \zeta(\tau) - \Omega_\mathrm{r}(\tau)\Big)\mathrm{d}\tau \\
&= \int_{t-T}^{t} g(t-\tau)\Omega(\tau)\mathrm{d}\tau + \int_{t-T}^{t} g(t-\tau)\zeta(\tau)\mathrm{d}\tau - \int_{t-T}^{t} g(t-\tau)\Omega_\mathrm{r}(\tau)\mathrm{d}\tau \\
&= \hat{\Omega}(t) + \hat{\zeta}(t) - \hat{\Omega}_\mathrm{r}(t)
\end{aligned}$$

In consideration of the low-pass characteristics of the algebraic differentiator, i.e. $\hat{\zeta}(t) \approx 0$, as well as the time delay δ_t, the latter equation can be approximated as follows

$$\begin{aligned}
\hat{e}_\Omega(t) &\approx \hat{\Omega}(t) - \hat{\Omega}_\mathrm{r}(t) \\
&\approx \Omega(t - \delta_t) - \Omega_r(t - \delta_t) = e_\Omega(t - \delta_t).
\end{aligned}$$

With the latter assumptions, (2.39) reads

$$\dot{e}_{\Omega}(t) + k_{\mathrm{p}} \frac{\rho_{\Omega}}{\gamma_{\Omega}} e_{\Omega}(t - \delta_t) \approx 0. \tag{2.40}$$

The stability of this TDS, depending on the parameters $\rho_{\Omega}, \gamma_{\Omega}, k_{\mathrm{p}}$ and δ_t, can be analysed, e.g. by using the generalisation of the Hermit-Biehler theorem as presented for instance in Silva et al. (2000, 2002) or Silva et al. (2005). Following the calculations in Appendix A.1, the proportional gain has to satisfy

$$0 < k_{\mathrm{p}} < \frac{\pi}{2} \frac{\gamma_{\Omega}}{\rho_{\Omega} \delta_t} \tag{2.41}$$

in order to obtain asymptotic stability of the error dynamics (2.40). As stated in Fridman (2014), the time delay in (2.40) changes its character from an ordinary differential equation to a functional differential equation, which is an infinite-dimensional system. Consequently, assigning an initial value, i.e. $e_{\Omega}(0) = e_{\Omega,0} \in \mathbb{R}$, is no longer sufficient as an initial condition and must be replaced by an initial profile, i.e. $e_{\Omega}(\tau) = e_{\Omega,0}(\tau)$, $\tau \in [-\delta_t, 0]$. Since the experiments considered in this work are designed such that they start from a stationary regime, it is assumed that all initial profiles are always zero.

With the latter finding, Question 3 in Section 2.2.3 is answered, choosing $k_{\mathrm{p}} > 0$ is not sufficient for a stable closed loop using the proposed MFC law (2.35). However, it is still up to discuss whether more precise conditions on the parameter k_{p} can be found by using the mathematical model of the DC motor. Therefore, case 2 is considered.

Case 2: Considerations based on the mathematical model of the DC motor

In the following, the effects of the MFC law (2.35) on the DC motor (2.31b) are analysed. The resulting closed loop dynamics reads

$$\dot{\Omega}(t) = -a\Omega(t) + \frac{b}{\gamma_{\Omega}} \left(\dot{\Omega}_{\mathrm{r}}(t) - k_{\mathrm{p}} \hat{e}_{\Omega}(t) - \hat{f}_{\Omega}(t) \right) + \eta(t). \tag{2.42}$$

As previously stated, comparing the ultra-local model (2.32) with the model of the DC motor (2.31b) reveals that

$$f_{\Omega}(t) = \eta(t) - a\Omega(t),$$

and the input gain of the ultra-local model is $\rho_{\Omega} = b$. If known in advance, the parameter γ_{Ω} of the MFC law (2.35) should be chosen such that $\gamma_{\Omega} \approx b$ which addresses Question 2 in Section 2.2.3. If the approximation error of the algebraic differentiators as well as the effect of disturbances on the measurement are neglected, the estimation of the unknown part used in the MFC law (2.35) reads

$$\hat{f}_{\Omega}(t) \approx \hat{\eta}(t) - a\hat{\Omega}(t) \tag{2.43a}$$

$$\approx \eta(t - \delta_t) - a\Omega(t - \delta_t). \tag{2.43b}$$

Remark 2.7 *As discussed in Appendix A.3, the approximation* (2.43a) *is justified for the considered DC motor. Without this simplification, the error e_Ω would obey a neutral delay differential equation, the stability of which cannot be analysed by the generalised Hermite-Biehler theorem (see, e.g. Assumption ($\mathcal{A}1$) in Appendix A).*

Subtracting $a\Omega_\mathrm{r}(t)$ as well as $\frac{b}{\gamma_\Omega} a\Omega_\mathrm{r}(t-\delta_t)$ on both sides of (2.42) and using (2.43b) yields

$$\dot{e}_\Omega(t) + a e_\Omega(t) + \frac{b}{\gamma_\Omega}\left(k_\mathrm{p} - a\right) e_\Omega(t-\delta_t) \approx g_\Omega(\Omega_\mathrm{r}(t), \dot{\Omega}_\mathrm{r}(t)) + q_\Omega(\eta(t)) \tag{2.44}$$

with

$$g_\Omega(\Omega_\mathrm{r}(t), \dot{\Omega}_\mathrm{r}(t)) = \left(\frac{b}{\gamma_\Omega} - 1\right)\dot{\Omega}_\mathrm{r}(t) - a\Omega_\mathrm{r}(t) + \frac{b}{\gamma_\Omega} a\Omega_\mathrm{r}(t-\delta_t),$$
$$q_\Omega(\eta(t)) = \eta(t) - \frac{b}{\gamma_\Omega}\eta(t-\delta_t).$$

To simplify the discussion, assuming a constant reference $t \mapsto \Omega_\mathrm{r}(t) = \Omega_{\mathrm{r},0} \in \mathbb{R}$ leads to $g_\Omega(\Omega_{\mathrm{r},0}, 0) = \left(1 - \frac{b}{\gamma_\Omega}\right) a\Omega_{\mathrm{r},0}$. Additionally, if a steady state is reached, the disturbance is assumed to be constant, i.e. $t \mapsto \eta(t) = \eta_0 \in \mathbb{R}$, yielding $q_\Omega(\eta_0) = \left(1 - \frac{b}{\gamma_\Omega}\right)\eta_0$. With these assumptions, the right hand side of (2.44) reads

$$g_\Omega(\Omega_{\mathrm{r},0}, 0) + q_\Omega(\eta_0) = \left(1 - \frac{b}{\gamma_\Omega}\right)\left(a\Omega_{\mathrm{r},0} + \eta_0\right).$$

Finally, for $g_\Omega(\Omega_{\mathrm{r},0}, 0) + q_\Omega(\eta_0) \approx 0$, the TDS (2.44) yields

$$\dot{e}_\Omega(t) + a e_\Omega(t) + \frac{b}{\gamma_\Omega}\left(k_\mathrm{p} - a\right) e_\Omega(t-\delta_t) \approx 0. \tag{2.45}$$

To analyse the asymptotic stability of (2.45), the results of Silva et al. (2000, Sec. 3.1) can be applied using substitutions and assumptions according to Appendix A.2, leading to the limits of the proportional gain

$$a\left(1 - \frac{\gamma_\Omega}{b}\right) < k_\mathrm{p} < a + \frac{\gamma_\Omega}{b\delta_t}\sqrt{\tilde{z}^2 + (\delta_t a)^2}, \tag{2.46}$$

where $\tilde{z}$ is the solution of

$$\tan(\tilde{z}) = -\frac{\tilde{z}}{a\delta_t}$$

in the interval $[\pi/2, \pi]$.

Remark 2.8 *If the system under consideration is unstable, i.e. $a < 0$ and $b > 0$, the results of Silva et al. (2000, Sec. 3.2) have to be applied, leading to*

$$a + \frac{\gamma_\Omega}{b\delta_t}\sqrt{\tilde{z}^2 + (\delta_t a)^2} < k_\mathrm{p} < a\left(1 - \frac{\gamma_\Omega}{b}\right),$$

where $\tilde{z}$ is the solution of

$$\tan(\tilde{z}) = -\frac{\tilde{z}}{a\delta_t}$$

in the interval $[0, \pi/2]$ and $\gamma_\Omega < 0$.

Regarding Question 3 in Section 2.2.3, the calculations made in this section show that the first suggestion $k_\mathrm{p} > 0$ might not be enough for a stable closed loop. The proportional gain k_p has an upper and lower bound according to the considerations based on the mathematical model of the DC motor. The remaining question on how good the approximation based on the ultra-local model (2.41) is will be answered in Chapter 3. In the following section the control of the angle $\theta(t)$ is discussed.

2.4.3 Control of the angle

To control the angle $\theta(t)$ using the MFC method presented, consider the ultra-local model

$$\ddot{\theta}(t) = f_\theta(t) + \rho_\theta u(t). \tag{2.47}$$

Once more, a comparison of the ultra-local model (2.47) with mathematical model of the DC motor (2.31) reveals $f_\theta(t) = \eta(t) - a\dot{\theta}(t)$ and $\rho_\theta = b$. A MFC law for (2.47) can simply be designed according to Section 2.2.2 as

$$u(t) = \frac{1}{\gamma_\theta}\left(\ddot{\theta}_\mathrm{r}(t) - k_\mathrm{d}\dot{e}_\theta(t) - k_\mathrm{p}e_\theta(t) - \hat{f}_\theta(t)\right), \tag{2.48}$$

with the tracking error $e_\theta(t) = \theta(t) - \theta_\mathrm{r}(t)$ and the sufficiently smooth reference trajectory $t \mapsto \theta_\mathrm{r}(t)$. In contrast to the considerations in Section 2.4.2, the tracking error in (2.48) can be calculated directly because the angle $\theta(t)$ is accessible. However, the quantity $\dot{e}_\theta(t) = \dot{\theta}(t) - \dot{\theta}_\mathrm{r}(t)$ has to be derived. The difference quotient (2.34) is still a valid solution but considering the aforementioned drawbacks and the fact that $1 < \min(\alpha, \beta)$ is not a restriction in this case, the algebraic differentiators can be used yielding

$$\dot{\hat{e}}_\theta(t) = \int_{t-T}^{t} \dot{g}(t-\tau)e_\theta(\tau)\mathrm{d}\tau.$$

To further reduce the influence of disturbances on the measurement $\theta(t)$, the error $e_\theta(t)$ is filtered as well yielding the MFC law

$$u(t) = \frac{1}{\gamma_\theta}\left(\ddot{\theta}_\mathrm{r}(t) - k_\mathrm{d}\dot{\hat{e}}_\theta(t) - k_\mathrm{p}\hat{e}_\theta(t) - \hat{f}_\theta(t)\right). \tag{2.49}$$

Once more, the selection of the parameters $k_\mathrm{d}, k_\mathrm{p}$ and γ_θ is essential for the stability of the closed-loop system and must be analysed in the following. Therefore, the cases 1 and 2 presented in Section 2.4.2 are considered again.

Remark 2.9 *For the estimation of the unknown part $f_\theta(t)$, the second derivative of the angle $\theta(t)$ has to be estimated. Therefore, the parameters of the algebraic differentiators used to realise the MFC law* (2.49) *have to obey* $1 < \min(\alpha, \beta)$.

Case 1: Considerations based on the ultra-local model

If the ultra-local model (2.47) is the only source of information that is available, the error dynamics using (2.49) after subtracting $\ddot{\theta}_\mathrm{r}(t)$ on both sides reads

$$\ddot{e}_\theta(t) + k_\mathrm{d}\frac{\rho_\theta}{\gamma_\theta}\dot{\hat{e}}_\theta(t) + k_\mathrm{p}\frac{\rho_\theta}{\gamma_\theta}\hat{e}(t) = f_\theta(t) - \frac{\rho_\theta}{\gamma_\theta}\hat{f}_\theta(t) + \left(\frac{\rho_\theta}{\gamma_\theta} - 1\right)\ddot{\theta}_\mathrm{r}(t). \tag{2.50}$$

Once more, for a constant reference trajectory, the right hand side of (2.50) can be simplified yielding

$$\ddot{e}_\theta(t) + k_\mathrm{d}\frac{\rho_\theta}{\gamma_\theta}\dot{\hat{e}}_\theta(t) + k_\mathrm{p}\frac{\rho_\theta}{\gamma_\theta}\hat{e}(t) = f_\theta(t) - \frac{\rho_\theta}{\gamma_\theta}\hat{f}_\theta(t). \tag{2.51}$$

Assuming the estimate $\hat{f}_\theta(t) \approx \frac{\gamma_\theta}{\rho_\theta} f_\theta(t)$ and neglecting the errors stemming from the estimation and the measurement disturbances using the algebraic differentiator, the error dynamics (2.51) reads

$$\ddot{e}_\theta(t) + k_\mathrm{d}\frac{\rho_\theta}{\gamma_\theta}\dot{e}_\theta(t-\delta_t) + k_\mathrm{p}\frac{\rho_\theta}{\gamma_\theta}e_\theta(t-\delta_t) \approx 0. \tag{2.52}$$

In Appendix A.4, the asymptotic stability of the TDS (2.52) depending on the parameters is analysed resulting in the bound for the differential gain

$$0 < k_\mathrm{d} < \frac{\gamma_\theta}{\delta_t \rho_\theta}\tilde{z}\sin(\tilde{z}), \tag{2.53}$$

with $\tilde{z}$ being the solution of

$$\tilde{z} = -\tan(\tilde{z})$$

in the interval $[\pi/2, \pi]$, leading to $\tilde{z} \approx 2.088$. Furthermore, the proportional gain has to satisfy

$$0 < k_\mathrm{p} < \min_{j=1,3,5,\ldots}\left(\frac{\gamma_\theta}{\rho_\theta \delta_t^2} z_j^2 \cos(z_j)\right), \tag{2.54}$$

with z_j being the roots, arranged in ascending order of magnitude, of

$$\frac{\rho_\theta k_\mathrm{d}}{\sin(z_j)} = \frac{\gamma_\theta}{\delta_t} z_j,$$

which have to be determined numerically once k_d is chosen by (2.53).

Once more, a detailed analysis of the error dynamics can be derived using the mathematical model of the DC motor.

Case 2: Considerations based on the mathematical model of the DC motor

In the following, the influence of the MFC law (2.49) on the model of the DC motor (2.31) is investigated. Comparing the ultra-local model (2.47) with (2.31) reveals that

$$f_\theta(t) = \eta(t) - a\dot{\theta}(t)$$

and if the parameter b is known in advance, the input gain should be chosen as $\gamma_\theta \approx b$. According to Remark 2.7 it is assumed that the estimate of the unknown part in (2.49) reads

$$\hat{f}_\theta(t) \approx \hat{\eta}(t) - a\dot{\hat{\theta}}(t).$$

Additionally, neglecting the effects from measurement disturbances as well as the approximation errors of the algebraic differentiators, leads to the differential equation

$$\ddot{\theta}(t) = -a\dot{\theta}(t) + \frac{b}{\gamma_\theta}\left(\ddot{\theta}_\mathrm{r}(t) - k_\mathrm{d}\dot{e}_\theta(t-\delta_t) - k_\mathrm{p}e_\theta(t-\delta_t) + a\dot{\theta}(t-\delta_t) - \eta(t-\delta_t)\right) + \eta(t). \tag{2.55}$$

Subtracting $\ddot{\theta}_\mathrm{r}(t)$, $a\dot{\theta}_\mathrm{r}(t)$ and $\frac{b}{\gamma_\theta}a\dot{\theta}_\mathrm{r}(t-\delta_t)$ from both sides of (2.55) yields

$$\ddot{e}_\theta(t) + a\dot{e}_\theta(t) + \frac{b}{\gamma_\theta}\left(k_\mathrm{d} - a\right)\dot{e}_\theta(t-\delta_t) + \frac{b}{\gamma_\theta}k_\mathrm{p}e_\theta(t-\delta_t) = g_\theta(\dot{\theta}_\mathrm{r}(t), \ddot{\theta}_\mathrm{r}(t)) + q_\theta(\eta(t)) \tag{2.56}$$

with

$$\begin{aligned} g_\theta(\dot{\theta}_\mathrm{r}(t), \ddot{\theta}_\mathrm{r}(t)) &= \left(\frac{b}{\gamma_\theta} - 1\right)\ddot{\theta}_\mathrm{r}(t) - a\dot{\theta}_\mathrm{r}(t) + \frac{b}{\gamma_\theta}a\dot{\theta}_\mathrm{r}(t-\delta_t), \\ q_\theta(\eta(t)) &= \eta(t) - \frac{b}{\gamma_\theta}\eta(t-\delta_t). \end{aligned}$$

For a constant reference $t \mapsto \theta_\mathrm{r}(t) = \theta_{\mathrm{r},0} \in \mathbb{R}$ and the assumption of a constant disturbance $t \mapsto \eta(t) = \eta_0 \in \mathbb{R}$, the right hand side of (2.56) reads

$$g_\theta(0,0) + q_\theta(\eta_0) = \left(1 - \frac{b}{\gamma_\theta}\right)\eta_0.$$

If $q_\theta(\eta_0) \approx 0$, the TDS

$$\ddot{e}_\theta(t) + a\dot{e}_\theta(t) + \frac{b}{\gamma_\theta}\left(k_\mathrm{d} - a\right)\dot{e}_\theta(t-\delta_t) + \frac{b}{\gamma_\theta}k_\mathrm{p}e_\theta(t-\delta_t) \approx 0 \tag{2.57}$$

results from (2.56). Therefore, the finding from Farkh et al. (2009) can be applied to determine the asymptotic stability of the TDS (2.57). In Appendix A.5 the notation of Farkh et al. (2009) is adjusted leading to the range of the differential gain as

$$a\left(1 - \frac{\gamma_\theta}{b}\right) < k_\mathrm{d} < a + \frac{\gamma_\theta}{b\delta_t}\sqrt{\tilde{z}^2 + (\delta_t a)^2}, \tag{2.58}$$

with $\tilde{z}$ the solution of

$$\tan(\tilde{z}) = -\frac{\tilde{z}}{a\delta_t}$$

in the interval $[\pi/2, \pi]$. The range of the proportional gain is

$$0 < k_\mathrm{p} < \min_{j=1,3,5,\ldots} \left(\frac{a\gamma_\theta z_j}{b\delta_t} \left(\sin(z_j) + \frac{z_j}{a\delta_t} \cos(z_j) \right) \right) \tag{2.59}$$

with z_j, the roots, arranged in ascending order of magnitude of

$$\frac{\gamma_\theta}{b} (k_\mathrm{d} - a) + a\cos(z_j) = \frac{z_j}{\delta_t} \sin(z_j),$$

the latter have to be determined numerically. With these results, the admissible parameter set of the MFC law (2.49) leading to a stable closed-loop system can be calculated.

Remark 2.10 *In Appendix A.6, the stability depending on the parameters for the second-order system*

$$\ddot{y}(t) = bu(t) - a_1\dot{y}(t) - a_0 y(t)$$

with $a_1, a_0, b > 0$ which is controlled by the MFC law (2.49) *is analysed and it is shown that the admissible parameter set is limited.*

Subsequently, with the help of experiments on a real test bed, a validation process will be undertaken in order to verify the theoretical findings thus far.

Chapter 3

Experimental results

In the following, the findings of Chapter 2 are evaluated using a DC motor as a test bed. First, the experimental setup is presented in Section 3.1 and it is shown how the parameters of the model (2.31) are identified in Section 3.2. Details concerning the implementation of the control laws are shared in Section 3.3. Thereafter, the parametrisation of the algebraic differentiators is analysed in Section 3.4 as well as the stability of the closed-loop system depending on the parameters of the MFC laws considered in Section 3.5. During the discussion of the experimental results, three guidelines are presented for the parametrisation of the algebraic differentiators used as well as the MFC laws based on first-order and second-order ultra-local models. Additionally, the derived guidelines are compared to the systematic parametrisation approach presented in Polack et al. (2019).

3.1 Experimental setup

The following experiments are carried out on the test bed depicted in Figure 2.6. A DC gear motor modelcraft RB350018-2A723R with a transmission ratio of 1:18 is used as the core element of the test bed. The required input voltage, which is limited to $\pm 12\,\mathrm{V}$, is provided by the DC driver MD10C R3 from Cytron. A Voltcraft USPS-2250 is used as the power supply for the whole setup. The angle of the load is measured by the incremental encoder 05.2420.1222.1024 from Kübler with two channels, each having a 10-bit resolution resulting in an 11-bit resolution using both. The proposed control laws are running on a STM32F407ZGT6 microcontroller with a 168 MHz processor that is used to run the algorithms with different sampling times. The load, which is supported by two ball bearings, consist of a 3D printed housing, containing small metal cylinders to increase its weight and inertia, respectively.

The system considered can be approximated by the mathematical model (2.31), the parameters of which are identified in the next section.

3.2 Parameter identification

To get a better understanding of the system under consideration presented in Section 2.4.1, experiments are conducted to perform a parameter identification. With this, numerical values for the parameters a and b of the model (2.31) can be found such that the mathematical model approximates the behaviour of the real system. As discussed in Chapter 2, the information about the parameters can help to find the region in the parameter set leading to a stable closed-loop system.

Consider the model (2.31) which can also be written as

$$\begin{aligned}\ddot{\theta}(t) &= \begin{pmatrix} u(t) & -\dot{\theta}(t) \end{pmatrix} \begin{pmatrix} b \\ a \end{pmatrix} \\ &= \begin{pmatrix} u(t) & -\dot{\theta}(t) \end{pmatrix} \boldsymbol{p}.\end{aligned}$$

Assuming that the derivatives of θ are known, a simple least squares minimisation problem can be solved to get access to the parameter vector $\boldsymbol{p}$. By using the algebraic differentiators as discussed in Othmane et al. (2022, Sec. 5.1), the identification task can be simplified, because with their help the needed derivatives can be estimated yielding

$$\ddot{\hat{\theta}}(t) = \begin{pmatrix} \hat{u}(t) & -\dot{\hat{\theta}}(t) \end{pmatrix} \hat{\boldsymbol{p}}, \tag{3.1}$$

with the estimated parameters $\hat{\boldsymbol{p}} = (\hat{a}, \hat{b})^{\mathrm{T}}$. In (3.1), the input signal $t \mapsto u(t)$ is also filtered such that all signals are affected by the same delay δ_t of the algebraic differentiator. Collecting K estimates in the matrix

$$G = \begin{pmatrix} \hat{u}[1] & -\dot{\hat{\theta}}[1] \\ \hat{u}[2] & -\dot{\hat{\theta}}[2] \\ \vdots & \vdots \\ \hat{u}[K] & -\dot{\hat{\theta}}[K] \end{pmatrix}$$

and the vector

$$\boldsymbol{y} = \begin{pmatrix} \ddot{\hat{\theta}}[1] \\ \ddot{\hat{\theta}}[2] \\ \vdots \\ \ddot{\hat{\theta}}[K] \end{pmatrix}$$

allows to formulate the simple least squares minimisation problem

$$\min_{\hat{\boldsymbol{p}}} J(\hat{\boldsymbol{p}}) \tag{3.2}$$

with the cost function

$$J(\hat{\boldsymbol{p}}) = (G\hat{\boldsymbol{p}} - \boldsymbol{y})^{\mathrm{T}}(G\hat{\boldsymbol{p}} - \boldsymbol{y}).$$

The solution of the minimisation problem (3.2) is

$$\hat{\boldsymbol{p}} = (G^{\mathrm{T}}G)^{-1}G^{\mathrm{T}}\boldsymbol{y},$$

which only depends on known or estimated values.

For the parameter identification, four step responses with an input of $-12\,\mathrm{V}$, $-6\,\mathrm{V}$, $+6\,\mathrm{V}$, and $+12\,\mathrm{V}$ are measured with a sampling frequency of $100\,\mathrm{Hz}$. The required derivatives of the measurement are estimated by algebraic differentiators with the parametrisation of $N = 0$, $\omega_{\mathrm{c}} = 50\,\mathrm{rad/s}$, and $\alpha = \beta = 6$, discretised using the mid-point rule. The latter parameter combination is chosen since it resulted in a small deviation of simulation and experiment. A more systematic way for the parametrisation of the algebraic differentiators used for parameter identification can be found in Othmane et al. (2022, Sec. 5.1). For each experiment, the least squares minimisation problem (3.2) is solved, leading to four sets of parameters $(\hat{a}_j, \hat{b}_j), j \in \{1, 2, 3, 4\}$. After that, the mean of the identified parameters is calculated, leading, under an abuse of notation, to $a = 1/4 \sum_{j=1}^{4} \hat{a}_j = 39.44\,\mathrm{s}^{-1}$ and $b = 1/4 \sum_{j=1}^{4} \hat{b}_j = 108.55\,\mathrm{rad/(Vs^2)}$. To verify the results, a different experiment is done using a sinusoidal input trajectory $t \mapsto u(t) = A \sin(2\pi f t)$, with $A = 6\,\mathrm{V}$ and $f = 1\,\mathrm{Hz}$. Thereafter, this experiment is compared to a simulation of (2.31) using the solver ode45, leading to the results depicted in Fig. 3.1. Therein, the angular velocity is approximated using the difference quotient (2.34). In Fig. 3.1 the unmodelled effects such as friction and the backlash of the gearbox are clearly visible, especially if a change in the sign of the angular velocity occurs, as highlighted in the figure. Nevertheless, the approximation of the DC motor using the model (2.31) is sufficiently accurate for the following analysis. With the identified parameters of the model (2.31), the theoretical findings of Sections 2.4.2 and 2.4.3 can be verified.

3.3 Implementation details

All considerations regarding the MFC from Chapter 2 are based in a continuous-time setting. Nonetheless, for an implementation of the algorithms on the proposed microcontroller, the discretisation techniques from Section 2.1 have to be applied. Therefore, based on the MFC law for the angular velocity (2.35), details concerning the implementation are shared. It should be noted that the following comments can be applied to the MFC law of the angle (2.49) as well.

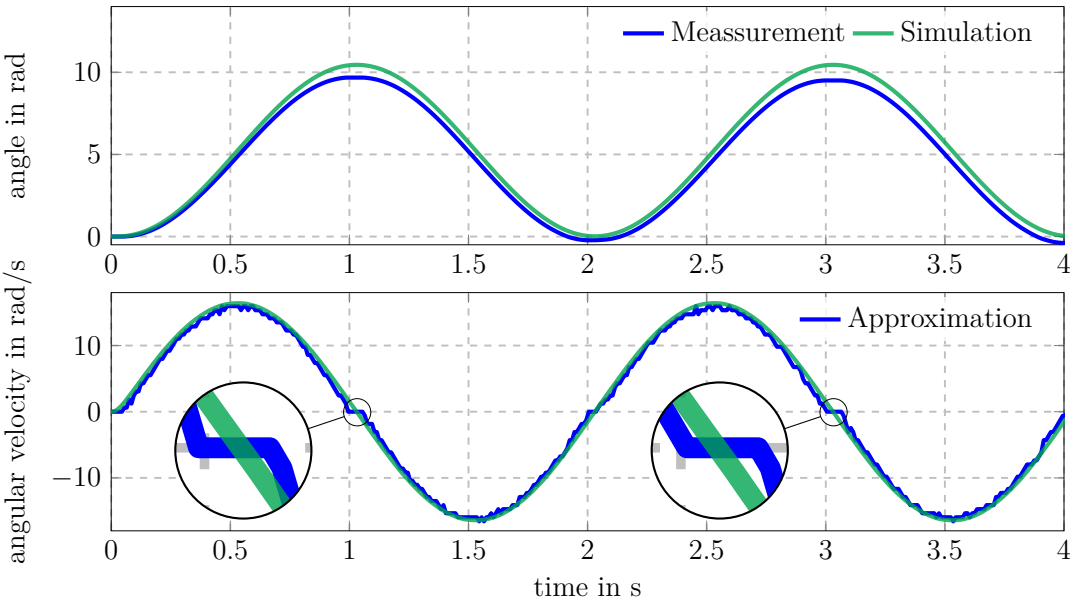

Fig. 3.1: Comparison of the experimental data and the corresponding simulation of the DC motor using a sinusoidal input trajectory $t \mapsto u(t) = A \sin(2\pi f t)$, with $A = 6\,\mathrm{V}$ and $f = 1\,\mathrm{Hz}$ as well as the parameters $a = 39.44\,\mathrm{s}^{-1}$ and $b = 108.55\,\mathrm{rad/(Vs^2)}$.

Implementation of the control law

As stated in Section 2.4.2, the angular velocity Ω at sampling instant k is obtained by the difference quotient

$$\Omega[k] = \frac{\theta[k] - \theta[k-1]}{t_\mathrm{s}}.$$

Using this quantity, the MFC law (2.35) can be written in discrete time as

$$u[k] = \frac{1}{\gamma_\Omega}\left(\dot{\Omega}_\mathrm{r}[k] - k_\mathrm{p}\hat{e}_\Omega[k+\theta] - \hat{f}_\Omega[k+\theta]\right). \tag{3.3}$$

It is assumed that the window length T of the differentiator is an integral multiple of the sampling time t_s, i.e. $T = n_\mathrm{s} t_\mathrm{s}$ and the parameter ε in (2.20) is chosen equal to t_s. Following the discussions from Sections 2.1 and 2.3, the quantities $\hat{f}_\Omega[k+\theta]$ and $\hat{e}_\Omega[k+\theta]$ in (3.3) can be computed as

$$\hat{f}_\Omega[k+\theta] = \frac{1}{\Phi_1}\sum_{j=0}^{L-1} w_1[j]\Omega[k-j-1] - \gamma_\Omega \frac{1}{\Phi_0}\sum_{j=0}^{L-1} w_0[j]u[k-j-1], \tag{3.4}$$

and

$$\hat{e}_\Omega[k+\theta] = \frac{1}{\Phi_0}\sum_{j=0}^{L-1} w_0[j]\left(\Omega[k-j] - \Omega_\mathrm{r}[k-j]\right),$$

with

$$\Phi_n = \frac{t_\mathrm{s}^n}{n!} \sum_{j=0}^{L-1} w_n[j](-j)^n.$$

According to Othmane et al. (2022), applying the mid-point rule for example, the parameters of the latter equations are $\theta = 1/2$, $w_n[j] = t_\mathrm{s} g^{(n)}[j + 1/2]$, and $L = n_\mathrm{s}$. The open-source toolbox AlgDiff (see Othmane (2022a)) already provides $w_n[j]$ as well as Φ_n which simplifies the use of the algebraic differentiators.

Input saturation

Since the input voltage of the DC motor is limited, the discrete-time input $u[k]$ in (3.3) is saturated such that the applied voltage $u_\mathrm{sat}[k]$ is in the interval $u_\mathrm{sat}[k] \in [-u_\mathrm{max}, u_\mathrm{max}]$ with $u_\mathrm{max} = 12\,\mathrm{V}$. Then, $u_\mathrm{sat}[k]$ is used for the motor at each sampling instant k.

Safety routine

Preliminary experiments showed that a sampling of the parameter sets for the algebraic differentiator and the MFC laws, can quickly lead to a failure of the DC motor. Due to fast oscillations of the commanded input voltage, especially for parameter combinations leading to an unstable closed loop, the wear of the DC motor is dramatically increased. To avoid damaging the setup a safety routine is implemented which stops the experiment if $|\dot{u}[k]| \geq 120\,\mathrm{V/s}$. During the preliminary experiments it has been shown that $120\,\mathrm{V/s}$ is a good trade-off between safety and normal operation of the motor. The derivative $\dot{u}[k]$ is obtained by an algebraic differentiator with the parametrisation $\alpha = \beta = 6$, $\omega_\mathrm{c} = 200\,\mathrm{rad/s}$, $N = 0$, discretised using the mid-point rule. The latter is determinant manually such that the discretisation error is small as well as the resulting computational burden of the routine is low. Assuming a sampling frequency of $f_\mathrm{s} = 200\,\mathrm{Hz}$, the latter combination leads to a discrete window of length $n_\mathrm{s} = 9$ for the estimator.

The implementation of the proposed MFC laws can be achieved based on the latter considerations. Subsequently, the parametrisation of the algebraic differentiators used to realise (3.3) is analysed.

3.4 Parameters of algebraic differentiators

In this section, the parametrisation of the algebraic differentiators and their effect on the stability of the closed loop is investigated. According to Mboup and Riachy (2018) and Othmane et al. (2022, Sec. 4) the parameters α and β are chosen equal because

this results in a high rejection of the additive measurement disturbance. Additionally, with the choice $N = 0$ the estimation delay δ_t is equal to half of the filter window length T, i.e. $\delta_t = T/2$. The parameters ω_c and $\alpha = \beta$ are varied. For each experiment, a polynomial of degree 5 is used as a reference trajectory (see, e.g. Fig. 3.4 for the reference of the angular velocity $t \mapsto \Omega_\mathrm{r}(t)$) for the respective control variable. At the end of this section, the collected findings are summarised in Guideline 1.

3.4.1 Control of the angular velocity

The objective of the following experiments is to investigate the stability of the DC motor (2.31) controlled by the MFC law (2.35) with respect to the parameters of the algebraic differentiators. To this end, several different parameter combinations for $\omega_\mathrm{c} \in \{25, 50, \ldots, 200\}\,\mathrm{rad/s}$ and $\alpha = \beta \in \{1, 2, \ldots, 8\}$ are tested using the mid-point rule as the discretisation method. According to Chapter 2, the first derivate of the angular velocity $\Omega(t)$ is needed for the estimation of the unknown part $f_\Omega(t)$. For this reason, the correct discretisation of the kernel $\dot{g}_{N,T,\vartheta}^{(\alpha,\beta)}$ is crucial for a good result of the algorithm. For each parameter combination, the mid-point rule is capable of approximating the continuous kernel up to the cutoff frequency ω_c, and the resulting discretisation errors are low (see, e.g. Fig. 3.2). For further considerations, the root mean square (RMS) value of the error e_Ω is introduced for each parametrisation considered. The parameters of the MFC law (2.35) are chosen as $k_\mathrm{p} = 50\,\mathrm{s}^{-1}$ and $\gamma_\Omega = b$. According to the considerations in Section 2.4.2, this choice should result in a stable closed loop for every delay δ_t of the estimators resulting from the combinations in the analysed parameter set. The sampling frequency is chosen to $f_\mathrm{s} = 200\,\mathrm{Hz}$. With this choice, some flexibility in choosing ω_c is available, because the cutoff frequency ω_c is limited by the Nyquist frequency $\omega_\mathrm{ny} = \pi f_\mathrm{s}$. A variation of the sampling frequency f_s is investigated for the control of the angle $\theta(t)$, covered in Section 3.4.2. This approach is not employed for the following experiments since the difference quotient (2.34) is used to estimate the angular velocity $\Omega(t)$, which increases the quantisation error significantly if the sampling frequency f_s is increased as discussed in Section 2.4.2.

In Fig. 3.3, the RMS values of the error e_Ω are depicted depending on the parametrisation of the estimator, whereas each red cross marks a tested combination. Several effects can be observed in the latter mentioned figure. On one hand, the limited sampling frequency of $f_\mathrm{s} = 200\,\mathrm{Hz}$ results in a mismatch of the desired cutoff frequencies $\omega_\mathrm{c} \in \{25, 50, \ldots, 200\}\,\mathrm{rad/s}$ and the resulting ones, especially for high cutoff frequencies. The reason for this is that there are only a few values inside the discrete filter window of length $T = n_\mathrm{s} t_\mathrm{s}$, thus not every cutoff frequency ω_c can be represented. This effect can be compensated by increasing $\alpha = \beta$ leading to a larger discrete filter window of length T and ultimately to a higher delay δ_t as seen in (2.3). On the other hand, the RMS values of the error e_Ω for $\omega_\mathrm{c} = 25\,\mathrm{rad/s}$ are increasing if the values of $\alpha = \beta$ are growing as a result of the increasing delay δ_t and the fact that the controller parameter k_p is fixed for all experiments.

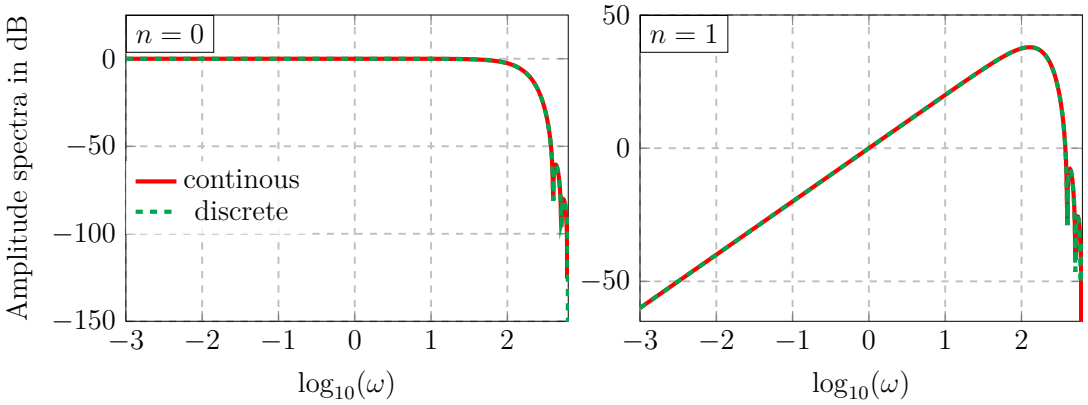

Fig. 3.2: Comparison of the amplitude spectra of the continuous-time and discrete-time differentiators with the parametrisation $N = 0, \omega_c = 200\,\mathrm{rad/s}$ and $\alpha = \beta = 9$ using the mid-point discretisation.

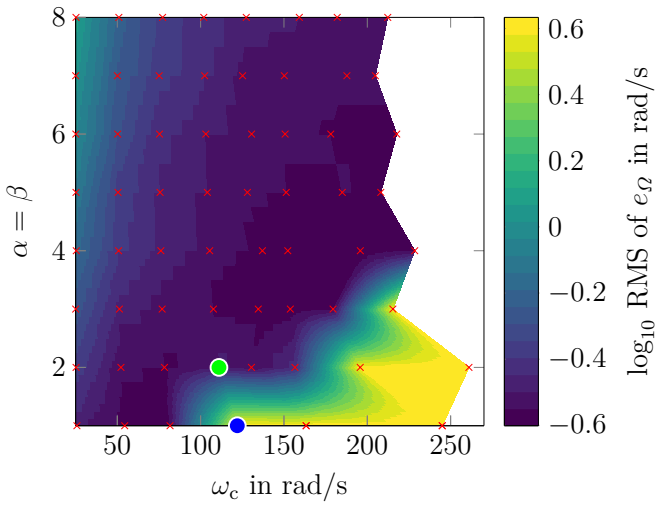

Fig. 3.3: RMS error of e_Ω of the different parameters $\omega_c \in \{25, 50, \ldots, 200\}\,\mathrm{rad/s}$ and $\alpha = \beta \in \{1, 2, \ldots, 8\}$ for the algebraic differentiators covered with a sampling frequency of $f_s = 200\,\mathrm{Hz}$ using the mid-point discretisation. The parameters of the MFC law are chosen as $k_p = 50\,\mathrm{s}^{-1}$ and $\gamma_\Omega = b$. Each red cross marks a tested parameter combination.

Besides the latter mentioned effects, the parameter combinations summarised in Table 3.1 are leading to an unstable closed loop, even though the findings from Section 2.4.2 predict a stable behaviour. In all cases, the safety routine is activated. Figure 3.4 shows a comparison of a parameter combination leading to a stable closed loop and an unstable one which is aborted by the safety routine, clearly showing the increasing amplitude of the input voltage $u(t)$. Both experiments are also marked in Fig. 3.3 with the green and blue circle, respectively. For comparison, the continuous and discrete amplitude spectra of both parametrisations are also depicted in Fig. 3.5,

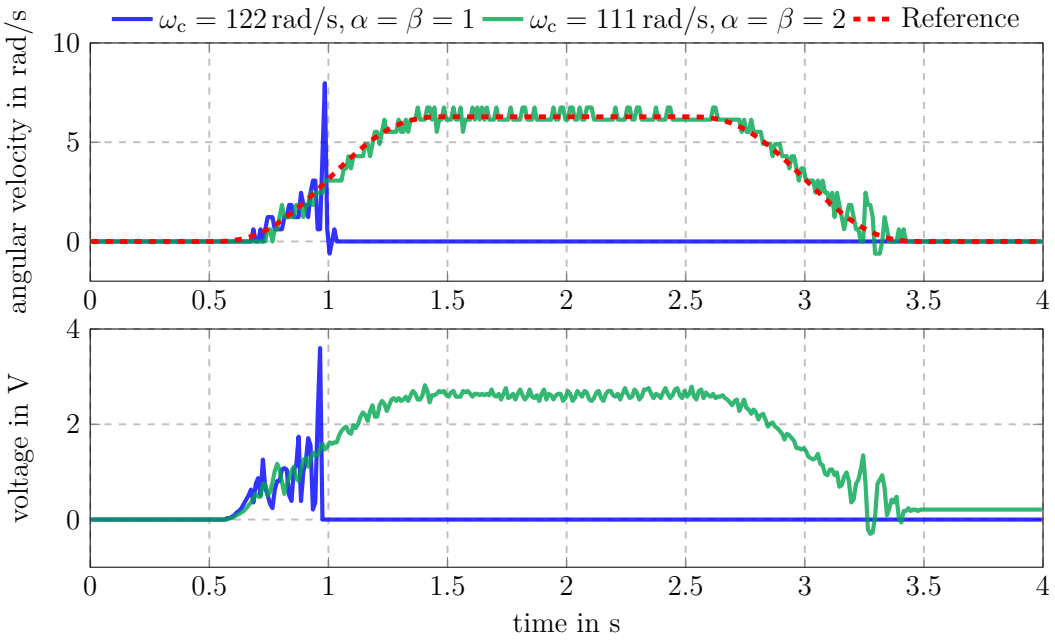

Fig. 3.4: Comparison of the experimental results using different parametrisations of the algebraic differentiator, marked in Fig. 3.3. The graphs depicted in green are showing the tracking performance of a stable closed loop, whereas the experiment depicted blue is aborted by the safety routine.

whereas no abnormalities are apparent. A similar behaviour is observed in Section 3.4.2 and some more details are discussed therein.

Table 3.1: Parameter combinations of the algebraic differentiators leading to an unstable closed loop for the control of the angular velocity $\Omega(t)$ with $f_s = 200\,\mathrm{Hz}$.

No.	$\alpha = \beta$	ω_c in rad/s
1	1	122
2	1	163
3	1	244
4	2	195
5	2	260
6	3	215

3.4.2 Control of the angle

The results of the following experiments are used to analyse the effects of the parametrisation of the algebraic differentiators on the stability of system (2.31) controlled with

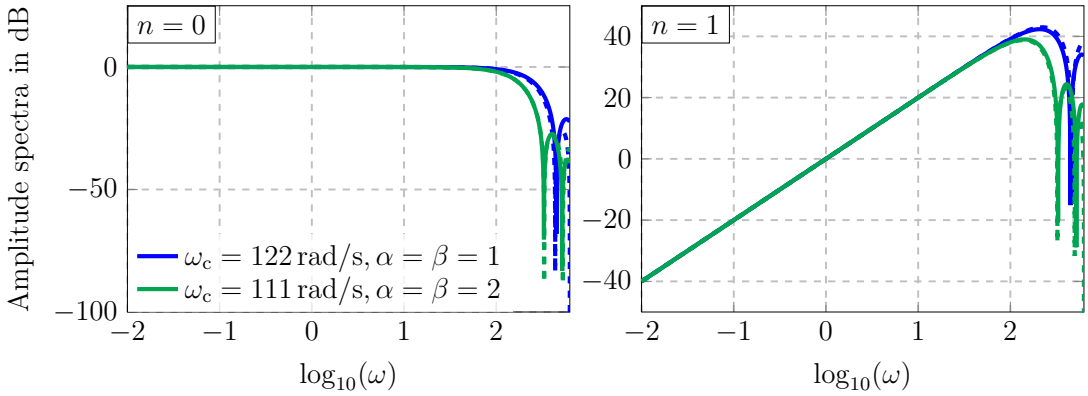

Fig. 3.5: Comparison of the amplitude spectra for different parametrisations of the algebraic differentiator, marked in Fig. 3.3. The continuous and discrete amplitude spectra are depicted by the solid and dashed lines, respectively.

the MFC law (2.49). Several experiments are conduced using different combinations for $\omega_c \in \{25, 50, \ldots, 200\}\,\mathrm{rad/s}$ and $\alpha = \beta \in \{2, 3, \ldots, 9\}$. To realise the MFC law (2.49), the second derivative of the angle θ has to be estimated. Therefore, the parameters $\alpha = \beta$ are limited to $1 < \min(\alpha, \beta)$. As discussed in Scherer et al. (2024), the discretisation of the algebraic differentiators is important to achieve satisfactory results and using the mid-point rule can lead to discretisation errors especially for frequencies below the cutoff frequency ω_c. It could be shown in the latter contribution that these errors can be reduced by increasing the parameter $\alpha = \beta$, which, however, leads to an increased delay δ_t. Using the analytical integration method (see, e.g. Kiltz (2017, Sec. 3.4.2) and Othmane et al. (2022, Sec. 4.3)) is favourable especially for small filter window lengths T and can be used instead of the latter solution using the mid-point rule. Nevertheless, it should be noted that the frequency-domain properties of the discretised filters can be distorted for specific parametrisations as mentioned in Othmane et al. (2022, Sec. 4.3). In Fig. 3.6, the amplitude spectra for the algebraic differentiators, which are used to approximate the second derivative, are plotted using the mid-point and the analytic integration rule, respectively. The results obtained by the mid-point rule are bad even if the parameters $\alpha = \beta = 9$ are chosen. Nonetheless, the parameters $\alpha = \beta$ could be chosen higher but this is not considered here.

The parameters of the MFC law (2.49) are chosen as $\gamma_\theta = b$, $k_\mathrm{p} = 100\,\mathrm{s}^{-2}$, and $k_\mathrm{d} = 50\,\mathrm{s}^{-1}$ which leads, according to the considerations made in Section 2.4.3, to a stable closed-loop for each parameter combination of the algebraic differentiator, i.e. for every resulting delay δ_t. The same polynomial set point transition as depicted in Fig. 3.4 is used as the reference trajectory $t \mapsto \theta_\mathrm{r}(t)$ and with this, the RMS values of the error e_θ can be used to indicate the stability of the closed loop. In addition to the parameters of the algebraic differentiators, the sampling frequency $f_\mathrm{s} \in \{20\,\mathrm{Hz}, 200\,\mathrm{Hz}, 1\,\mathrm{kHz}\}$ is varied, to showcase different problems that might occur using the proposed realisation of the MFC approach.

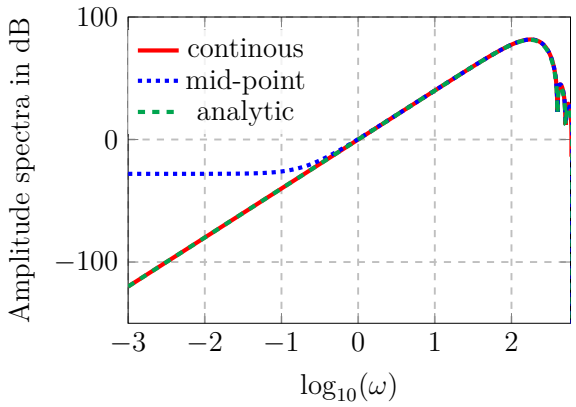

Fig. 3.6: Comparison of the amplitude spectra of the continuous-time and discrete-time differentiators with the parametrisation $N = 0, \omega_c = 200\,\mathrm{rad/s}$ and $\alpha = \beta = 9$ using the mid-point and the analytic integration rule for the second derivate, i.e. $n = 2$.

The experimental results using a sampling frequency of $f_s = 20\,\mathrm{Hz}$ are depicted in Fig. 3.7. In this case, only $\omega_c = 25\,\mathrm{rad/s}$ is chosen because the Nyquist frequency limits the choice of the cutoff frequency ω_c. Therefore, only $\alpha = \beta \in \{2, 3, \ldots, 9\}$ is varied. As discussed in Section 3.4.1, these parameter combinations are leading to a high delay which is the main reason for the resulting RMS values of the error e_θ. Nevertheless, none of these parameter combinations is leading to an unstable closed loop. This effect can also be observed if the sampling frequency is increased to $f_s = 200\,\mathrm{Hz}$ in Fig. 3.8. In the latter figure, the parameter combinations summarised in Table 3.2 (a) are leading to an unstable closed loop. In each case, the safety routine aborts the experiment. By comparing the latter table with the results obtain in Section 3.4.1, it is noticeable that the combinations with the numbers 4, 5, and 6 from Table 3.1 can also be found in Table 3.2 (a). If the sampling frequency is increased to $f_s = 1\,\mathrm{kHz}$, the latter concordance becomes less evident. In Fig. 3.9, it can be observed that the combinations summarised in Table 3.2 (b) are leading to an unstable closed loop. At least some similarities can be found by comparing the results of Table 3.2 (a) and (b). In Fig. 3.9 the black squares indicate parameter combinations that are unrealisable with the available hardware due to the limited computational capabilities. The discrete convolutions (see, e.g. (2.4)) cannot be calculated in time, thus loosing the real-time capability of the algorithm. Comparing Fig. 3.9 with Fig. 3.8 shows that the desired cutoff frequencies are better matched if the sampling frequency is high enough. The experiments conducted at different sampling frequencies exhibited a consistent trend: Low values of $\alpha = \beta$ and a high cutoff frequency ω_c are leading to an unstable closed loop and a low cutoff frequency ω_c in combination with increasing $\alpha = \beta$ values is leading to a high delay δ_t ultimately resulting in increasing RMS values of the error e_θ.

Comparing Fig. 3.8 with Fig. 3.9 shows that the sampling frequency is not the reason for the instability of the controlled system. Additionally, a comparison of the experiments

Table 3.2: Parameter combinations of the algebraic differentiators leading to an unstable closed loop for the control of the control of the angle $\theta(t)$ with $f_\mathrm{s} = 200\,\mathrm{Hz}$ in (a) and $f_\mathrm{s} = 1\,\mathrm{kHz}$ in (b).

(a)

No.	$\alpha = \beta$	ω_c in rad/s
1	2	163
2	2	195
3	2	260
4	3	215

(b)

No.	$\alpha = \beta$	ω_c in rad/s
1	2	153
2	2	177
3	2	206
4	3	179
5	3	207

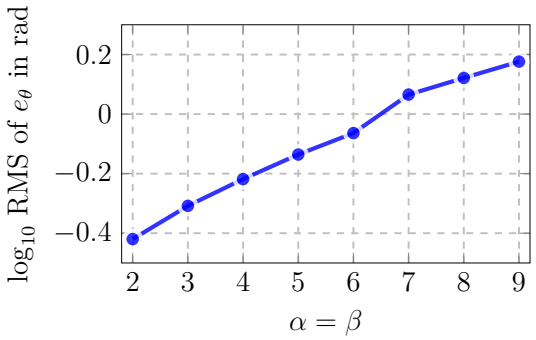

Fig. 3.7: RMS error of e_θ of the different parameters $\alpha = \beta \in \{2, 3, \ldots, 9\}$ and $\omega_\mathrm{c} = 25\,\mathrm{rad/s}$ for the algebraic differentiators covered with a sampling frequency of $f_\mathrm{s} = 20\,\mathrm{Hz}$ using the analytic integration rule. The parameters of the MFC law are chosen as $k_\mathrm{p} = 100\,\mathrm{s}^{-2}$, $k_\mathrm{d} = 50\,\mathrm{s}^{-1}$ and $\gamma_\Omega = b$.

discussed in this section and in Section 3.4.1 is indicating that the discretisation method used is also not affecting the stability of the closed loop. Nevertheless, the stability issues can still be overcome by increasing $\alpha = \beta$. As stated in Section 2.3, usually only $\alpha = \beta = 2$ is considered in the current literature and as shown in Scherer et al. (2024) as well as the latter experiments, using the generalisation of the MFC law proposed in Chapter 2 solves this issue.

Remark 3.1 *Comparing Fig. 6 from Scherer et al. (2024) with the results obtained in this section shows that the dependency of the stability is more pronounced for the magnetically supported plate. The reason for this might be the fact that the magnetically supported plate is an unstable MIMO system in comparison to the stable DC motor considered here or the unmodelled higher order mechanical eigenfrequencies of the plate. The new results reported in this section are indicating that neither the sampling frequency nor the discretisation of the algebraic differentiators is the reason for this behaviour. Nevertheless, the origin of this effect is still open to discuss.*

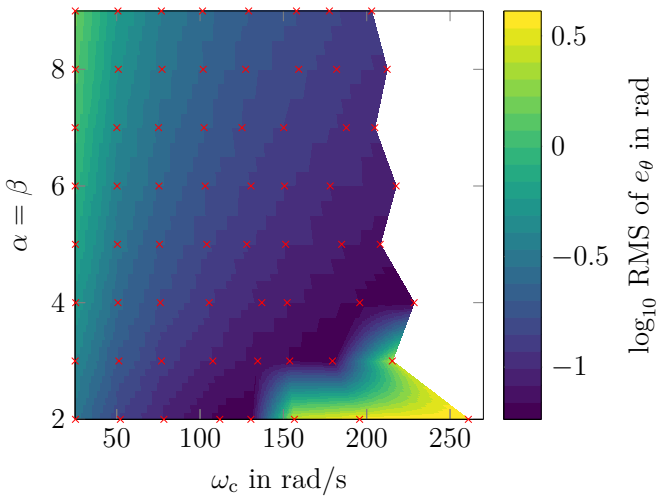

Fig. 3.8: RMS error of e_θ of the different parameters $\omega_c \in \{25, 50, \ldots, 200\}$rad/s and $\alpha = \beta \in \{2, 3, \ldots, 9\}$ for the algebraic differentiators covered with a sampling frequency of $f_s = 200\,\mathrm{Hz}$ using the analytic integration rule. The parameters of the MFC law are chosen as $k_p = 100\,\mathrm{s}^{-2}$, $k_d = 50\,\mathrm{s}^{-1}$ and $\gamma_\Omega = b$.

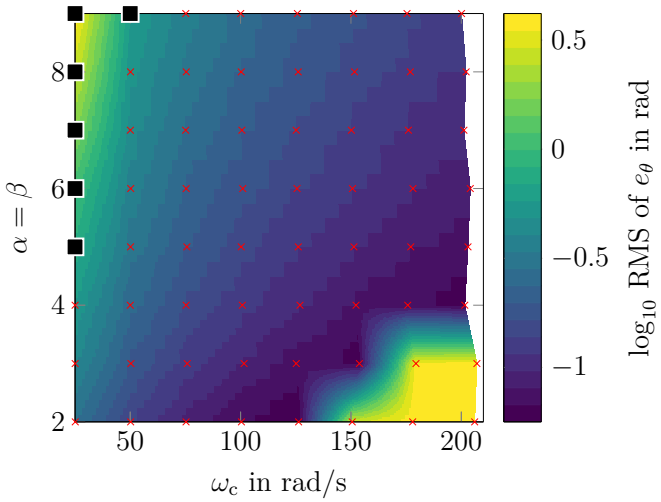

Fig. 3.9: RMS error of e_θ of the different parameters $\omega_c \in \{25, 50, \ldots, 200\}$rad/s and $\alpha = \beta \in \{2, 3, \ldots, 9\}$ for the algebraic differentiators covered with a sampling frequency of $f_s = 1\,\mathrm{kHz}$ using the analytic integration rule. The parameters of the MFC law are chosen as $k_p = 100\,\mathrm{s}^{-2}$, $k_d = 50\,\mathrm{s}^{-1}$ and $\gamma_\Omega = b$. Parameter combinations marked with a black square are unrealisable with the hardware used, i.e. the filter window lengths are too high, such that the real-time capability of the algorithm gets lost.

For all further experiments, the cutoff frequency $\omega_c = 200\,\mathrm{rad/s}$ is chosen, which allows to follow rapid changes in the reference trajectory. The parameters $\alpha = \beta = 9$ are chosen to suppress additive high frequency disturbances corrupting the measurement and to ensure a good approximation of the desired cutoff frequency ω_c. For the control

of the angular velocity $\Omega(t)$, the used algebraic differentiators are discretised with the mid-point rule and the analytic integration rule is chosen for the control of the angle $\theta(t)$ to eliminate discretisation errors as discussed in this section. The latter parametrisation results, with a sampling frequency of $f_\mathrm{s} = 200\,\mathrm{Hz}$, in a delay of $\delta_t = 35\,\mathrm{ms}$, which has to be considered in the following section for the tuning of the controller parameters.

Based on the findings of Section 3.4, Guideline 1 can be formulated.

Guideline 1: Parametrisation of the algebraic differentiators for their use in a MFC law based on ultra-local models

The parameters of the algebraic differentiators used to realise a MFC law based on ultra-local models should be chosen as follows:

Step 1: If possible, the sampling frequency f_s should be chosen as high as possible but not too high to ensure the real-time capability of the algorithm on the hardware used.

Step 2: The cutoff frequency ω_c should be chosen as high as possible, such that rapid changes in the reference trajectory $t \mapsto y_\mathrm{r}(t)$ can be followed but also as low as possible to suppress additive high frequency disturbances corrupting the measurement.

Step 3: The parameters $\alpha = \beta$ should be chosen high to get a satisfying damping of high frequency disturbances but not too high, to minimise the resulting delay δ_t of the algebraic differentiator whereas $n < \min(\alpha, \beta) + 1$, with n being the highest derivative to be estimated, has to be considered as the lower bound.

Step 4: The parameter $N = 0$ should be chosen which leads to the delay[a] $\delta_t = T/2$.

Step 5: If the filter window length T is short in comparison to the sampling period t_s, the analytic integration rule should be chosen, otherwise the mid-point rule. In either case, it should be ensured that the discretisation error is small especially for frequencies below the cutoff frequency ω_c. If this is not the case, the parameter $\alpha = \beta$ should be increased and/or the cutoff frequency ω_c should be reduced.

Step 6: If the desired cutoff frequency is not matched in a satisfactory manner, either go back to Step 1 and increase the sampling frequency or go back to Step 3 and increase $\alpha = \beta$.

[a] A delay-free estimation is not recommanded because according to Mboup et al. (2009) and Othmane et al. (2022) allowing a small but known delay δ_t increases the accuracy of the approximation.

Remark 3.2 *Once the cutoff frequency ω_c in Step 2 of Guideline 1 is set, the parameters $\alpha = \beta$ can also be chosen according to Othmane et al. (2022, Sec. 5.1.2), using the weakest relative attenuation $k_{N,\min}$ at the Nyquist frequency. With a small $k_{N,\min}$, aliasing problems can be avoided. Nonetheless, the increased delay δ_t resulting from higher values of $\alpha = \beta$ have to be considered.*

3.5 Parameters of the MFC law

In the following section, the parametrisation of the MFC laws, i.e. the choice of the parameters γ_Ω, γ_θ, k_p as well as k_d and their influence on the stability of the closed loop, is investigated. The theoretical findings from Chapter 2 have to be validated by experiments on the test bed presented in Section 3.1. Therefore, the parameter set is sampled in the same way as it is done in Scherer et al. (2023, 2024).

3.5.1 Control of the angular velocity

After parametrising the algebraic differentiators, the parameters of the MFC law (2.35), namely γ_Ω and k_p, have to be tuned. Therefore, the γ_Ω-k_p parameter set is sampled and the RMS values of the error e_Ω are used as a quality gauge. In addition, for each experiment made, the energy of the input signal (see, e.g. Oppenheim and Schafer (1975, Sec. 1.1))

$$\mathcal{E}(u) = \sum_{j=0}^{M} |u[j]|^2 ,$$

with M depending on the duration of the experiment, is calculated. In comparison to the experiments made in Scherer et al. (2023), using the maximum of the input voltage u is not as meaningful, because the implemented safety routine often aborts the experiment before this value is reached. The same set point transition as in Section 3.4 is used as the reference trajectory $t \mapsto \Omega_\mathrm{r}(t)$ (see, e.g. Fig. 3.12).

The results of the experiments are presented in Fig. 3.10. Each marker represents an individual experiment whereas a red triangle indicates an experiment that is aborted by the safety routine, a white circle marks a parameter combination leading to a voltage that is not high enough to overcome the friction and a black cross indicates an experiment with a stable closed loop and a moving load. Furthermore, the theoretical boundaries for the stability of the TDS according to Section 2.4.2 are indicated. The pink line represents the considerations based on the ultra-local model (2.41), showing a rather conservative indication. The theoretical stability boundaries of the controlled system obtained by the model of the DC motor (2.31) are marked by the red lines, whereas the dashed line indicates the minimum values of k_p and the solid line its maximum values. Additionally, the white vertical line marks the identified input gain

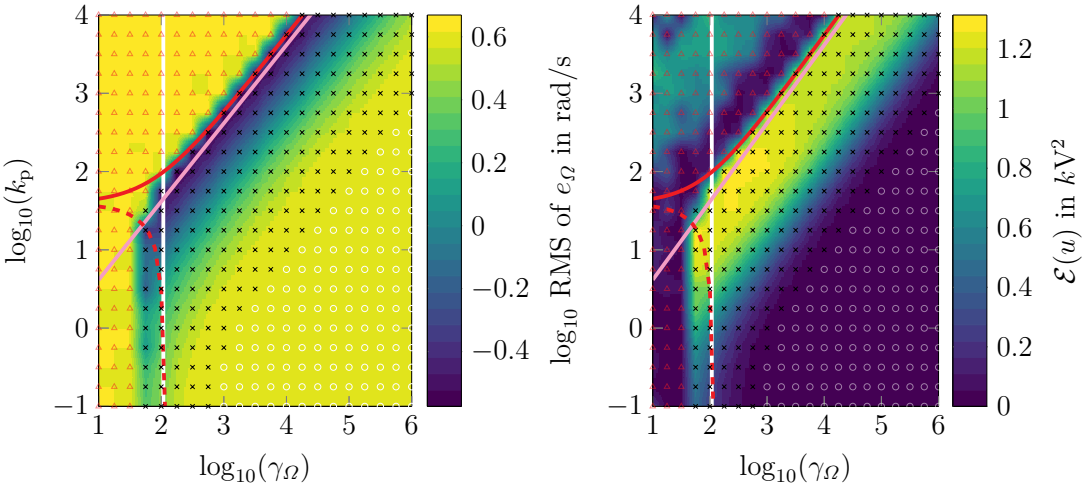

Fig. 3.10: Experimental results of the parameter sweep of the MFC law (2.35) for the DC motor using the parametrisation of the algebraic differentiators $N = 0$, $\omega_\mathrm{c} = 200\,\mathrm{rad/s}$, and $\alpha = \beta = 9$, discretised with the mid-point rule, to validate the theoretical findings from Section 2.4. The white line represents the identified input gain b, the pink line the conservative result from (2.41), and the red lines depict the results from (2.46), whereas the dashed line indicates the minimum values of k_p and the solid line its maximum values. Each marker represents an individual experiment: A red triangle marks an experiment that is aborted by the safety routine, a white circle marks an experiment with an input voltage too low to even move the load and a black cross marks a regular experiment.

b. Using the model information from (2.31), a prediction that is much more precise is obtainable and the latter shows that the approximation of the error dynamics by the TDS (2.40) is a valid explanation for this specific depiction of the parameter set. Nevertheless, the real experiments differ from the theoretical results especially for $(\gamma_\Omega, k_\mathrm{p}) \in [10\,\mathrm{rad/(Vs^2)}, 100\,\mathrm{rad/(Vs^2)}] \times [0.1\,\mathrm{s^{-1}}, 100\,\mathrm{s^{-1}}]$. On one hand, the boundary for the minimal k_p is rather conservative and on the other hand, the region between the solid and the dashed red line should be stable, but the experiments show the opposite. The reason for this difference between theory and experiment needs further investigations. Furthermore, some parameter combinations result in a stable closed loop even if they are either at or slightly above the solid red line which indicates the theoretical upper bound of k_p. Possible reasons for this observation are the influence of unmodelled effects such as friction and the backlash of the gearbox as well as parameter uncertainties of the identified values for a and b.

Remark 3.3 *The results depicted in Fig. 3.10 can be compared to Fig. 5 in Scherer et al. (2023) for the MFC of a proportional valve. In both cases, the proposed algorithm shows similar experimental results for the sampling of the corresponding parameter set. This evidence demonstrates that the observed behaviour of the valve is not specific to the test bed in question.*

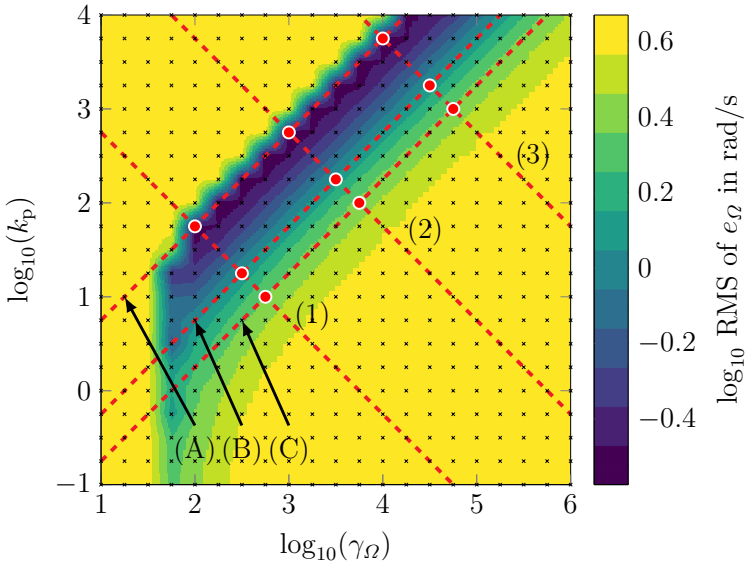

Fig. 3.11: Marked parameter combinations on the lines lines (A) to (C) and (1) to (3), to show the similar closed-loop behaviour in Fig. 3.12.

Taking a closer look at the individual experiments reveals another similarity to the results obtained in Scherer et al. (2023). Therefore, the experimental results over time for the parameter combinations marked with red dots in Fig. 3.11 are compared in Fig. 3.12. The experiments are grouped according to their location on each dashed red line (A) to (C), whereas A1 marks the crossing of lines (A) and (1) as presented in Fig. 3.11. All experiments on the lines (A) to (C) share the same ratio $\gamma_\Omega/k_\mathrm{p}$ between input and proportional gain. The individual value of each parameter does not impact the closed-loop behaviour. Fig. 3.11 shows that the best results are obtained at the edge of the stability boundary, and increasing the ratio $\gamma_\Omega/k_\mathrm{p}$ leads to a degradation of the tracking behaviour of the controlled system, ultimately leading to a voltage that is too low to overcome friction and move the load. Furthermore, the effects of friction can be observed in Fig. 3.12, which depicts the experiments on the lines (A) and (B). For times $t > 3.5\,\mathrm{s}$ the reference velocity $\Omega_\mathrm{r}(t)$ is zero but the applied voltages are not, which indicates that the algorithm (3.4) is capable of estimating friction.

Remark 3.4 *Assuming the input gain b of the system is unknown and γ_Ω has to be chosen without additional model information, Fig. 3.11 reveals that an overestimation, of the input gain is not as crucial as its underestimation since the value of b acts like a lower bound.*

In consideration of the results obtained in this section, the following guideline can be formulated.

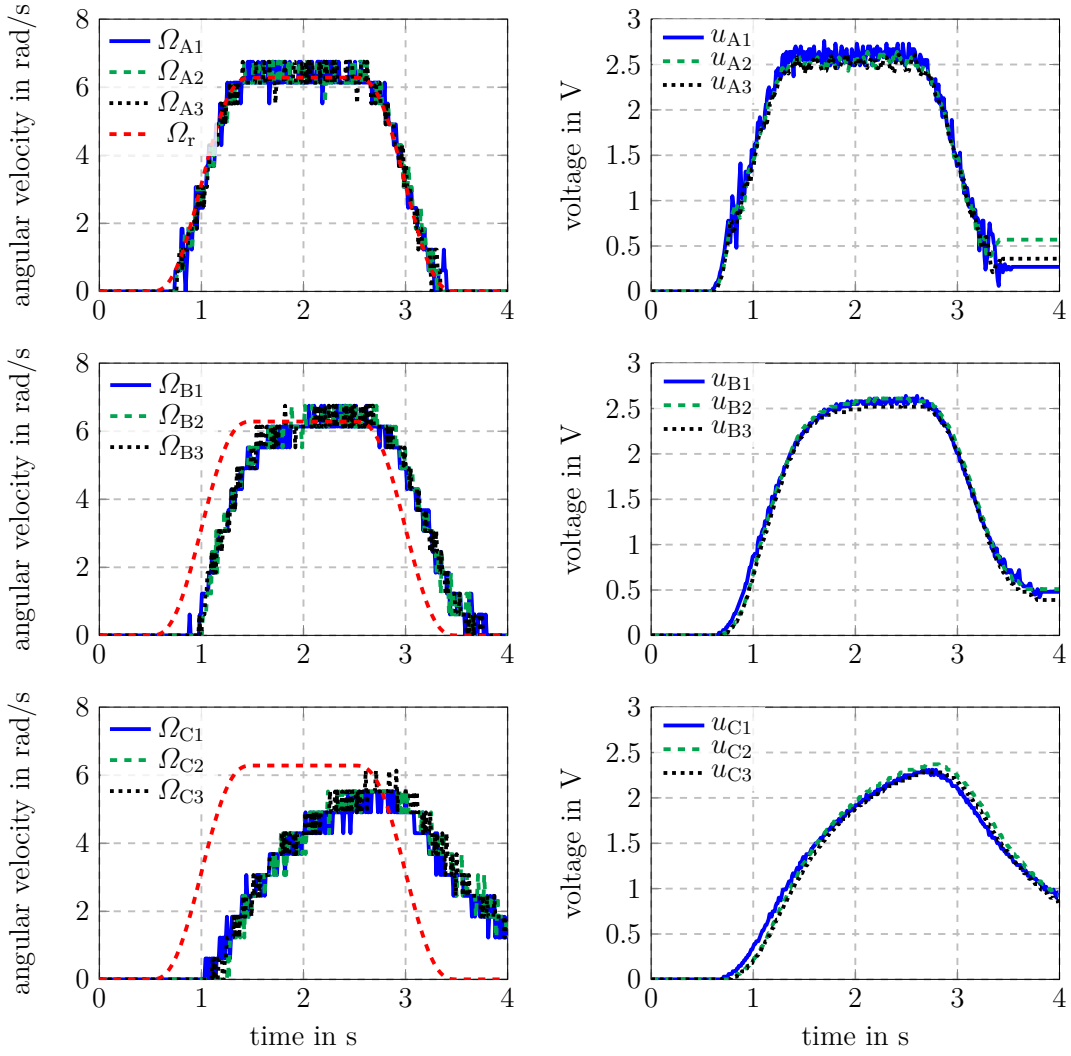

Fig. 3.12: Controlled angular velocity and corresponding voltage for parameter combinations with the same ratio of γ_Ω and k_p, marked in Fig. 3.11 with lines (A) to (C) and (1) to (3). Parameter combinations on the same line show similar closed-loop behaviour.

Guideline 2: Parametrisation of a MFC law based on a first-order ultra-local model

Consider a stable system that can be approximated by a first-order ultra-local model

$$\dot{y}(t) = f(t) + \rho u(t), \tag{3.5}$$

with the output $y(t)$, the unknown part $f(t)$, the input $u(t)$ and its constant gain $\rho > 0$. The MFC law

$$u(t) = \frac{1}{\gamma}\left(\dot{y}_\mathrm{r}(t) - k_\mathrm{p}\hat{e}(t) - \hat{f}(t)\right), \quad e(t) = y(t) - y_\mathrm{r}(t) \tag{3.6}$$

can be applied for the control of the ultra-local model (3.5). Two cases have to be considered (see also Fig. 3.13 for a visualisation of the guideline):

Case 1: A value for the input gain ρ of the ultra-local model is not available.

Step 1: Choose a large enough value $\tilde{\gamma}$ for the input gain as well as a small value for the proportional gain, e.g. $\tilde{k}_\mathrm{p} = 1\,\mathrm{s}^{-1}$, as a starting point.

Step 2: Choose the proportional gain k_p in (3.6) as

$$k_\mathrm{p}(\gamma) = \frac{\tilde{k}_\mathrm{p}\tilde{\gamma}}{\gamma}, \tag{3.7}$$

with $\gamma \in (0, \tilde{\gamma}]$.

Step 3: Decrease $\gamma \in (0, \tilde{\gamma}]$ in (3.6) until either the controlled system starts oscillating or the tracking error is appropriately small.

Case 2: A value for the input gain ρ of the ultra-local model is available, e.g. by the method proposed in Polack et al. (2019) for the feed-forward tuning.

Step 1: Choose a value for $\tilde{\gamma} = \kappa\rho$ with $\kappa > 1$, resulting in a proportional gain

$$\tilde{k}_\mathrm{p} = \frac{\pi}{2\delta_t}\kappa,$$

using the conservative bound derived in Appendix A.1.

Step 2: Choose the proportional gain k_p in (3.6) as

$$k_\mathrm{p}(\gamma) = \frac{\pi\kappa^2\rho}{2\delta_t\gamma},$$

with $\gamma \in [\rho, \kappa\rho]$.

Step 3: Decrease $\gamma \in [\rho, \kappa\rho]$ in (3.6) until either the controlled system starts oscillating or the tracking error is appropriately small.

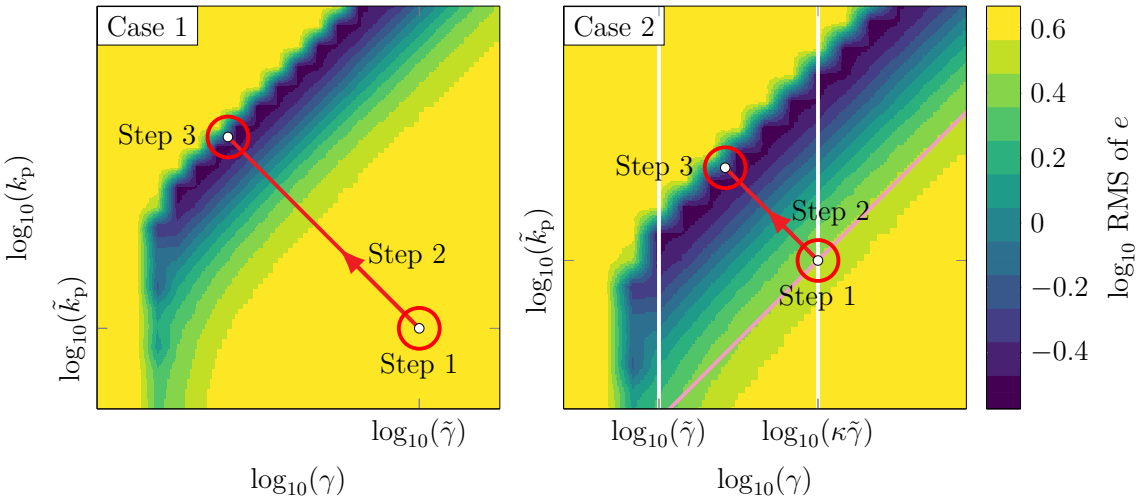

Fig. 3.13: Visual interpretation of the Guideline 2. Even though the results from the DC motor experiments are used, this visualisation is only intended to convey the idea of the guideline. Especially for Case 2 the pink line which is marking the considerations based on the ultra-local model does not correspond to the parameters of the system.

Remark 3.5 *According to the considerations based on the ultra-local model in Section 2.4.2, the maximum proportional gain is calculated using* (2.41)*, i.e.*

$$k_{\mathrm{p,max}} = \frac{\pi}{2}\frac{\gamma}{\rho\delta_t}.$$

In logarithmic coordinates the expression (2.41) *reads*

$$\log_{10}(k_{\mathrm{p,max}}) = \log_{10}(\pi) + \log_{10}(\gamma) - \log_{10}(2) - \log_{10}(\rho) - \log_{10}(\delta_t) \tag{3.8}$$

A line perpendicular to (3.8)*, i.e. the red line in Fig. 3.13 for Case 1, Step 2 of Guideline 2, can be calculated in the logarithmic coordinates as*

$$h(\gamma) = \log_{10}(\tilde{k}_\mathrm{p}) + \log_{10}(\tilde{\gamma}) - \log_{10}(\gamma),$$

which is equivalent to

$$k_\mathrm{p}(\gamma) = 10^{h(\gamma)} = \frac{\tilde{k}_\mathrm{p}\tilde{\gamma}}{\gamma}.$$

3.5.2 Control of the angle

In this section the control of the angle $\theta(t)$ using the MFC law (2.49) is considered. Numerous experiments are conducted on the test bed to investigate the influence of the parameters k_p, k_d, and γ_θ on the stability of the closed loop. The goal of these

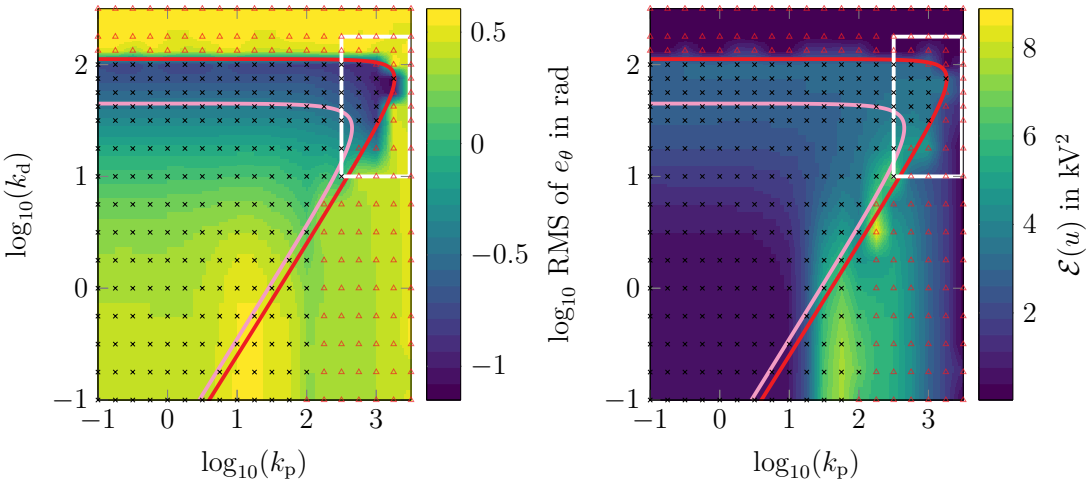

Fig. 3.14: Experimental results of the parameter sweep for the control of the angle with the MFC law (2.49). The sampling frequency is chosen to be $f_\mathrm{s} = 200\,\mathrm{Hz}$ and the input gain is $\gamma_\theta = b$. The pink and the red lines are depicting the boundaries of the admissible values of k_p and k_d according to the considerations based on the ultra-local model by (2.53)–(2.54) and based on the model of the DC motor by (2.58)–(2.59), respectively. The red triangles mark an experiment that is aborted by the safety routine and the black crosses represent experiments in which no problems occurred.

experiments is to validate the theoretical findings of Chapter 2. To save time during the sampling of the parameter set, the same set point transition as in the Section 3.4.2 is used as the reference trajectory $t \mapsto \theta_\mathrm{r}(t)$, but the transition time as well as the holding time is reduced to 0.5 s. Furthermore, the energy of the input signal $t \mapsto u(t)$ as well as the RMS values of e_θ are used as an indicator for the quality of the resulting tracking performance.

In a first step, the input gain of the MFC law is chosen as $\gamma_\theta = b$ and the parameters k_p and k_d are varied. The results on the sampled parameter set are shown in Fig. 3.14, whereas each marker represents an individual experiment made. Once more, the red triangle marks a parameter combination that leads to the activation of the safety routine and is thus aborted. Moreover, the black cross resembles an experiment that is completed without any problem. The pink and the red lines depict the boundaries of the admissible values of k_p and k_d according to the considerations based on the ultra-local model by (2.53)–(2.54) and based on the model of the DC motor by (2.58)–(2.59), respectively. Again, using only the information of the ultra-local model leads to a very conservative result. Nevertheless, this simplification can be used to design a stable closed loop since the set predicted by (2.53)–(2.54) is included within the set predicted by (2.58)–(2.59). The influence of the parameter a pushes the boundary of the admissible k_d further than predicted by (2.53)–(2.54). Furthermore, the parameter k_d has a dominant impact on the tracking performance. The smallest RMS values of the error e_θ are obtained for parameter combinations in the interval $k_\mathrm{d} \in [49.3\,\mathrm{s}^{-1}, 119.5\,\mathrm{s}^{-1}]$, which marks the region between the red and the pink line in Fig. 3.14. If both parameters

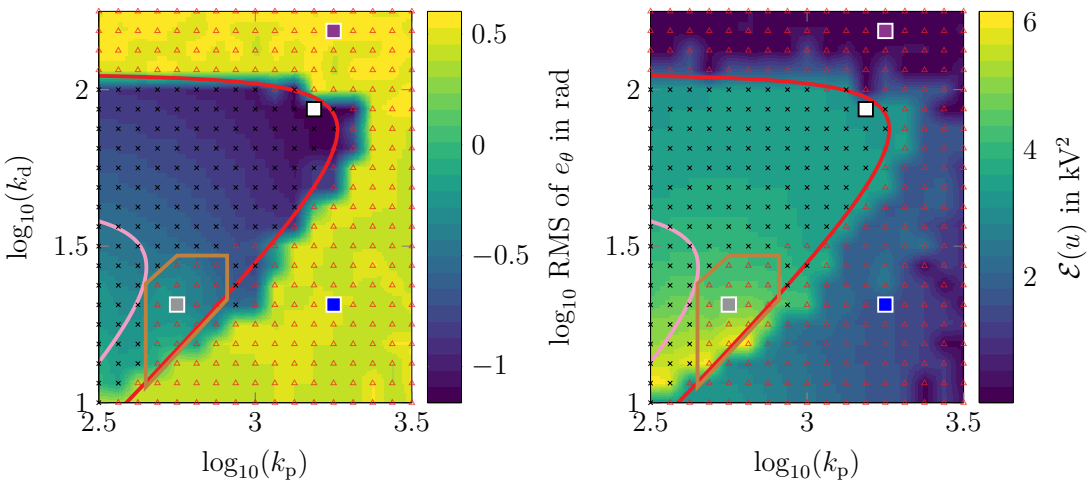

Fig. 3.15: Experimental results for the parameter combinations within the white rectangle in Fig. 3.14. The area surrounded by the brown line marks experiments which are aborted by the safety routine even though they are leading to a stable closed loop.

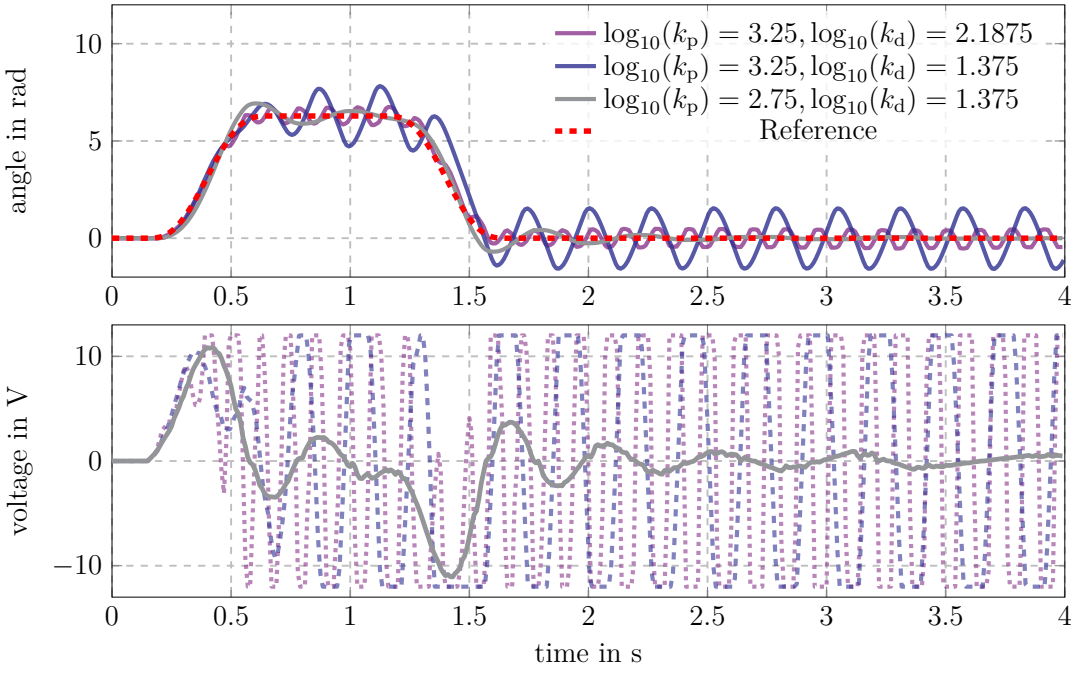

Fig. 3.16: Comparison of different experiments marked with rectangles in Fig. 3.15 with a deactivated safety routine. The results show, that the experiments surrounded by the brown line are falsely aborted, whereas the experiments beyond the red line, which marks the bound for a stable closed loop, are not asymptotically stable.

k_p and k_d are below the value of $10\,\mathrm{s}^{-2}$ and $10\,\mathrm{s}^{-1}$, respectively, the resulting tracking performance is bad because the RMS values of the error e_θ are high and the energy of the input signal is low.

A more detailed sampling of the area marked with the white rectangle in Fig. 3.14 is provided in Fig. 3.15. Within this figure, it can be observed that the theoretical findings of Chapter 2 for the boundaries resulting from (2.58)–(2.59) are quite accurate. Nevertheless, the region surrounded by the brown line shows several experiments that are aborted by the safety routine even though they are within the stability set. This behaviour raises the question if the safety routine distorts the results obtained. To further investigate this phenomenon, three experiments with the parameter combination marked by the gray, blue and purple squares in Fig. 3.15 are made without the safety routine, the results of which can be observed in Fig. 3.16. The gray graph obtained with the parameter combination $\log_{10}(k_\mathrm{p}) = 2.75$ and $\log_{10}(k_\mathrm{d}) = 1.375$, which lies within the region surrounded by the brown line, clearly shows a stable closed-loop behaviour in opposition to the remaining experiments in the latter figure. For the blue and purple graphs, a fast switching for the input voltage $u(t)$ between its maximum and minimum values of $\pm 12\,\mathrm{V}$ is observed. Consequently, the angle $\theta(t)$ oscillates around its reference value. These experiments show that the safety routine is conservative but has no negative effect on the obversions made to validate the parameter boundaries which results from (2.58)–(2.59). Nonetheless, the latter results show that further analysis considering the input saturation is needed in future work.

Fig. 3.17 shows a sampling of the parameter set with an input gain of $\gamma_\theta = 1.1b$. With an increase of the latter parameter, the red line, which marks the boundary of the stable set, is changing because the minimal value of $k_{\mathrm{d,min}} = -3.54\,\mathrm{s}^{-1}$ is allowed to be negative. This change leads to a new evaluation of the quality of the theoretical results from (2.58)–(2.59), especially for parameter combinations below $k_\mathrm{d} = 10\,\mathrm{s}^{-1}$. Therefore, two experiments with parameters marked in Fig. 3.17 with a green and brown square are presented in Fig. 3.18. Once more, these experiments are made without the safety routine. Both graphs show an oscillation around the reference but the brown graph, the parameter combination of which is considered to be leading to an unstable closed loop, is reaching $\pm 12\,\mathrm{V}$. Nevertheless, the parameter combination which leads to the green graph does not show a stable closed-loop behaviour because of insufficient damping induced by the algorithm. Regardless of that, the stability for parameter combinations with $k_\mathrm{d} > 10\,\mathrm{s}^{-1}$ is correctly predicted.

To obtain the results depicted in Fig. 3.19, the input gain is chosen to be $\gamma_\theta = 0.9b$. As a consequence of this, the theoretical boundary for k_p and k_d calculated by (2.58)–(2.59) results in a minimum value of $k_{\mathrm{d,min}} = 4.33\,\mathrm{s}^{-1}$. Parameter combinations below this value are now classified to be unstable even if they do not lead to an unstable closed loop. A similar effect can be observed for the MFC law based on a first-order ultra-local model as presented in Section 3.5.1 for parameter combinations with $\gamma_\theta < b$. Nevertheless, the reasons for this behaviour needs further investigation.

The experimental results presented in this section show that the theoretical findings from Chapter 2 are valid if the model of the DC motor is considered. They also explain the experimental results for the sampling of the parameter set observed in Scherer et al. (2024, Fig. 7). The variation of the input gain γ_θ in Fig. 3.17 and Fig. 3.19 shows

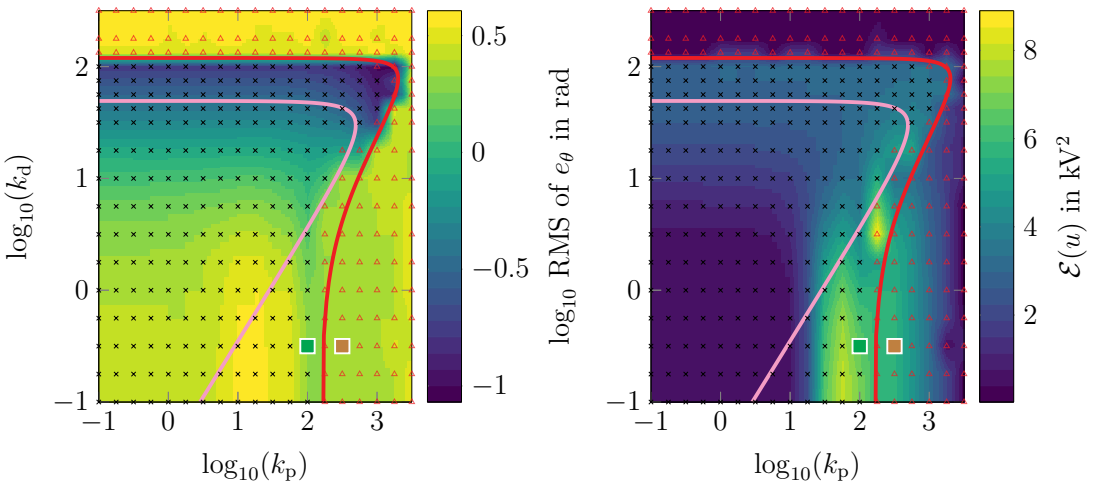

Fig. 3.17: Experimental results of the k_p-k_d parameter sweep for the control of the angle with the MFC law (2.49). The sampling frequency is chosen to be $f_\mathrm{s} = 200\,\mathrm{Hz}$ and the input gain is $\gamma_\theta = 1.1b$.

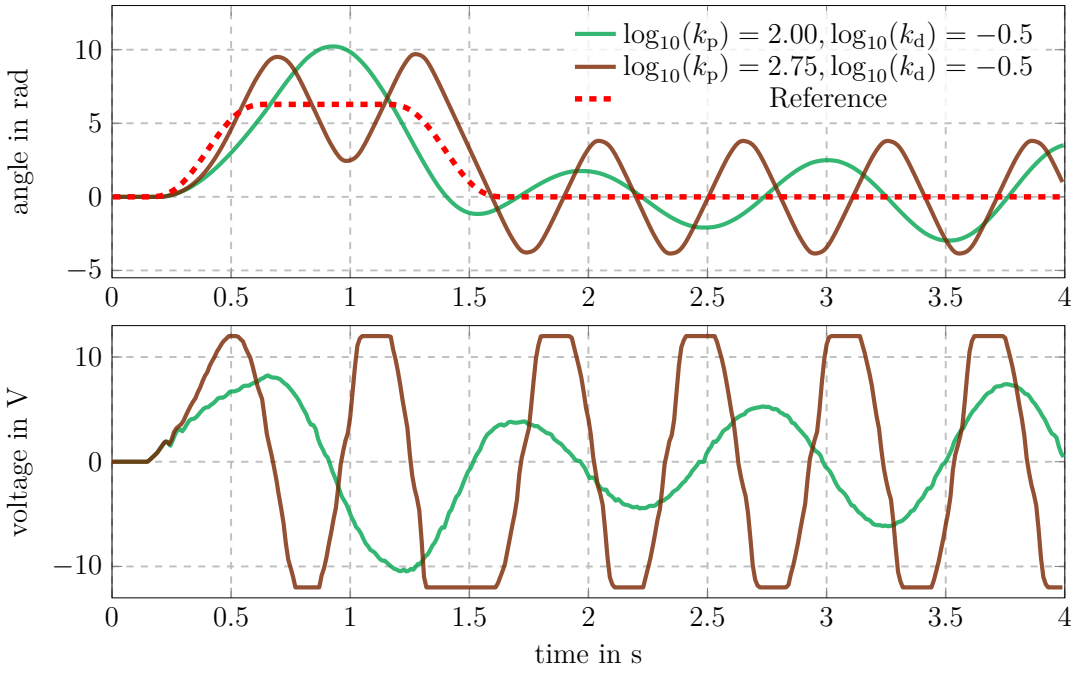

Fig. 3.18: Angle and voltage over time for the parameter combinations marked in Fig. 3.17.

that the experimental results differ in some regions of the parameter set and that these effects need further investigation. However, all figures of the parameter set have in common that there is an optimum for the RMS values of the error e_θ for high values of both k_p and k_d. This can be seen for example in Fig. 3.20, the parameter combination of which is also marked with a white square in Fig. 3.16. The compensation of the

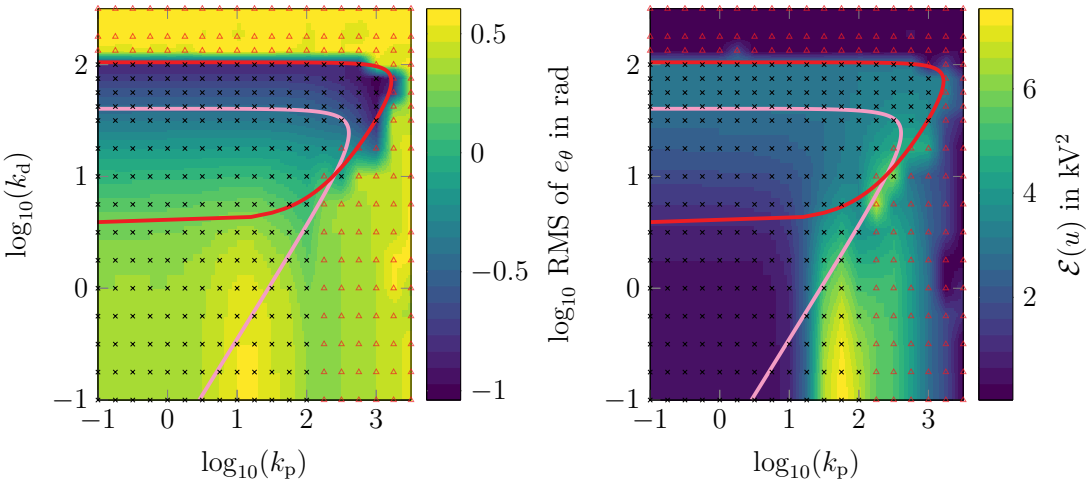

Fig. 3.19: Experimental results of the k_p-k_d parameter sweep for the control of the angle with the MFC law (2.49). The sampling frequency is chosen to be $f_\mathrm{s} = 200\,\mathrm{Hz}$ and the input gain is $\gamma_\theta = 0.9b$.

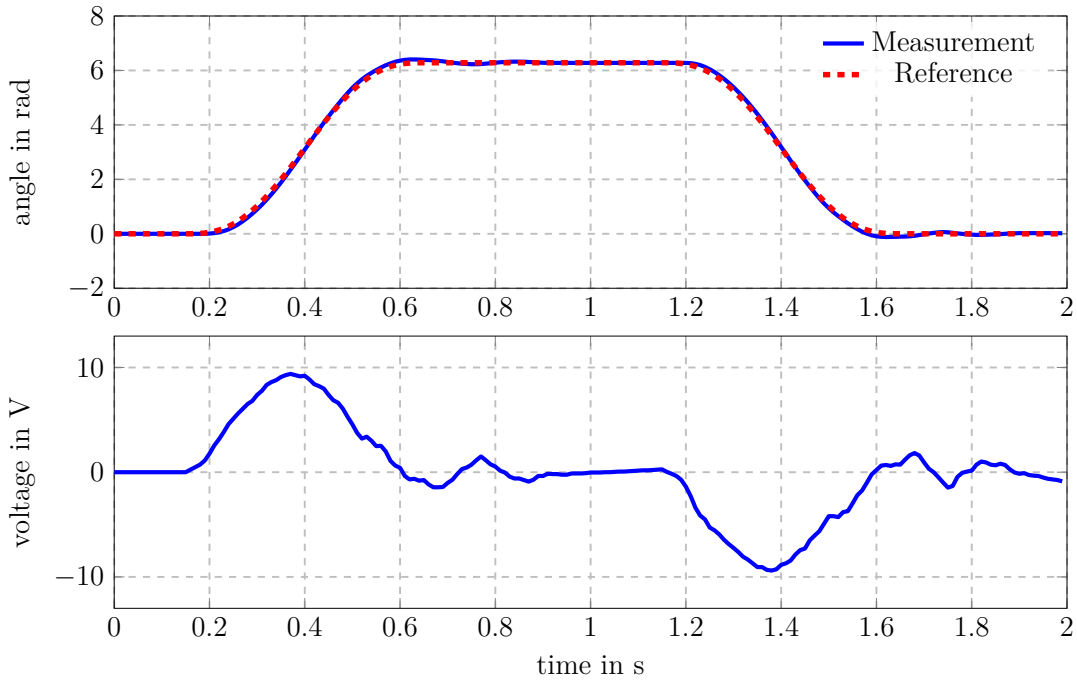

Fig. 3.20: Angle and voltage over time for the parameter combination $\gamma_\theta = b$, $\log_{10}(k_\mathrm{p}) = 3.1875$, and $\log_{10}(k_\mathrm{d}) = 1.9375$, marked with the white rectangle in Fig. 3.15, which leads to the lowest RMS values of the error e_θ.

unknown part $f_\theta(t)$ is capable of leading to steady state accuracy even without the explicit consideration of an integral part within the MFC law (2.49).

In consideration of the results obtained in this section, Guideline 3 can be formulated.

However, in opposition to Guideline 2, only the case of a known input gain ρ of the ultra-local model is considered because the investigated parameter range of the input gain γ_θ is insufficient.

Guideline 3: Parametrisation of a MFC law based on a second-order ultra-local model

Consider a stable system that can be approximated by a second-order ultra-local model

$$\ddot{y}(t) = f(t) + \rho u(t), \tag{3.9}$$

with the output $y(t)$, the unknown part $f(t)$, the input $u(t)$ and its constant gain $\rho > 0$. The MFC law

$$u(t) = \frac{1}{\gamma}\left(\dot{y}_\mathrm{r}(t) - k_\mathrm{p}\hat{e}(t) - k_\mathrm{d}\dot{\hat{e}}(t) - \hat{f}(t)\right), \quad e(t) = y(t) - y_\mathrm{r}(t) \tag{3.10}$$

can be applied for the control of the ultra-local model (3.9). It is assumed that a value for the input gain ρ of the ultra-local model is available.

Step 1: Choose $\gamma = \rho$.

Step 2: Calculate $\tilde{k}_\mathrm{p}$ as the highest values of the proportional gain and $\tilde{k}_\mathrm{d}$ as its corresponding value for the differential gain using the results from Appendix A.4 and use them as a staring point in (3.10).

Step 3: Increase k_d in (3.10) until the boundary of the stability set is reached and reduce it such that no oscillations occur in the resulting tracking behaviour.

Step 4: Increase k_p in (3.10) until either the controlled system starts oscillating or the tracking error is appropriately small.

3.5.3 Comparison to the results of Polack et al. (2019)

As stated in Chapter 1, Polack et al. (2019) introduced a systematic tuning approach for a stable system using a MFC law based on a first-order ultra-local model. In this section, the findings of Polack et al. (2019) are repeated and applied to the DC motor as well as compared to Case 1 of Guideline 2, i.e. the tuning of the MFC law under the assumption that no a priori knowledge about the input gain γ_Ω is available. The guidelines introduced by Polack et al. (2019) are not explicitly considering the delay δ_t introduced by the algebraic differentiators.

In a first step, the tuning guideline proposed by Polack et al. (2019) suggests to identify

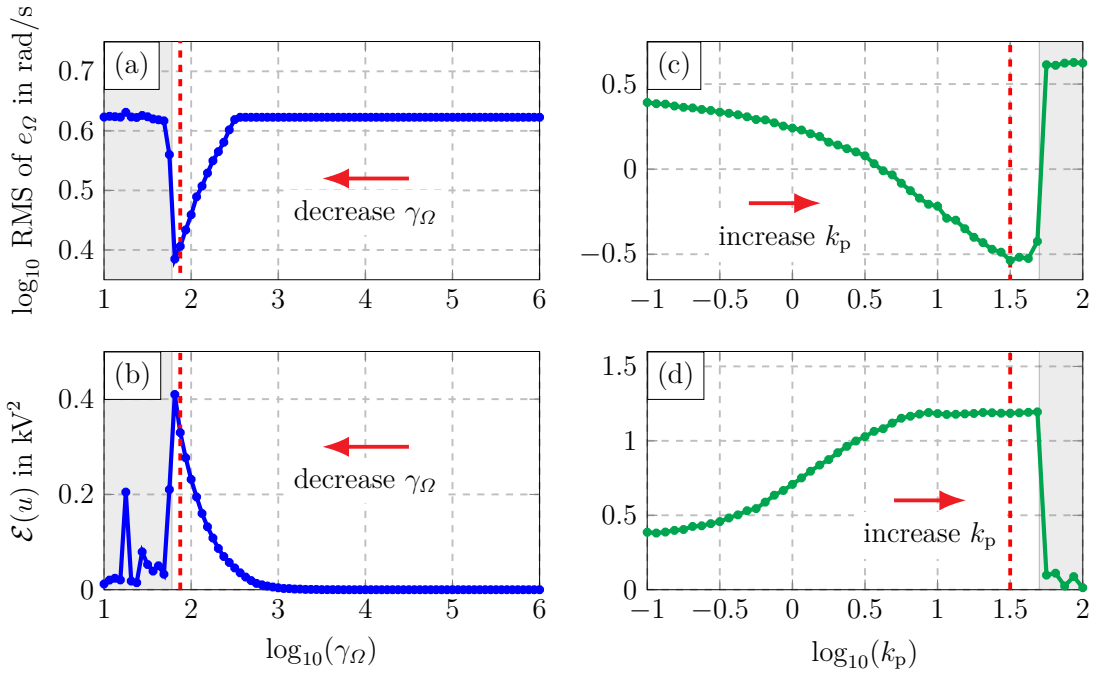

Fig. 3.21: Results of the feed-forward ((a) and (b)) and feedback tuning ((c) and (d)) of the guideline proposed in Polack et al. (2019). The red dashed lines indicate the chosen values for $\gamma_\Omega = 74.98\,\mathrm{rad/(Vs^2)}$ and $k_\mathrm{p} = 31.62\,\mathrm{s^{-1}}$, and the gray background marks the experiments which are aborted by the safety routine.

the input gain γ_Ω. For that, a so-called feed-forward tuning is proposed by setting the proportional gain of the MFC law (2.35) to zero, which yields

$$u(t) = \frac{1}{\gamma_\Omega}\left(\dot{\Omega}_\mathrm{r}(t) - \hat{f}_\Omega(t)\right). \tag{3.11}$$

In a next step, the parameter γ_Ω is chosen large enough and experiments on the test bed are conducted. For large values of γ_Ω the resulting voltages $u(t)$ from (3.11) are small. Therefore, γ_Ω is decreased until the closed loop oscillates or gets unstable. The value of γ_Ω that results in the smallest error is chosen for the so-called feedback tuning, i.e. increasing k_p in (2.35) until the tracking error is sufficiently small.

For the following experiments, the parametrisation of the algebraic differentiators presented in Section 3.4 is used with a sampling frequency of $f_\mathrm{s} = 200\,\mathrm{Hz}$. To get comparable results to the experiments from Section 3.5.1, the reference trajectory $t \mapsto \Omega_\mathrm{r}(t)$ depicted in Fig. 3.12 is chosen. The RMS values of the error e_Ω as well as the energy of the input signal $t \mapsto u(t)$ are used once again as a quality gauge of the parametrisations.

The results of the feed-forward tuning are depicted in Fig. 3.21 (a) and (b), starting with $\gamma_\Omega = 10^6\,\mathrm{rad/(Vs^2)}$. It can be observed that the safety routine aborts the experiment if $\gamma_\Omega < 64.93\,\mathrm{rad/(Vs^2)}$, indicating a lower bound for the stability. This is in line with the observed effects from Fig. 3.10 for $k_\mathrm{p} = 0.1\,\mathrm{s^{-1}}$. In Fig. 3.21, the aborted

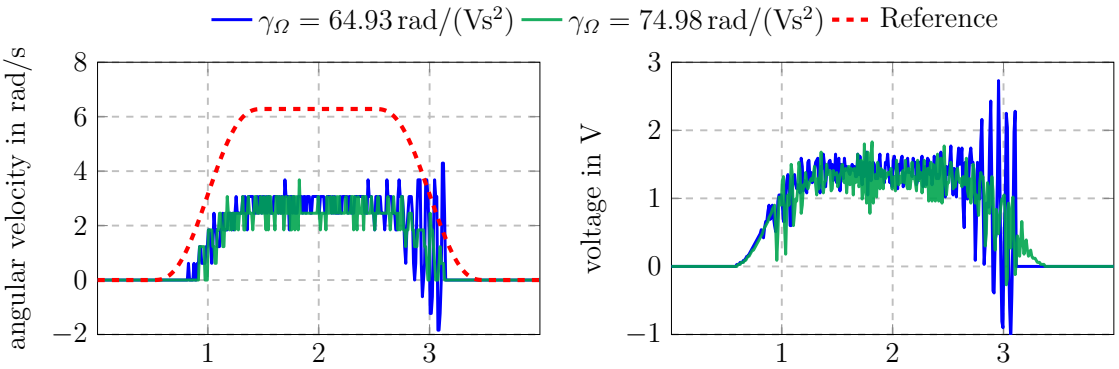

Fig. 3.22: Comparison of the experimental results for two parametrisations of the feed-forward tuning proposed by Polack et al. (2019). The value of $\gamma_\Omega = 64.93\,\mathrm{rad/(Vs^2)}$ results in a smaller RMS value of the error e_Ω but for further experiments, the value $\gamma_\Omega = 74.98\,\mathrm{rad/(Vs^2)}$ is chosen because of the oscillations of the blue graph.

experiments are marked with a gray background. Fig. 3.22 depicts the voltage $u(t)$ and the angular velocity $\Omega(t)$ over time for two parametrisations of γ_Ω resulting in the lowest RMS values of the error e_Ω. The blue graph leads to a smaller RMS value compared to the green graph, however, this graph also shows oscillations when the reference velocity $t \mapsto \Omega_\mathrm{r}(t)$ transitions to zero. Therefore, the parametrisation leading to the green graph, i.e. $\gamma_\Omega = 74.98\,\mathrm{rad/(Vs^2)}$, is chosen for the feedback tuning since no oscillation occurs. The latter value is marked in Fig. 3.21 (a) and (b) with a red dashed line. With regard to Remark 3.4, it should be noted that the proposed feed-forward tuning leads to an input gain of $\gamma_\Omega = 74.98\,\mathrm{rad/(Vs^2)}$ which is smaller in comparison to the value of $b = 108.55\,\mathrm{rad/(Vs^2)}$, identified in Section 3.2.

The results of the feedback tuning, starting with $k_\mathrm{p} = 0.1\,\mathrm{s^{-1}}$, are depicted in Fig. 3.21 (c) and (d). According to the latter figure, increasing the proportional gain leads to a reduction of the RMS values of the error e_Ω until a minimum is reached. A further increase of k_p leads to a rise of the RMS values until the safety routine aborts the experiments. The proportional gain leading to the smallest tracking errors, i.e. $k_\mathrm{p} = 31.62\,\mathrm{s^{-1}}$, is chosen as the resulting parametrisation of the control law. The latter value is again indicated with a red dashed line in Fig. 3.21 (c) and (d).

The results of Guideline 2 can be observed in Fig. 3.23. To get a fair comparison of both approaches, the values of $\tilde{\gamma}_\Omega = 10^6\,\mathrm{rad/(Vs^2)}$ and $\tilde{k}_\mathrm{p} = 0.1\,\mathrm{s^{-1}}$ are chosen equal to the application of the guideline suggested by Polack et al. (2019). The parametrisation $\gamma_\Omega = 421.69\,\mathrm{rad/(Vs^2)}$ and $k_\mathrm{p} = 237.13\,\mathrm{s^{-1}}$ is chosen because the resulting RMS value of the error e_Ω is with $0.29\,\mathrm{rad/s}$ equivalent to the value obtained by the guideline proposed by Polack et al. (2019).

In Fig. 3.24 the results of both approaches can be compared. The latter figure shows that each tuning guideline can be used to achieve a comparable result. Nonetheless, the proposed Guideline 2 only needs 54 steps to reach a satisfactory result whereas

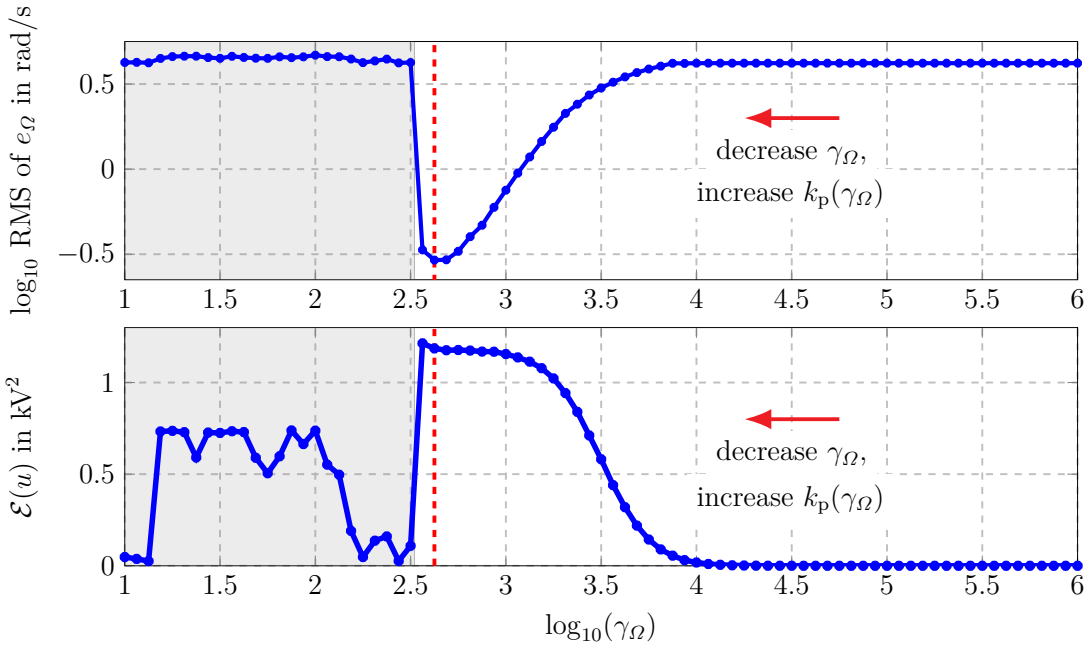

Fig. 3.23: Experimental results of the application of Guideline 2 on the DC motor. Instead of changing γ_Ω and k_p separately, this guideline makes use of the finding from Section 3.5.1 that only the ratio $\gamma_\Omega/k_\mathrm{p}$ has an influence on the stability of the closed loop. Thus the proportional gain k_p can be employed as a function of the input gain γ_Ω. The red dashed lines indicate the chosen value for $\gamma_\Omega = 421.69\,\mathrm{rad/(Vs^2)}$ and the gray background marks the experiments which are aborted by the safety routine.

the approach suggested by Polack et al. (2019) needs 107 steps in total, 66 to find the value of $\gamma_\Omega = 75\,\mathrm{rad/(Vs^2)}$ and additionally 41 to find $k_\mathrm{p} = 31.62\,\mathrm{s}^{-1}$. This is due to the findings from Section 3.5.1 that only the ratio $\gamma_\Omega/k_\mathrm{p}$ has an influence on the stability. Thus the proportional gain k_p can be employed, according to (3.7), as a function of the input gain γ_Ω. It should be remarked that the number of steps required to find a satisfactory parametrisation heavily depends on the sampling used as well as the starting values $\tilde{\gamma}$ and $\tilde{k}_\mathrm{p}$. A more sophisticated algorithm, e.g. the bisection method, can be used to speed up the sampling. By comparing the results in Fig. 3.24 it can be observed that the results obtained by Guideline 2 lead to a less noisy input trajectory $t \mapsto u(t)$ since the value of γ_Ω is higher in comparison to the value obtained by the feed-forward tuning. This behaviour can also be observed in Fig. 3.12 with the plots of line (A).

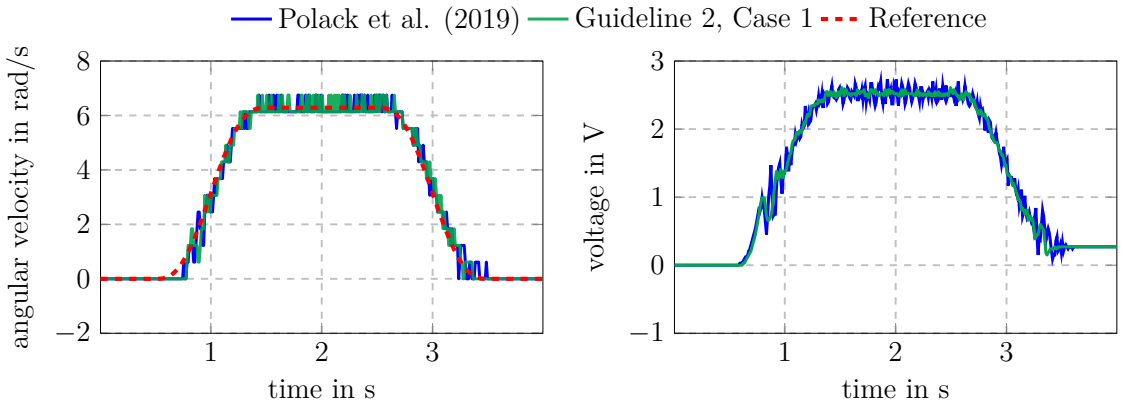

Fig. 3.24: Comparison of the best results obtained by the tuning guidelines proposed by Polack et al. (2019), which leads to $\gamma_\Omega = 74.98\,\mathrm{rad/(Vs^2)}$ and $k_\mathrm{p} = 31.62\,\mathrm{s^{-1}}$ as well as Guideline 2 which leads to $\gamma_\Omega = 421.69\,\mathrm{rad/(Vs^2)}$ and $k_\mathrm{p} = 237.13\,\mathrm{s^{-1}}$.

Chapter 4

Conclusion and future work

In this thesis, the MFC approach as introduced by Fliess and Join (2009, 2013) is considered in the light of new findings regarding the algebraic differentiators which leads to new insights into the stability analysis of the closed loop and the systematic parametrisation of the approach. The two peer-reviewed and published journal papers Scherer et al. (2023) and Scherer et al. (2024), attached in Chapter 5, lay the foundation for the systematic tuning. In the latter works, the sampling of the controller parameter set is introduced as a straightforward method to find parameter combinations which lead to a stable closed loop, revealing a special pattern in the parameter set. Additionally, the tuning of the algebraic differentiators is analysed and it is shown that not only a single parametrisation leads to a successful realisation of the control approach.

In order to gain a deeper understanding of the tuning process, the DC motor in Section 2.4.1 represents the basis of considerations. This system is considered because it is easy to understand and to model, used in many applications, and the results could be reproduced by other research groups as well without much effort. Depending on the chosen output quantity, the DC motor can be either considered as a first-order or second-order system. Consequently, the two common approximations using differential equations of first or second order with unknown parts, so-called ultra-local models, are applied to the DC motor. Using the ultra-local model, MFC laws are derived in Section 2.2 depending on the compensation of the unknown part, the estimation of which is done using algebraic differentiators in the sense of Mboup et al. (2007, 2009). It is shown in Section 2.3 that the estimation of the unknown part can be realised with a special parametrisation of the algebraic differentiators and can thus be generalised. Considering the delay of the estimators and the mathematical model of the DC motor, the stability of the closed loop is analysed using TDSs in Section 2.4. With the help of the generalised Hermite-Biehler theorem (see, e.g. Silva et al. (2005, Ch. 5)), bounds for the controller parameters, i.e. the proportional and derivative gain, can be derived depending on the delay of the estimators, the input gain of the controller and the model parameters. Additionally, an approximation that is only depending on the ultra-local model can be derived using the same method.

In Chapter 3, the theoretical findings of Chapter 2 are validated using a test bed. The hardware used is presented and the parameters of the mathematical model of the system are identified in the Sections 3.1 and 3.2, respectively. Additionally, details concerning the implementation of the control law, the input saturation as well as the implemented safety routine are shared in Section 3.3. In Section 3.4, the influence of the parametrisation and discretisation of the algebraic differentiators on the stability of the closed loop is investigated. Therefore, the associated cutoff frequency ω_c and the filter order $\mu = \min(\alpha, \beta) + 1$ as well as the sampling frequency f_s are varied. Interestingly, not all parameter combinations lead to a stable closed loop but in comparison to the results from Scherer et al. (2024), there are no distinct systematic effects to find. Nevertheless, neither the sampling frequency nor the discretisation has an influence on this behaviour. The findings of Section 3.4 lead to Guideline 1 on how to design the algebraic differentiators for their use in the MFC law based on first-order and second-order ultra-local models.

With the parameters of the motor model (2.31) identified in Section 3.2, the theoretical findings from Section 2.4 are experimentally validated in Section 3.5. At first, the parametrisation of the MFC law based on a first-order ultra-local model for the control of the angular velocity is investigated by sampling of the γ_Ω-k_p parameter set in Section 3.5.1. The results show that the parameter bounds which are only based on the ultra-local model are conservative in comparison to considerations based on the mathematical model of the DC motor. Nevertheless, the experimental results validate that the stability of a system controlled by a MFC law based on a first-order ultra-local model can be analysed with a TDS. Additionally, the results from Scherer et al. (2023), showing that the closed-loop behaviour is only affected by the ratio of the parameters γ_Ω and k_p, is confirmed. Interestingly, the observed pattern in the parameter set (see, e.g. Fig. 3.11) for the DC motor is similar to the pattern for the proportional valve (see, e.g. Fig. 5 in Scherer et al. (2023)) which can now be explained by the generalised Hermite-Biehler theorem. Finally, Guideline 2 for the systematic parametrisation of the MFC law based on a first-order ultra-local model is derived from the findings of Section 3.5.1. The same strategy for the validation of the theoretical results from Section 2.4 is applied for the control of the angle with a MFC law based on a second-order ultra-local model. For this purpose, the k_p-k_d parameter set is sampled with a constant input gain $\gamma_\theta = b$. Once more, the parameter bounds obtained by the considerations based only on the ultra-local are conservative whereas the results based on the mathematical model of the DC motor show a high accuracy, validating the theoretical findings. Additionally, experiments with an input gain of $\gamma_\theta = 1.1b$ and $\gamma_\theta = 0.9b$ are made, proving the results. In contrast to Guideline 2, Guideline 3 focuses on the control of a system with a MFC law based on a second-order ultra-local model and only the case of a known input gain is considered because the influence of this parameter is insufficiently investigated by experiments to give an adequate guideline.

In Section 3.5.3, Case 1 of Guideline 2, i.e. the parametrisation of the MFC law based on a first-order ultra-local model without a priori knowledge of the input gain, is compared to a systematic tuning approach presented in Polack et al. (2019). It is demonstrated

that both approaches lead to a stable closed loop. Nevertheless, the objective is reached with fewer steps by employing the strategy of adjusting the ratio of γ_Ω and k_p, as represented by the Guideline 2. This approach circumvents the necessity of modifying each individual parameter, thereby streamlining the tuning. It should be noted that Polack et al. (2019) does not explicitly consider the delay introduced by the algebraic differentiators in opposition to the guidelines presented in this thesis.

Even though guidelines for the parametrisation of the algebraic differentiators and the MFC laws based on first-order and second-order ultra-local models are given, there are still many open research problems in the field of MFC. Concerning the algebraic differentiators, the following questions arise:

- Why do a few parametrisations of the algebraic differentiators that result in a small delay δ_t lead to an unstable closed loop (see the combinations highlighted with yellow in, e.g. Fig. 3.3 or Fig. 3.9), although the theory presented in Chapter 2 predicts the opposite?
- What is the effect of increasing the order N of the truncated generalised Fourier expansion in (2.2)?
- Is it beneficial to vary α and β independently, even though this decreases the rejection of the additive measurement disturbance?
- Is a delay-free parametrisation beneficial, even though this decreases the estimation accuracy (see, e.g. Othmane et al. (2022, Sec. 4.2))?
- Is there a benefit of using other orthogonal polynomials such as Laguerre or the Hermite instead of the Jacobi polynomials for the realisation of the algebraic differentiators? This would affect the implementation as well as the step and impulse response of the corresponding filters (see, e.g. Othmane (2022b)).

The MFC approach, which relies on ultra-local models, also raises questions besides the parametrisation of the algebraic differentiators:

- Is it useful to chose a higher-order ultra-local model, e.g. a third-order model, as an approximation of the system?
- Is there a bound for the sampling time such that a system can be approximated with an ultra-local model as discussed in Tabuada et al. (2017) for the MFC approach therein?
- Are the guidelines presented in this thesis still valid for linear system of arbitrary order or nonlinear systems?
- How does an input saturation affect the closed-loop behaviour?

- How is the MFC method introduced by Fliess and Join (2009, 2013) related to active disturbance rejection control (see, e.g. Han (2009))?

The latter questions show that there is much work to do in the field of MFC based on ultra-local models to further improve this yet powerful approach.

Chapter 5

Scientific publications

The peer-reviewed and published journal papers

> Scherer, P. M., Othmane, A., and Rudolph, J. (2023). Combining model-based and model-free approaches for the control of an electro-hydraulic system. *Control Engineering Practice*, 133:105453.
> DOI: 10.1016/j.conengprac.2023.105453

and

> Scherer, P. M., Othmane, A., and Rudolph, J. (2024). Model-free control of a magnetically supported plate. *Control Engineering Practice*, 148:105950.
> DOI: 10.1016/j.conengprac.2024.105950

are attached below. For each paper, the following terminology suggested in Allen et al. (2019) is used to indicate the authors' contribution.

- **Conceptualization**
  Ideas; formulation of overarching research goals and aims
- **Methodology**
  Development or design of methodology; creation of models
- **Software**
  Programming, software development; designing computer programs; implementation of the computer code and supporting algorithms; testing of existing code components

- **Formal analysis**
  Application of statistical, mathematical, computational, or other formal techniques to analyze or synthesize study data
- **Investigation**
  Conducting a research and investigation process, specifically performing the experiments, or data/evidence collection
- **Data Curation**
  Management activities to annotate (produce metadata), scrub data and maintain research data (including software code, where it is necessary for interpreting the data itself) for initial use and later reuse
- **Writing – Original Draft**
  Preparation, creation and/or presentation of the published work, specifically writing the initial draft (including substantive translation)
- **Writing – Review & Editing**
  Preparation, creation and/or presentation of the published work by those from the original research group, specifically critical review, commentary or revision – including pre- or postpublication stages
- **Visualization**
  Preparation, creation and/or presentation of the published work, specifically visualization/ data presentation
- **Supervision**
  Oversight and leadership responsibility for the research activity planning and execution, including mentorship external to the core team
- **Funding acquisition**
  Acquisition of the financial support for the project leading to this publication

5.1 Combining model-based and model-free approaches for the control of an electro-hydraulic system

The contributions of each author are listed in what follows.

P.M. Scherer (55 %)
Methodology, Software, Investigation, Data Curation, Visualization, Writing – Original Draft, Writing – Review & Editing

A. Othmane (40 %)
Conceptualization, Methodology, Writing – Original Draft, Writing – Review & Editing

J. Rudolph (5 %)
Funding acquisition, Writing – Review & Editing

Control Engineering Practice 133 (2023) 105453

Contents lists available at ScienceDirect

Control Engineering Practice

journal homepage: www.elsevier.com/locate/conengprac

Combining model-based and model-free approaches for the control of an electro-hydraulic system

P.M. Scherer *, A. Othmane, J. Rudolph

Chair of Systems Theory and Control Engineering, Saarland University, Campus A5 1, Saarbrücken, 66123, Germany

ARTICLE INFO

Keywords:
Algebraic differentiators
Flatness
Nonlinear control
Model-free control
Hydraulics

ABSTRACT

Model-free control, as introduced by Fliess and Join, is a compelling feedback control method for complex systems that can only be modelled with considerable effort. However, systematic parametrisation techniques, the concrete implementation, and the analysis of the approaches deserve further investigations. The present paper serves to propose a systematic way to parameterise a model-free controller for a system approximated by a first-order differential equation with unknown parts. Furthermore, model-based and model-free approaches are combined to efficiently control a hydraulic piston (model-based) actuated by four pilot-operated proportional valves (model-free) as a practical example of a typical electro-hydraulic system. Only pressure measurements and the position signal of the piston are used. No measurement of hydraulic flows or spool positions are required. The effects of the different parameters of the model-free controller are investigated and the implementation is discussed in detail. Several experiments on a test bed are carried out, showing a high positioning accuracy for a wide range of piston velocities and a behaviour robust against leakages. An open-access toolbox is used for the design of advanced differentiators to estimate unmeasured quantities required in the controller. This contribution shows that with the right tools, it is possible to design an efficient model-free controller and benefit from its advantages.

1. Introduction

Model-free control (MFC) methods, i.e., approaches that do not rely on a physical model of a considered system, are omnipresent in the control literature. Their ability to handle systems, whose mathematical models can only be derived after a cumbersome analysis, or are too complex for efficient controller design, has attracted much attention. The wording *model-free* has been employed by numerous authors for various techniques ranging from algorithms based on neural networks to fuzzy systems and robust control approaches, see, e.g., the discussions in the Remarks 1 and 5 in Fliess and Join (2013).

Fliess and Join (2008, 2009, 2013), Fliess et al. (2011) have proposed a simple control technique that is called model-free control, too. It has been successfully applied in diverse fields ranging from electrical to biomedical systems, see, e.g., the recent experimental applications in Fliess and Join (2021), Guilloteau et al. (2022), Michel et al. (2022) and Pereira das Neves and Augusto Angélico (2021), and the extensive lists in Fliess and Join (2013) and Othmane et al. (2022). These works use the term model-free control in the sense that there is no need for any "good" or "global" physical modelling. In contrast, it is assumed that during a short period of time the system is well described by a differential equation of low order with a single excitation signal that needs to be estimated online. This model is then called an *ultra-local model*, see, for instance, in Remark 3 and the Appendix B from Fliess and Join (2013) for further details.

Despite the miscellaneous and very successful applications of the approach, tuning the involved parameters remains challenging and relies on sound knowledge of the system behaviour and design expertise. The work Fliess and Join (2013) and more recent ones (Fliess & Join, 2021; Guilloteau et al., 2022; Pereira das Neves & Augusto Angélico, 2021), for example, report that parameters need to be "selected by the practitioner", obtained by "trials and errors", and chosen "quite small". Despite the successful experimental results, applying the approach to new problems, reproducing known results, and expending the methods would be simplified by systematic design guidelines.

Tuning of the filters used for estimation of the unknown parts of the ultra-local model has been discussed in Othmane, Rudolph, and Mounier (2021) using the recently developed methods for a systematic design of algebraic differentiators, see, e.g., Kiltz (2017), Kiltz and Rudolph (2013) and Othmane et al. (2022). Tuning of the input gain parameter is investigated in Hegedüs et al. (2022) where also a design procedure based on an optimisation problem is proposed. Classical control theory tools are used in Li et al. (2022) to analyse the properties of MFC when applied to single-input single-output linear systems. The stability margin of the approach is investigated and it is proven that

* Corresponding author.
E-mail address: p.scherer@lsr.uni-saarland.de (P.M. Scherer).

https://doi.org/10.1016/j.conengprac.2023.105453
Received 1 December 2022; Received in revised form 24 January 2023; Accepted 28 January 2023
Available online 9 February 2023

MFC can achieve higher robustness than single-loop linear controllers. The current contribution aims to make design, implementation, and tuning of these powerful approaches more systematic.

Many industrial processing systems and mobile machines (e.g., brakes, road construction vehicles, machining tools) use electro-hydraulic components to achieve a high power density. Numerous of these systems use proportional valves. The latter are cheap, robust to fluid contamination, and easy to use. A spool attached to a solenoid controls the hydraulic flow by closing and opening different orifices. Deriving a mathematical model describing the relevant electrical, mechanical, and hydraulic dynamics is challenging and can yield complex nonlinear differential equations, see, e.g., Eryilmaz and Wilson (2006), Ferreira et al. (2002), Merritt (1967) and Steinboeck et al. (2013). This renders the design of controllers challenging. Moreover, large manufacturing tolerances may significantly deteriorate the performance of nonlinear controllers. Thus, developing simple but efficient MFC approaches is promising.

In the present work, the design of a model-free controller for pilot-operated proportional valves is investigated. This kind of valves consists of two stages, thus having a more complex design compared to traditional proportional valves. Therefore, a MFC approach is used for these valves. Implementation and parametrisation of the applied differentiators is simplified by the toolbox (Othmane, 2022). The developed algorithms are validated on a test bench. The effects of manufacturing tolerances are investigated by analysing the performance of the approach using different valves.

The approach is then combined with a model-based design for the efficient control of a double-acting hydraulic piston actuated by four of these valves using a cascade structure. Only the hydraulic pressure measurements and a position signal of the piston are required. In particular, no measurements of positions of spools of valves or hydraulic flows are required for the model-free valve controllers. The model-based controller exploits the flatness of the system, see, e.g., Fliess et al. (1995), Rothfuss et al. (1996) and Rudolph (2021) for detailed discussions on flatness. The approach developed yields an increase in the positioning accuracy for a wide operating range and is, compared to a model-based feed-forward control, more robust against leakages. Thus, a key contribution of this work is the inclusion of MFC approaches, useful for ultra-local models, within a model-based structure incorporating major system dynamics to profit from the advantages of both.

The present paper is organised as follows. In Section 2 background material on algebraic differentiators is provided because they are significant for the methods. Furthermore, notation used in the following and important aspects are recalled. The electro-hydraulic system is presented and modelling issues are discussed in Section 3. A tracking controller for the piston actuator and a model-free controller for the valves are proposed in Section 4. A nonlinear observer and estimation of flow rates are also considered. In Section 5, the implementation of the approaches and experimental results are discussed.

2. Background material on algebraic differentiators

In this section the fundamentals of algebraic differentiators, initially developed in Mboup et al. (2007), Mboup et al. (2009) and discussed e.g., in Kiltz (2017), Kiltz and Rudolph (2013), are briefly summarised. A survey summarising existing results, interpretations, relations to established methods, and discussing tuning guidelines and applications can be found in Othmane et al. (2022). The open-source toolbox (Othmane, 2022) can be used for the design and implementation of these differentiators. Within the suggested control structure, they are not only needed to calculate derivates of desired signals, they are also crucial for the implementation of the MFC algorithms. In fact, they are used to estimate the unknown signals in the ultra-local model. While the differentiators are designed and analysed in the continuous-time domain, the implementation of the algorithms has to be done in discrete time. Therefore, the discretisation has to preserve the properties of the filters.

2.1. Continuous-time formulation

Consider an arbitrary closed non-empty interval $\mathcal{I}_t = [t-T, t] \subset \mathbb{R}$ and a function $f : \mathcal{I}_t \to \mathbb{R}$. In the following, it is assumed that the square of f is Lebesgue integrable. The approximation of f and its derivatives up to a finite order $n \in \mathbb{N}$, denoted by $f^{(n)}$, will be considered.

The function f and its derivatives can be approximated using a generalised Fourier expansion, see, e.g., Szegö (1939), by mapping $\mathcal{I}_t$ to the interval $\mathcal{I}_P = [-1, 1]$. The latter corresponds to the orthogonality interval of Jacobi polynomials defined as

$$P_N^{(\alpha,\beta)}(\tau) = \sum_{k=0}^{N} c_k^{(\alpha,\beta)} (\tau-1)^k,\ c_k^{(\alpha,\beta)} = \frac{\Gamma(\alpha+N+1)\Gamma(\alpha+\beta+N+k+1)}{2^k N!\Gamma(\alpha+\beta+N+1)\Gamma(\alpha+k+1)},$$

for $\tau \in \mathcal{I}_P$, $N \in \mathbb{N}$, $\alpha, \beta > -1$ and Γ the Gamma function, see, e.g., Szegö (1939). Jacobi polynomials are orthogonal with respect to the weight function

$$w^{(\alpha,\beta)}(\tau) = \begin{cases} (1-\tau)^\alpha (1+\tau)^\beta, & \tau \in [-1,1], \\ 0, & \text{otherwise.} \end{cases}$$

By considering the N-th order truncated generalised Fourier expansion, the function f and all derivatives up to a finite order $n < \min\{\alpha, \beta\} + 1$ can be approximated by

$$\hat{f}^{(n)}(t) = \int_{t-T}^{t} g^{(n)}(t-\tau) f(\tau) \mathrm{d}\tau, \quad g(\tau) = g_{N,T,\vartheta}^{(\alpha,\beta)}(\tau), \tag{1}$$

where

$$g_{N,T,\vartheta}^{(\alpha,\beta)}(t) = \frac{2w^{(\alpha,\beta)}(\nu(t))}{T} \sum_{j=0}^{N} \frac{P_j^{(\alpha,\beta)}(\vartheta)}{\left\| P_j^{(\alpha,\beta)} \right\|^2} P_j^{(\alpha,\beta)}(\nu(t)), \tag{2}$$

with $\nu(t) = 1 - 2t/T$ and $\|x\| = \sqrt{\langle x, x \rangle}$ the norm induced by the inner product $\langle x, y \rangle = \int_{-1}^{1} w^{(\alpha,\beta)}(\tau) x(\tau) y(\tau) \mathrm{d}\tau$. Recall that this corresponds to a least squares approximation.

The estimate $\hat{f}$ corresponds to a delayed approximation of f at time t and the delay, denoted by δ_t, can be parameterised by ϑ. The reader is referred to Othmane et al. (2022) for a detailed discussion. Alternatively, a delay-free approximation can be achieved for $\vartheta = 1$. Assume that f is a $m+1$ times differentiable function. Then, the approximation satisfies

$$\left| f(t-\delta_t) - \hat{f}(t) \right| \leq \frac{M}{q!} \left(\frac{T}{2} \right)^{q+1} \sup_{\tau \in \mathcal{I}_t} \left| f^{(n+q+1)}(\tau) \right|, \tag{3}$$

with $M > 0$ depending on α, β, and N, $q = \min\{m, \zeta - n\}$,

$$\zeta = \begin{cases} \bar{N}+1, & N = 0 \vee \vartheta = p_k, \\ \bar{N}, & \text{otherwise,} \end{cases} \quad \delta_t = \begin{cases} \frac{\alpha+1}{\alpha+\beta+2} T, & N = 0, \\ \frac{1-\vartheta}{2} T, & N \neq 0, \end{cases}$$

$\bar{N} = n + N$, and p_k the k-th zero of $P_{N+1}^{(\alpha,\beta)}$. Thus, accepting a small but known delay δ_t increases the order of the approximation, as first pointed out in Mboup et al. (2009).

It follows from Eq. (1) that $\hat{f}^{(n)}$ is the output of a finite-impulse response (FIR) filter with window length T driven by f. The kernel $g_{N,T,\vartheta}^{(\alpha,\beta)}$ defined in Eq. (2) is called an algebraic differentiator.[1] The results in Kiltz (2017), Kiltz and Rudolph (2013) and Othmane et al. (2022) show that $g_{N,T,\vartheta}^{(\alpha,\beta)}$ can be interpreted as a low-pass filter and that its parameters can be computed from a desired cutoff frequency

[1] The reader is referred to Othmane et al. (2022) for the historical developments, see, e.g., Mboup et al. (2007), Mboup et al. (2009), of this numerical differentiation approach that led to the wording "algebraic differentiators".

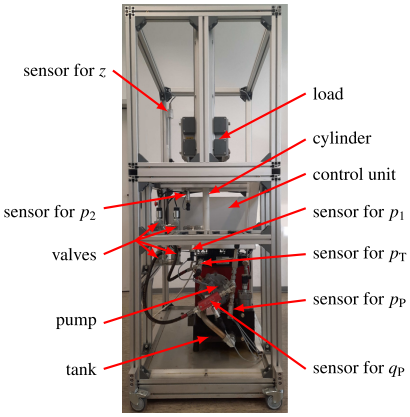

Fig. 1. Detailed photo of the considered test bed with all important system components marked.

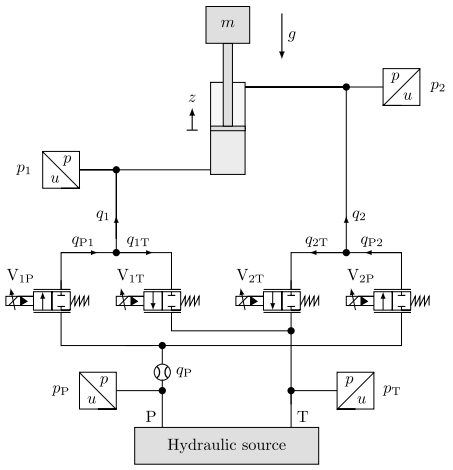

Fig. 2. Hydraulic circuit diagram of the system with four pilot-operated proportional valves, a double-acting hydraulic piston actuator, a flow rate sensor, four pressure sensors and a hydraulic source.

denoted by ω_c and a desired filter order. The filter window length T can then be computed.

2.2. Discrete-time formulation

In most applications, the function f is available at discrete sampling instants only. Thus, the convolution integral (1) must be approximated by an appropriate quadrature method. Discrete FIR filters are then recovered.

In the following, equidistant sampling with sampling period t_s is assumed and the window length of the differentiator is an integral multiple of t_s, i.e., $T = n_s t_s$. For the sake of brevity, the abbreviation $f_k = f(kt_s)$, $k \in \mathbb{N}$, for a sample of a function f at time kt_s is used. Then, a discrete-time approximation of (1) in the form

$$\hat{f}^{(n)}_{k+\theta} = \frac{1}{\Phi} \sum_{i=0}^{L-1} w_i f_{k-i}, \quad \Phi = \frac{t_s^n}{n!} \sum_{k=0}^{L-1} w_k (-k)^n,$$

can be achieved, where θ, L, and w_i depend on the numerical integration method used (Othmane, Mounier, & Rudolph, 2021, Sec. 4.3). For the mid-point rule $\theta = \frac{1}{2}$, $w_i = t_s g^{(n)}_{i+\theta}$, and $L = n_s$. The normalisation factor Φ ensures that the DC component of the sought derivative is preserved. To assess the error stemming from the discretisation and aliasing effects two indicators are introduced in Kiltz (2017) and Othmane et al. (2022). The reader is referred to these references for in-depth discussions. The open-source toolbox (Othmane, 2022) can be used for the discretisation of the differentiators and the assessment of discretisation effects.

3. Hydraulic system and problem statement

The system under consideration is depicted in Fig. 1. The main component is a double-acting hydraulic piston actuator. Four identical pilot-operated proportional valves control the hydraulic flows to the cylinder chambers. A sketch of the hydraulic circuit diagram can be found in Fig. 2. A motor pump unit and a pressure limiting valve, which are not considered in the mathematical model, serve as the hydraulic source. The position of the piston as well as the pressure of pump, tank, and each cylinder chamber are measured. A sensor measuring the pump flow rate is available for preliminary experimental investigations, as discussed in the results section.

3.1. Model of the double-acting hydraulic piston actuator

The modelling of the cylinder system starts with considering the dynamics of the pressures p_c, $c \in \{1,2\}$, in each chamber using the balance of mass under the assumption of a constant bulk modulus B:

$$\dot{p}_c = \frac{B}{V_c(z)} \left((-1)^c A_c \dot{z} + q_c - q_{c,l} \right). \tag{4a}$$

In (4a), z denotes the position of the piston with respect to the middle of the cylinder with length $2l$, q_c and $q_{c,l}$ are the flow rate into the chambers and a leakage, A_c is the effective cylinder surface, and $V_c(z) = V_0 - (-1)^c A_c (l - (-1)^c z)$ describes the volumes of the cambers with V_0 the volume of the supply pipe.

The mechanical subsystem can be modelled using the force balance on the cylinder rod given by

$$m\ddot{z} = A_1 p_1 - A_2 p_2 - k_v \dot{z} - mg - F_f, \tag{4b}$$

with m the mass of the load, k_v a viscous friction coefficient, g the gravitational acceleration, and F_f a friction force that, together with the leakage, can be seen as a time-varying parameter.

3.2. Differential flatness of the cylinder system

Differential flatness is a property of controlled dynamic systems and has shown to be very powerful for the control of nonlinear systems, see, e.g., Fliess et al. (1995), Rothfuss et al. (1996) and Rudolph (2021). The cylinder system (4) is differentially flat, with $y = (z, p_1 + p_2)$ as a flat output, which means the following:

(I) The pair y is differentially independent, i.e., its components are not restricted by any differential equation. As a consequence, reference trajectories may be chosen freely for these quantities.
(II) The remaining system variables p_c and q_c, $c \in \{1,2\}$, can be expressed as functions of y and its derivatives up to a finite order.

In order to verify property (II), introduce

$$p_\Sigma = p_1 + p_2. \tag{5}$$

Then, differentiating (4b) and (5) with respect to time and substituting into (4a), a relationship of the form

$$q_c = f_{q_c}\left(\dot{p}_\Sigma, z, \dot{z}, \ddot{z}, z^{(3)}\right) \tag{6}$$

can be obtained. Furthermore, by solving (4b) and (5) for p_1 and p_2, relationships for the pressures as functions of y and its derivatives can be calculated. Property (I) is a direct consequence of property (II) together with the dimension of the pair y. Thus, properties (I) and (II) are proven and the pair y is indeed a flat output.

Remark 1. Observe that by substituting $\dot{p}_\Sigma, z, \dot{z}, \ddot{z}$ and $z^{(3)}$ with their corresponding reference trajectories in Eq. (6), a feed-forward controller for the cylinder system is obtained. Nevertheless, such a controller would be insufficient because of model and parameter uncertainties. Thus, differential flatness is used in Section 4 to design a nonlinear controller for y in order to track a desired reference trajectory $t \mapsto y_\mathrm{r}(t) = (z_\mathrm{r}(t), p_{\Sigma,\mathrm{r}}(t))$.

3.3. Valve subsystem

The cylinder rod is actuated by the flow rates

$$q_c = q_{\mathrm{P}c} - q_{c\mathrm{T}}, \quad c \in \{1,2\}, \tag{7}$$

into the chambers, which are delivered by two identical valves each, as shown in Fig. 2. The quantities $q_{\mathrm{P}c}$, $c \in \{1,2\}$, denote the flows from the pump to the chambers c. Similarly, $q_{c\mathrm{T}}$ are the flows from the chambers to the tank. These valves are pilot-operated proportional flow control valves, the modelling of which is briefly described in the following.

Each valve consists of a main and a pilot spool connected via a spring, as depicted in Fig. 3. A solenoid actuates the pilot spool. When the current of the coil is increased, the pilot spool moves towards the main spool and fluid flows into a chamber inside the valve between the spools. The fluid then flows to the outlet of the valve by passing through the chamber. Thereby, the pressure of the inner chamber is changing, as well as the pressure force acting on the main spool. If the forces acting on the latter are high enough, which is the case when an electrical current of approximately 50% of the maximal current is set, it starts moving, opening its orifice area and directly connecting in- and outlet, thus releasing the main flow.

By neglecting the flow of the pilot spool, the flow rate of the main spool can be approximated by

$$q_{ab}(p_a, p_b) = \bar{\kappa} A(x_\mathrm{m}) \sqrt{(p_a - p_b)},$$

with $(a,b) \in \{(\mathrm{P},1),(\mathrm{P},2),(1,\mathrm{T}),(2,\mathrm{T})\}$, $\bar{\kappa}$ a positive constant, and $A(x_\mathrm{m})$ the orifice area depending on the main spool position x_m. The latter is coupled by the spring to the pilot spool on which the force F_mag of the magnet is acting. This means that the main spool, responsible for most of the flow rate, is not directly actuated. This behaviour can be modelled using the force balance of each spool, taking care of the spring, magnetic, hydraulic, flow and friction forces, as well as the pressure dynamics of the valves inner chamber. Moreover, friction and hysteresis effects have to be taken into account. This yields complex mathematical models, as opposed to what has been discussed above for the cylinder system. A MFC design for the flow rates $q_{\mathrm{P}c}$ and $q_{c\mathrm{T}}$ is thus desirable.

4. Control design

The cascade structure of the proposed algorithms is summarised in Fig. 4. A trajectory generator delivers a sufficiently smooth reference trajectory y_r for the flat output y. The proposed feedback controller for the cylinder system provides desired flow rates $q_{c,\mathrm{d}}, c \in \{1,2\}$, using the state $\hat{\xi}$ of the nonlinear observer and the trajectory y_r. The computed flow rates are references for the underlying MFC and in combination with the flow rate estimator the currents of the valves can be calculated using the state $\hat{\xi}$ of the observer. The individual algorithms mentioned are discussed in detail in the following.

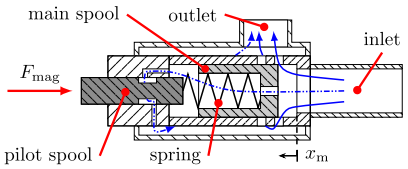

Fig. 3. Sketch of the used pilot-operated valve during operation. The dash dotted, blue line is indicating the flow, resulting from the pilot spool, whereas the solid blue lines show the flow rate of the main spool. If no magnetic force F_mag is applied, the precompressed spring pushes both spools in their rest position such that all orifices are blocked. (For interpretation of the references to colour in this figure legend, the reader is referred to the web version of this article.)

4.1. Feedback controller for the cylinder system

A closed-loop controller for system (4) can be designed by observing that $\xi = (z, \dot{z}, \ddot{z}, p_\Sigma)$ is a Brunovský state with respect to the input $u = (q_1, q_2)$, see, e.g., Rudolph (2021, Sec. 2.7.5) for an in-depth discussion on Brunovský states. By introducing two auxiliary inputs, $v_1 = z^{(3)}$ and $v_2 = \dot{p}_\Sigma$, a stabilising tracking feedback

$$v_1 = z_\mathrm{r}^{(3)} - k_{13}\ddot{e}_1 - k_{12}\dot{e}_1 - k_{11}e_1, \qquad e_1 = z - z_\mathrm{r}, \tag{8a}$$

$$v_2 = \dot{p}_{\Sigma,\mathrm{r}} - k_{21}e_2 - k_{20}\int_{t_0}^{t} e_2(\tau)\mathrm{d}\tau, \qquad e_2 = p_\Sigma - p_{\Sigma,\mathrm{r}}, \tag{8b}$$

can be calculated, where the parameters $k_{1j}, j \in \{1,2,3\}$ and $k_{2j}, j \in \{0,1\}$ are chosen in such a way that the eigenvalues of the differential equation of the errors have negative real parts (Rudolph, 2021, Sec. 4.2).

Remark 2. In (8b) the integral part is chosen to ensure steady state accuracy because only constant reference trajectories for $t \mapsto p_{\Sigma,\mathrm{r}}(t)$ are considered in this work. Nevertheless, it should be remarked that it is also possible to choose an arbitrary reference trajectory for a component of a flat output, according to property (I) from Section 3.2.

A nonlinear tracking control, for the desired flow rates, can afterwards be derived as

$$q_{c,\mathrm{d}} = f_{q_c}\left(v_2, z, \dot{z}, \ddot{z}, v_1\right), \quad c \in \{1,2\}, \tag{9}$$

by combining (8) together with (6), which is the inverse of the model (4) with respect to y. The flow rates derived in (9) are used with (7) to calculate the desired flow rate

$$q_{\mathrm{P}c,\mathrm{d}} = \begin{cases} q_{c,\mathrm{d}}, & q_{c,\mathrm{d}} > 0 \\ 0, & q_{c,\mathrm{d}} \le 0 \end{cases}, \quad q_{c\mathrm{T},\mathrm{d}} = \begin{cases} 0, & q_{c,\mathrm{d}} > 0 \\ -q_{c,\mathrm{d}}, & q_{c,\mathrm{d}} \le 0 \end{cases}, \tag{10}$$

with $c \in \{1,2\}$, for each individual valve.

4.2. Feed-forward control of the valves

If the valve dynamics are modelled following the suggestions in Section 3.3, a simplified feed-forward control (FFC) can be calculated as

$$i_{ab}(q_{ab,\mathrm{d}}, p_a, p_b) = \kappa \frac{q_{ab,\mathrm{d}}}{\sqrt{p_a - p_b}} + i_0 \tag{11}$$

with $(a,b) \in \{(\mathrm{P},1),(\mathrm{P},2),(1,\mathrm{T}),(2,\mathrm{T})\}$ for the flow rate, using a singular perturbation analysis. For simplicity this calculation is omitted. In Eq. (11), $q_{ab,\mathrm{d}}$ denotes the desired flow rate of the valve, p_a and p_b are the pressures at the primary and the secondary side of the valve, i_0 is a minimal current at which a significant flow rate passes through the valve, and κ is a constant parameter. If the minimal current i_0 is chosen too small, the FFC would fail to generate a flow rate, because the resulting current would not be high enough to indirectly move the main spool as discussed in Section 3.3.

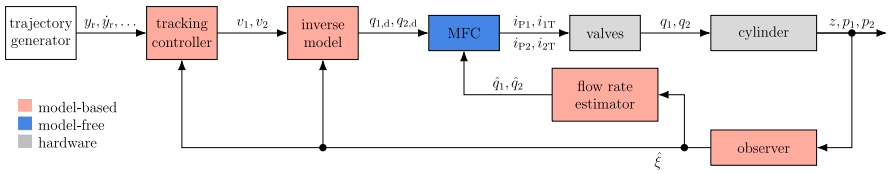

Fig. 4. Signal flow diagram of the proposed algorithms for the control of the cylinder system.

4.3. Nonlinear observer

The implementation of the control law (9) requires the knowledge of the Brunovský state ξ. Thus, the unmeasured components must be estimated. By modelling the friction and the leakage in (4) as piecewise constant parameters, a state representation of the system (4) with state $\boldsymbol{x} = [z, \dot{z}, p_1, p_2, F_f, q_{1,l}, q_{2,l}]^T$ with respect to the input $u = (q_1, q_2)$ can be easily introduced. In the following η_1, η_2, and η_3 are the measurements of the position z and the pressures p_1 and p_2, respectively. The system is observable since the components of a flat output are measured, see, e.g., Rudolph (2021, Sec. 5.3).

Consider the nonlinear observer

$$\dot{\hat{\boldsymbol{x}}} = \begin{pmatrix} \hat{x}_2 - l_1(\eta_1 - \hat{x}_1) \\ \frac{A_1}{m}\eta_2 - \frac{A_2}{m}\eta_3 - \frac{k_v}{m}\hat{x}_2 - g - \frac{1}{m}\hat{x}_5 - l_2(\eta_1 - \hat{x}_1) \\ \frac{B}{V_1(\eta_1)}\left(-A_1\hat{x}_2 + u_1 - \hat{x}_6\right) - l_3(\eta_2 - \hat{x}_3) \\ \frac{B}{V_2(\eta_1)}\left(\ A_2\hat{x}_2 + u_2 - \hat{x}_7\right) - l_4(\eta_3 - \hat{x}_4) \\ -l_5(\eta_1 - \hat{x}_1) \\ -l_6(\eta_2 - \hat{x}_3) \\ -l_7(\eta_3 - \hat{x}_4) \end{pmatrix} \tag{12}$$

with time-varying observer gains $t \mapsto l_i(t)$, $i \in \{1, \ldots, 7\}$. The linear time-varying dynamics $\dot{\tilde{\boldsymbol{x}}} = \bar{A}\tilde{\boldsymbol{x}}$ of the observer error $\tilde{\boldsymbol{x}} = \boldsymbol{x} - \hat{\boldsymbol{x}}$ breaks down into three decoupled parts. Then, the time-varying gains can be chosen to recover linear time-invariant exponentially stable error dynamics. An estimate $\hat{\xi}$ of the Brunovský state is computed using the affine time-independent transformation $\hat{\xi} = (\hat{x}_1, \hat{x}_2, \frac{A_1}{m}\hat{x}_3 - \frac{A_2}{m}\hat{x}_4 - \frac{k_v}{m}\hat{x}_2 - g - \frac{1}{m}\hat{x}_5, \hat{x}_3 + \hat{x}_4)$.

4.4. Model-free control of the valves

4.4.1. Controller design

While the model of the cylinder system is simple and its flatness allows an easy control design, a model describing the dynamics of the proportional valves is complex. Due to numerous simplifications used for the derivation of the feed-forward controller (11), a desired flow rate cannot be accurately achieved. Thus, a MFC approach is desirable.

In the following, q is the flow rate at a valve and i is the electrical current driving the solenoid connected to the pilot spool. It is first assumed that q is measured. This assumption will be dropped when the complete system is considered. The simplified model

$$\dot{q} = f + \gamma i, \quad \gamma > 0, \tag{13}$$

is considered for the flow rate. In Eq. (13), $t \mapsto f(t)$ is a bounded unknown square-integrable function that comprises all unmodelled effects and γ is a parameter the tuning of which will be addressed in the next section.

Remark 3. The parameter γ is restricted to positive values, because, if an ultra-local model $\dot{q} = \gamma i$ is considered a positive value of γ together with a positive electrical current i is resulting in a positive change of the flow rate $\dot{q}$, which matches the physical behaviour of the valve. Adjusting the sign of γ is required, because there is no physical background for the ultra-local model which also means that there is no physical interpretation of the function f and parameter γ, only the phenomenological side of the system is reflected.

Let $t \mapsto q_d(t)$ be a desired sufficiently smooth trajectory for the flow rate q, and consider the controller

$$i = \frac{1}{\gamma}\left(\dot{q}_d - k_p e - \hat{f}\right), \quad e = q - q_d, \tag{14}$$

with $k_p > 0$ and $t \mapsto \hat{f}(t)$ an approximation of f given by

$$\hat{f}(t) = \int_{t-T-\varepsilon}^{t-\varepsilon} g(t-\tau) f(\tau) \mathrm{d}\tau, \tag{15a}$$

$$= \int_{t-T-\varepsilon}^{t-\varepsilon} \dot{g}(t-\tau) q(\tau) - \gamma g(t-\tau) i(\tau) \mathrm{d}\tau \tag{15b}$$

where $g = g_{N,T,\vartheta}^{(\alpha,\beta)}$ is an algebraic differentiator as defined in Section 2 by (2) with $\alpha, \beta > 0$, and a positive constant ε. Eq. (15b) is obtained from (15a) using (13) and integration by parts. By recalling the properties of the differentiator from Section 2, it can be concluded from (15a) that $\hat{f}(t)$ is a least squares approximation of $f(t - \delta_t - \varepsilon)$, with δ_t the approximation delay of $g_{N,T,\vartheta}^{(\alpha,\beta)}$. However (15a) cannot be implemented, as $f(t)$ is unknown. Instead, (15b) shows that $\hat{f}(t)$ can be computed using only known quantities in the interval $[t - T - \varepsilon, t - \varepsilon]$.

Remark 4. It would be possible to tune a PID controller for the flow rate for the valves. Nevertheless, according to d'Andréa-Novel et al. (2010) every classic PID controller is inferior to a MFC. This is because they can be tuned such that they have the same closed loop characteristics, but the MFC has the advantage of compensating additional effects such as hysteresis, friction, heat effects, ageing processes, production tolerances, etc..

4.4.2. Closed-loop analysis

Substituting the controller (14) into the model (13) yields

$$\dot{e} + k_p e = f - \hat{f}.$$

Assuming that f is sufficiently smooth, it follows from (3) and Taylor's theorem that

$$\begin{aligned} &\left|\hat{f}(t) - f(t - \delta_{t,\varepsilon})\right| \leq \left|\hat{f}(t) - f(t)\right| + \left|f(t) - f(t - \delta_{t,\varepsilon})\right| \\ &\leq \frac{M}{s!}\left(\frac{T}{2}\right)^{s+1} \sup_{\tau \in [t-T-\varepsilon, t-\varepsilon]} \left|f^{(2+s)}(\tau)\right| + \delta_{t,\varepsilon} \sup_{\tau \in [t-\bar{\delta}_{t,\varepsilon}, t]} \left|\ddot{f}(\tau)\right| \\ &\leq \mathcal{O}(T + \varepsilon), \quad \bar{\delta}_{t,\varepsilon} = \delta_t + \varepsilon, \end{aligned}$$

for M and s depending on the parameters of $g_{N,T,\vartheta}^{(\alpha,\beta)}$ as discussed in Section 2 and $\varepsilon, T \to 0$. Thus, the approximation error drives the dynamics of the tracking error e. The latter exponentially converges towards a ball around zero. The radius of the ball is reduced by reducing T and ε.

4.4.3. Implementation and input saturation

The tuning guidelines for algebraic differentiators summarised in Othmane et al. (2022) and the controller (14) have been developed for continuous-time systems. However, in most applications, signals are only known at equidistant discrete time instants. Thus, the convolution integrals in (15b) must be approximated by discrete sums. The parameters of the differentiators can be chosen such that the discretisation error is made arbitrarily small by considering the error norm defined

in Othmane et al. (2022, Sec. 4.3). The computation of the latter does not require any knowledge about the function to be approximated. Hence, discretisation effects are neglected in the following. Assume that the window length of the differentiator is an integral multiple of the sampling time t_s, i.e., $T = n_s t_s$ and choose ϵ in (15b) equal to t_s. Then, at instant kt_s, the input i from (14) satisfies

$$i_k = \frac{1}{\gamma}\left(\dot{q}_{d,k} - k_p e_k - \hat{f}_k\right), \tag{16}$$

where, following the discussions from Section 2 and applying the mid-point rule, $\hat{f}_k$ can be computed as

$$\hat{f}_k = \frac{1}{\Phi_1}\sum_{i=0}^{L-1} w_{1,i} q_{k-i-1} - \gamma \frac{1}{\Phi_0}\sum_{i=0}^{L-1} w_{0,i} i_{k-i-1},$$

with $\Phi_m = \frac{t_s^q}{n!}\sum_{i=0}^{L-1} w_{m,i}(-i)^n$, $w_{m,i} = t_s g_{i+1/2}^{(m)}$, $m \in \{0,1\}$, and $L = n_s$.

To avoid damaging the valves, the discrete-time input in (16) is saturated such that the applied electrical current $i_{\mathrm{sat},k}$ is in the interval $i_{\mathrm{sat},k} \in [i_{\min}, i_{\max}]$. Then, $i_{\mathrm{sat},k}$ is used for the valve at each sampling instant k. Analysing the effects of this saturation on the closed-loop dynamics is a challenging and open problem that should be addressed in future work. However, the experiments reported in Section 5 validate the approach.

4.4.4. Control of valves in the complete system

In order to implement the feedback (16), the flow rates through the valves have to be estimated. The pressure dynamics (4a) together with the observer (12) yield an estimate

$$\hat{q}_c = \frac{V_c(\hat{x}_1)}{B}\dot{\hat{p}}_c - (-1)^c A_c \hat{x}_2 + q_{c,1} \approx (-1)^{(c+1)} A_c \hat{x}_2 \tag{17}$$

of q_c. The approximation in (17) is justified because $\left|\dot{\hat{p}}_c V_c(\hat{x}_1)/B\right| \ll \left|A_c \hat{x}_2\right|$, as it will be validated in Section 5. The relation (10) can then be used for the estimation of the flow rate at each valve.

Remark 5. The algebraic differentiators introduced in Section 2 could also be used to estimate the Brunovský state as well as the flow rate, but this is not in the scope of the present work.

The overall system depicted in Fig. 2 contains four pilot-operated proportional valves. Two control strategies are investigates in the following:

1. Controlled valves: Each of the four valves is controlled by an individual MFC controller. The relationship (10) is used to assign the desired and estimated flow rates for each chamber from Eq. (9) to each individual valve. The electrical current is set to $i_{\min}$ if the desired flow rate is zero.
2. Controlled pairs: The relation (10) is used to assign the desired and the estimated flow rates to each chamber. If $q_{\mathrm{P}c,\mathrm{d}}$ is different from zero then $q_{\mathrm{P}c,\mathrm{d}}$ and $\hat{q}_{\mathrm{P}c}$ are used in the MFC to control $i_{\mathrm{P}c}$, and $i_{c\mathrm{T}}$ is set to $i_{\min}$. Otherwise the tank specific values are used in the same MFC to control $i_{c\mathrm{T}}$ while $i_{\mathrm{P}c}$ is set to $i_{\min}$.

Remark 6. A minimal current $i_{\min} > 0$ is not required for the MFC, but it considerably increases the performance of the MFC, which has two reasons. First, the valve is designed in such a way that it starts generating a significant flow rate at approximately 50% of the maximal current. Second, as discussed in Section 5.1 the combinations of the controller parameters γ and k_p resulting in a stable closed-loop behaviour are constrained.

5. Experimental results

The proposed algorithms are now validated using experiments on the test bed shown in Fig. 1. The double-acting hydraulic piston has a maximum stroke of 300 mm and lifts a load of 34.5 kg. As mentioned in Section 3.3, the valves used are four proportional flow control valves PWK12120WP-02-C-V-11 that are pilot-operated. Each valve has a dedicated PSV1010-24-10-000 power electronics with 160 Hz dither and a hardware current controller. The flow and pressure supply is provided by a Hydac Tankpac TPL-2, which is a combination of tank, pump, filter, and motor unit. The motor limits the pump unit to a 91 bar output pressure and a flow rate of 21.9 l/min. Additionally a pressure limiting Hydac DB4E-012-100S valve is installed to ensure a constant pump pressure. To sense the pressure of each cylinder chamber along with pump and tank pressures four HDA3844B-100-000 strain gauge sensors are available. The position of the piston can be directly measured with a Hydac HLT2000-L2-M08-B01-0350-000 sensor. To validate the algorithms described in Section 4, a turbine flow rate sensor Hydac EVS 3104-A-0020-00, with a measurement range of 1.2-20 l/min is used. The algorithms are running on a real-time hardware INFO-SAM2 from Indel with a sampling rate of $f_s = 1/t_s = 4$ kHz.

Table 1
Parameters of the different filters that are investigated.

No.	$\alpha = \beta$	ω_c in $\frac{\mathrm{rad}}{\mathrm{s}}$	δ_t in ms	$T \cdot f_s$
1	2	250	7.75	62
2	2	450	4.25	34
3	4	850	4.0	32
4	3	450	5.875	47
5	2	150	13.0	104
6	8	250	23.375	203

5.1. Parameters of algebraic differentiators and MFC

The parameters N, α, β, and ω_c of the algebraic differentiators have to be chosen in such a way that the estimation delay δ_t will be small and a high approximation accuracy is achieved for the sought derivative. The degree N of the polynomial approximating the signals is set to zero. The preferable parametrisation $\alpha = \beta$ is chosen to achieve a maximum robustness with respect to measurement noise. See, e.g., Othmane et al. (2022, Sec. 4) for a discussion on noise rejection properties when $\alpha = \beta$ and $N = 0$. With this choice the estimation delay δ_t is equal to $T/2$. Several parameter combinations are used in this discussion to show that not one specific parametrisation is needed to get a satisfying solution. These parameters are collected in Table 1.

To choose the parameters γ and k_p of the MFC a parameter sweep is done using the test bed. To this end, the electrical currents of the valves are set in a special configuration such that the cylinder rod is not moving. If, for example, valve $\mathrm{V}_{1\mathrm{P}}$ is used, the currents of the valve pair 2 is set to zero, while the current of valve $\mathrm{V}_{1\mathrm{T}}$ is set to the maximum value. Thereby, the hydraulic medium is flowing from the pump over valve pair 1 to the tank and only valve $\mathrm{V}_{1\mathrm{P}}$ is responsible for the occurring flow rate. As mentioned above, a sensor for the flow rate of the pump q_p is available and used for the experiments with an individual valve, because an estimate of the flow rate, such as suggested in Section 4.3, is not available while the piston is not moving. The desired flow rate trajectory $t \mapsto q_d(t)$ is designed as a set point transition from 1 to 5 l/min and back to 1 l/min again, with a polynomial of degree 5 and a transition time as well as a holding time of 5 s. Even though the derivative of this reference is known in advance, the algebraic differentiator is used, as proposed, to estimate the signal $t \mapsto \dot{q}_d(t)$. It should be remarked that during such an experiment the pressure difference over the valve is changing, which is an additional challenge the MFC has to overcome. The results of the parameter sweep with the algebraic differentiator parameterised as in No. 1 from Table 1 can be seen in Fig. 5. Each marker stands for a individual experiment with a corresponding combination of γ and k_p.

It can be seen that there exists a large area in the parameter space that results in a small root mean square (RMS) value of the error $e_q = q_p - q_d$, which will be called the stability region of the algorithm. Although this region is large, Fig. 5 clearly shows that for some

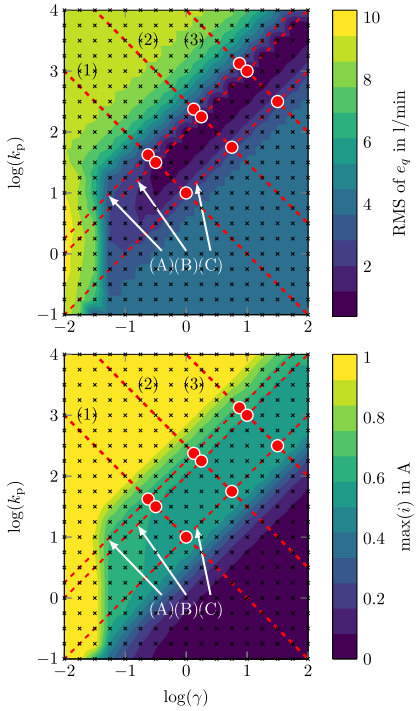

Fig. 5. Results of the parameter sweep of the MFC for valve V_{1P} using the parametrisation No. 1 from Table 1 to determine the region of parameter combinations that yield satisfying tracking behaviour.

parameter combinations of $\gamma > 0$ and $k_p > 0$ undesired behaviour can occur.

Above the stability region the experiments show that the flow rate starts to oscillate, which is indicated by the maximal current as well as a value of approximately 8 l/min for the RMS of e_q. Below the stability region the MFC is not setting up a current that is high enough to move the main spool in an appropriate manner and thus to provide a flow rate.

The parameter sweep has also be carried out for the three other valves of the same type. A similar result can be seen in Fig. 6 and it shows that all of them are behaving in the same way. With this in mind, it is justified to only look at valve V_{1P} for the rest of this work and assume that a different valve would behave similarly.

The remaining parameter combinations from Table 1 are also tested using a parameter sweep with valve V_{1P}, and the results are shown in Fig. 7. All combinations show a similar shape of the stability region in approximately the same parameter set. It is noticeable that for large delay values (see parametrisations 5 and 6) the borderline of the maximal current occurs only when the value of k_p is reaching a certain level. However, further investigation of this phenomenon is out of the scope of the present paper.

For the remainder of this work the parameter combination No. 1 for the algebraic differentiators is used. Preliminary investigations showed that the combination No. 3 with a smaller window length T results in comparable results for the overall system. Nevertheless, using No. 1 a

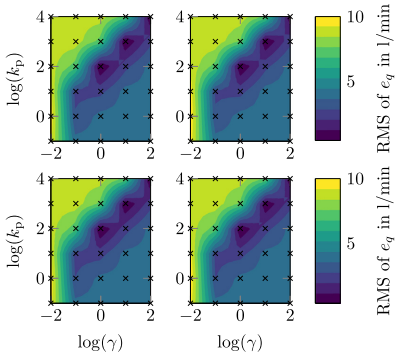

Fig. 6. Results of the parameter sweep for the valves (from left to right, top to bottom) V_{1P}, V_{1T}, V_{2P}, and V_{2T} using the parametrisation No. 1 from Table 1. The similar valves show almost exactly the same behaviour, which justifies considering only one valve for further experiments.

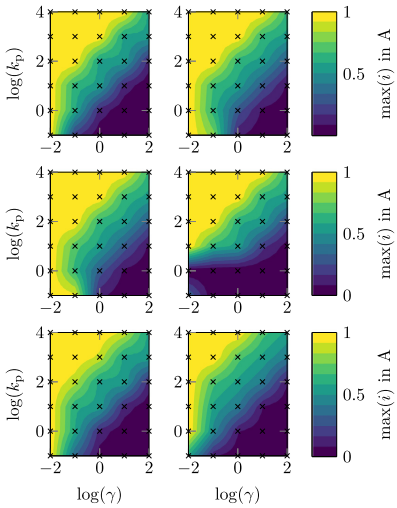

Fig. 7. Results of the parameter sweep for valve V_{1P} using the different parametrisations No. 1 to 6 (from left to right, top to bottom) from Table 1. All parametrisations yield comparable results in the parameter space.

certain robustness of the control approach with respect to this delay can be observed.

5.2. Parameter combinations with constant γ/k_p

A closer look on some individual experiments will be taken now. To this end, the parameter combinations, marked by red dots, for γ and k_p in Fig. 5 will be used to show an interesting behaviour. The flow rate over time as well as the corresponding electrical current for each marked combination can be seen in Fig. 8. The graphs are grouped regarding the position on the lines (A) to (C), whereas A1 marks the crossing of lines (A) and (1) as depicted in Fig. 5. It is interesting that even if the parameter tuples differ by one magnitude they still

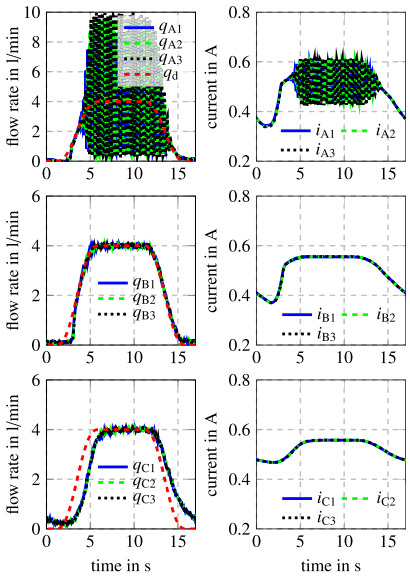

Fig. 8. Controlled flow rate and corresponding current of valve V_{1P} for parameter combinations with the same ratio of γ and k_p, marked in Fig. 5 with lines (A) to (C) and (1) to (3). Parameter combinations on the same line show similar closed-loop behaviour.

yield similar behaviour. On each line the ratio of the parameters is the same, which means that the individual values of γ or k_p are not important for the feedback. From line (A) to line (C) the response of the controlled system changes drastically. The plots corresponding to line (C) show a flow rate that follows its reference with a delay of approximately 0.8 to 1.2 s. If the holding time is long enough, steady state accuracy can be achieved. Compared to (C), the plots from line (B) show that with increasing parameter ratio the controller is much more aggressive, resulting in smaller errors during the transition. The system response from line (A) instead shows that by further increasing the ratio the system starts oscillating, but the current is not reaching its maximum value i_{max} yet. The analysis of this behaviour merits further investigation.

5.3. FFC in comparison with the MFC

In this section the results of the FFC (11) and the derived MFC (16) are studied. As discussed above, only valve V_{1P} is used to compare the proposed algorithm using the settings described in Section 5.1. The controller parameters of the MFC are chosen as $\gamma = 0.4\,\mathrm{m^3 A^{-1} s^{-2}}$ and $k_p = 30\,\mathrm{s^{-1}}$, because in the experiments this combination showed a good trade-off between overshoot and settling time. As mentioned above, all combinations with the same parameter ratio yield similar results. However, the current is restricted to $i_{max} = 1.01$ A and $i_{min} = 0.0$ A. For the FFC the parameter $\kappa = 6.596 \cdot 10^5 \sqrt{\mathrm{kg\,mA}}\,\mathrm{m^{-3}}$ follows from the geometry of the valve, and the minimal current is set to $i_0 = 0.53$ A for a fair comparison. Fig. 9 shows two exemplary experiments. A polynomial of degree 5 and a transition time of 0.9 s is connecting the stationary regimes. This transition time is set as a benchmark, resulting from the FFC control $q_{c,r}$ of Eq. (6) for the fastest piston movement that will be investigated later on in Section 5.6.

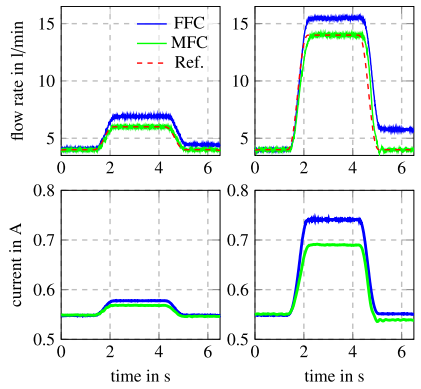

Fig. 9. Comparison of the FFC and the MFC using valve V_{1P}. Flow rate over time for two different end values. Tracking and steady-state errors of the FFC are due to unmodelled magnetic hysteresis and friction.

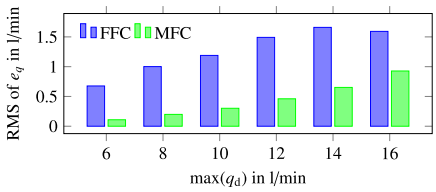

Fig. 10. Comparison of the FFC and the MFC using valve V_{1P}. RMS values of e_q for different final values of the commanded flow rate. The proposed MFC shows significantly better results due to steady state accuracy and robustness against unmodelled effects.

In every experiment the FFC results in a flow rate that is higher than the commanded one, but the polynomial form of the transition trajectory is quite accurate. Especially the experiment with a reference reaching 14 l/min shows the unmodelled effects, such as hysteresis resulting from the magnet as well as the friction of the pilot and main spool. As observed above, a huge effort is required to model these phenomena, but they can be compensated by MFC. Even the proposed MFC has its limits during the transition, which might result from a combination of the delay of the underlying hardware current controller and the flow sensor as well as the algebraic differentiators used in the implemented algorithm. Nevertheless, in Fig. 10 the RMS of e_q is depicted and it shows that the MFC is always resulting in a lower quality gauge. The rising RMS values are caused by the errors during transition, because the algorithm ensures steady state accuracy even without an explicit integral part in the control law, which is emulated by the estimate $\hat{f}$.

5.4. Validation of the flow rate estimation

In order to apply the MFC (16) in the overall system (4), the estimation of the flow rate (17) is used instead of the sensor values. A comparison of both can be seen in Fig. 11. The experimental results obtained clearly justify the approximation proposed in Section 4.3. The derivative $\dot{p}_c$ of the pressure is estimated using the algebraic differentiator presented in Section 5.1. The minimal currents of the valves, i_0 and i_{min} respectively, are set in such a way that there is always a loss of flow rate q_{P,i_0} that flows from the pump over the valves directly

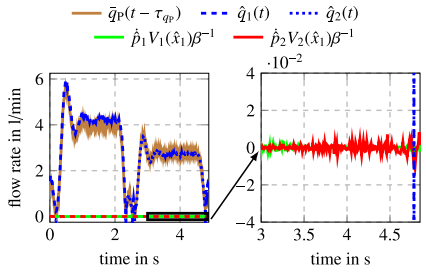

Fig. 11. Validation of the flow rate estimation. The zoom on the right shows that the flow rate resulting from the pressure change is insignificant and the proposed approximation is justified.

Table 2
Parameters of the model (4) used for the cylinder system.

Parameter	Value	Parameter	Value
A_1	$7.068 \cdot 10^{-4}$ m^2	B	1.7 G N m^{-2}
A_2	$4.523 \cdot 10^{-4}$ m^2	g	9.81 m s^{-2}
V_0	$5.026 \cdot 10^{-5}$ m^3	m	34.5 kg
k_v	332.6 N s^{-1}	l	0.15 m

to the tank, without contributing to the cylinder stroke. This loss is determined and subtracted from the measured sensor values to compare them with the chamber flow rates $\hat{q}_c$. Preliminary investigation showed that the sensor has a delay of approximately $\tau_{q_P} = 50$ ms and a nonlinear characteristics resulting from the measurement principle. Therefore, the signal $t \mapsto \bar{q}_P(t) = q_P(t) - q_{P,i_0}$ in Fig. 11 is shifted in time to visualise the quality of the estimate (17). These results clearly validate the estimation approach.

5.5. Implementation and reference trajectories

The model parameters from Table 2 are used for the implementation of the controller in Eq. (8). The gains $k_{1j}, j \in \{1,2,3\}$ and $k_{2j}, j \in \{0,1\}$ are chosen in such a way that the eigenvalues of the dynamics of the error e_1 are $-28\,\mathrm{s}^{-1}$, $-35\,\mathrm{s}^{-1}$, $-1563\,\mathrm{s}^{-1}$, and those of e_2 are $-1\,\mathrm{s}^{-1}$ and $-500\,\mathrm{s}^{-1}$. The control law is implemented in a quasi-continuous manner, except for the integral in Eq. (8b) that is discretised using Tustin's method.

The gains $l_j, j \in \{1,\dots,7\}$ of the observer in (12), used to reconstruct the Brunovský state ξ, are chosen in such a way that three decoupled error dynamics result, with the eigenvalues $-100\,\mathrm{s}^{-1}$, $-110\,\mathrm{s}^{-1}$, $-120\,\mathrm{s}^{-1}$ for $\tilde{x}_1$, and $-500\,\mathrm{s}^{-1}$, $-580\,\mathrm{s}^{-1}$ for $\tilde{x}_3$ as well as for $\tilde{x}_4$. The parameters l_6 and l_7 are time-varying, since the measurement η_1 in Eq. (12) can be used to compensate the nonlinearity $V_c(\eta_1)$ in order to obtain linear error dynamics. The observer is discretised using Euler's method.

In the complete system, comprising the cylinder and the valves, the estimation in (17) is used instead of the sensor. The dynamics of the latter are no longer influencing the closed-loop behaviour. Therefore, the proportional gain $k_p = 140\,\mathrm{s}^{-1}$ is set higher. This improves the behaviour of the algorithm especially for reference trajectories $t \mapsto q_d(t)$ with fast changes commanded by the cylinder controller (8), (9) when compensating friction phenomena at low piston velocities.

The pressure of the pump is set to 30 bar and the reference of the pressure p_Σ to 20 bar. This ensures that the piston can lift the load. The reference trajectory $t \mapsto z_r(t)$ for the cylinder position is shown in Figs. 12 and 13 for two different transition times. The trajectory is designed in such a way that a polynomial of sufficiently high degree is connecting trajectory pieces with a linear slope between

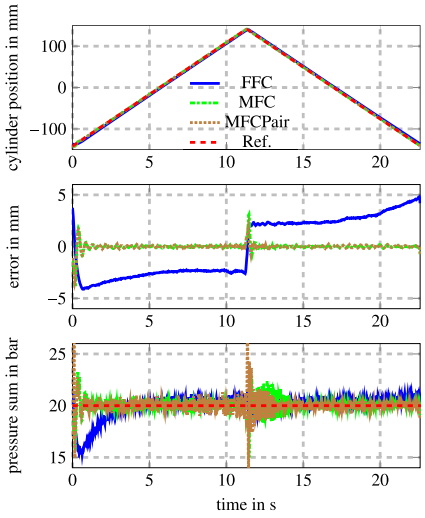

Fig. 12. Controlled flat output y for a slow reference trajectory by using the FFC and the MFC for the valves. The proposed MFC shows almost no tracking error in e_1.

two stationary regimes. In particular, this yields constant velocities, which is beneficial for the proposed MFC algorithms. Additionally, the sufficiently smooth polynomials connecting the trajectory pieces ensure a continuous controller output $q_{c,d}$.

5.6. Results for the overall system

Fig. 12 shows the trajectories of the controlled flat output y for a stroke of 280 mm in approximately 11.3 s and a maximum piston velocity equal to 25 mm/s. The FFC of the valves shows a tracking error of more than ± 2 mm during the transition. Moreover, the two MFC algorithms are able to decrease this error by one magnitude of scale, to less than ± 0.2 mm. The largest error occurs during the change of direction, when no estimation of the flow rate is possible and static friction is acting on the cylinder piston. Using the MFC to control the valve pairs, a maximum error of 1.9 mm can be achieved, which is significantly less than the corresponding value of 4.8 mm for the FFC. By comparing the resulting pressures p_Σ it can be seen that all algorithms yield similar results, except for some peaks during the change of direction.

If the piston velocity is further increased the differences between the algorithms are no longer that significant. However, the MFC still yields better results, see Fig. 13. Again the maximum error can be reduced from 4.2 mm using the FFC to 2.5 mm using the MFC for all four valves, but when the pair is controlled the error increases to 7.7 mm. Nevertheless, both MFC algorithms ensure a smaller absolute value of the minimal error (FFC: -10.0 mm, MFC: -7.5 mm, MFCPair: -6.0 mm). By reducing the transition time to approximately 2.3 s the switching between the valves becomes more crucial, which is especially visible for the controlled pressure sum p_Σ. The peaks occurring during low velocity are more dominant.

In Fig. 14 the RMS values for the position error e_1 and the three different control laws are depicted. Especially for low velocities, controlling the valve system with the MFC is advantageous. When increasing the velocity reduced accuracy for the proposed algorithm is observed, which might be explained by two arguments. First, the stroke that the

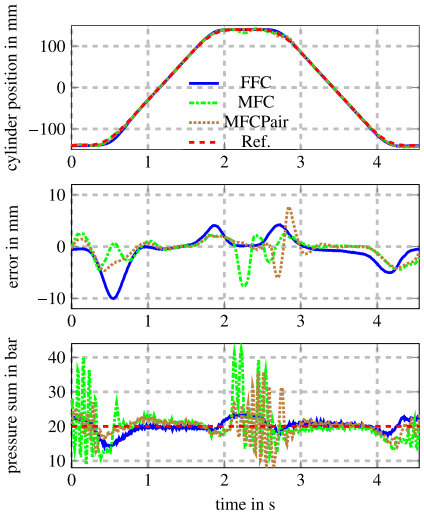

Fig. 13. Results of the controlled flat output y for a higher piston velocity by using the FFC and the MFC for the valves.

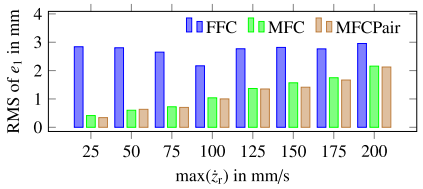

Fig. 14. Comparison of the RMS values of the error e_1 for different maximal piston velocities. Especially for low velocities the MFC shows a significantly better performance.

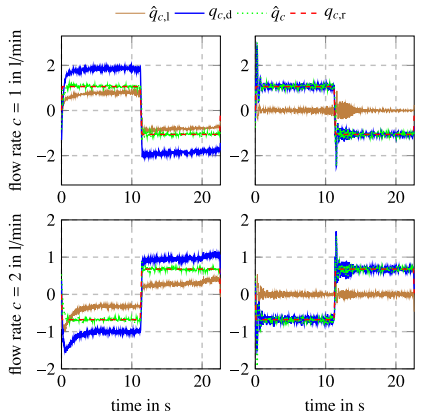

Fig. 15. Flow rate over time for the FFC on the left and the MFC on the right. The observer falsely estimates a leakage by using the FFC, because the commanded and the reconstructed flow rate are different.

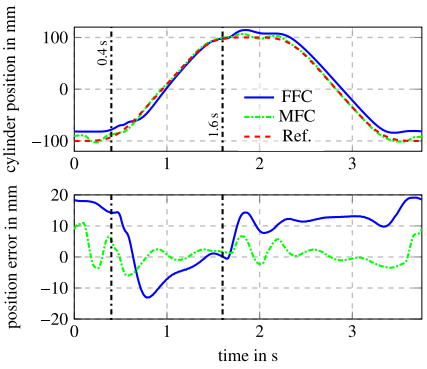

Fig. 16. System behaviour in presence of a leakage. MFC can easily compensate the effects of the leakage.

piston can perform is restricted. This results in a shorter time period when the desired flow rate is constant. As seen in Section 5.3, the MFC has steady state accuracy and would, therefore, outperform the FFC. Second, because the estimation of the flow rate is not available during the change of direction, the MFC is responding too aggressively, which leads to larger errors in the initial phase of the trajectory. Thus, the combination of MFC and FFC during this crucial phase is an interesting path to follow for future work.

In Fig. 15 the flow rate of the FFC (on the left) and the MFC for all valves (on the right) are compared. The FFC of the valves yields higher input signals, required to compensate for model uncertainties as well as the tracking error during transition. This leads to a false estimation of leakage by the observer (12). Compared to the left hand side the graphs on the right hand side are almost identical, except for measurement noise, which is also a validation of the model (4). The peaks in the flow rate are again resulting from the compensation of friction and the fact that the flow rate estimation is not available for low velocities.

5.7. Leakage compensation

An additional advantage of the proposed MFC is the almost immediate compensation of leakage. Therefore, a leakage of valve V_{P1} is simulated by increasing its minimal current i_{min} and i_0, respectively, from 0.5 to 0.6 A, which corresponds to an increase of approximately 20% of the available effective current. This means that whenever the desired flow rate of this valve is zero it will deliver an additional flow rate that has to be dealt with, because it will flow into the chamber $c = 1$ and will disturb the movement of the piston. Fig. 16 shows the influence of this simulated leakage, by comparing the MFC for the valve pair with the FFC. From 0.4 to 1.6 s valve V_{P1} will be used as proposed, but otherwise the minimal current is risen. Due to the fast reaction of MFC to this disturbance, the behaviour is comparable to that in Fig. 13, where no leakage affects the system. By calculating the RMS value of e_1 this fact becomes clearer. The quality gauge is increasing by the factor 4 (from 2.9 mm to 11.7 mm) for the FFC, whereas only by 1.7 for the MFC (from 2.1 mm to 3.5 mm). The cylinder controller cannot compensate such a disturbance in a satisfying manner.

6. Conclusion and future work

In this contribution, a systematic tuning approach for the parameters of a MFC for systems approximated by first-order differential

equations is investigated by considering the control of the flow rate of a pilot-operated proportional valve. The results are illustrated using numerous experiments. In addition, a model-based control for a double-acting hydraulic piston actuator is provided, with a nonlinear observer. The combination of the two approaches is resulting in high position accuracy for the overall system and robustness against leakages, as demonstrated in experiments.

It could be seen, that for high reference velocities the performance of the MFC may degrade. However, this is not a drawback of the proposed combination of the model-based control approach and the MFC. The absence of a good flow rate estimate when the cylinder rod is moving slowly and an increasing influence of the friction for these trajectories explain this deterioration of the performance. Since the distance the cylinder rod can travel is limited, the errors in the starting and ending phases of trajectories with high reference velocities dominate. Thus, combining the MFC with the FFC to enhance the performance, especially for the starting and stopping phase of the piston, might deserve additional investigation. Moreover, every feedback controller relying on the estimate of the flow rate would show a low performance during these trajectories portions. Also the effects of the input saturation on the closed-loop dynamics should be addressed in future work, besides the effects of the delay to the stability region.

Future work should also apply the MFC approach to an approximation of a second order system in a structured manner. Additionally, further investigations should be made to check whether the observed behaviour of same system response with the same parameter ratio of the MFC applies to other systems as well.

Declaration of competing interest

The authors declare that they have no known competing financial interests or personal relationships that could have appeared to influence the work reported in this paper.

Acknowledgement

Long-term support from HYDAC Fluidtechnik GmbH and Intronik GmbH is acknowledged. Preliminary simulation results of L. Jose are acknowledged. We would also like to thank the reviewers for their valuable feedback.

Funding

The authors thank the European Regional Development Fund (ERDF) for partly supporting their research within the project number 14.2.1.4-2019/1.

References

d'Andréa-Novel, B., Fliess, M., Join, C., Mounier, H., & Steux, B. (2010). A mathematical explanation via "intelligent" PID controllers of the strange ubiquity of PIDs. In *18th Mediterranean conference on control and automation* (pp. 395–400).

Eryilmaz, B., & Wilson, B. H. (2006). Unified modeling and analysis of a proportional valve. *Journal of the Franklin Institute*, *343*(1), 48–68.

Ferreira, J. A., Gomes de Almeida, F., & Quintas, M. R. (2002). Semi-empirical model for a hydraulic servo-solenoid valve. *Proceedings of the Institution of Mechanical Engineers, Part I (Journal of Systems and Control Engineering)*, *216*(3), 237–248.

Fliess, M., & Join, C. (2008). Commande sans modèle et commande à modèle restreint. *e-STA Sciences et Technologies de l'Automatique*, *5*(4), 1–23.

Fliess, M., & Join, C. (2009). Model-free control and intelligent PID controllers: Towards a possible trivialization of nonlinear control? *IFAC Proceedings Volumes*, *42*(10), 1531–1550.

Fliess, M., & Join, C. (2013). Model-free control. *International Journal of Control*, *86*(12), 2228–2252.

Fliess, M., & Join, C. (2021). An alternative to proportional-integral and proportional-integral-derivative regulators: Intelligent proportional-derivative regulators. *International Journal of Robust and Nonlinear Control*.

Fliess, M., Join, C., & Riachy, S. (2011). Revisiting some practical issues in the implementation of model-free control. *IFAC Proceedings Volumes*, *44*(1), 8589–8594, 18th IFAC World Congress.

Fliess, M., Lévine, J., Martin, P., & Rouchon, P. (1995). Flatness and defect of non-linear systems: introductory theory and examples. *International Journal of Control*, *61*(6), 1327–1361.

Guilloteau, Q., Robu, B., Join, C., Fliess, M., Rutten, É., & Richard, O. (2022). Model-free control for resource harvesting in computing grids. In *Conference on control technology and applications*. IEEE.

Hegedüs, T., Fényes, D., Németh, B., Szabó, Z., & Gáspár, P. (2022). Design of model free control with tuning method on ultra-local model for lateral vehicle control purposes. In *2022 American control conference* (pp. 4101–4106).

Kiltz, L. (2017). *Algebraische Ableitungsschätzer in Theorie und Anwendung* (Doctoral dissertation), Germany: Saarland University.

Kiltz, L., & Rudolph, J. (2013). Parametrization of algebraic numerical differentiators to achieve desired filter characteristics. In *Proceedings of the 52nd IEEE conference on decision and control* (pp. 7010–7015).

Li, W., Yuan, H., Li, S., & Zhu, J. (2022). A revisit to model-free control. *IEEE Transactions on Power Electronics*, *37*(12), 14408–14421.

Mboup, M., Join, C., & Fliess, M. (2007). A revised look at numerical differentiation with an application to nonlinear feedback control. In *Proceedings of the 15th Mediterranean conference on control and automation*.

Mboup, M., Join, C., & Fliess, M. (2009). Numerical differentiation with annihilators in noisy environment. *Numerical Algorithms*, *50*(4), 439–467.

Merritt, H. E. (1967). *Hydraulic control systems*. New York, Santa Barbara, London, Sydney, Toronto: John Wiley & Sons.

Michel, L., Neunaber, I., Mishra, R., Braud, C., Plestan, F., Barbot, J.-P., Boucher, X., Join, C., & Fliess, M. (2022). Model-free control of the dynamic lift of a wind turbine blade section: experimental results. *Journal of Physics: Conference Series*, *2265*(3), Article 032068.

Othmane, A. (2022). AlgDiff: A Python package with MATLAB coupling implementing all necessary tools for the design, analysis, and discretization of algebraic differentiators. Available at https://github.com/aothmane-control/Algebraic-differentiators, version 1.1.0.

Othmane, A., Kiltz, L., & Rudolph, J. (2022). Survey on algebraic numerical differentiation: Historical developments, parametrization, examples, and applications. *International Journal of Systems Science*, *53*(9), 1848–1887.

Othmane, A., Mounier, H., & Rudolph, J. (2021). Parametrization of algebraic differentiators for disturbance annihilation with an application to the differentiation of quantized signals. *IFAC-PapersOnLine*, *54*(9), 335–340.

Othmane, A., Rudolph, J., & Mounier, H. (2021). Systematic comparison of numerical differentiators and an application to model-free control. *European Journal of Control*, *62*, 113–119.

Pereira das Neves, G., & Augusto Angélico, B. (2021). Model-free control of mechatronic systems based on algebraic estimation. *Asian Journal of Control*.

Rothfuss, R., Rudolph, J., & Zeitz, M. (1996). Flatness based control of a nonlinear chemical reactor model. *Automatica*, *32*(10), 1433–1439.

Rudolph, J. (2021). *Flatness-based control: An introduction*. Shaker Verlag.

Steinboeck, A., Kemmetmüller, W., Lassl, C., & Kugi, A. (2013). Model-based condition monitoring of an electro-hydraulic valve. *Journal of Dynamic Systems, Measurement and Control*, *135*(6).

Szegö, G. (1939). *Orthogonal polynomials*. New York: AMS.

5.2 Model-free control of a magnetically supported plate

The contributions of each author are listed in what follows.

P.M. Scherer (75 %)
Methodology, Software, Investigation, Data Curation, Visualization, Writing – Original Draft, Writing – Review & Editing

A. Othmane (20 %)
Conceptualization, Formal analysis, Writing – Review & Editing

J. Rudolph (5 %)
Writing – Review & Editing

Control Engineering Practice 148 (2024) 105950

Contents lists available at ScienceDirect

Control Engineering Practice

journal homepage: www.elsevier.com/locate/conengprac

Model-free control of a magnetically supported plate

P.M. Scherer [a,*], A. Othmane [b], J. Rudolph [a]

[a] Chair of Systems Theory and Control Engineering, Saarland University, Campus A5 1, Saarbruecken, 66123, Germany
[b] Systems Modeling and Simulation, Saarland University, Campus A5 1, Saarbruecken, 66123, Germany

ARTICLE INFO

Keywords:
Algebraic differentiators
Model-free control
Model-based control

ABSTRACT

Established model-based methods often use a combination of state feedback and observer to control complex systems. They rely on detailed mathematical models that are often hard to derive. Nonetheless, such methods may achieve a high level of accuracy, which justifies the cumbersome modelling. An alternative approach is model-free control, in a form introduced by Fliess and Join, where the system is approximated in a short time interval by a low-order differential equation with unknown parts, a so-called ultra-local model. This control method is a powerful tool, but the parametrisation and the concrete implementation may require time, effort, and experience. The present paper investigates the systematic tuning of a model-free controller for a magnetically supported plate that is modelled as an unstable multiple-input multiple-output system. Furthermore, the incorporation of model information into the model-free controller is investigated. These adaptations ultimately improve results by simplifying parameter tuning and interpretation of estimates. Several experiments are carried out on a test bed to show the capabilities of the proposed algorithms for set point stabilisation and trajectory tracking. The effects of the different parameters in the model-free controllers are addressed, and excellent robustness with respect to actuator faults is demonstrated. Filters for estimating derivatives and unknown quantities are designed using an open-source toolbox.

1. Introduction

Model-free control (MFC) has become a popular term in the broad field of control engineering and includes approaches based on proportional integral derivative (PID) control, fuzzy control, reinforcement learning, and data-based control. Fliess and Join (2008, 2009, 2013) have proposed algorithms that do not rely on physically motivated mathematical models of the systems considered and do not require time consuming and data intensive training. In this approach, a system is locally approximated by a low-order differential equation with unknown parts, which is called a ultra-local model. The unknown part of the system consists of unmodelled dynamics as well as disturbances, without any distinction between the latter. With the help of algebraic differentiators (see Mboup et al., 2009 and the survey Othmane et al., 2022 for an overview) the unknown part can be estimated for a subsequent compensation in the feedback control.

This simple yet powerful and real-time capable method has been applied to various systems, ranging from direct fuel injection systems in Carvalho et al. (2024), unmanned aerial vehicles in Al Younes et al. (2014), grid-tied inverters in Wachter et al. (2023), wind turbines in Lafont et al. (2020), active suspensions in Haddar et al. (2019), proportional valves in Scherer et al. (2023), green houses in Lafont et al. (2015) and video streaming in Fliess and Join (2023), to mention only a small selection of successful simulations and experiments.

The works Li et al. (2022) and Zhang et al. (2022) focus on classical control theoretical tools in the frequency domain to analyse the MFC, whereas Hegedűs et al. (2022) investigates the tuning of the input gain. In Belhadjoudja et al. (2023) the MFC is analysed using methods from linear systems. An alternative MFC approach is considered in Tabuada et al. (2017), where the knee joint of a bipedal walking robot is controlled based on a linear approximation of the nonlinear system with guarantees on stability depending on the sampling time. Nonetheless, systematic tuning of the MFC algorithms for unstable multiple-input multiple-output (MIMO) systems remains a challenging problem, despite the successful realisation in Bekcheva et al. (2018) or Neves and Angélico (2021).

In Othmane, Rudolph, and Mounier (2021) the tuning of estimators used for the approximation of the unknown part of the ultra-local model is investigated. These estimators are called algebraic differentiators, the systematic tuning of which has already been analysed in Kiltz (2017), Kiltz and Rudolph (2013) and Othmane et al. (2022). The design, analysis, and discretisation of the differentiators is done with the easy to use open-source toolbox AlgDiff (see Othmane, 2022), the

* Corresponding author.
E-mail address: p.scherer@lsr.uni-saarland.de (P.M. Scherer).

https://doi.org/10.1016/j.conengprac.2024.105950
Received 23 January 2024; Received in revised form 15 March 2024; Accepted 12 April 2024
Available online 3 May 2024

use of which has been described in the tutorial-like paper (Othmane & Rudolph, 2023).

The present paper focuses on active magnetic bearings. This technology can, for example, be used for flywheels (cf. Lei & Palazzolo, 2008), designed for energy storage, to dampen the vibration of circular saws (Ellis & Mote, 1977), or for the exact positioning of a tool attached to a rotating shaft (Eckhardt & Rudolph, 2004). Due to the inherent nonlinearity and instability in the system, control algorithms are always needed for the realisation of the technology. These algorithms are typically based on mathematical models of the magnets (cf. Collon et al., 2007) and the rigid body dynamics of the rotating shaft. The same technology of the bearings can also be used for the position control of a plate as discussed in Kiltz et al. (2014). The magnetically supported plate described therein is also considered in the present work as an example for the magnetic bearing technology, dealing with interesting problems like over-actuation, nonlinearity of the magnets as well as the unstable MIMO characteristic of the system that is challenging in the MFC context. The contributions De Miras et al. (2013) and Moraes and da Silva (2015) have already successfully described the experimental implementation of MFC techniques for simple lab setups with magnetic bearings. However, questions such as parametrisation, discrete implementation, incorporation of physical knowledge into the controller design, and comparisons with model-based approaches remain open. The current work explores these issues.

Here, the systematic design and tuning of algebraic differentiators and MFC algorithms based on a second order ultra-local model is investigated. The differentiators are essential to online estimate unknown parts of the ultra-local model as well as velocities that are not directly measured but needed for the controller. Additionally, details concerning the implementation of these algorithms are shared that are necessary for a successful application of the latter. It is shown that model information, e.g. known input gains or a simple model of an electromagnet, can be utilised not only to increase the accuracy of the algorithms, but also to simplify the tuning. In addition to the systematic analysis, a model-based approach is designed in such a way that the results of both the MFC and the model-based control (MBC) are comparable. Several experiments on a test bed depicted in Fig. 1 are conducted showing the capabilities of the MFC in different scenarios, such as trajectory tracking and robustness to sensor and actuator faults.

The present paper is organised as follows. In Section 2 the system under consideration is introduced and a mathematical model is provided. A model-based tracking controller, the MFCs using different inputs as well as information concerning the implementation of the latter are discussed in Section 3. In Section 4 experimental results on the test bed are presented and details for the parametrisation of the algorithms are provided.

2. Magnetically supported plate: problem statement and modelling

The test bed considered, depicted in Fig. 1, consists of a 10 mm thick, rectangular aluminium plate with four laminated iron packs at each corner. These packs are acting as the yokes of four electromagnets mounted at a rigid frame above the plate. The electromagnets generate four forces that can lift the plate, as depicted in the schematic drawing in Fig. 2. Four inductive sensors are available to measure the distances denoted by $y_j, j \in \{1,2,3,4\}$, between the plate and the outer frame. This system has already been considered in Kiltz et al. (2014, 2012). Due to its simple construction this setup could be relatively easily rebuilt by other groups for use in educational labs.

2.1. Model of the plate

The plate, as shown in the schematic drawing in Fig. 2, is modelled as a rigid body that can only perform translational motions in the z_0 direction of the space-fixed coordinate system C_0 and tilt around the

Fig. 1. Photo of the considered test bed. The aluminium plate is hovering with an air gap of 5 mm.

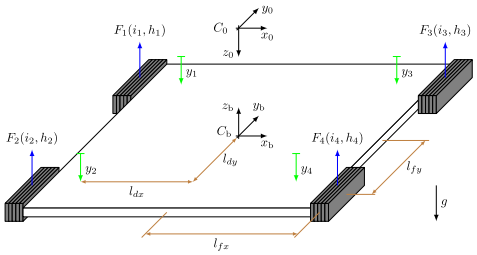

Fig. 2. Schematic drawing of the plate with the body fixed frame C_b and reference frame C_0.

x_b- and y_b-axes of the body-fixed coordinate system C_b, located in the centre of mass of the plate. Thus, motions in any other direction are neglected. Due to the limited air gaps $h_j, j \in \{1,2,3,4\}$, possible tilt angles are small, resulting in the assumption that the forces $F_j, j \in \{1,2,3,4\}$ of the magnets are acting at the centre of each yoke as depicted in Fig. 2. Each force $F_j, j \in \{1,2,3,4\}$ is generated by an electric current denoted by $i_j, j \in \{1,2,3,4\}$. However, the dynamics of the magnetic fields are neglected, because of the lamination of the magnets as well as the current controllers incorporated in the industrial hardware.

Using the latter considerations, the motion of the plate in the remaining three degrees of freedom can be modelled by

$$\boldsymbol{B}\boldsymbol{f} = m\boldsymbol{g} + \boldsymbol{P}(\ddot{\boldsymbol{y}} - \boldsymbol{\eta}) \tag{1}$$

with

$$\boldsymbol{B} = \begin{pmatrix} 1 & 1 & 1 & 1 \\ 1 & -1 & 1 & -1 \\ 1 & 1 & -1 & -1 \end{pmatrix}, \quad \boldsymbol{P} = \begin{pmatrix} 0 & -\frac{m}{2} & -\frac{m}{2} \\ -\frac{k_1}{2} & \frac{k_1}{2} & 0 \\ -\frac{k_2}{2} & 0 & \frac{k_2}{2} \end{pmatrix},$$

$\boldsymbol{f} = (F_1, F_2, F_3, F_4)^{\mathrm{T}}$, $\boldsymbol{y} = (y_1, y_2, y_3)^{\mathrm{T}}$, $\boldsymbol{g} = (g, 0, 0)^{\mathrm{T}}$, and the parameters $k_1 = \frac{J_x}{l_{dy} l_{fy}}$ and $k_2 = \frac{J_y}{l_{dx} l_{fx}}$. The mass of the plate is denoted by m, the gravitational acceleration by g, J_x and J_y are describing the moments of inertia with respect to the x_b- and y_b-axes respectively. As depicted in Fig. 2, the distances from the centre of the plate to the sensors and the forces are denoted by l_{dx} and l_{dy} as well as l_{fx} and l_{fy}, respectively. Unmodelled system dynamics and disturbances are summarised in the variable $\boldsymbol{\eta}$.

As usual, the forces generated by the magnets are modelled as

$$F_j = \frac{i_j^2}{d_j^2(h_j)}, \quad j \in \{1,2,3,4\}, \tag{2}$$

with functions $d_j : \mathbb{R} \to \mathbb{R}$ depending on the air gaps $h_j, j \in \{1,2,3,4\}$. These functions can be determined in a parameter identification with an appropriate ansatz. In the following, the air gaps $h_j, j \in \{1,2,3,4\}$, have to be calculated using the available measurements. The easiest way of doing so is to use the assumption that the aluminium plate is a rigid body. Then it can be mathematically described by a plane defined by

$$\boldsymbol{r}^0 = \boldsymbol{r}_1^0 + a(\boldsymbol{r}_3^0 - \boldsymbol{r}_1^0) + b(\boldsymbol{r}_2^0 - \boldsymbol{r}_1^0) \tag{3}$$

in the reference frame C_0 with the sensor locations $\boldsymbol{r}_1^0 = (-l_{dx}, l_{dy}, y_1)^{\mathrm{T}}$, $\boldsymbol{r}_2^0 = (-l_{dx}, -l_{dy}, y_2)^{\mathrm{T}}$, and $\boldsymbol{r}_3^0 = (l_{dx}, l_{dy}, y_3)^{\mathrm{T}}$, whereas the parameters a and b depend on the point of interest on the plane. With this, only three of the four sensor values have to be used. Now, (3) can be used to calculate the midpoint of the yokes, where the forces of the magnets are acting on, and with this the needed air gaps. This yields

$$\begin{pmatrix} h_1 \\ h_2 \\ h_3 \\ h_4 \end{pmatrix} = \frac{1}{2} \begin{pmatrix} k_x + k_y & 1 - k_y & 1 - k_x \\ k_x - k_y & 1 + k_y & 1 - k_x \\ -k_x + k_y & 1 - k_y & 1 + k_x \\ -k_x - k_y & 1 + k_y & 1 + k_x \end{pmatrix} \begin{pmatrix} y_1 \\ y_2 \\ y_3 \end{pmatrix} = K\boldsymbol{y}, \tag{4}$$

with $k_x = \frac{l_{fx}}{l_{dx}}$ and $k_y = \frac{l_{fy}}{l_{dy}}$, which maps the sensor values to the air gaps.

Remark 1. The term $\boldsymbol{\eta}$ describes several hard to model dynamics and disturbances. These have various origins, such as errors within the magnetic force model stemming from inaccuracies in the functions $d_j : \mathbb{R} \to \mathbb{R}, j \in \{1,2,3,4\}$, unmodelled hysteresis and magnetic saturation, temperature dependencies within the coils, effects originating from magnetic field dynamics, and magnetic flux leakage. Additionally, high-frequency oscillations occur due to plate vibrations, as the real plate deviates from the assumed rigid body model.

Remark 2. Using a different combination of three sensor values would be possible, e.g. y_2, y_3, and y_4. In this case, Eq. (3) has to be adjusted, resulting in a different matrix relating $\boldsymbol{h}$ and $(y_2, y_3, y_4)^{\mathrm{T}}$. A possible method of using four sensors is to calculate the centre of gravity of the plate, where the coordinate system C_{b} is located, as the mean value of all measurements. The tilt angles around the x_{b}- and y_{b}-axes can be calculated afterwards using again only three sensor values, and with this all informations to determine the air gaps are provided. An other possibility is to use the redundancy of the sensors for fault detection. For the sake of simplicity, only the suggested choice is considered in the sequel.

3. Control design

In the following section, a MBC approach is presented in addition to several MFC algorithms, which differ in the choice of the input. This choice is based on different degrees of model information used to determine a feedback law.

3.1. Model-based control

The MBC of the plate is based on (1), which can be rewritten as

$$\begin{aligned} \ddot{\boldsymbol{y}} &= P^{-1}(B\boldsymbol{f} - m\boldsymbol{g}) + \boldsymbol{\eta} \\ &= \boldsymbol{v} + g\begin{pmatrix} 1 & 1 & 1 \end{pmatrix}^{\mathrm{T}} + \boldsymbol{\eta}, \end{aligned} \tag{5}$$

with the new input $\boldsymbol{v} = P^{-1}B\boldsymbol{f}$. The latter system of differential equations can also be written as three independent scalar equations

$$\ddot{y}_k = v_k + g + \eta_k, \quad k \in \{1,2,3\}. \tag{6}$$

Hereafter, the index k will be omitted, due to the similarity of the equations. Based on (6) a stabilising feedback law

$$v = \ddot{y}_{\mathrm{r}} - c_{\mathrm{D}}\dot{e} - c_{\mathrm{P}}e - g - \eta, \quad e = y - y_{\mathrm{r}}, \tag{7}$$

can be calculated to track a sufficiently smooth reference trajectory $t \mapsto y_{\mathrm{r}}(t)$. Using the control law (7) on system (6) leads to the differential equation of the error

$$\ddot{e} + c_{\mathrm{D}}\dot{e} + c_{\mathrm{P}}e = 0. \tag{8}$$

The controller parameters c_{P} and c_{D} are chosen positive, which results in a stable closed-loop behaviour. This approach can be interpreted as a typical flatness-based controller as discussed e.g. in Rudolph (2021).

Since the velocity $\dot{y}$ and the acceleration η required in the feedback law (7) are not measured, an observer is designed, based on the assumption of a piecewise constant disturbance η, which means $\dot{\eta} = 0$ on intervals. To this end, the state representation of (6) can be introduced as

$$\dot{\boldsymbol{x}} = \begin{pmatrix} 0 & 1 & 0 \\ 0 & 0 & 1 \\ 0 & 0 & 0 \end{pmatrix} \boldsymbol{x} + \begin{pmatrix} 0 \\ 1 \\ 0 \end{pmatrix} (v + g) = A\boldsymbol{x} + \boldsymbol{b}(v + g) \tag{9a}$$

$$y = \begin{pmatrix} 1 & 0 & 0 \end{pmatrix} \boldsymbol{x} = \boldsymbol{c}^{\mathrm{T}}\boldsymbol{x} \tag{9b}$$

with the input v and the tuple $\boldsymbol{x} = (y, \dot{y}, \eta)^{\mathrm{T}}$. Discontinuities of η correspond to resetting initial conditions. Based on (9) a simple linear disturbance observer

$$\dot{\hat{\boldsymbol{x}}} = A\hat{\boldsymbol{x}} + \boldsymbol{b}(v + g) + \boldsymbol{l}\left(y - \boldsymbol{c}^{\mathrm{T}}\hat{\boldsymbol{x}}\right) \tag{10}$$

with $\hat{\boldsymbol{x}}(0) = \hat{\boldsymbol{x}}_0 \in \mathbb{R}^3$ provides an estimate $\hat{\boldsymbol{x}}$ of the tuple $\boldsymbol{x}$. The observer gains $\boldsymbol{l} = (l_1, l_2, l_3)$ are chosen such that $A - \boldsymbol{l}\boldsymbol{c}^{\mathrm{T}}$ is Hurwitz. With this choice the error $\tilde{\boldsymbol{x}} = \boldsymbol{x} - \hat{\boldsymbol{x}}$ exponentially converges to zero. Using the feedback law (7) in combination with the observer (10) the accelerations $\boldsymbol{v}$ can be calculated.

The next step is to exploit the relation $\boldsymbol{v} = P^{-1}B\boldsymbol{f}$ from (5) to derive desired forces $\boldsymbol{f}_{\mathrm{d}}$ that can be realised using the electric currents. Due to the redundancy stemming from the over-actuation of the system, a choice has to be made. One approach is to use the Moore–Penrose pseudo inverse $B^{\dagger} = B^{\mathrm{T}}(BB^{\mathrm{T}})^{-1}$ of B to calculate

$$\boldsymbol{f}_{\mathrm{d}} = B^{\dagger}P\boldsymbol{v} = \frac{1}{4} \begin{pmatrix} \frac{-k_1-k_2}{2} & \frac{-m+k_1}{2} & \frac{-m+k_2}{2} \\ \frac{k_1-k_2}{2} & \frac{-m-k_1}{2} & \frac{-m+k_2}{2} \\ \frac{-k_1+k_2}{2} & \frac{-m+k_1}{2} & \frac{-m-k_2}{2} \\ \frac{k_1+k_2}{2} & \frac{-m-k_1}{2} & \frac{-m-k_2}{2} \end{pmatrix} \boldsymbol{v} = V\boldsymbol{v} \tag{11}$$

that distributes the input $\boldsymbol{v}$ evenly to the four desired forces $F_{\mathrm{d},j}, j \in \{1,2,3,4\}$, which is beneficial especially if an abrupt actuator fault occurs, as discussed in Section 4.4.1.

Remark 3. Using the Moore–Penrose pseudo inverse is equivalent to minimising the mean variation $\sum_{i=1}^{4}\left(F_{\mathrm{d},i} - \frac{1}{4}\sum_{j=1}^{4}F_{\mathrm{d},j}\right)^2$ as suggested in Kiltz et al. (2012).

Solving (2) for the current yields

$$i_{\mathrm{d},j} = \sqrt{F_{\mathrm{d},j}}\, d_j(h_j), \quad j \in \{1,2,3,4\}, \tag{12}$$

which can be used together with (4) to generate the reference for the underlying current controller.

3.2. Model-free control

In the following, various MFC approaches are presented, gradually reducing from one subsection to the next the amount of physically motivated model knowledge. For each controller three decoupled systems with identical structure are considered and the corresponding index will again be dropped when appropriate.

3.2.1. Acceleration as input

Hereafter, the input v is used just as it has been done in the design of the MBC law in (7). Each of the decoupled subsystems is described by

$$\ddot{y} = \gamma_v v + f_v, \quad \gamma_v > 0, \tag{13}$$

where $t \mapsto f_v(t)$ is a bounded unknown square-integrable function representing unmodelled dynamics as well as other disturbances. Comparing (13) and (6) yields $f_v = \eta + g$ and suggests the choice $\gamma_v = 1$. This means that f_v has a physical meaning as opposed to a similar case study discussed in Remark 3 of Scherer et al. (2023).

Remark 4. Comparing (13) and (6) suggests to use $\gamma_v = 1$. Nevertheless, a different choice of the input gain γ_v is possible (see Fig. 8).

Based on (13), the control input v is chosen as

$$v = \frac{1}{\gamma_v}\left(\ddot{y}_\mathrm{r} - k_\mathrm{p} e - k_\mathrm{d}\dot{e} - \hat{f}_v\right) \tag{14}$$

with $k_\mathrm{p}, k_\mathrm{d} > 0$, and estimates $\hat{f}_v$ and $\hat{\dot{y}}$ of f_v and $\dot{y}$, respectively, the calculation of which will be discussed in Section 3.3. Under the assumption that $\hat{f}_v \approx f_v$, using (14) with the model (13) leads to the differential equation

$$\ddot{e} + k_\mathrm{d}\dot{e} + k_\mathrm{p} e = 0,$$

which has the same structure as (8).

The controller (14) can then be used together with (4), (11) and (12) to calculate the desired forces and currents, respectively. An advantage of this implementation is that there is no need for a model-based observer to estimate the derivative $\dot{y}$ and the disturbance f_v. Instead, with the algebraic differentiators presented in Appendix A, an approach that is solely based on the measured signal y is used.

Remark 5. This combination of MBC and MFC is also suggested in Villagra and Herrero-Pérez (2012). Therein the MFC is combined with a nonlinear flatness-based control.

3.2.2. Magnetic force as input

Instead of choosing the acceleration v as an input, it is possible to directly calculate the magnetic forces $\tilde{F}_k, k \in \{1,2,3\}$. Based on this consideration, the model (5) can be written as

$$\ddot{y}_k = -\rho F_k - \varpi_k(F_{\neq k}) + g + \eta_k, \tag{15}$$

with $F_{\neq k} = \{F_1, F_2, F_3, F_4\}\backslash\{F_k\}$, where $\varpi_k(F_{\neq k})$ is a weighted sum of the different magnetic forces acting on the plate and the parameter $\rho = 1/k_1 + 1/k_2 + 1/m$ resulting from $P^{-1}B$. The structure of (15) leads to ultra-local models

$$\ddot{y}_k = f_{\tilde{F},k} - \gamma_{\tilde{F}}\tilde{F}_k, \quad \gamma_{\tilde{F}} > 0, \tag{16}$$

with $\gamma_{\tilde{F}} = \rho$ and the unknown parts are $f_{\tilde{F},k} = \varpi_k(F_{\neq k}) + g + \eta_k$. With (15) in mind, (16) can be interpreted as a model of three implicitly coupled point masses.

Remark 6. As an alternative to the considerations based on the model (5), assuming that there is no unknown part $f_{\tilde{F}}$, the model (16) would be $\ddot{y} = -\gamma_{\tilde{F}}\tilde{F}$. The force $\tilde{F}$ and the parameter $\gamma_{\tilde{F}}$ are assumed to be always positive, which means that if the force is increased the acceleration $\ddot{y}$ is negative and the resulting position y will decrease. This matches the physical behaviour, because the air gap of the magnet is getting smaller if the force is increased and the magnet pulls the plate towards the rigid outer frame.

A controller that directly commands the forces is

$$\tilde{F} = \frac{1}{\gamma_{\tilde{F}}}\left(-\ddot{y}_\mathrm{r} + k_\mathrm{p} e + k_\mathrm{d}\dot{e} + \hat{f}_{\tilde{F}}\right), \tag{17}$$

where the estimate $t \mapsto \hat{f}_{\tilde{F}}(t)$ is derived according to (24) by substituting v with $\tilde{F}$.

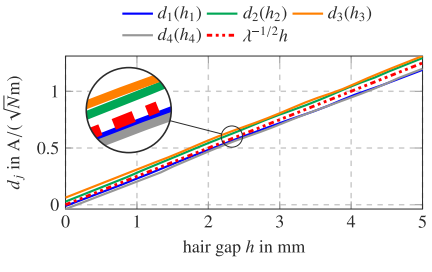

Fig. 3. Graphical representation of the identified functions $d_j(h_j), j \in \{1,2,3,4\}$ and the approximation with the parameter λ used to further simplify the design of the MFC approach.

Again, the remaining degree of freedom, caused by the over-actuation of the system, has to be considered. The transformation resulting from the pseudo inverse is not a valid solution for this. To see this, assuming the plate hovers horizontally with a constant distance to the frame. Then, the available forces have to compensate the gravitational forces and are approximately equal to $\tilde{F}_k \approx \bar{F} > 0, k \in \{1,2,3\}$. In this case, the last row of the pseudo inverse reads $F_{\mathrm{d},4} = \frac{1}{4}(\tilde{F}_1 - \tilde{F}_2 - \tilde{F}_3) = -\frac{1}{4}\bar{F}$, which cannot be realised on the test bed because the magnetic forces $F_j, j \in \{1,2,3,4\}$ are restricted to positive values. Instead of directly coupling all forces, one can use $F_{\mathrm{d},k} = \tilde{F}_k, k \in \{1,2,3\}$ and get the remaining force as

$$F_{\mathrm{d},4} = \sum_{k=1}^{3} a_k \tilde{F}_k, \tag{18}$$

with $\sum_{k=1}^{3} a_k = 1$ and $a_k \geq 0$. Thereafter, (4) and (12) can again be used to calculate the desired electrical currents.

3.2.3. New input $u = (i/h)^2$

To further simplify the design of the MFC, the functions $d_j : \mathbb{R} \to \mathbb{R}$ in (2) can be approximated with $d_j \approx \lambda^{-1/2} h_j, j \in \{1,2,3,4\}, \lambda > 0$, as depicted in Fig. 3, which results in

$$F \approx \lambda\left(\frac{i}{h}\right)^2 = \lambda u.$$

Considering this relation, the quantity $u = (i/h)^2$ is chosen as a new input and can be interpreted as a special case of the considerations from Section 3.2.2.

Thus, according to the model (16) it follows that

$$\ddot{y} = f_u - \gamma_u u,$$

with $\gamma_u = \lambda\gamma_{\tilde{F}}$. The control input u can be derived using (17) and by substituting $\tilde{F}$ and $\gamma_{\tilde{F}}$ with u and γ_u, respectively, which yields

$$u = \frac{1}{\gamma_u}\left(-\ddot{y}_\mathrm{r} + k_\mathrm{p} e + k_\mathrm{d}\dot{e} + \hat{f}_u\right). \tag{19}$$

As described in Section 3.2.2 the estimation of f_u is realised according to (24) by substituting v with u. Similar to (18) the remaining input u_4 can be calculated. Finally, using $i_{\mathrm{d},j} = \sqrt{u_j} h_j, j \in \{1,2,3,4\}$ together with (4), the desired currents for the underlying current controller are obtained.

Remark 7. From an engineering perspective the input u is a reasonable choice if no identified model of the force (2) is available. From a physical understanding of the system it is known that the force of the magnets is approximately proportional to $(i/h)^2$.

3.2.4. Current as input

Using even less model information, the equation

$$\ddot{y} = f_i - \gamma_i(y)i \tag{20}$$

can be assumed to describe the system. In this case, however, the input gain

$$\gamma_i(y) = \frac{\gamma_{i,0}}{y}$$

is a function of the position, with $\gamma_{i,0} > 0$, obviously inspired by the input u from Section 3.2.3. For the implementation of this gain the singularity of γ_i is not an issue, because of a safety routine that limits the air gaps $h_j, j \in \{1,2,3,4\}$ to a minimum of 0.8 mm. The MFC law can be derived as

$$i = \frac{1}{\gamma_i(y)}\left(-\ddot{y}_\mathrm{r} + k_\mathrm{p}e + k_\mathrm{d}\dot{e} + \hat{f}_i\right), \tag{21}$$

and again the estimation of f_i is realised by substituting v with i in (24). The additional input can be derived as in (18).

Remark 8. Choosing a constant input gain in (20) works in simulation, but it was not leading to a stable closed-loop behaviour on the test bed.

3.3. Implementation of the MFC algorithms

In the following section, details about the implementation of the MFC are shared. For additional information about the algebraic differentiators used in the implementation of the proposed algorithms, the interested reader is referred to Appendix A and the references therein.

3.3.1. Estimation of the disturbance f

The proposed MFC algorithms, i.e. (14), (17), (19) and (21), are designed for continuos-time systems. Nevertheless, for a discrete-time realisation of the control algorithms, a evaluation at equidistant time instants is needed. In the following the MFC law (14) will be considered as an example, but all remarks can be applied to the other approaches in a similar way.

Estimation of f_v can be done with

$$\hat{f}_v(t) = \frac{5!}{2T^5}\int_{t-T-\varepsilon}^{t-\varepsilon}\left(T^2 - 6T\sigma + 6\sigma^2\right)y(\tau) - \frac{\gamma_v}{2}\sigma^2(T-\sigma)^2 v(\tau)\mathrm{d}\tau, \tag{22}$$

where $\sigma = t - \tau - \varepsilon$ and $\varepsilon > 0$, which is based on algebraic considerations and commonly used in the literature, e.g. Bekcheva et al. (2018) or Barth et al. (2020). In Appendix B it is shown that (22) can be interpreted as

$$\hat{f}_v(t) = \int_{t-T-\varepsilon}^{t-\varepsilon} \ddot{g}_{0,T,\vartheta}^{(2,2)}(t-\tau-\varepsilon)y(\tau) - \gamma_v g_{0,T,\vartheta}^{(2,2)}(t-\tau-\varepsilon)v(\tau)\mathrm{d}\tau. \tag{23}$$

In the latter $g_{0,T,\vartheta}^{(2,2)}$ denotes an algebraic differentiator as first developed in Mboup et al. (2009), using here the notation from Othmane et al. (2022) with the parameters $\alpha = \beta = 2$ and $N = 0$. With these considerations, (23) can thus be generalised to

$$\hat{f}_v(t) = \int_{t-T-\varepsilon}^{t-\varepsilon} g(t-\tau-\varepsilon)f(\tau)\mathrm{d}\tau, \tag{24a}$$

$$= \int_{t-T-\varepsilon}^{t-\varepsilon} \ddot{g}(t-\tau-\varepsilon)y(\tau) - \gamma_v g(t-\tau-\varepsilon)v(\tau)\mathrm{d}\tau, \tag{24b}$$

where $g = g_{N,T,\vartheta}^{(\alpha,\beta)}$ is the algebraic differentiator with parameters as discussed in Appendix A. As seen in Section 4, in some cases this generalisation is needed to realise the MFC.

The convolution integrals in (24b) have to be approximated using a suitable quadrature method. The open-source toolbox AlgDiff (see Othmane, 2022) provides all necessary features for the design and analysis as well as the discretisation of algebraic differentiators used for the estimation of f_v and the time derivatives of y. The tutorial Othmane and Rudolph (2023) offers an introduction with examples to the toolbox and the systematic parametrisation of these differentiators.

As discussed in Scherer et al. (2023), the formulation in (24b) can be derived by integrating (24a) by parts using (13). Again (24b) can be implemented, because it depends on quantities known in the interval $[t-T-\varepsilon, t-\varepsilon]$ only.

In the following, the time window of length T is an integral multiple of the sampling time t_s, i.e. $T = n_\mathrm{s}t_\mathrm{s}$ and the parameter ε in (24) is chosen to be equal to t_s. The abbreviation $v[k] = v(kt_\mathrm{s}), k \in \mathbb{N}$ is used for v evaluated at the time kt_s. With this abuse of notation, (14) yields in a discrete-time setting

$$v[k] = \frac{1}{\gamma_v}\left(\ddot{y}_\mathrm{r}[k] - k_\mathrm{p}\hat{e}[k] - k_\mathrm{d}\dot{\hat{e}}[k] - \hat{f}_v[k]\right) \tag{25}$$

with $\hat{e}^{(n)}[k] = \hat{y}^{(n)}[k] - y_\mathrm{r}^{(n)}[k], n \in \{0,1\}$. Applying the mid-point rule, $\hat{f}_v$ and the estimates of the derivatives $y^{(n)}, n \in \{0,1\}$ can be computed as

$$\hat{f}_v[k] = \frac{1}{\Phi_2}\sum_{j=0}^{L-1} w_2[j]y[k-j-1] - \frac{\gamma_v}{\Phi_0}\sum_{j=0}^{L-1} w_0[j]v[k-j-1]$$

$$\hat{y}^{(n)}[k] = \frac{1}{\Phi_n}\sum_{j=0}^{L-1} w_n[j]y[k-j],$$

with $\Phi_n = \frac{t_\mathrm{s}^n}{n!}\sum_{j=0}^{L-1} w_n[j](-j)^n$, $w_n[j] = t_\mathrm{s}g^{(n)}[j+1/2]$, $n \in \{0,1\}$, and $L = n_\mathrm{s}$.

4. Experimental results

The following, experiments are carried out on the test bed depicted in Fig. 1. Four inductive sensors manufactured by Intronik GmbH are measuring the distance between the rigid outer frame and the 4.69 kg weighing aluminium plate. For safety reasons, the air gaps $h_j, j \in \{1,2,3,4\}$ of the magnets are limited to $0.8 - 5.5$ mm and the currents to $0 - 8$ A. The real-time hardware used is a GIN-SAM3 from Indel. The proposed algorithms are executed with a sampling rate of $f_\mathrm{s} = 1/t_\mathrm{s} = 32$ kHz. The power electronics are included in a GIN-SAC3x3 also from Indel.

4.1. Parameters of algebraic differentiators and MFC

The algebraic differentiators used depend on the design parameters α, β, N, and ω_c that have to be chosen in such a way that the accuracy of the resulting approximation as well as the rejection of measurement noise are high and the error stemming from the delay δ_t is as small as possible (see Appendix A for more information about the algebraic differentiators used). To achieve a high noise rejection the parameters α and β are chosen equal (see Othmane et al., 2022, Sec. 4 and Mboup & Riachy, 2018). Additionally the parameter N describing an N-th order truncated generalised Fourier expansion is set to zero, thus, resulting in an estimation delay of $\delta_t = T/2$.

With these choices, several experiments are made using different parameter combinations for $\alpha = \beta \in \{2,3,\dots,8\}$ and $\omega_\mathrm{c} \in \{540, 640, \dots, 1440\}$ rad/s. The MFC from (14) is implemented with the parameters $k_\mathrm{p} = 5000\,\mathrm{s}^{-2}$, $k_\mathrm{d} = 195\,\mathrm{s}^{-1}$ and $\gamma_v = 1$. At the beginning, the plate rests on four screws at a distance of approximately 5.5 mm and individual polynomial reference trajectories $t \mapsto y_{\mathrm{r},k}(t), k \in \{1,2,3\}$ of degree 5 are planned, connecting the rest position with a vertical position at 2 mm and a transition time of 2 s. If the algorithm can lift and afterwards stabilise the plate, the experiment will continue, otherwise it is aborted. Thereafter, a set point transition from 2 mm to 5 mm and back again to 2 mm with polynomial trajectories of degree 5 are calculated, having a transition time of 0.5 s as well as a holding time of 0.2 s (see Fig. 11 for a visualisation of the reference trajectory).

For this set point change, the root mean square (RMS) of the delayed errors $\hat{e}_k = \hat{y}_k - y_{\mathrm{r},k}, k \in \{1,2,3\}$, is calculated and used as a quality gauge of the resulting parametrisation. Fig. 4 shows the variation of the RMS values of the errors for different combinations of the parameters $\alpha = \beta$ and ω_c. The experiments show that the RMS values are

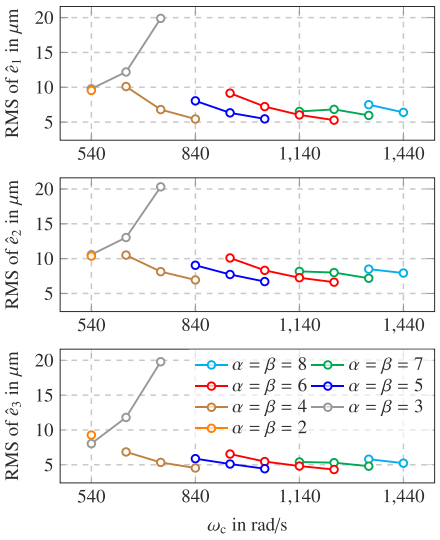

Fig. 4. Evaluating the RMS values of the delayed error $\hat{e}_k, k \in \{1,2,3\}$ for varying parameter combinations of ω_c and $\alpha = \beta$ for the algebraic differentiators.

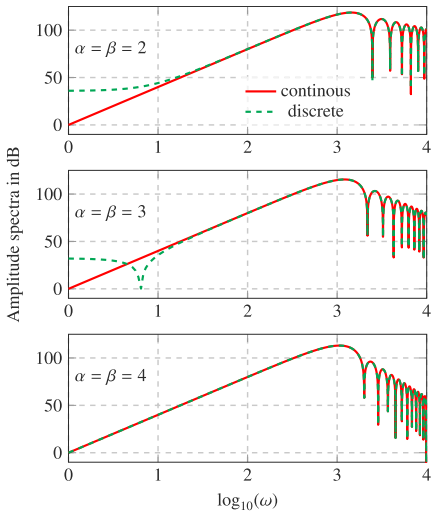

Fig. 5. Comparison of the amplitude spectra of the continuous-time and discrete-time differentiators used for the approximation of a second order derivative for different $\alpha = \beta$ and $\omega_c = 840\,\text{rad/s}$. The mid-point rule is considered in the discretisation, the corresponding error of which is dominant for $\alpha = \beta \in \{2,3\}$, resulting in a bad estimation of the second order derivative of $y_k, k \in \{1,2,3\}$.

Table 1
Comparison of the cost function values J_2 for $\omega_c = 840\,\text{rad/s}$ and varying $\alpha = \beta$ with the discretisation methods used.

Method	$\alpha = \beta = 2$	$\alpha = \beta = 3$	$\alpha = \beta = 4$
mid-point	−67.1 dB	−130.6 dB	−222.1 dB
trapezoidal	−56.5 dB	−120.7 dB	−220.7 dB
Simpson's rule	−22.5 dB	−33.4 dB	−31.2 dB

significantly larger for $\alpha = \beta \in \{2,3\}$ compared to the results of the experiments for $\alpha = \beta > 3$. This confirms the general choice of the formulation with algebraic differentiators in e.g. (14) compared to the restriction to $\alpha = \beta = 2$ as discussed in Appendix B, at least for the current application. The large discretisation error is the reason for the results from Fig. 4, which can be seen in Fig. 5, where the amplitude spectra of the continuous-time and discrete-time differentiators used for the approximation of a second order derivative are depicted for the choice $\omega_c = 840\,\text{rad/s}$, $N = 0$, and varying $\alpha = \beta$. The differentiator has been discretised using the mid-point rule. Specifically, for very low frequencies compared to ω_c the estimation of $\ddot{y}$ is bad, resulting in an inaccurate estimation and compensation of f_v in the controller. Using the cost function J_n introduced in Kiltz (2017, Sec. 3.4.2) and discussed in Othmane et al. (2022), as a measure for the discretisation reveals that for values above -200 dB the discretisation error is unacceptable. In Table 1 results obtained using the mid-point rule, the trapezoidal rule and Simpson's rule for the discretisation are compared. The comparison shows that the trapezoidal rule or Simpson's rule result in even higher values for J_n. Therefore, the mid-point rule is used in the sequel. In addition, using the latter, fewer filter parameters have to be stored and fewer calculations have to be done as discussed in Kiltz (2017, Sec. 3.4.2) or Othmane, Rudolph, and Mounier (2021, Sec. 3.3).

Remark 9. The plate has a dominant mechanical resonance frequency at approximately 942 rad/s, which causes instability of the closed loop if not suppressed correctly. Choosing $N = 0$ and $\alpha = \beta$, the amplitude spectrum of the algebraic differentiator shows a distinct stopband ripple, as depicted in Fig. 5. In this case, the transfer function has zeros which correspond to those of the Bessel function of the first kind and order $\alpha + 1/2$ as mentioned in Kiltz and Rudolph (2013) or Kiltz (2017, Sec. 3.3.3). Because of the sampling in combination with the logarithmic scale of the plot these zeros are not correctly displayed in Fig. 5. Nevertheless, this property can be used to design filters that have the same effect as a notch filter. Unfortunately, in this case, it is not suitable to use this effect for the dominant mechanical resonance frequency. The reason for this is the large window length T resulting in a computational burden that is too high for the computational capabilities of the hardware used. Therefore, a conventional notch filter will later be used to suppress this frequency.

The available computation time of the real-time hardware used is limited. Therefore, some parameter combinations, e.g. $\omega_c = 540\,\text{rad/s}$ and $\alpha = \beta = 8$, required large filter window lengths which are not realisable since the computation time becomes too large. The parameter range covered is depicted in Fig. 6 . Green and red squares are marking the parameter combinations resulting in a stable and unstable closed-loop behaviour, respectively. Parameter combinations marked with a black square are unrealisable with the hardware used. It is noticeable that Fig. 6 shows some kind of pattern for a stable and realisable combination. Nevertheless, the discretisation error is not the reason for this pattern, because it mainly effects combinations with $\alpha = \beta \in \{2,3\}$. The origin of this phenomenon is still up to further investigation.

For the following experiments, the parametrisation $\alpha = \beta = 4$ and $\omega_c = 840\,\text{rad/s}$ is chosen, because according to Fig. 4, this combination has resulted in the smallest RMS values.

With γ_v, k_p, and k_d, the MFC law (14) has three parameters that have to be chosen. As discussed in Remark 4, the model (6) suggests $\gamma_v = 1$, which leaves only two parameters to vary. Fig. 7 shows a parameter sweep in the k_p-k_d-plane carried out on the test bed. Every mark represents a unique parameter combination and an experiment that was made. The maximal currents as well as the RMS values in

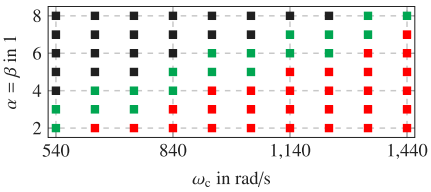

Fig. 6. Visualisation of the different parameters $\omega_c \in \{540, 640, \ldots, 1440\}$ rad/s and $\alpha = \beta \in \{2, 3, \ldots, 8\}$ for the algebraic differentiators covered. Green and red squares are marking the parameter combinations resulting in a stable and unstable closed-loop behaviour, respectively. Parameter combinations marked with a black square are unrealisable with the hardware used. (For interpretation of the references to colour in this figure legend, the reader is referred to the web version of this article.)

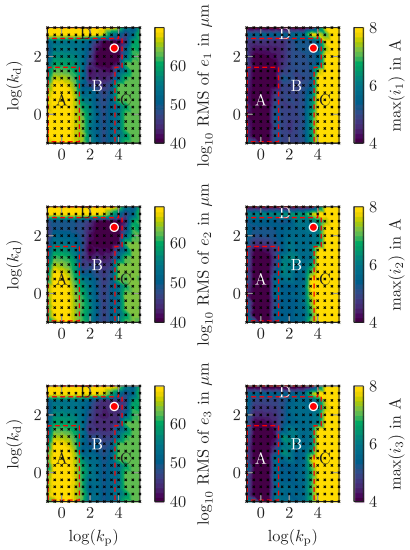

Fig. 7. Results of the parameter sweep of the MFC from (14) with $\gamma_v = 1$, to determine stable tracking behaviour. The red dot marks the parameter combination $k_p = 5000\,\mathrm{s}^{-2}$ and $k_d = 195\,\mathrm{s}^{-1}$ used for further experiments. (For interpretation of the references to colour in this figure legend, the reader is referred to the web version of this article.)

dB of each error $e_k, k \in \{1, 2, 3\}$ are shown. In the region marked with A the RMS values are high and the maximal current is not exceeding 4.2 A, which is not enough to even lift the plate, whereas region C shows the maximum current of 8 A and also high RMS values. For parameter combinations in this region the feedback is not resulting in a stable closed-loop behaviour. Between these two areas, in the region marked with B, the combinations result in low error values and a medium current. There, the closed loop is stable and a local optimum of the RMS values can be found. For the experiments in region D, the maximal current is low but the RMS values are high. This is because the aforementioned safety routine has been activated and the experiment was aborted. In this region the MFC cannot achieve a stable closed loop.

For further experiments the choice $k_p = 5000\,\mathrm{s}^{-2}$ and $k_d = 195\,\mathrm{s}^{-1}$ is made, because according to Fig. 7 (see the red dot) this combination is near a minimum of all three RMS values.

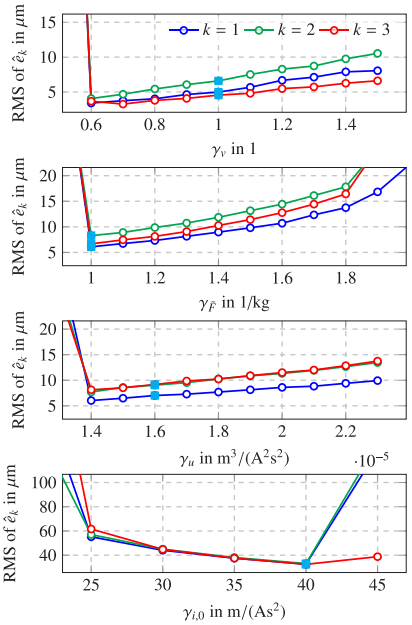

Fig. 8. Parameter sweep of the input gains γ_v, $\gamma_{\bar{F}}$, γ_u and γ_i with fixed $k_p = 5000\,\mathrm{s}^{-2}$ and $k_d = 195\,\mathrm{s}^{-1}$ to validate the suggestions made by the mathematical model (1). The blue square is marking the parameter used for further experiments. (For interpretation of the references to colour in this figure legend, the reader is referred to the web version of this article.)

Based on the model (1) and (2), several choices for the input gains $\gamma_j, j \in \{v, \bar{F}, u, i\}$ have been discussed in Section 3. Therefore, the proposed algorithms are verified by performing experiments using various parameter combinations. Fig. 8 shows that with a value of $\gamma_v = 0.6$ the lowest RMS value could be obtained. Nevertheless, $\gamma_v = 1$ is chosen to compare the results with the MBC algorithm. A value of 0.5 is resulting in an unstable closed loop. This shows that the choice of the input gain has also an influence on the stability of the MFC. According to (15) and the model parameters summarised in Table 2, $\gamma_{\bar{F}} = 0.84\,\mathrm{kg}^{-1}$ is a suitable choice. Unfortunately, this combination is resulting in an unstable closed-loop behaviour on the test bed. This observation might point to model errors. For that reason, $\gamma_{\bar{F}} = 1\,\mathrm{kg}^{-1}$. As explained in Section 3.2.3, with the choice of $\gamma_{\bar{F}} = 1\,\mathrm{kg}^{-1}$ and the parameter $\lambda^{-1/2} = 250\,\mathrm{As}/(\mathrm{kgm}^3)^{\frac{1}{2}}$ stemming from the identification of the force model, $\gamma_u = 1.6^{-5}\ \mathrm{m}^3/(\mathrm{A}^2\mathrm{s}^2)$. Again Fig. 8 shows that with a value of $1.4^{-5}\ \mathrm{m}^3/(\mathrm{A}^2\mathrm{s}^2)$ a better result can be obtained, but for the sake of comparison this value is not chosen. For the MFC law (21) the input gain is set to $\gamma_{i,0} = 40\,\mathrm{m}/(\mathrm{As}^2)$. This choice is made only according to Fig. 8, because no model information can be used in this case.

For the MFC algorithms (17), (19), and (21) the free parameter is set to $F_{d,4} = \frac{1}{2}(\bar{F}_2 + \bar{F}_3)$ and similarly for u and i.

4.2. Implementation of the MBC

The goal of the following section is to tune the MBC in such a way that it is suitable for a fair comparison with the proposed MFC

Table 2
Parameters of the model (1) used for the MBC.

Param.	Value	Param.	Value
J_x	$5.13 \cdot 10^{-2}\,\mathrm{kgm^2}$	m	4.69 kg
J_y	$8.19 \cdot 10^{-2}\,\mathrm{kgm^2}$	g	$9.81\,\mathrm{m/s^2}$
l_{dx}	135 mm	l_{fx}	182.5 mm
l_{dy}	144 mm	l_{fy}	117 mm

algorithms. Table 2 summarises the model parameters required by the MBC law in (7), (11), and (12). The gains $c_\mathrm{p} = 5000\,\mathrm{s}^{-2}$ and $c_\mathrm{D} = 195\,\mathrm{s}^{-1}$ of the MBC are chosen such that they match the parameters k_p and k_d of the MFC. The control law is implemented in a quasi-continuous manner, which means that the control inputs are sampled and held.

The observer gain $\boldsymbol{l}$ is chosen such that the eigenvalues of the error dynamics are at $820\,\mathrm{s}^{-1}$, $840\,\mathrm{s}^{-1}$, and $860\,\mathrm{s}^{-1}$. With this choice the cutoff frequency of transfer functions, $\omega \mapsto \mathcal{G}_y^{\hat{x}_k}(\mathrm{j}\omega), k \in \{1,2,3\}$, from the measurement y to the estimate $\hat{x}_k, k \in \{1,2,3\}$ of the observer (10) is also around 840 rad/s. Furthermore, a notch filter, as described in Tietze et al. (2008, Sec. 13.8), is used to eliminate the dominant mechanical resonance frequency 942 rad/s of the plate corrupting the position measurement.

Comparing the amplitude spectrum of the transfer functions of the observer and the algebraic differentiators combined with the notch filter in Fig. 9, called $\tilde{\mathcal{G}}_y^{\hat{x}_k}(\mathrm{j}\omega), k \in \{1,2,3\}$ and $\mathcal{D}_y^{\hat{y}^{(n)}}(\mathrm{j}\omega), n \in \{0,1,2\}$, respectively, shows similar results up to the cutoff frequency ω_c. For higher frequencies, according to Othmane et al. (2022, Sec. 4.2.2), the algebraic differentiators have a stopband slope of $20(\mu - n)$ dB with $\mu = 1 + \min\{\alpha, \beta\}$ for the n-th order derivative, which would result, according to Fig. 9, in an unfair comparison of MBC and MFC. For this reason, additional low-pass filters are added to the estimations of the observer, to match the stopband slope of the algebraic differentiator. The resulting transfer functions of the observer, the low-pass, and the notch filter are denoted by $\tilde{\mathcal{G}}_y^{\hat{x}_k}(\mathrm{j}\omega), k \in \{1,2,3\}$.

A block diagram in Fig. 10 illustrates the estimation algorithms used. The observer (10), the notch filter, and the low-pass filters are discretised using Tustin's method with frequency prewarp of their respective cutoff frequency, resulting in a sharp drop of the transfer function near the Nyquist frequency $\omega_\mathrm{N} = \frac{\pi}{t_\mathrm{s}} \approx 1.0 \cdot 10^5$ Hz in Fig. 9 (see also Oppenheim & Schafer, 1975, Sec. 5.1.3).

As mentioned before, the computational burden differs in the proposed algorithms. The MBC takes approximately 11.6% of the controller cycle, whereas the MFC law (14) with $N = 0$, $\alpha = \beta = 4$ and $\omega_\mathrm{c} = 840\,\mathrm{rad/s}$ takes 49.7% of the cycle. The reason for this is the evaluation of several discrete convolutions, needed for the estimation. Nonetheless, a more efficient implementation of the MFC might be possible, but is out of the scope of this paper.

4.3. Trajectory tracking

In the following, the capabilities of the different algorithms designed in Section 3 are compared for different trajectory tracking scenarios.

4.3.1. Vertical motion

This experiment uses the same set point transition as described in Section 4.1 for the parametrisation of the algebraic differentiator. Fig. 11 shows the measured position y_1 in green and the reference trajectory $y_{\mathrm{r},1}$ in red when the MFC law (14) is used. Interestingly, the green graph is ahead of the reference, which will be clear by looking at the error $e_1(t) = y_1(t) - y_{\mathrm{r},1}(t)$. According to the discrete control law (25) the filtered measurement $\hat{y}_1(t)$ is used to calculate the error $\hat{e}_1(t) = \hat{y}_1(t) - y_{\mathrm{r},1}(t)$. The reason of being ahead of the reference is the known delay δ_t of the algebraic differentiator and the suggested choice to only filter the measured signals and not the errors as in Scherer et al. (2023). This results in a prediction of the reference signal and

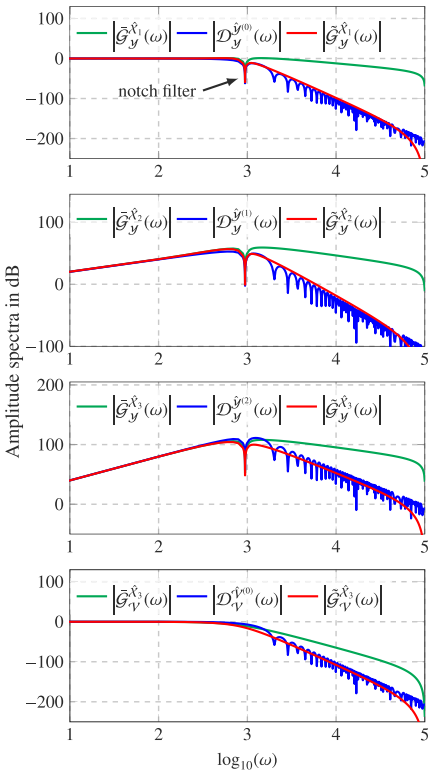

Fig. 9. Comparison of the amplitude spectra of the observer in combination with a notch filter $\omega \mapsto \left|\tilde{\mathcal{G}}_y^{\hat{x}_k}(\mathrm{j}\omega)\right|, k \in \{1,2,3\}$, the same combination extended with additional low-pass filters according to Fig. 10 $\omega \mapsto \left|\mathcal{D}_y^{\hat{y}^{(n)}}(\mathrm{j}\omega)\right|, n \in \{0,1,2\}$, and the algebraic differentiators with the notch filter $\omega \mapsto \left|\tilde{\mathcal{G}}_y^{\hat{x}_k}(\mathrm{j}\omega)\right|, k \in \{1,2,3\}$.

the behaviour seen in Fig. 11, because the delay δ_t of the algebraic differentiator is known and independent of the filtered signal. This effect can be compensated by also delaying the reference signal, which results in the blue graph marked with $\bar{y}_1(t)$ matching the dashed reference. By also delaying the reference by δ_t, the error $\bar{e}_1(t) = \bar{y}_1(t) - y_{\mathrm{r},1}(t)$ shows the same course as $\hat{e}_1(t)$ up to more disturbances on $\bar{y}_1(t)$. The MBC is showing the same behaviour, because of the additional filters, but in this case the delay is unknown. Therefore, knowing exactly the signal independent delay of the algebraic differentiator is a significant advantage compared to a conventional low-pass filter.

In further experiments the RMS values of $\hat{e}_k, k \in \{1,2,3\}$, are used for a fair comparison of the algorithms, because $\hat{e}_k, k \in \{1,2,3\}$, are the errors the corresponding controller can react on. The values are summarised in Table 3 and marked with different colours. The MBC is seen as a benchmark, therefore, the values of this algorithm are given in black. If an algorithm can achieve a smaller RMS value, it is marked with green, otherwise with red. For the MBC and the MFC law (14) the experiment was repeated ten times, to calculate the mean value as well as the standard deviation of the RMS values. For both algorithms and all sensors, the standard deviation was smaller than

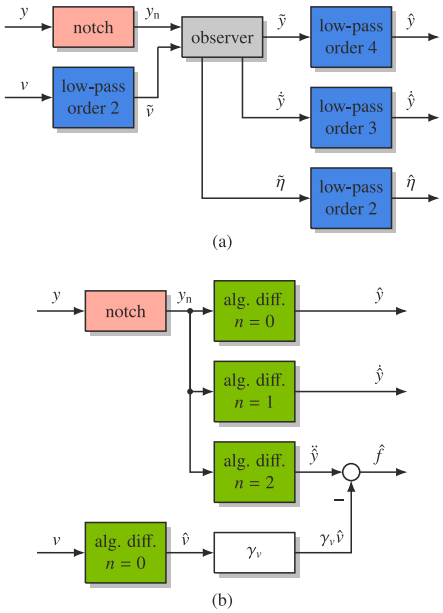

Fig. 10. Diagrams of the proposed estimation algorithms. (a) model based disturbance observer with additional low-pass and notch filters to ensure a fair comparison between the MBC and MFC, (b) estimation using algebraic differentiators and a notch filter for the proposed MFC.

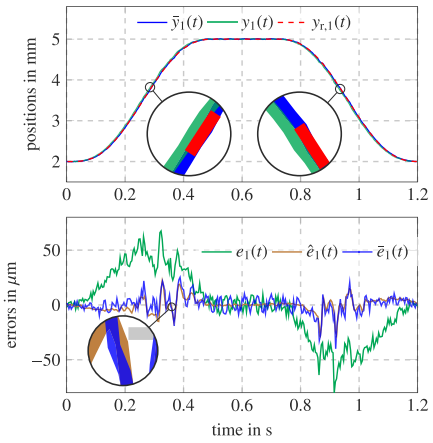

Fig. 11. Results for the trajectory tracking of MFC law (14), to show the effect of the known delay δ_t introduced by the algebraic differentiator and how to compensate it.

30 nm, which is negligible in view of the resolution of the sensors. Therefore, only one experiment is performed and the resulting RMS values are compared. Table 3 reveals that the proposed MFC algorithms (14), (17), and (19) are outperforming the MBC. The RMS values of the errors obtained with the MFC control law (14) are approximately half as high as those observed with the MBC approach. It is also noticeable that in general using less model information results in higher RMS of the errors. Nonetheless, the control laws (17) and (19), with exception of the error in y_3, are still showing better results than the MBC. Only the MFC of the current (21) shows errors the RMS values of which are approximately five times higher than those with the other algorithms. This can be explained by the amount of model information used. Instead of the air gaps, the sensor values are used to calculate the input gains $\gamma_{i,k}, k \in \{1,2,3\}$. Moreover, a linear current model is assumed for the nonlinear behaviour of the magnets. Nevertheless, with this algorithm steady state accuracy is guaranteed.

4.3.2. Tilting of the plate

At the start of a tilting experiment, the plate hovers horizontally at a position of 2 mm. After that, three individual reference trajectories, with different transition times marked with dashed vertical lines, are planned as depicted in the first row of Fig. 12. The MBC and MFC law (14) use the pseudo inverse $B^\dagger$ to decouple the three points where the sensors are located. This model-based method is in contrast to the remaining MFC algorithms that have to realise the decoupling by the estimate of the disturbance f. The reason for this is that these algorithms are based on three ultra-local models that are only implicitly coupled by the disturbance f, as discussed in Section 3. Fig. 12 shows the results of tilting the plate using the MFC law (17). The second row of this figure shows the errors $e_k(t), \hat{e}_k(t), k \in \{1,2,3\}$, and the third row the estimates $\hat{f}_{\bar{F},k}(t), k \in \{1,2,3\}$. Especially the plots of $\hat{e}_2(t)$ and $\hat{f}_{\bar{F},2}(t)$ are displaying the decoupling of the MFC. The transition of $y_2(t)$ is completed after 0.25 s, resulting in an error oscillating around zero and an estimation of the disturbance of approximately 13 m/s^2. Nonetheless, after 0.5 s the transition of $y_3(t)$ is completed as well and the estimate $\hat{f}_{\bar{F},2}(t)$ starts converging to 14 m/s^2, even though, the error $\hat{e}_2(t)$ still oscillates around zero. This example demonstrates that the MFC ensures the decoupling.

The RMS values in Table 3 show similar results as the vertical movement of the plate. The MFC law (14) is almost twice as accurate as the MBC and the algorithms (17) and (19) can obtain better results, except for $y_3(t)$. Again the MFC law (21) cannot achieve results that are as good as the other MFC laws. Nevertheless, the experiments show that a combination of the MFC with additional model information can lead to excellent results and outperform the MBC.

4.4. Robustness against sensor and actuator faults

The robustness with respect to actuator and sensors faults of the algorithms from Section 3 shall now be investigated. Therefore, the plate hovers horizontally at a position of 2 mm for each experiment.

4.4.1. Abrupt constant and multiplicative actuator fault

To investigate the robustness against abrupt actuator faults, these faults are modelled using the shifted Heaviside step function

$$\theta(t,\tau) = \begin{cases} 0, & t < \tau, \\ 1, & \tau \le t. \end{cases} \tag{26}$$

For the abrupt fault at time τ the current $\Delta i_1(t,\tau) = K_i \theta(t,\tau)$ is added to $i_1(t)$, whereas $K_i = 400$ mA, which corresponds to 5% of the maximal current. To simulate a multiplicative fault, the current $i_1(t)$ is changed to $(1 + \bar{K}_i \theta(t,\tau)) i_1(t)$, with $\bar{K}_i = 0.4$.

Fig. 13 shows the results of the abrupt constant actuator fault over time for the proposed algorithms. All have in common that after approximately 150 ms the measured values are back at the reference of 2 mm, which is the result of the same parametrisation of the controllers. The direct comparison in Table 3 shows that the quality gauge of the MFC law (14) is almost half as high compared to that of the

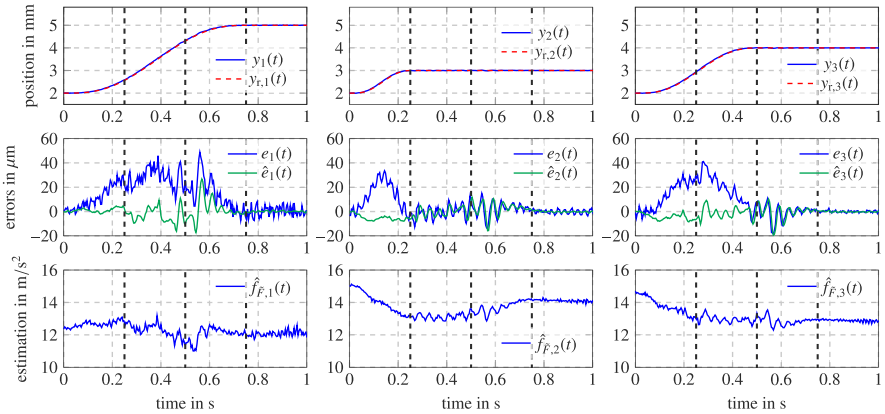

Fig. 12. Experimental results for the tilting of the plate with MFC law (17). The graphs show that the proposed MFC is capable of decoupling the three ultra-local models.

MBC. Additionally the minimal error of $\min(\hat{e}_1(t)) = -114.1$ µm is significantly smaller than the value of $\min(\hat{e}_1(t)) = -184.1$ µm for the MBC. This behaviour can be seen for all MFC algorithms, but for the remaining algorithms (17), (19) and (21) a decaying oscillation around the position 2 mm can be observed, which cannot be observed for the MBC and MFC law (14). Probably the reason for this is the choice of parameter $F_{d,4}$ and similarly for u and i, because the reaction to the disturbance resulting form the abrupt error is not distributed equally on all four magnets, as depicted in Fig. 14. The estimate of the disturbance for the MFC law (17) is shown with solid lines. For $\hat{f}_{\tilde{F},1}$ the reaction to the fault is immediate and can be compared to the reaction of the MBC depicted in the blue dashed line. The estimates $\hat{f}_{\tilde{F},2}$ and $\hat{f}_{\tilde{F},3}$ on the other hand are oscillating around 14.3 m/s^2 and 15 m/s^2, the values that they converge to, after the motion of the plate has stabilised after approximately 150 ms. The reaction of the MBC is different, because the control input $\boldsymbol{v}$ is split evenly to all magnets using the pseudo inverse $B^{\dagger}$. After the fault occurs, all estimates converge to lower values. This shows that in this case the implicit decoupling of the MFC algorithms (17), (19), and (21) is resulting in a different transient behaviour, whereas the MFC law (21) again provides results that are not as good compared to the other MFC algorithms.

According to Table 3, similar behaviour can be seen as for the abrupt actuator fault. Interestingly, the results from MFC law (17) show higher RMS values than the algorithm using the input u. This is because the plate started oscillating after the stabilisation. The reason for this behaviour is unknown.

4.4.2. Abrupt sensor fault

To simulate an abrupt sensor fault, the Heaviside step function (26) is used again. An error in the sensor value y_1 is modelled as $\Delta y_1(t,\tau) = K_y \theta(t,\tau)$ with $K_y = 0.2$ mm, which corresponds to 10% of the current sensor value. With this change, the sensor value becomes $y_1(t) + \Delta y_1(t,\tau)$. The results of this experiment in Table 3 show that the MFC cannot outperform the MBC. Comparing the estimate of the disturbance $\hat{f}_{v,1}(t)$ with $\hat{\eta}_1(t) + g$ in Fig. 15 shows that the peaks of $\hat{f}_{v,1}(t)$ are almost twice as high. This results from the additional low-pass filters depicted in Fig. 10, which will be clear by comparing the responses to a unit step in Fig. 15. There, the step responses of $-\omega^2 \mathcal{F}\{\ddot{g}\}(\mathrm{j}\omega)$ and $\mathcal{G}_y^{\hat{\chi}_3}(\mathrm{j}\omega)$ show almost the same maximum values, but adding the notch and low-pass filters changes the peaks of $\mathcal{G}_y^{\tilde{\chi}_3}(\mathrm{j}\omega)$ to approximately half of the values of $\mathcal{D}_y^{\hat{y}^{(2)}}(\mathrm{j}\omega)$, which makes the MBC less sensitive to abrupt changes in the sensor value.

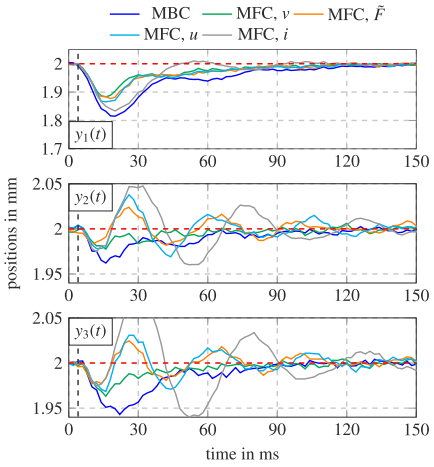

Fig. 13. Response of the different proposed controllers to an abrupt constant actuator fault. The MFC approaches show a high robustness against these faults.

5. Conclusion and future work

In this paper, a systematic tuning approach of a MFC algorithm for an unstable MIMO system that can be approximated by three implicitly coupled second-order differential equations is investigated. Numerous experiments carried out on a test bed show the capabilities of the MFC approaches combined with physically motivated model knowledge. The experiments show that the proposed algorithms can achieve a high level of robustness with respect to actuator faults and much better results if they are coupled with model information.

It could be seen that the MFC needs more computational power compared to the model based approach, because multiple convolutions have to be carried out. This has limited the choice of the cutoff frequency ω_c and the parameters $\alpha = \beta$ of the algebraic differentiators.

Table 3
Summary of the experimental results with the RMS values of $\hat{e}_k, k \in \{1,2,3\}$ as a quality gauge. The values of the MBC are seen as a benchmark and therefore depicted in black. If an algorithm can achieve lower RMS values it is marked in green, otherwise in red.

Experiment	Sensor	MBC	MFC, v	MFC, $\hat{F}$	MFC, u	MFC, i
Horizontal movement	y_1	8.1 µm	5.1 µm	6.0 µm	6.6 µm	31.4 µm
	y_2	11.7 µm	6.2 µm	7.8 µm	8.6 µm	31.4 µm
	y_3	7.5 µm	4.2 µm	6.5 µm	8.8 µm	31.0 µm
Tilting the plate	y_1	6.2 µm	3.6 µm	4.6 µm	4.5 µm	24.6 µm
	y_2	4.7 µm	2.3 µm	3.8 µm	4.0 µm	15.9 µm
	y_3	3.4 µm	1.8 µm	3.8 µm	5.0 µm	19.9 µm
Abrupt actuator faults, i_1	y_1	37.2 µm	20.1 µm	22.3 µm	23.8 µm	29.9 µm
	y_2	6.5 µm	3.6 µm	5.0 µm	6.3 µm	10.9 µm
	y_3	10.7 µm	5.6 µm	5.3 µm	6.7 µm	16.8 µm
Multiplicative actuator fault, i_1	y_1	46.4 µm	27.2 µm	42.8 µm	29.4 µm	35.3 µm
	y_2	8.6 µm	4.9 µm	7.7 µm	6.3 µm	12.0 µm
	y_3	13.5 µm	7.2 µm	11.3 µm	6.9 µm	18.6 µm
Abrupt Sensor fault, y_1	y_1	41.9 µm	56.4 µm	45.8 µm	17.0 µm	46.1 µm
	y_2	10.6 µm	8.8 µm	21.0 µm	14.6 µm	28.6 µm
	y_3	10.4 µm	5.7 µm	24.9 µm	19.2 µm	50.3 µm

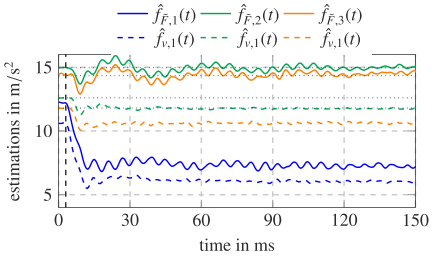

Fig. 14. Estimation of the disturbance of MFC laws (14) and (17) caused by an abrupt constant actuator fault. The plot illustrates the different decoupling strategies used, on the one hand the pseudo inverse $B^\dagger$ and on the other hand $F_{\mathrm{d},4} = \frac{1}{2}(\bar{F}_2 + \bar{F}_3)$.

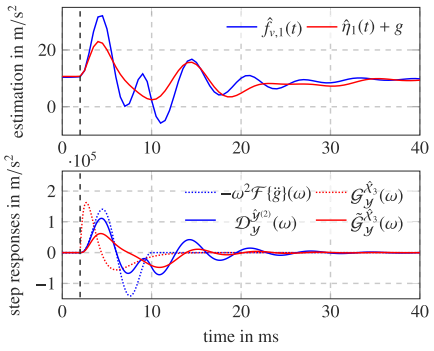

Fig. 15. Estimation of the disturbance of MBC and MFC law (14) for an abrupt sensor fault and the responses of several filters to a unit step starting at $t = 2$ ms. The reaction of the MBC is less dominant compared to the MFC.

As stated before, a more efficient implementation of the convolution integrals of the MFC is possible, e.g. by using dedicated signal processors. However, this is out of the scope of the present paper. Nonetheless, using the differentiators has shown to be beneficial, because this signal based approach does not rely on a model of the system to estimate unknown quantities, compared to a classical observer based approach. However, this comes with the price that results of the estimates of the disturbance f are harder to interpret, if no mathematical model of the system is available. To realise a fair comparison of the proposed MBC and the MFC law (14), additional low-pass filters are added to the disturbance observer, to match the filter order of the used algebraic differentiators.

Future work should investigate why some parameter combinations of the algebraic differentiator are resulting in an unstable closed-loop system, or respectively what the parameter combinations resulting in a stable closed loop have in common. Further, the estimation delay should explicitly be taken into account during the controller design. Additionally, a systematic tuning approach without parameter sweeps that are carried out on the test bed would be beneficial. Similarly, approximations with higher order systems are still open for investigation. This also goes along with the estimation of higher order derivatives, which probably needs more computation time, a problem that has to be tackled as must be the discretisation of the algebraic differentiators.

CRediT authorship contribution statement

P.M. Scherer: Writing – review & editing, Writing – original draft, Visualization, Software, Methodology, Investigation, Data curation. **A. Othmane:** Writing – review & editing, Formal analysis, Conceptualization. **J. Rudolph:** Writing – review & editing.

Declaration of competing interest

The authors declare that they have no known competing financial interests or personal relationships that could have appeared to influence the work reported in this paper.

Acknowledgement

Long-term support from Intronik GmbH is acknowledged. The authors would also like to thank the reviewers for their valuable feedback.

Appendix A. Information about algebraic differentiators

In this section, useful background information on algebraic differentiators, initially developed in Mboup et al. (2007, 2009) are recalled. The interested reader is referred to Othmane et al. (2022) for an overview on this topic and Szegö (1939) for the discussion and analyses of the required orthogonal polynomials.

In the sequel Γ denotes the gamma function and

$$w^{(\alpha,\beta)}(\tau) = \begin{cases} (1-\tau)^\alpha(1+\tau)^\beta, & \tau \in [-1,1], \\ 0, & \text{otherwise}, \end{cases}$$

with real scalar parameters $\alpha, \beta > -1$, is the weight function associated with the orthogonal Jacobi polynomial of degree $N \in \mathbb{N}$ defined as

$$P_N^{(\alpha,\beta)}(\tau) = \sum_{k=0}^{N} \binom{N}{k} c_k^{(\alpha,\beta)} (\tau-1)^k,$$
$$c_k^{(\alpha,\beta)} = \frac{\Gamma(\alpha+N+1)\Gamma(\alpha+\beta+N+k+1)}{2^k N!\Gamma(\alpha+\beta+N+1)\Gamma(\alpha+k+1)}.$$

Denote by $x^{(n)}$ the n-th order derivative of a function x, where $x^{(0)}$ denotes the function x itself. Assume for an arbitrary n that $x^{(n)}$ is square Lebesgue integrable and let $\alpha, \beta \in \mathbb{R}$ be arbitrary such that $\min(\alpha,\beta) > n-1$. Then, $x^{(n)}$ can be approximated by a N-th order truncated generalised Fourier expansion as

$$\hat{x}^{(n)}(t) = \int_{t-T}^{t} g^{(n)}(t-\tau)x(\tau)\mathrm{d}\tau, \quad g(\tau) = g_{N,T,\vartheta}^{(\alpha,\beta)}(\tau) \tag{A.1}$$

with the kernel

$$g(\tau) = \begin{cases} \frac{2w^{(\alpha,\beta)}(\nu(\tau))}{T} \sum_{j=0}^{N} \frac{P_j^{(\alpha,\beta)}(\vartheta)}{\left\|P_j^{(\alpha,\beta)}\right\|^2} P_j^{(\alpha,\beta)}(\nu(\tau)), & \tau \in [0,T], \\ 0, & \text{otherwise}, \end{cases}$$

depending on ϑ parametrising the approximation delay and $\nu(\tau) = 1 - 2\tau/T$, where $\|z\| = \sqrt{\langle z,z\rangle}$ is the norm induced by the inner product

$$\langle z, y\rangle = \int_{-1}^{1} w^{(\alpha,\beta)}(\tau)z(\tau)y(\tau)\mathrm{d}\tau.$$

All calculations are based on the sliding time window $[t-T,t]$, where T describes the filter window length, associated with the cutoff frequency ω_c, as discussed in Kiltz and Rudolph (2013). As first pointed out in Mboup et al. (2009), the estimate is delayed by a small but known delay given as

$$\delta_t = \begin{cases} \frac{\alpha+1}{\alpha+\beta+2}T, & N = 0, \\ \frac{1-\vartheta}{2}T, & N \neq 0. \end{cases}$$

A delay-free estimation is possible by choosing $N > 0$ and $\vartheta = 1$. However, accepting a delay increases the accuracy of the approximation and yields desirable frequency-domain properties (see Mboup et al., 2009; Mboup & Riachy, 2014, 2018 and Othmane et al., 2022).

The estimate of $\hat{x}^{(n)}$ can be interpreted as the output of a finite impulse response (FIR) filter driven by the input x. The kernel $g_{N,T,\vartheta}^{(\alpha,\beta)}$ has also a system theoretic interpretation. As shown for example in Kiltz (2017) or Othmane et al. (2022) and used in Section 4.1, $g_{N,T,\vartheta}^{(\alpha,\beta)}$ can be interpreted as a low-pass filter driven by the sought derivative $x^{(n)}$ and with cutoff frequency ω_c. This interpretation makes the filter design more intuitive.

All considerations so far were done in a continuous time setting. Nonetheless, for the implementation of the algorithms suggested in this contribution, a discrete-time realisation of the estimators is required. Therefore, the integral (A.1) has to be discretised using an appropriate quadrature method. For that, equidistant sampling with t_s is considered. This results in a filter window of length T that is of an integral multiple of the sampling time t_s, i.e. $T = n_s t_s$. The abbreviation $x[k] = x(kt_s), k \in \mathbb{N}$ is used for x evaluated at the time kt_s. With this notation, the convolution (A.1) can be approximated with

$$\hat{x}^{(n)}[k+\theta] = \frac{1}{\Phi}\sum_{j=0}^{L-1} w_n[j]x[k-j], \quad \Phi = \frac{t_s^n}{n!}\sum_{j=0}^{L-1} w_n[j](-j)^n,$$

where the parameters θ, L, and $w_n[j]$ depend on the numerical integration method used, as described in Othmane, Mounier, and Rudolph (2021). For instance, for the mid-point rule $\theta = 1/2$, $L = n_s$, and $w_n[j] = t_s g^{(n)}[j+1/2]$. The design and discretisation of the differentiators are done using the open-source toolbox AlgDiff (see Othmane, 2022), which comes with detailed examples for a correct application of the filters.

Appendix B. Derivation of the MFC

In the following, the MFC for a second order ultra-local model is derived using the Laplace transformation and it is shown that it is a special case of the considerations made in Section 3.3.

B.1. An algebraic point of view

Consider the second order ultra-local model

$$\ddot{y}(t) = \gamma u(t) + f(t), \tag{B.1}$$

with measurement $y(t)$, input $u(t)$, input gain $\gamma \in \mathbb{R}$ and piecewise constant disturbance $f(t)$. Applying the Laplace transform to (B.1) under the assumption that $f(t)$ is constant on the interval $[0,T]$ yields

$$s^2Y(s) - \dot{y}(0) - sy(0) = \gamma U(s) + \frac{1}{s}F \tag{B.2}$$

with $Y(s), U(s)$ and F the Laplace transform of $y(t), u(t)$ and $f(t)$, respectively, and the initial conditions $y(0)$ and $\dot{y}(0)$. To get rid of the initial conditions, (B.2) is differentiated twice with respect to s yielding

$$2Y(s) + 4s\frac{\mathrm{d}Y}{\mathrm{d}s}(s) + s^2\frac{\mathrm{d}^2Y}{\mathrm{d}s^2}(s) = \gamma\frac{\mathrm{d}^2U}{\mathrm{d}s^2}(s) + \frac{2}{s^3}F. \tag{B.3}$$

In the latter equation the expressions $s^2\frac{\mathrm{d}^2Y}{\mathrm{d}s^2}(s)$ and $4s\frac{\mathrm{d}Y}{\mathrm{d}s}(s)$ are hindering an implementation. Therefore, (B.3) is multiplied by s^{-2} and again by s^{-1} to remove differentiation in the time domain and increase the noise attenuation, respectively, which results in

$$\frac{2}{s^3}Y(s) + \frac{4}{s^2}\frac{\mathrm{d}Y}{\mathrm{d}s}(s) + \frac{1}{s}\frac{\mathrm{d}^2Y}{\mathrm{d}s^2}(s) = \gamma\frac{1}{s^3}\frac{\mathrm{d}^2U}{\mathrm{d}s^2}(s) + \frac{2}{s^6}F. \tag{B.4}$$

With this, only integrals of measured signals occur when the expressions are transformed back into the time domain, which will be the next step. Therefore, the following inverse transformations

$$\frac{\mathrm{d}^n}{\mathrm{d}s^n}X(s) \bullet\!\!-\!\!\circ (-t)^n x(t) \tag{B.5a}$$
$$\frac{1}{s^n} \bullet\!\!-\!\!\circ \frac{t^{n-1}}{(n-1)!} \tag{B.5b}$$
$$\frac{X(s)}{s} \bullet\!\!-\!\!\circ \int_0^t x(\sigma)\mathrm{d}\sigma. \tag{B.5c}$$

are used (see e.g. in the appendix of Doetsch, 1974). Applying them to (B.4) and rearranging the expressions yields

$$\frac{2t^5}{5!}\hat{f} = 2\int_0^t\int_0^{\sigma_1}\int_0^{\sigma_2} y(\tau)\mathrm{d}\tau\mathrm{d}\sigma_1\mathrm{d}\sigma_2 - 4\int_0^t\int_0^{\sigma_1}\tau y(\tau)\mathrm{d}\tau\mathrm{d}\sigma_1 + \int_0^t\tau^2 y(\tau)\mathrm{d}\tau - \gamma\int_0^t\int_0^{\sigma_1}\int_0^{\sigma_2}\tau^2 u(\tau)\mathrm{d}\tau\mathrm{d}\sigma_1\mathrm{d}\sigma_2.$$

Now the Cauchy-formula for repeated integration (see e.g. Chapter 11 in Doetsch (1974)) can be used to simplify the expression for $\hat{f}$, resulting in

$$\hat{f} = \frac{5!}{2t^5}\int_0^t \left[(t-\tau)^2 - 4(t-\tau)\tau + \tau^2\right] y(\tau) - \frac{\gamma}{2}(t-\tau)^2\tau^2 u(\tau)\mathrm{d}\tau.$$

Considering only the interval $[0, T]$ instead of $[0, t]$ and further simplifying the equation yields

$$\hat{f} = \frac{5!}{2T^5}\int_0^T \left(T^2 - 6T\tau + 6\tau^2\right) y(\tau) - \frac{\gamma}{2}(T-\tau)^2\tau^2 u(\tau)\mathrm{d}\tau.$$

A moving time window $[t-T-\varepsilon, t-\varepsilon], \varepsilon > 0$ can be introduced by evaluating the signals y and u at $\sigma + t - T - \varepsilon$ instead of σ. With this change, the expression

$$\hat{f}(t) = \frac{5!}{2T^5}\int_0^T \left(T^2 - 6T\sigma + 6\sigma^2\right) y(\sigma + t - T - \varepsilon) - \frac{\gamma}{2}(T-\sigma)^2\sigma^2 u(\sigma + t - T - \varepsilon)\mathrm{d}\sigma$$

is now a function of time. Thereafter, the substitution $\tau = \sigma + t - T - \varepsilon$ leads to

$$\hat{f}(t) = \frac{5!}{2T^5}\int_{t-T-\varepsilon}^{t-\varepsilon} \left(T^2 - 6T(t-\tau-\varepsilon) + 6(t-\tau-\varepsilon)^2\right) y(\tau) - \frac{\gamma}{2}(t-\tau-\varepsilon)^2(T-(t-\tau-\varepsilon))^2 u(\tau)\mathrm{d}\tau. \tag{B.6}$$

This expression for the estimation of f is slightly different from that commonly used in the literature (e.g. Bekcheva et al., 2018 or Barth et al., 2020) in the sense that the current time t appears in the filter kernel and the parameter ε is explicitly considered.

B.2. A system theoretic point of view

The estimation of $f(t)$ according to the ultra-local model (B.1) reads

$$\hat{f}(t) = \int_{t-T-\varepsilon}^{t-\varepsilon} g(t-\tau-\varepsilon) f(\tau)\mathrm{d}\tau, \quad \varepsilon > 0, \tag{B.7a}$$

$$= \int_{t-T-\varepsilon}^{t-\varepsilon} \ddot{g}(t-\tau-\varepsilon) y(\tau) - \gamma g(t-\tau-\varepsilon) u(\tau)\mathrm{d}\tau \tag{B.7b}$$

with $g = g^{(\alpha,\beta)}_{N,T,\vartheta}$ denoting the kernel of the algebraic differentiator presented in Appendix A. Now consider the special parametrisation $N = 0$, which leads to the kernel

$$g^{(\alpha,\beta)}_{0,T,\vartheta}(\tau) = \begin{cases} \frac{(\alpha+\beta+1)!}{\alpha!\beta!T^{\alpha+\beta+1}}\tau^\alpha(T-\tau)^\beta, & \tau \in [0,T], \\ 0, & \text{otherwise.} \end{cases} \tag{B.8}$$

If the parameters $\alpha = \beta = 2$ are chosen, the kernel (B.8) further simplifies to

$$g^{(2,2)}_{0,T,\vartheta}(\tau) = \bar{g}(\tau) = \begin{cases} \frac{1}{2}\frac{5!}{2T^5}\tau^2(T-\tau)^2, & \tau \in [0,T], \\ 0, & \text{otherwise.} \end{cases} \tag{B.9}$$

Calculating the second derivative of $\bar{g}$ with respect to τ leads to

$$\frac{\mathrm{d}^2\bar{g}}{\mathrm{d}\tau^2}(\tau) = \begin{cases} \frac{5!}{2T^5}(6\tau^2 - 6T\tau + T^2), & \tau \in [0,T], \\ 0, & \text{otherwise.} \end{cases} \tag{B.10}$$

Using both (B.9) and (B.10) in (B.7) results in an expression that is equivalent to (B.6). This shows, that the propositions made in this paper are a generalisation of the ansatz that is commonly used in the literature. As seen in Section 4 this generalisation is needed in some cases to realise the MFC.

B.3. Validation of the derivation

To validate the calculations made in this section, consider the differential equation

$$\ddot{y}(t) = F, \tag{B.11}$$

with $F \in \mathbb{R}$, the solution of which is $y(t) = \frac{1}{2}Ft^2$. The relation (B.6) with $u(t) = 0$ can now be used together with the solution of the differential equation (B.11) to estimate the parameter F resulting in

$$\hat{F}(t) = \int_{t-T-\varepsilon}^{t-\varepsilon} \ddot{\bar{g}}(t-\tau) y(\tau)\mathrm{d}\tau$$

$$= \frac{5!}{2T^5}\int_{t-T-\varepsilon}^{t-\varepsilon} \left(T^2 - 6T(t-\tau-\varepsilon) + 6(t-\tau-\varepsilon)^2\right)\frac{1}{2}F\tau^2\mathrm{d}\tau$$

$$= F.$$

The reason for this result lies in the approximation of the second order derivative of $y(t)$ with a constant according to the choice of $N = 0$. For further theoretical analysis the degree of exactness introduced in Kiltz (2017) can be considered (see also Othmane et al., 2022). The results $\hat{F} = F$ shows that the calculations made in this section are correct.

References

Al Younes, Y., Drak, A., Noura, H., Rabhi, A., & El Hajjaji, A. (2014). Model-Free Control of a Quadrotor Vehicle. In *2014 International Conference on Unmanned Aircraft Systems* (pp. 1126–1131). IEEE.

Barth, J., Condomines, J. P., Bronz, M., Moschetta, J. M., Join, C., & Fliess, M. (2020). Model-free control algorithms for micro air vehicles with transitioning flight capabilities. *International Journal of Micro Air Vehicles*, *12*, 1–22.

Bekcheva, M., Join, C., & Mounier, H. (2018). Cascaded Model-Free Control for trajectory tracking of quadrotors. In *2018 International Conference on Unmanned Aircraft Systems* (pp. 1359–1368). IEEE.

Belhadjoudja, M. C., Maghenem, M., & Witrant, E. (2023). On the Intelligent Proportional Controller Applied to Linear Systems. In *62nd IEEE Conference on Decision and Control* (pp. 938–943). IEEE.

Carvalho, A. D., Pereira, B. S., Angélico, B. A., Laganá, A. A. M., & Justo, J. F. (2024). Model-free control applied to a direct injection system: Experimental validation. *Fuel*, *358*, Article 130071.

Collon, C., Eckhardt, S., & Rudolph, J. (2007). A network approach to the modelling of active magnetic bearings. *Mathematical and Computer Modelling of Dynamical Systems*, *13*(5), 455–469.

De Miras, J., Join, C., Fliess, M., Riachy, S., & Bonnet, S. (2013). Active magnetic bearing: A new step for model-free control. In *52nd IEEE Conference on Decision and Control* (pp. 7449–7454). IEEE.

Doetsch, G. (1974). *Introduction to the Theory and Application of the Laplace Transformation*. Springer.

Eckhardt, S., & Rudolph, J. (2004). High precision synchronous tool path tracking with an AMB machine tool spindle. In *9th International Symposium on Magnetic Bearings*.

Ellis, R. W., & Mote, C. D. (1977). A feedback vibration controller for circular saws. In *Joint Automatic Control Conference, No. 14* (pp. 1193–1198).

Fliess, M., & Join, C. (2008). Commande sans modèle et commande à modèle restreint. *e-STA Sciences et Technologies de l'Automatique*, *5*(4), 1–23.

Fliess, M., & Join, C. (2009). Model-free control and intelligent PID controllers: Towards a possible trivialization of nonlinear control? *IFAC Proceedings Volumes*, *42*(10), 1531–1550.

Fliess, M., & Join, C. (2013). Model-free control. *International Journal of Control*, *86*(12), 2228–2252.

Fliess, M., & Join, C. (2023). Towards a control-theoretic trivialization of ABR video streaming. http://dx.doi.org/10.48550/arXiv.2310.00934, arXiv preprint arXiv:2310.00934.

Haddar, M., Chaari, R., Baslamisli, S. C., Chaari, F., & Haddar, M. (2019). Intelligent PD controller design for active suspension system based on robust model-free control strategy. *Proceedings of the Institution of Mechanical Engineers, Part C*, *233*(14), 4863–4880.

Hegedűs, T., Fényes, D., Németh, B., Szabó, Z., & Gáspár, P. (2022). Design of Model Free Control with tuning method on ultra-local model for lateral vehicle control purposes. In *2022 American Control Conference* (pp. 4101–4106).

Kiltz, L. (2017). *Algebraische Ableitungsschätzer in Theorie und Anwendung* (Ph.D. thesis), Saarland University, Germany.

Kiltz, L., Join, C., Mboup, M., & Rudolph, J. (2014). Fault-tolerant control based on algebraic derivative estimation applied on a magnetically supported plate. *Control Engineering Practice*, *26*, 107–115.

Kiltz, L., Mboup, M., & Rudolph, J. (2012). Fault diagnosis on a magnetically supported plate. In *2012 1st International Conference on Systems and Computer Science* (pp. 1–6). IEEE.

Kiltz, L., & Rudolph, J. (2013). Parametrization of algebraic numerical differentiators to achieve desired filter characteristics. In *52nd IEEE Conference on Decision and Control* (pp. 7010–7015).

Lafont, F., Balmat, J.-F., Join, C., & Fliess, M. (2020). First steps toward a simple but efficient model-free control synthesis for variable-speed wind turbines. http://dx.doi.org/10.46300/9106.2020.14.146, arXiv preprint arXiv:2011.06415.

Lafont, F., Balmat, J.-F., Pessel, N., & Fliess, M. (2015). A model-free control strategy for an experimental greenhouse with an application to fault accommodation. *Computers and Electronics in Agriculture*, *110*, 139–149.

Lei, S., & Palazzolo, A. (2008). Control of flexible rotor systems with active magnetic bearings. *Journal of Sound and Vibration*, *314*(1–2), 19–38.

Li, W., Yuan, H., Li, S., & Zhu, J. (2022). A Revisit to Model-Free Control. *IEEE Transactions on Power Electronics*, *37*(12), 14408–14421.

Mboup, M., Join, C., & Fliess, M. (2007). A revised look at numerical differentiation with an application to nonlinear feedback control. In *Proceedings of the 15th Mediterranean Conference on Control and Automation*.

Mboup, M., Join, C., & Fliess, M. (2009). Numerical differentiation with annihilators in noisy environment. *Numerical Algorithms*, *50*(4), 439–467.

Mboup, M., & Riachy, S. (2014). A Frequency Domain Interpretation of the Algebraic Differentiators. *IFAC Proceedings Volumes*, *47*(3), 9147–9151.

Mboup, M., & Riachy, S. (2018). Frequency-domain analysis and tuning of the algebraic differentiators. *International Journal of Control*, *91*(9), 2073–2081.

Moraes, M. S., & da Silva, P. S. P. (2015). Model-free control of magnetic levitation systems through algebraic derivative estimation. In *Proceedings 23rd ABCM International Congress of Mechanical Engineering*.

Neves, G. P., & Angélico, B. A. (2021). Model-free control of mechatronic systems based on algebraic estimation. *Asian Journal of Control*, *24*(4), 1575–1584.

Oppenheim, A. V., & Schafer, R. W. (1975). *Digital Signal Processing*. Englewood Cliffs, N. J.: Prentice-Hall Inc.

Othmane, A. (2022). AlgDiff: A Python package with MATLAB coupling implementing all necessary tools for the design, analysis, and discretization of algebraic differentiators. http://dx.doi.org/10.5281/zenodo.5172198, Available at https://github.com/aothmane-control/Algebraic-differentiators, version 2.3.

Othmane, A., Kiltz, L., & Rudolph, J. (2022). Survey on algebraic numerical differentiation: Historical developments, parametrization, examples, and applications. *International Journal of Systems Science*, *53*(9), 1848–1887.

Othmane, A., Mounier, H., & Rudolph, J. (2021). Parametrization of algebraic differentiators for disturbance annihilation with an application to the differentiation of quantized signals. *IFAC-PapersOnLine*, *54*(9), 335–340.

Othmane, A., & Rudolph, J. (2023). AlgDiff: An open source toolbox for the design, analysis and discretisation of algebraic differentiators. *at-Automatisierungstechnik*, *71*(8), 612–623.

Othmane, A., Rudolph, J., & Mounier, H. (2021). Systematic comparison of numerical differentiators and an application to model-free control. *European Journal of Control*, *62*, 113–119.

Rudolph, J. (2021). *Flatness-based control: An Introduction*. Shaker Verlag.

Scherer, P. M., Othmane, A., & Rudolph, J. (2023). Combining model-based and model-free approaches for the control of an electro-hydraulic system. *Control Engineering Practice*, *133*, Article 105453.

Szegö, G. (1939). *Orthogonal Polynomials*. New York: AMS.

Tabuada, P., Ma, W.-L., Grizzle, J., & Ames, A. D. (2017). Data-driven control for feedback linearizable single-input systems. In *56th IEEE Conference on Decision and Control* (pp. 6265–6270). IEEE.

Tietze, U., Schenk, C., & Gamm, E. (2008). *Electronic Circuits*. Berlin, Heidelberg: Springer.

Villagra, J., & Herrero-Pérez, D. (2012). A comparison of control techniques for robust docking maneuvers of an AGV. *IEEE Transactions on Control Systems Technology*, *20*(4), 1116–1123.

Wachter, J., Gröll, L., & Hagenmeyer, V. (2023). Application of Model-Free Control to Reduce the Total Harmonic Distortion of Inverters. In *2023 8th IEEE Workshop on the Electronic Grid* (pp. 1–7).

Zhang, H., Li, H., Mao, J., Pan, C., & Luan, Z. (2022). Model-free control of single-phase boost AC/DC converters. *IEEE Transactions on Power Electronics*, *37*(10), 11828–11838.

Appendix A

Stability of particular linear time-delay systems

In this appendix, the stability depending on the parameters of the considered TDSs is analysed. Therefore, the required theorems and assumptions according to Silva et al. (2000) are briefly restated with a slightly different notation.

In the following, linear TDSs with a characteristic equation of the form

$$0 = d(s) + \exp(-sT_1)n_1(s) + \exp(-sT_2)n_2(s) + \cdots + \exp(-sT_m)n_m(s),$$

are considered. To simplify the discussion of the latter equation, the so-called quasi-polynomial

$$\Delta^*(s) = d(s) + \exp(-sT_1)n_1(s) + \exp(-sT_2)n_2(s) + \cdots + \exp(-sT_m)n_m(s), \quad \text{(A.1)}$$

is introduced. The occurring functions $s \mapsto d(s)$ and $s \mapsto n_j(s)$, $j \in \{1, 2, \ldots, m\}$ are polynomials with real coefficients and the parameters $T_j \in \{1, 2, \ldots, m\}$ are delay times. For (A.1) the following assumptions must hold in order to apply the generalised Hermite-Biehler theorem (see, e.g. (Silva et al., 2005, Ch. 5)):

($\mathcal{A}$1) The degrees of the polynomials satisfy $\deg(d(s)) = n$ and $\deg(n_j(s)) < n$ for $j \in \{1, 2, \ldots, m\}$, i.e. only retarded TDSs are considered.

($\mathcal{A}$2) The time delays obey $0 < T_1 < T_2 < \cdots < T_m$.

Consider the quasi-polynomial

$$\begin{aligned}\Delta(s) &= \exp(sT_m)\Delta^*(s) \\ &= \exp(sT_m)d(s) + \exp(s(T_m - T_1))n_1(s) + \exp(s(T_m - T_2))n_2(s) + \cdots + n_m(s),\end{aligned} \quad \text{(A.2)}$$

which has the same zeros as (A.1). Therefore, stability of (A.2) has to be checked, which is done using the necessary and sufficient conditions stated in the following theorems from Silva et al. (2000).

Theorem 1

Let $\Delta(s)$ be given by (A.2), and write

$$\Delta(\mathrm{j}\omega) = \Delta_{\mathrm{Re}}(\omega) + \mathrm{j}\Delta_{\mathrm{Im}}(\omega) \tag{A.3}$$

where $\Delta_{\mathrm{Re}}(\omega)$ and $\Delta_{\mathrm{Im}}(\omega)$ represent the real and imaginary parts of $\Delta(\mathrm{j}\omega)$, respectively. Under Assumptions ($\mathcal{A}1$) and ($\mathcal{A}2$), Δ is asymptotically stable if and only if

1. Δ_{Re} and Δ_{Im} have only simple real roots and these interlace and
2. $\mathfrak{E}(\omega_0) = \frac{\mathrm{d}\Delta_{\mathrm{Im}}}{\mathrm{d}\omega}(\omega_0)\Delta_{\mathrm{Re}}(\omega_0) - \Delta_{\mathrm{Im}}(\omega_0)\frac{\mathrm{d}\Delta_{\mathrm{Re}}}{\mathrm{d}\omega}(\omega_0) > 0$, for some ω_0 in $(-\infty, \infty)$.

To apply Theorem 1, it has to be ensured that Δ_{Re} and Δ_{Im} have only real roots. A possible way to do so is to use the following Theorem 2 from Silva et al. (2000).

Theorem 2

Let M and N denote the highest powers of s and $\exp(s)$ in Δ from (A.3), respectively. Let η be an appropriate constant such that the coefficients of terms of highest degree in $\Delta_{\mathrm{Re}}(\omega)$ and $\Delta_{\mathrm{Im}}(\omega)$ do not vanish at $\omega = \eta$. Then, for the equations $\Delta_{\mathrm{Re}}(\omega) = 0$ or $\Delta_{\mathrm{Im}}(\omega) = 0$ to have only real roots, it is necessary and sufficient that in the interval

$$-2l\pi + \eta \leq \omega \leq 2l\pi + \eta$$

Δ_{Re} or Δ_{Im} has exactly $4lN + M$ real roots starting with a sufficiently large l.

Remark A.1 *In the following sections, the symbols such as Δ, Δ_{Re}, Δ_{Im}, or $\mathfrak{E}$, just to name a few, are used multiple times but are only valid in the respective sections.*

A.1 Simple first-order time-delay system

Consider the following retarded TDS (see, e.g. Fridman (2014, Sec. 1.2))

$$\gamma_\Omega \dot{e}_\Omega(t) + k_{\mathrm{p}}\rho_\Omega e_\Omega(t - \delta_t) = 0,$$

with the positive parameters $k_\mathrm{p}, \rho_\Omega, \gamma_\Omega$ and δ_t, the quasi-polynomial of which is

$$\Delta^*(s) = \gamma_\Omega s + k_\mathrm{p}\rho_\Omega \exp(-s\delta_t).$$

The term $\Delta^*(s)$ meets the previously introduced Assumptions ($\mathcal{A}1$) and ($\mathcal{A}2$). Thereafter, multiplying $\Delta^*(s)$ with $\exp(s\delta_t)$ yields

$$\Delta(s) = \exp(s\delta_t)\gamma_\Omega s + k_\mathrm{p}\rho_\Omega, \tag{A.4}$$

the asymptotic stability of which has to be checked by applying Theorem 1. Substituting $s = \mathrm{j}\omega$ in (A.4) and splitting into real and imaginary parts leads to

$$\Delta(\mathrm{j}\omega) = \tilde{\Delta}_\mathrm{Re}(\omega) + \mathrm{j}\tilde{\Delta}_\mathrm{Im}(\omega)$$

with

$$\begin{aligned}\tilde{\Delta}_\mathrm{Re}(\omega) &= k_\mathrm{p}\rho_\Omega - \gamma_\Omega\omega\sin(\omega\delta_t),\\ \tilde{\Delta}_\mathrm{Im}(\omega) &= \omega\gamma_\Omega\cos(\omega\delta_t).\end{aligned}$$

For symmetry reasons only $\omega > 0$ has to be considered in the following. With the substitution $z = \omega\delta_t$, the real and imaginary parts of Δ are

$$\Delta_\mathrm{Re}(z) = k_\mathrm{p}\rho_\Omega - \frac{\gamma_\Omega}{\delta_t} z\sin(z)$$

and

$$\Delta_\mathrm{Im}(z) = \frac{\gamma_\Omega}{\delta_t} z\cos(z).$$

Afterwards, Condition 2

$$\mathfrak{E}(\omega_0) = \frac{\mathrm{d}\tilde{\Delta}_\mathrm{Im}}{\mathrm{d}z}(\omega_0)\tilde{\Delta}_\mathrm{Re}(\omega_0) - \frac{\mathrm{d}\tilde{\Delta}_\mathrm{Re}}{\mathrm{d}z}(\omega_0)\tilde{\Delta}_\mathrm{Im}(\omega_0) > 0$$

of Theorem 1 for arbitrary $\omega_0 \in (-\infty, \infty)$, can easily be checked by choosing $\omega_0 = 0$ which results in

$$\mathfrak{E}(\omega_0) = \rho_\Omega k_\mathrm{p}\gamma_\Omega > 0,$$

fulfilling Condition 2. In a next step, Condition 1 of Theorem 1, the interlacing of the roots of Δ_Re and Δ_Im has to be analysed. The roots of the imaginary part $\Delta_\mathrm{Im}(z_j) = 0$ can be calculated analytically as

$$z_j = \begin{cases} 0, & j = 0,\\ \frac{\pi}{2} + (j-1)\pi, & j > 0,\end{cases}$$

with $j \in \mathbb{N}$ and Δ_{Im} as only simple real roots. Hereafter, the real part Δ_{Re} can be evaluated at z_j yielding

$$\begin{aligned}
\Delta_{\mathrm{Re}}(z_0) &= \rho_\Omega k_\mathrm{p} > 0 \\
\Delta_{\mathrm{Re}}(z_1) &= \rho_\Omega k_\mathrm{p} - \frac{\pi}{2}\frac{\gamma_\Omega}{\delta_t} \\
\Delta_{\mathrm{Re}}(z_2) &= \rho_\Omega k_\mathrm{p} + \frac{3\pi}{2}\frac{\gamma_\Omega}{\delta_t} > 0 \\
\Delta_{\mathrm{Re}}(z_3) &= \rho_\Omega k_\mathrm{p} - \frac{5\pi}{2}\frac{\gamma_\Omega}{\delta_t} \\
&\vdots \\
\Delta_{\mathrm{Re}}(z_j) &= \begin{cases} \rho_\Omega k_\mathrm{p}, & j = 0, \\ \rho_\Omega k_\mathrm{p} - (-1)^{j+1} z_j \frac{\gamma_\Omega}{\delta_t}, & j > 0. \end{cases}
\end{aligned}$$

If the roots of Δ_{Im} and Δ_{Re} interlace, then $\Delta_{\mathrm{Re}}(z_1), \Delta_{\mathrm{Re}}(z_3), \Delta_{\mathrm{Re}}(z_5), \ldots$ are smaller than zero, because $\Delta_{\mathrm{Re}}(z_0) > 0$. For the parameter k_p the conditions

$$\begin{aligned}
k_\mathrm{p} &> 0 \\
\rho_\Omega k_\mathrm{p} - z_1\frac{\gamma_\Omega}{\delta_t} &< 0 \\
k_\mathrm{p} &< z_1\frac{\gamma_\Omega}{\rho_\Omega\delta_t} =: M_1 \\
\rho_\Omega k_\mathrm{p} + z_2\frac{\gamma_\Omega}{\delta_t} &> 0 \\
k_\mathrm{p} &> -z_2\frac{\gamma_\Omega}{\rho_\Omega\delta_t} =: M_2 \\
\rho_\Omega k_\mathrm{p} - z_3\frac{\gamma_\Omega}{\delta_t} &< 0 \\
k_\mathrm{p} &< z_3\frac{\gamma_\Omega}{\rho_\Omega\delta_t} =: M_3 \\
\rho_\Omega k_\mathrm{p} + z_4\frac{\gamma_\Omega}{\delta_t} &> 0 \\
k_\mathrm{p} &> -z_4\frac{\gamma_\Omega}{\rho_\Omega\delta_t} =: M_4 \\
&\vdots
\end{aligned}$$

have to hold. As a consequence, $z_j < z_i$ for $j < i \in \mathbb{N}$ and $|M_j| < |M_i|$ for $j < i \in \mathbb{N}$. Now intersecting these conditions leads to

$$\cdots < M_4 < M_2 < 0 < k_\mathrm{p} < M_1 < M_3 < \ldots$$

and k_p has to meet

$$0 < k_\mathrm{p} < M_1 = \frac{\pi}{2}\frac{\gamma_\Omega}{\rho_\Omega\delta_t}$$

as the smallest upper bound.

A.2 Application of the results from Silva et al. (2000)

In the following, the results from Silva et al. (2000) are presented using a different notation based on the retarded TDS

$$\dot{e}_{\Omega}(t) + a e_{\Omega}(t) + \frac{b}{\gamma_{\Omega}} (k_{\mathrm{p}} - a)\, e_{\Omega}(t - \delta_t) = 0,$$

according to (2.45), with the positive parameters a, b, δ_t and γ_{Ω}. The corresponding quasi-polynomial reads

$$\Delta^*(s) = \frac{1}{a} s + 1 + \frac{b}{a\gamma_{\Omega}} (k_{\mathrm{p}} - a) \exp(-s\delta_t),$$

which can be multiplied with $\exp(s\delta_t)$ yielding the expression

$$\Delta(s) = \exp(s\delta_t) \left(\frac{1}{a} s + 1 \right) + \frac{b}{a\gamma_{\Omega}} (k_{\mathrm{p}} - a),$$

the asymptotic stability of which can be analysed using the generalised Hermite-Biehler theorem. The results from Silva et al. (2000) can be applied using the substitutions and assumptions

$$L = \delta_t > 0, \qquad T = \frac{1}{a} > 0, \qquad k = \frac{b}{a\gamma_{\Omega}} > 0, \qquad k_{\mathrm{c}} = k_{\mathrm{p}} - a,$$

which are yielding the limits of k_{c} as

$$-\frac{1}{k} < k_{\mathrm{c}} < \frac{T}{kL} \sqrt{\tilde{z}^2 + \left(\frac{L}{T} \right)^2},$$

where $\tilde{z}$ is the solution of

$$\tan(\tilde{z}) = -\frac{T}{L} \tilde{z}$$

in the interval $[\pi/2, \pi]$. The limits for the proportional gain k_{p} are thus following as

$$k_{\mathrm{p,min}} = a - \frac{1}{k}$$

and

$$k_{\mathrm{p,max}} = a + \frac{T}{kL} \sqrt{\tilde{z}^2 + \left(\frac{L}{T} \right)^2}.$$

A.3 Neutral first-order time-delay system

In the following section, the calculations for *Case 2: Considerations based on the mathematical model of the DC motor* from Section 2.4.2 are restated, i.e. the approximation (2.43a) is not considered. For that, the model of the motor regarding the angular velocity

$$\dot{\Omega}(t) = \eta(t) - a\Omega(t) + bu(t) \tag{A.5}$$

is taken into account. According to (2.35), the corresponding MFC law reads

$$u(t) = \frac{1}{\gamma_\Omega}\left(\dot{\Omega}_\mathrm{r}(t) - \hat{f}_\Omega(t) - k_\mathrm{p}\hat{e}_\Omega(t)\right), \tag{A.6}$$

with the estimate of the unknown part

$$\hat{f}_\Omega(t) = \dot{\hat{\Omega}}(t) - \gamma_\Omega\hat{u}(t). \tag{A.7}$$

The quantity $\dot{\hat{\Omega}}(t)$ in (A.7) can be replaced by a filtered version of (A.5) yielding

$$\hat{f}_\Omega(t) = \hat{\eta}(t) - a\hat{\Omega}(t) + (b - \gamma_\Omega)\hat{u}(t). \tag{A.8}$$

The experimental results depicted in Fig. A.1 can be used to validate (A.8) since this figure shows the graphs of both sides of (A.8) over time under the assumption $\hat{\eta}(t) \approx 0$. The parameter combinations used to generate these results are marked with red dots on line (A) in Fig. 3.11. In Fig. A.1 (a) the effects from the assumption $\hat{\eta}(t) \approx 0$ and the uncertainty of the identified parameter b is clearly visible since both graphs do not match exactly, especially for $t > 3.3\,\mathrm{s}$. However, this figure shows that the approximation (2.43a) is justified for $\gamma_\Omega \approx b$. An increase in the value of γ_Ω leads to a less distinct difference between both sides of (A.8) because the expression $\gamma_\Omega\hat{u}(t)$ becomes more dominant (see Fig. A.1 (b) and (c)). To simplify the following discussion, the dependence of the variable $\hat{u}(t)$ in (A.8) is eliminated by replacing it with a filtered version of the input from (A.5) leading to

$$\hat{f}_\Omega(t) = \hat{\eta}(t) - a\hat{\Omega}(t) + \frac{b - \gamma_\Omega}{b}\left(\dot{\hat{\Omega}}(t) + a\hat{\Omega}(t) - \hat{\eta}(t)\right). \tag{A.9}$$

Remark A.2 *It should be remarked that neither* (A.8) *nor* (A.9) *would be used for the implementation of the feedback law* (A.6) *since they undermine the benefits of the proposed MFC scheme by explicitly using a model of the considered system.*

Inserting the MFC law (A.6) together with the estimate (A.9) into (A.5) yields

$$\dot{\Omega}(t) - \frac{\gamma_\Omega - b}{\gamma_\Omega}\dot{\hat{\Omega}}(t) + a\Omega(t) + \frac{b}{\gamma_\Omega}\left(k_\mathrm{p}\hat{e}_\Omega(t) - a\hat{\Omega}(t)\right) - \frac{(\gamma_\Omega - b)a}{\gamma_\Omega}\hat{\Omega}(t) = \frac{b}{\gamma_\Omega}\dot{\Omega}_\mathrm{r}(t) - \left(\frac{\gamma_\Omega - b}{\gamma_\Omega} + \frac{b}{\gamma_\Omega}\right)\hat{\eta}(t) + \eta(t). \tag{A.10}$$

Subtracting $a\Omega_\mathrm{r}(t)$, $-ba/\gamma_\Omega\hat{\Omega}_\mathrm{r}(t)$, $\dot{\Omega}_\mathrm{r}(t)$, and $-(\gamma_\Omega - b)/\gamma_\Omega\dot{\hat{\Omega}}_\mathrm{r}(t)$ from both sides of (A.10) leads to

$$\dot{e}_\Omega(t) - \frac{\gamma_\Omega - b}{\gamma_\Omega}\dot{\hat{e}}_\Omega(t) + ae_\Omega(t) + \frac{b}{\gamma_\Omega}\left(k_\mathrm{p} - a\right)\hat{e}_\Omega(t) - \frac{(\gamma_\Omega - b)a}{\gamma_\Omega}\hat{e}_\Omega(t) = g_\Omega(\Omega_\mathrm{r}(t), \dot{\Omega}_\mathrm{r}(t)) + q_\Omega(\eta(t))$$

with

$$g_\Omega(\Omega_\mathrm{r}(t), \dot{\Omega}_\mathrm{r}(t)) = \left(\frac{b}{\gamma_\Omega} - 1\right)\dot{\Omega}_\mathrm{r}(t) + \frac{\gamma_\Omega - b}{\gamma_\Omega}\dot{\hat{\Omega}}_\mathrm{r}(t) - a\Omega_\mathrm{r}(t) + \frac{ba}{\gamma_\Omega}\hat{\Omega}_\mathrm{r}(t)$$
$$q_\Omega(\eta(t)) = \eta(t) - \left(\frac{\gamma_\Omega - b}{\gamma_\Omega} + \frac{b}{\gamma_\Omega}\right)\hat{\eta}(t).$$

Assuming $g_\Omega(\Omega_\mathrm{r}(t), \dot{\Omega}_\mathrm{r}(t)) + q_\Omega(\eta(t)) \approx 0$ and neglecting the estimation error of the algebraic differentiators as well as the effect of disturbances on the measurement yields

$$\dot{e}_\Omega(t) - \frac{\gamma_\Omega - b}{\gamma_\Omega}\dot{e}_\Omega(t - \delta_t) + ae_\Omega(t) + \frac{b}{\gamma_\Omega}\left(k_\mathrm{p} - a\right)e_\Omega(t - \delta_t) - \frac{(\gamma_\Omega - b)a}{\gamma_\Omega}e_\Omega(t - \delta_t) \approx 0, \tag{A.11}$$

which is a neutral TDS since the highest derivative of e_Ω occurs delayed and undelayed (see, e.g. Fridman (2014, Sec. 1.2)). The stability of (A.11) cannot be analysed using the generalised Hermite-Biehler theorem since the corresponding quasi-polynomial does not satisfy Assumption ($\mathcal{A}1$). Nonetheless, the numerical results depicted in Fig. A.2 justify the approximation of the neutral TDS (A.11) with the retarded TDS (2.45). In Fig. A.2 (a) and (b) the sign of the spectral abscissa (see, e.g. Appeltans et al. (2022, Sec. 2)), i.e. the real part of the rightmost characteristic root, of the quasi-polynomials of (2.45) and (A.11) are depicted. Yellow and dark blue mark a positive and a negative spectral abscissa, respectively. The red lines are identical in all subfigures and depict the results from (2.46), whereas the dashed line indicates the minimum values of k_p and the solid line its maximum values. The spectral abscissa is obtained by the MATLAB package *TDS-CONTROL* (see Appeltans et al. (2022) and Appeltans and Michiels (2023)) by sampling the depicted parameter set and using the provided functions *tds_create*, *tds_create_neutral*, and *tds_roots* which is called with the *region* variable set to zero but no other options are set. Fig. A.2 (a) validates the bound calculated by (2.46) except for a small number of parameter combinations. Numerical errors during the calculation of the roots using *tds_roots* might be the origin of this mismatch. Comparing Fig. A.2 (a) with (b) shows that for values of $\gamma_\Omega \ll b$ and $b \ll \gamma_\Omega$, i.e. the regions marked with (I) and (II), respectively, the approximation $\hat{f}_\Omega(t) \approx -a\hat{\Omega}(t)$ is not valid, which matches the considerations made for (A.8). Nonetheless, the approximation using the retarded TDS is justified because Fig. A.2 (a) and (b) show qualitatively the same stability characteristics. In Fig. A.2 (c), experimental results from Section 3.5.1 are presented in a different way. Parameter combinations leading to an activation of the safety routine are coloured yellow and a

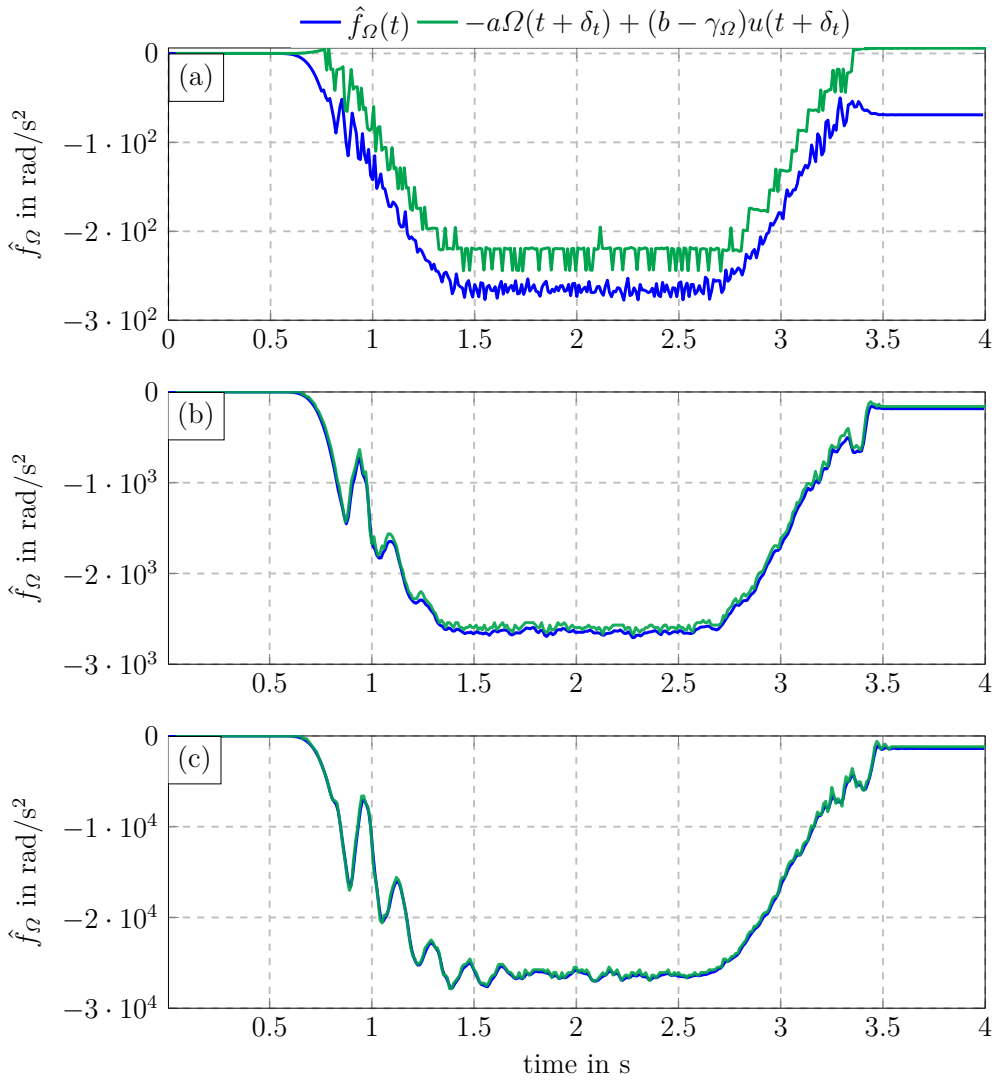

Fig. A.1: Validation of (A.8) for the parameter combinations marked with red dots on line (A) in Fig. 3.11 under the assumption $\hat{\eta}(t) \approx 0$.

stable closed loop is coloured dark blue. The white circles again indicate parameter combinations that are not generating a high enough voltage to overcome friction. Interestingly, the region marked with (I) in Fig. A.2 (b) can also be found in Fig. A.2 (c) but the region marked with (II) is non existing. This might be due to unmodelled effects such as friction and backlash of the gearbox. Nonetheless, the experimental data proves that the considerations made in Section 2.4.2 are valid.

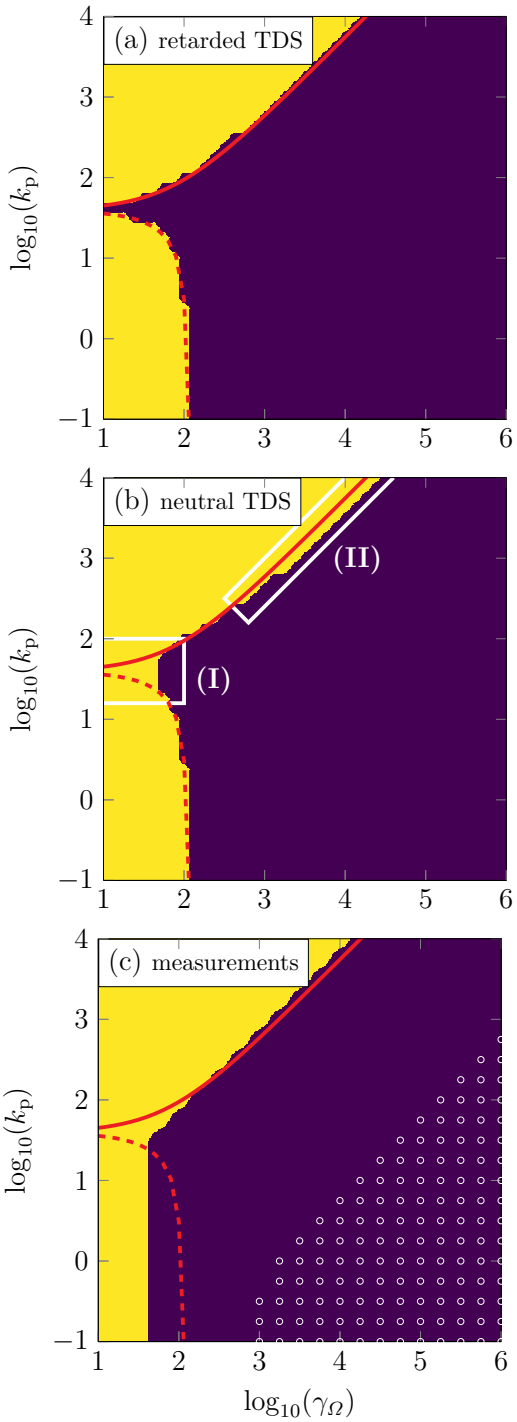

Fig. A.2: Comparison of the spectral abscissa of (2.45) in (a) and (A.11) in (b), obtained by the MATLAB package *TDS-CONTROL*. Yellow and dark blue mark a positive and a negative spectral abscissa, respectively. Subfigure (c) presents the experimental results from Section 3.5.1 in a different way. The red lines depict the results from (2.46), whereas the dashed line indicates the minimum values of k_p and the solid line its maximum values.

A.4 Simple second-order time-delay system

In the following, the asymptotic stability of the retarded TDS

$$\gamma_\theta \ddot{e}_\theta(t) + k_\mathrm{d}\rho_\theta \dot{e}_\theta(t-\delta_t) + k_\mathrm{p}\rho_\theta e_\theta(t-\delta_t) = 0, \tag{A.12}$$

with the positive parameters $\gamma_\theta, \rho_\theta$ and δ_t is investigated. The quasi-polynomial of (A.12) reads

$$\Delta^*(s) = \gamma_\theta s^2 + (k_\mathrm{d}\rho_\theta s + k_\mathrm{p}\rho_\theta)\exp(-s\delta_t)$$

and multiplication with $\exp(s\delta_t)$ yields

$$\Delta(s) = \exp(s\delta_t)\gamma_\theta s^2 + k_\mathrm{d}\rho_\theta s + k_\mathrm{p}\rho_\theta.$$

Using the substitution $s = \mathrm{j}\omega$ and splitting $\Delta(\mathrm{j}\omega)$ into real and imaginary parts leads to

$$\begin{aligned}\tilde{\Delta}_\mathrm{Re}(\omega) &= \rho_\theta k_\mathrm{p} - \gamma_\theta\omega^2\cos(\delta_t\omega)\\ \tilde{\Delta}_\mathrm{Im}(\omega) &= \omega\left(\rho_\theta k_\mathrm{d} - \gamma_\theta\omega\sin(\delta_t\omega)\right).\end{aligned}$$

For further considerations, the substitution $z = \delta_t\omega$ is applied, yielding

$$\begin{aligned}\Delta_\mathrm{Re}(z) &= \rho_\theta k_\mathrm{p} - \frac{\gamma_\theta}{\delta_t^2}z^2\cos(z)\\ \Delta_\mathrm{Im}(z) &= \frac{z}{\delta_t}\left(\rho_\theta k_\mathrm{d} - \frac{\gamma_\theta}{\delta_t}z\sin(z)\right).\end{aligned}$$

In the next step, Condition 2 of Theorem 1 has to be checked, which is done using $\omega_0 = 0$ as in Appendix A.1, leading to

$$\mathfrak{E}(\omega_0) = \rho_\theta^2 k_\mathrm{d} k_\mathrm{p} > 0,$$

which fulfils the condition of the theorem. The latter equation reveals that the parameters k_d and k_p are both either greater or smaller than zero. To test Condition 1 of Theorem 1, the roots z_j of $\Delta_\mathrm{Im}(z_j) = 0$ are calculated yielding

$$z_0 = 0$$

and

$$\frac{\rho_\theta k_\mathrm{d}}{\sin(z_j)} = \frac{\gamma_\theta}{\delta_t}z_j \tag{A.13}$$

the latter of which has no analytical solution. In Fig. A.3 (a) a graphical representation of (A.13) can be found for the case that $0 < k_\mathrm{d} < k_\mathrm{d,max}$ whereas $k_\mathrm{d,max}$ is the largest value of the parameter k_d, such that (A.13) has two zeros in the interval $(0, \pi)$. Fig. A.3

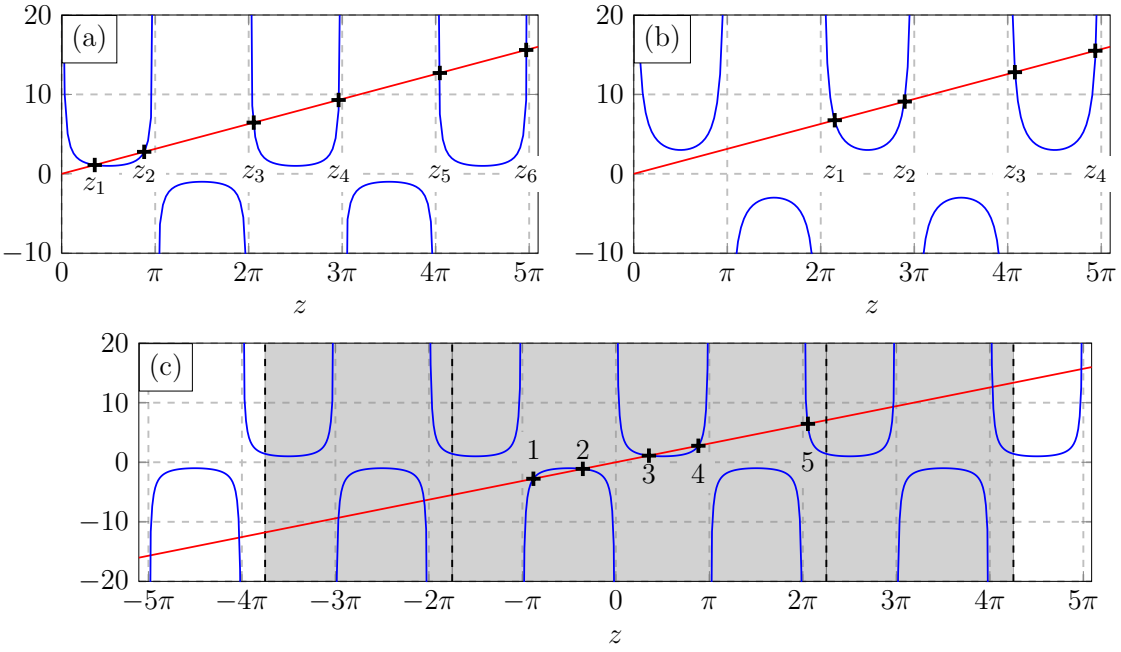

Fig. A.3: Graphical representation of (A.13) for (a) $0 < k_\mathrm{d} < k_\mathrm{d,max}$ and (b) $k_\mathrm{d} \geq k_\mathrm{d,max}$, whereas $k_\mathrm{d,max}$ marks the largest value such that (A.13) has two zeros in the interval $(0, \pi)$.

(b) shows the case that $k_\mathrm{d} \geq k_\mathrm{d,max}$ and (A.13) has no zeros in the interval $(0, \pi)$. In the following, if $0 < k_\mathrm{d} < k_\mathrm{d,max}$, this is called Case 1, and if $k_\mathrm{d,max} < k_\mathrm{d}$ Case 2.

Theorem 2 is used, to check whether Δ_Im has solely real roots. In accordance with the specified values of $M = 2$ and $N = 1$, $\eta = \pi/4$ is chosen, resulting in $\Delta_\mathrm{Re}(\eta) \neq 0$, $\Delta_\mathrm{Im}(\eta) \neq 0$. For Case 1, observing Fig. A.3 (c), one can easily verify that Δ_Im has six real roots in the interval $[-2\pi + \eta, 2\pi + \eta]$, including a root at the origin, fulfilling the conditions of Theorem 2 for $l = 1$. From Fig. A.3 c) it is also clear that Δ_Im has two real roots in the interval $[2l\pi + \eta, 2(l+1)\pi + \eta]$ and $[-2(l+1)\pi + \eta, -2l\pi + \eta]$, respectively. Therefore, for Case 1, Theorem 2 is satisfied for any $l > 0$ which implies that Δ_Im has only real roots. For Case 2, Theorem 2 can be used together with the fact that Δ_Im has no roots within the interval $[0, \pi]$ to demonstrate that Δ_Im has not only real roots, thus no stability can be achieved. Considering the latter findings, $k_\mathrm{d,max}$ is the upper bound for the parameter k_d. This bound is reached if the graphs of $\rho_\theta k_\mathrm{d}/\sin(z_j)$ and $\gamma_\theta z_j/\delta_t$ are touching each other. This point is called $\tilde{z}$ and the condition is equivalent to

$$\frac{\mathrm{d}}{\mathrm{d}z} \frac{\rho_\theta k_\mathrm{d}}{\sin(z)}\bigg|_{z=\tilde{z}} = \frac{\gamma_\theta}{\delta_t},$$

together with (A.13) resulting in

$$\tilde{z} = -\tan(\tilde{z}).$$

Evaluating the latter equation numerically yields $\tilde{z} \approx 2.0288$ and with this the range of the parameter k_d is set to

$$0 < k_\mathrm{d} < \frac{\gamma_\theta}{\delta_t \rho_\theta} \tilde{z} \sin(\tilde{z}).$$

For further considerations the following notation for the real part

$$\Delta_\mathrm{Re}(z) = \rho_\theta \left(k_\mathrm{p} - \mathfrak{a}(z)\right)$$

with

$$\mathfrak{a}(z) = \frac{\gamma_\theta}{\rho_\theta \delta_t^2} z^2 \cos(z)$$

is introduced, which has to be evaluated at the roots of the imaginary part Δ_Im called z_j, starting with

$$\Delta_\mathrm{Im}(z_0) = \rho_\theta k_\mathrm{p} \Rightarrow k_\mathrm{p} > 0.$$

Based on the latter result it is now clear, that $k_\mathrm{d} > 0$. The remaining $z_j, j = 1, 2, 3, \ldots$ result in

$$\Delta_\mathrm{Im}\Big(z_j(k_\mathrm{d})\Big) = \rho_\theta \left(k_\mathrm{p} - \mathfrak{a}\Big(z_j(k_\mathrm{d})\Big)\right)$$

and in combination with the interlacing of the roots of Δ_Im and Δ_Re it is clear that

$$\begin{aligned}
\Delta_\mathrm{Im}\Big(z_1(k_\mathrm{d})\Big) < 0 &\Rightarrow k_\mathrm{p} < \mathfrak{a}\Big(z_1(k_\mathrm{d})\Big) \\
\Delta_\mathrm{Im}\Big(z_2(k_\mathrm{d})\Big) > 0 &\Rightarrow k_\mathrm{p} > \mathfrak{a}\Big(z_2(k_\mathrm{d})\Big) \\
\Delta_\mathrm{Im}\Big(z_3(k_\mathrm{d})\Big) < 0 &\Rightarrow k_\mathrm{p} < \mathfrak{a}\Big(z_3(k_\mathrm{d})\Big) \\
&\vdots
\end{aligned}$$

To get an upper bound for k_p, the odd values $\mathfrak{a}\Big(z_1(k_\mathrm{d})\Big), \mathfrak{a}\Big(z_3(k_\mathrm{d})\Big), \ldots$ have to be considered. The smallest of these bounds is the one restricting the parameter k_p, leading to

$$0 < k_\mathrm{p} < \min_{j=1,3,\ldots} \mathfrak{a}(z_j).$$

Finally, if the delay δ_t and the input gains γ_θ and ρ_θ are given, the admissible parameter set of k_p and k_d can be calculated.

A.5 Application of the results from Farkh et al. (2009)

In this section, the results of Farkh et al. (2009) are presented and the notation is changed, to fit the considerations of Section 2.4.3. In the previously mentioned section,

the retarded TDS

$$\ddot{e}_\theta(t) + a\dot{e}_\theta(t) + \frac{b}{\gamma_\theta}\left(k_\mathrm{d} - a\right)\dot{e}_\theta(t-\delta_t) + \frac{b}{\gamma_\theta}k_\mathrm{p}e_\theta(t-\delta_t) = 0 \tag{A.14}$$

is determined, the asymptotic stability of which has to be analysed. The corresponding modified quasi-polynomial is

$$\Delta(s) = \frac{b}{\gamma_\theta}(k_\mathrm{d} - a)s + \frac{b}{\gamma_\theta}k_\mathrm{p} + (s+a)\,s\exp(s\delta_t).$$

In Farkh et al. (2009, Sec. 3) the stability of a PI controller for a first-order delay system with the quasi-polynomial

$$\Delta(s) = (KK_\mathrm{i} + KK_\mathrm{p}s) + (1+Ts)\,s\exp(Ls)$$

is investigated, with $K, T, L > 0$, leading to the range of the proportional gain

$$-\frac{1}{K} < K_\mathrm{p} < \frac{T}{KL}\sqrt{\tilde{z}^2 + \left(\frac{L}{T}\right)^2},$$

with $\tilde{z}$ the solution of

$$\tan(\tilde{z}) = -\frac{T}{L}\tilde{z}$$

in the interval $[\pi/2, \pi]$. The admissible range of the integral gain is

$$0 < K_\mathrm{i} < \min_{j=1,3,5,\ldots} \mathfrak{a}(z_j)$$

with

$$\mathfrak{a}(z_j) = \frac{z_j}{KL}\left(\sin(z_j) + \frac{T}{L}z_j\cos(z_j)\right)$$

whereas z_j being the roots of the imaginary part

$$\Delta_\mathrm{Im}(z) = \frac{z}{L}\left(KK_\mathrm{p} + \cos(z) - \frac{T}{L}z\sin(z)\right),$$

which are $z_0 = 0$ and the solution of

$$KK_\mathrm{p} + \cos(z_j) = \frac{T}{L}z_j\sin(z_j).$$

Applying the substitutions

$$L = \delta_t, \qquad a = \frac{1}{T}, \qquad K = \frac{b}{\gamma_\theta}, \qquad k_\mathrm{p} = aK_\mathrm{i}, \qquad k_\mathrm{d} = aK_\mathrm{p} + a,$$

to the latter results is yielding the conditions for the stability of (A.14).

A.6 Generalisation of the results from Laabidi et al. (2011)

In the following, the asymptotic stability of the linear second-order system

$$\ddot{y}(t) = bu(t) - a_1\dot{y}(t) - a_0 y(t) \tag{A.15}$$

with $a_1, a_0, b > 0$ which is controlled with the MFC law

$$u(t) = \frac{1}{\gamma}\left(\ddot{y}_\mathrm{r}(t) - k_\mathrm{d}\dot{\hat{e}}(t) - k_\mathrm{p}\hat{e}(t) - \hat{f}(t)\right) \tag{A.16}$$

with $e(t) = y(t) - y_\mathrm{r}(t)$ and $\gamma > 0$ is investigated. The MFC law (A.16) is based on the ultra-local model

$$\ddot{y}(t) = \rho u(t) + f(t). \tag{A.17}$$

Comparing (A.15) with (A.17) leads to

$$f(t) = -a_1\dot{y}(t) - a_0 y(t)$$

and

$$\hat{f}(t) \approx -a_1\dot{y}(t-\delta_t) - a_0 y(t-\delta_t).$$

According to Remark 2.7, it is necessary to verify the validity of this approximation. Using the controller (A.16) in (A.15) under the assumption that no disturbance occurs and the effects of the approximation error of the algebraic differentiator is negligible yields

$$\ddot{y}(t) = \frac{b}{\gamma}\left(\ddot{y}_\mathrm{r}(t) - k_\mathrm{d}\dot{\hat{e}}(t) - k_\mathrm{p}\hat{e}(t) - \hat{f}(t)\right) - a_1\dot{y}(t) - a_0 y(t). \tag{A.18}$$

Thereafter, subtracting $\ddot{y}_\mathrm{r}(t)$, $-b\gamma^{-1}a_j\hat{y}_\mathrm{r}^{(j)}(t), j \in \{0,1\}$ and $a_j y_\mathrm{r}^{(j)}(t), j \in \{0,1\}$ on both sides of (A.18) leads to the differential equation

$$\ddot{e}(t) + \frac{b}{\gamma}(k_\mathrm{d} - a_1)\dot{\hat{e}}(t) + \frac{b}{\gamma}(k_\mathrm{p} - a_0)\hat{e}(t) + a_1\dot{e}(t) + a_0 e(t) = g_y(\ddot{y}_\mathrm{r}(t), \dot{y}_\mathrm{r}(t), y_\mathrm{r}(t))$$

with

$$\begin{aligned} g_y(\ddot{y}_\mathrm{r}(t), \dot{y}_\mathrm{r}(t), y_\mathrm{r}(t)) = {} & \left(\frac{b}{\gamma} - 1\right)\ddot{y}_\mathrm{r}(t) - a_1\dot{y}_\mathrm{r}(t) - a_0 y_\mathrm{r}(t) \\ & + \frac{b}{\gamma}a_1\dot{y}_\mathrm{r}(t-\delta_t) + \frac{b}{\gamma}a_0 y_\mathrm{r}(t-\delta_t). \end{aligned}$$

Neglecting the effects of the function g_y yields the modified quasi-polynomial

$$\Delta(s) = \left(s^2 + a_1 s + a_0\right)\exp(s\delta_t) + (\kappa_\mathrm{d} s + \kappa_\mathrm{p})$$

with the substitutions and assumptions

$$\kappa_\mathrm{p} = \frac{b}{\gamma}(k_\mathrm{p} - a_0) > 0, \qquad \kappa_\mathrm{d} = \frac{b}{\gamma}(k_\mathrm{d} - a_1) > 0.$$

The following considerations are a generalisation of the results from Laabidi et al. (2011) and most findings can be transferred to this case. Using $s = \mathrm{j}\omega$, splitting into real and imaginary part and applying the substitution $z = \delta_t\omega$ yields the expressions

$$\begin{aligned}\Delta_\mathrm{Re}(z) &= -\left(\frac{z}{\delta_t}\right)^2 \cos(z) - a_1 \sin(z)\frac{z}{\delta_t} + a_0\cos(z) + \kappa_\mathrm{p}\\ \Delta_\mathrm{Im}(z) &= -\left(\frac{z}{\delta_t}\right)^2 \sin(z) + (a_1\cos(z) + \kappa_\mathrm{d})\frac{z}{\delta_t} + a_0\sin(z).\end{aligned}$$

Thereafter, Condition 2 of Theorem 1 can be checked by choosing $\omega_0 = 0$, leading to

$$\mathfrak{E}(\omega_0) = (a_0 + \kappa_\mathrm{p})\,(a_1 + \kappa_\mathrm{d} + a_0\delta_t) > 0,$$

which implies $\kappa_\mathrm{p} > -a_0$ as well as $\kappa_\mathrm{d} > -a_1 - \delta_t a_0$. In the next step, the interlacing condition of Δ_Im and Δ_Re has to be checked. The roots z_j of the imaginary part are $z_0 = 0$ on one hand and the solution of

$$f(z_j) = g(z_j)$$

with

$$\begin{aligned}f(z) &= \left(\frac{z}{\delta_t} - \frac{\delta_t}{z}a_0\right)\sin(z)\\ g(z) &= a_1\cos(z) + \kappa_\mathrm{d},\end{aligned}$$

on the other hand. Form here on out, two cases have to be considered. In the first case, the parameter κ_d has to obey $\kappa_\mathrm{d,min} = -a_1 - \delta_t a_0 < \kappa_\mathrm{d} < \kappa_\mathrm{d,max}$, whereas $\kappa_\mathrm{d,max}$ is the biggest value of the parameter, such that the graphs of f and g are tangent in the interval $[0, 3\pi/2]$. In the second case, the condition $\kappa_\mathrm{d,max} < \kappa_\mathrm{d}$ is fulfilled. Following the statements made in Laabidi et al. (2011) regarding Theorem 2, with $\eta = \pi/4$ it can be shown that in the first case Δ_Im has only real roots and the opposite is true for the second case. The touching condition for f and g can be calculated by

$$\left.\frac{\mathrm{d}f}{\mathrm{d}z}\right|_{z=\tilde{z}} = \left.\frac{\mathrm{d}g}{\mathrm{d}z}\right|_{z=\tilde{z}}$$

resulting in

$$\tan(z) = -\frac{\frac{z}{\delta_t} - \frac{\delta_t}{z}a_0}{\frac{1}{\delta_t} + \frac{\delta_t}{z^2}a_0 + a_1}.$$

Thereafter, numerically solve

$$\tan(\tilde{z}) = -\frac{\frac{\tilde{z}}{\delta_t} - \frac{\delta_t}{\tilde{z}} a_0}{\frac{1}{\delta_t} + \frac{\delta_t}{\tilde{z}^2} a_0 + a_1},$$

in order to obtain $\tilde{z} \in [0, 3\pi/2]$. Now the latter value can be used to calculate

$$\kappa_{\mathrm{d,max}} = \kappa_{\mathrm{d}}(\bar{z}) = \left(\frac{\bar{z}}{\delta_t} - \frac{\delta_t}{\bar{z}} a_0 \right) \sin(\bar{z}) - a_1 \cos(\bar{z}),$$

the upper bound of the parameter κ_{d}. To determine the admissible values of κ_{p}, the real part $\Delta_{\mathrm{Re}}(z)$ is evaluated at z_j, leading to

$$\Delta_{\mathrm{Re}}(z_j) = \kappa_{\mathrm{p}} - \mathfrak{a}(z_j)$$

with

$$\mathfrak{a}(z_j) = \left(\left(\frac{z_j}{\delta_t} \right)^2 - a_0 \right) \cos(z_j) + a_1 \sin(z_j) \frac{z_j}{\delta_t}.$$

The root $z_0 = 0$ yields with $-a_0$ the lower bound of the parameter κ_{p}. The upper bound is obtained by the interlacing property with the odd values for j, i.e. $j = 1, 3, 5, \ldots$ from

$$\Delta_{\mathrm{Re}}(z_j) = \kappa_{\mathrm{p}} - \mathfrak{a}(z_j) < 0$$

which leads to

$$-a_0 < \kappa_{\mathrm{p}} < \min_{j=1,3,5,\ldots} \mathfrak{a}(z_j).$$

At last, if the values for κ_{p} and κ_{d} are found, the corresponding values for k_{p} and k_{d} can be calculated as

$$k_{\mathrm{p}} = \frac{\gamma}{b} \kappa_{\mathrm{p}} + a_0$$

as well as

$$k_{\mathrm{d}} = \frac{\gamma}{b} \kappa_{\mathrm{d}} + a_1.$$

Bibliography

Al Younes, Y., Drak, A., Noura, H., Rabhi, A., and El Hajjaji, A. (2014). Model-Free Control of a Quadrotor Vehicle. In *2014 Int. Conf. on Unmanned Aircraft Systems (ICUAS)*, pages 1126–1131. IEEE. DOI: 10.1109/ICUAS.2014.6842366.

Allen, L., O'Connell, A., and Kiermer, V. (2019). How can we ensure visibility and diversity in research contributions? How the Contributor Role Taxonomy (CRediT) is helping the shift from authorship to contributorship. *Learn. Publ.*, 32(1):71–74. DOI: 10.1002/leap.1210.

Appeltans, P. and Michiels, W. (2023). Analysis and controller-design of time-delay systems using TDS-CONTROL. A tutorial and manual. *arXiv preprint arXiv:2305.00341*. DOI: 10.48550/arXiv.2305.00341.

Appeltans, P., Silm, H., and Michiels, W. (2022). TDS-CONTROL: a MATLAB package for the analysis and controller-design of time-delay systems. *IFAC-PapersOnLine*, 55(16):272–277. DOI: 10.1016/j.ifacol.2022.09.036.

Bara, O., Olama, M., Djouadi, S., Kuruganti, T., Fliess, M., and Join, C. (2017). Model-free Load Control for High Penetration of Solar Photovoltaic Generation. In *2017 North American Power Symposium (NAPS)*, pages 1–6. IEEE. DOI: 10.1109/NAPS.2017.8107328.

Barth, J., Condomines, J.-P., Bronz, M., Moschetta, J.-M., Join, C., and Fliess, M. (2020). Model-free control algorithms for micro air vehicles with transitioning flight capabilities. *Int. J. Micro Air Veh.*, 12:1–22. DOI: 10.1177/1756829320914264.

Bekcheva, M., Join, C., and Mounier, H. (2018). Cascaded Model-Free Control for trajectory tracking of quadrotors. In *2018 Int. Conf. on Unmanned Aircraft Systems (ICUAS)*, pages 1359–1368. IEEE. DOI: 10.1109/ICUAS.2018.8453339.

Belhadjoudja, M. C., Maghenem, M., and Witrant, E. (2023). On the Intelligent Proportional Controller Applied to Linear Systems. In *62nd IEEE Conf. on Decision and Control (CDC)*, pages 938–943. IEEE. DOI: 10.1109/CDC49753.2023.10383795.

Carvalho, A. D., Pereira, B. S., Angélico, B. A., Laganá, A. A. M., and Justo, J. F. (2024). Model-free control applied to a direct injection system: Experimental validation. *Fuel*, 358:130071. DOI: 10.1016/j.fuel.2023.130071.

d'Andréa-Novel, B., Fliess, M., Join, C., Mounier, H., and Steux, B. (2010). A mathematical explanation via "intelligent" PID controllers of the strange ubiquity of PIDs. In *18th Mediterranean Conf. on Control and Automation, MED'10*, pages 395–400. DOI: 10.1109/MED.2010.5547700.

De Miras, J., Join, C., Fliess, M., Riachy, S., and Bonnet, S. (2013). Active magnetic bearing: A new step for model-free control. In *52nd IEEE Conf. on Decision and Control (CDC)*, pages 7449–7454. IEEE. DOI: 10.1109/CDC.2013.6761072.

Delaleau, E. (2014). A Proof of Stability of Model-Free Control. In *2014 IEEE Conf. on Norbert Wiener in the 21st Century (21CW)*, pages 1–7. IEEE. DOI: 10.1109/NORBERT.2014.6893908.

Doetsch, G. (1974). *Introduction to the Theory and Application of the Laplace Transformation*. Springer.

Doublet, M., Join, C., and Hamelin, F. (2016). Model-free control for unknown delayed systems. In *2016 3rd Conf. on Control and Fault-Tolerant Systems (SysTol)*, pages 630–635. DOI: 10.1109/SYSTOL.2016.7739819.

Farkh, R., Laabidi, K., and Ksouri, M. (2009). PI Control for Second Order Delay System with Tuning Parameter Optimization. *Int. J. of Electrical and Electronics Eng.*, 3(1):1–7. DOI: hal-00588322.

Fliess, M. and Join, C. (2009). Model-free control and intelligent PID controllers: Towards a possible trivialization of nonlinear control? *IFAC Proc. Volumes*, 42(10):1531–1550. DOI: 10.3182/20090706-3-FR-2004.00256.

Fliess, M. and Join, C. (2013). Model-free control. *Int. J. Control*, 86(12):2228–2252. DOI: 10.1080/00207179.2013.810345.

Fliess, M. and Join, C. (2023). Towards a control-theoretic trivialization of ABR video streaming. *arXiv preprint arXiv:2310.00934*. DOI: 10.48550/arXiv.2310.00934.

Fliess, M., Lévine, J., Martin, P., and Rouchon, P. (1992). Sur lessystèmesnon linéaires différentiellement plats. *CR Acad. Sci. Paris*, page 619.

Fliess, M., Lévine, J., Martin, P., and Rouchon, P. (1995). Flatness and defect of nonlinear systems: introductory theory and examples. *Int. J. Control*, 61(6):1327–1361. DOI: 10.1080/00207179508921959.

Fridman, E. (2014). *Introduction to Time-Delay Systems: Analysis and Control*. Birkhäuser Cham. DOI: 10.1007/978-3-319-09393-2.

Gédouin, P.-A., Delaleau, E., Bourgeot, J.-M., Join, C., Arbab Chirani, S., and Calloch, S. (2011). Experimental comparison of classical PID and model-free control: Position control of a shape memory alloy active spring. *Control Eng. Pract.*, 19(5):433–441. DOI: 10.1016/j.conengprac.2011.01.005.

Haddar, M., Chaari, R., Baslamisli, S. C., Chaari, F., and Haddar, M. (2019). Intelligent PD controller design for active suspension system based on robust model-free control strategy. *Proc. of the Institution of Mechanical Engineers, Part C*, 233(14):4863–4880. DOI: 10.1177/0954406219836443.

Han, J. (2009). From PID to Active Disturbance Rejection Control. *IEEE Trans. Ind. Electron.*, 56(3):900–906. DOI: 10.1109/TIE.2008.2011621.

Hegedűs, T., Fényes, D., Németh, B., Szabó, Z., and Gáspár, P. (2022). Design of Model Free Control with tuning method on ultra-local model for lateral vehicle control purposes. In *2022 American Control Conf. (ACC)*, pages 4101–4106. DOI: 10.23919/ACC53348.2022.9867837.

Kiltz, L. (2017). *Algebraische Ableitungsschätzer in Theorie und Anwendung*. Doctoral dissertation, Saarland University, Germany. DOI: 10.22028/D291-27034.

Kiltz, L. and Rudolph, J. (2013). Parametrization of algebraic numerical differentiators to achieve desired filter characteristics. In *52nd IEEE Conf. on Decision and Control (CDC)*, pages 7010–7015, Florence, Italy. DOI: 10.1109/CDC.2013.6761000.

Krishnan, R. (2001). *Electric Motor Drives: Modeling, Analysis, and Control*. Prentice Hall, New Jersey.

Laabidi, K., Farkh, R., and Ksouri, M. (2011). First Order Controller for Time Delay System. *J. Dyn. Sys., Meas., and Control*, 133(5):054502. DOI: 10.1115/1.4003798.

Lafont, F., Balmat, J.-F., Join, C., and Fliess, M. (2020). First steps toward a simple but efficient model-free control synthesis for variable-speed wind turbines. *arXiv preprint arXiv:2011.06415*. DOI: 10.46300/9106.2020.14.146.

Lafont, F., Balmat, J.-F., Pessel, N., and Fliess, M. (2015). A model-free control strategy for an experimental greenhouse with an application to fault accommodation. *Comput. Electron. Agric.*, 110:139–149. DOI: 10.1016/j.compag.2014.11.008.

Li, W., Yuan, H., Li, S., and Zhu, J. (2022). A Revisit to Model-Free Control. *IEEE Trans. Power Electron.*, 37(12):14408–14421. DOI: 10.1109/TPEL.2022.3197692.

Mamdani, E. H. (1974). Application of fuzzy algorithms for control of simple dynamic plant. In *Proc. of the Institution of Electrical Engineers*, volume 121, pages 1585–1588. IET. DOI: 10.1049/piee.1974.0328.

Mboup, M., Join, C., and Fliess, M. (2007). A revised look at numerical differentiation with an application to nonlinear feedback control. In *Proc. of the 15th Mediterranean Conf. on Control and Automation*. DOI: 10.1109/MED.2007.4433728.

Mboup, M., Join, C., and Fliess, M. (2009). Numerical differentiation with annihilators in noisy environment. *Numer. Algorithms*, 50(4):439–467. DOI: 10.1007/s11075-008-9236-1.

Mboup, M. and Riachy, S. (2014). A Frequency Domain Interpretation of the Algebraic Differentiators. *IFAC Proc. Volumes*, 47(3):9147–9151. DOI: 10.3182/20140824-6-ZA-1003.02132.

Mboup, M. and Riachy, S. (2018). Frequency-domain analysis and tuning of the algebraic differentiators. *Int. J. Control*, 91(9):2073–2081. DOI: 10.1080/00207179.2017.1421776.

Menhour, L., d'Andréa Novel, B., Fliess, M., Gruyer, D., and Mounier, H. (2017). An Efficient Model-Free Setting for Longitudinal and Lateral Vehicle Control: Validation Through the Interconnected Pro-SiVIC/RTMaps Prototyping Platform. *IEEE Trans. Intell. Transp. Syst.*, 19(2):461–475. DOI: 10.1109/TITS.2017.2699283.

Moraes, M. S. and da Silva, P. S. P. (2015). Model-free control of magnetic levitation systems through algebraic derivative estimation. In *Proc. 23rd ABCM Int. Congress of Mechanical Engineering, Rio de Janeiro*. DOI: 10.1002/asjc.2596.

Neves, G. P. and Angélico, B. A. (2021). Model-free control of mechatronic systems based on algebraic estimation. *Asian J. Control*, 24(4):1575–1584. DOI: 10.1002/asjc.2596.

Oppenheim, A. V. and Schafer, R. W. (1975). *Digital Signal Processing*. Englewood Cliffs, N. J., Prentice-Hall Inc.

Othmane, A. (2022a). AlgDiff: A Python package with MATLAB coupling implementing all necessary tools for the design, analysis, and discretization of algebraic differentiators. Available at `https://github.com/aothmane-control/Algebraic-differentiators`, version 2.3.

Othmane, A. (2022b). *Contributions to numerical differentiation using orthogonal polynomials and its application to fault detection and parameter identification*. Doctoral dissertation, Saarland University, Germany. DOI: 10.22028/D291-38806.

Othmane, A. (2024). On the parametrization of algebraic differentiators in the light of 'A survey on the discrete-time differentiators in closed-loop control systems: Experiments on an electro-pneumatic system'. *Control Eng. Pract.*, 144:105811. DOI: 10.1016/j.conengprac.2023.105811.

Othmane, A., Kiltz, L., and Rudolph, J. (2022). Survey on algebraic numerical differentiation: Historical developments, parametrization, examples, and applications. *Int. J. Syst. Sci.*, 53(9):1848–1887. DOI: 10.1080/00207721.2022.2025948.

Othmane, A., Mounier, H., and Rudolph, J. (2021a). Parametrization of algebraic differentiators for disturbance annihilation with an application to the differentiation of quantized signals. *IFAC-PapersOnLine*, 54(9):335–340. DOI: 10.1016/j.ifacol.2021.06.091.

Othmane, A. and Rudolph, J. (2023). AlgDiff: An open source toolbox for the design, analysis and discretisation of algebraic differentiators. *at-Automatisierungstechnik*, 71(8):612–623. DOI: 10.1515/auto-2023-0035.

Othmane, A., Rudolph, J., and Mounier, H. (2021b). Systematic comparison of numerical differentiators and an application to model-free control. *Eur. J. Control*, 62:113–119. DOI: 10.1016/j.ejcon.2021.06.020.

Polack, P., Delprat, S., and d'Andréa Novel, B. (2019). Brake and velocity model-free control on an actual vehicle. *Control Eng. Pract.*, 92:104072. DOI: 10.1016/j.conengprac.2019.06.011.

Polack, P., d'Andréa Novel, B., Fliess, M., de La Fortelle, A., and Menhour, L. (2017). Finite-Time Stabilization of Longitudinal Control for Autonomous Vehicles via a Model-Free Approach. *IFAC-PapersOnLine*, 50(1):12533–12538. DOI: 10.1016/j.ifacol.2017.08.2191.

Qin, S. J. and Badgwell, T. A. (2003). A survey of industrial model predictive control technology. *Control Eng. Pract.*, 11(7):733–764. DOI: 10.1016/S0967-0661(02)00186-7.

Rudolph, J. (2021). *Flatness-based control: An Introduction*. Shaker Verlag. DOI: 10.2370/9783844078930.

Scherer, P. M., Othmane, A., and Rudolph, J. (2023). Combining model-based and model-free approaches for the control of an electro-hydraulic system. *Control Eng. Pract.*, 133:105453. DOI: 10.1016/j.conengprac.2023.105453.

Scherer, P. M., Othmane, A., and Rudolph, J. (2024). Model-free control of a magnetically supported plate. *Control Eng. Pract.*, 148:105950. DOI: 10.1016/j.conengprac.2024.105950.

Silva, G. J., Datta, A., and Bhattacharyya, S. P. (2000). Stabilization of Time Delay Systems. In *Proc. of the 2000 American Control Conf. (ACC)*, volume 2, pages 963–970. IEEE. DOI: 10.1109/ACC.2000.876643.

Silva, G. J., Datta, A., and Bhattacharyya, S. P. (2002). New Results on the Synthesis of PID Controllers. *IEEE Trans. Automat. Contr.*, 47(2):241–252. DOI: 10.1109/9.983352.

Silva, G. J., Datta, A., and Bhattacharyya, S. P. (2005). *PID Controllers for Time-Delay Systems*. Birkhäuser Boston, MA. DOI: 10.1007/b138796.

Tabuada, P., Ma, W.-L., Grizzle, J., and Ames, A. D. (2017). Data-driven control for feedback linearizable single-input systems. In *56th IEEE Conf. on Decision and Control (CDC)*, pages 6265–6270. IEEE. DOI: 10.1109/CDC.2017.8264603.

Ushirobira, R. (2018). Algebraic differentiators through orthogonal polynomials series expansions. *Int. J. Control*, 91(9):2082–2089. DOI: 10.1080/00207179.2017.1406151.

Villagra, J. and Herrero-Pérez, D. (2012). A comparison of control techniques for robust docking maneuvers of an AGV. *IEEE Trans. on Control Syst. Technol.*, 20(4):1116–1123. DOI: 10.1109/TCST.2011.2159794.

Wachter, J., Gröll, L., and Hagenmeyer, V. (2023). Application of Model-Free Control to Reduce the Total Harmonic Distortion of Inverters. In *2023 8th IEEE Workshop on the Electronic Grid (eGRID)*, pages 1–7. DOI: 10.1109/eGrid58358.2023.10380817.

Willems, J. C. (1972). Dissipative Dynamical Systems Part i: General Theory. *Arch. Rational Mech. Anal.*, 45(5):321–351. DOI: 10.1007/BF00276493.

Yeşildirek, A. and Lewis, F. L. (1995). Feedback Linearization Using Neural Networks. *Automatica*, 31(11):1659–1664. DOI: 10.1016/0005-1098(95)00078-B.

Zadeh, L. A. (1965). Fuzzy Sets. *Information and Control*, 8(3):338–353. DOI: 10.1016/S0019-9958(65)90241-X.

Zhang, H., Li, H., Mao, J., Pan, C., and Luan, Z. (2022). Model-free control of single-phase boost AC/DC converters. *IEEE Trans. on Power Electron.*, 37(10):11828–11838. DOI: 10.1109/TPEL.2022.3176937.

Ziane, M. A., Rafaralahy, H., Zasadzinski, M., and Join, C. (2023). Model-free control of alkaline electrolysis temperature with time delays. In *2023 IEEE 11th Inter. Conf. on Systems and Control (ICSC)*, pages 50–55. IEEE. DOI: 10.1109/ICSC58660.2023.10449752.